FLOW PHENOMENA IN FIXED–GAP AND GRAVURE ROLL COATING SYSTEMS

by

Nikil Kapur

Submitted in accordance with the requirements for the degree of

Doctor of Philosophy

The University of Leeds

School of Mechanical Engineering

May 1999

The candidate confirms that the work submitted is his own and that appropriate credit has been given where reference has been made to the work of others.

ABSTRACT

This thesis describes investigations into a number of coating processes using experimental, analytical and computational techniques.

The first problem, considered experimentally, is that of reverse roll coating with a liquid reservoir positioned directly above horizontally aligned rollers. Measurements of the film thickness as a function of the height of fluid in the reservoir and speed ratio are presented. When the wetting line is located downstream of the nip, either a decrease in the height of the associated hydrostatic head or an increase in the speed ratio causes a reduction in the thickness of the outgoing film. However, when the wetting line is located upstream of the nip the opposite is found to be true.

The bead–break instability in forward meniscus coating is considered both experimentally and analytically. Agreement between predictions from a simple mathematical model of the stable bead and experimentally determined meniscus positions is seen to be excellent. A perturbation hypothesis is used to predict the onset of the bead–break instability, at which the upstream meniscus accelerates rapidly towards the downstream one, so the two collide and the bead collapses. The results from the model compare well with experiments. An outline of a method for using the bead–break instability as a design criterion is also presented.

Typically in a slot, blade or knife coater the downstream meniscus is assumed to pin at a corner of the coating device. In chapter 5, a series of experiments and a corresponding computational study, are presented which illustrate that the meniscus can advance up the face of such coating devices (in this case a roll–flat plate system). Reducing the corner angle is seen to reduce the size of the climb region and the associated recirculation at this point at the downstream meniscus. It is also shown that the meniscus can detach from the corner and retreat into the gap, which can in turn give rise to the ribbing instability.

An offset gravure coating arrangement is considered in chapter 6. The coating arrangement is split into two areas of study — the offset gravure nip and the kiss coating bead. An experimental investigation of the offset nip with the two rolls

vertically aligned and running at the same speed in forward mode reveals two ways in which the metered film thickness can be influenced. Either increasing the nip force by pressing the two rolls together or decreasing the roll speeds causes a reduction in the metered film thickness. At higher speeds the metered film thickness is observed to asymptote to a limiting value, the value of which depends on the gravure pattern.

The reverse mode kiss coating bead operating at speed ratios greater than one is also investigated. Experiments reveal that under these conditions, all the fluid is transferred from the roll surface to the web and the two make contact due to the generation of a sub–ambient pressure field within the bead. Two models based on lubrication theory are derived, one assuming an infinitely tensioned web and a second that incorporates the effect of web flexibility. The latter is found to give much better agreement with the experimental data. Finally a perturbation hypothesis is applied to these to models in order to predict the onset of the ribbing instability, both of which are found to give reasonable agreement with the experimental data.

Finally, the results of a systematic experimental investigation of reverse mode direct gravure coating is reported, where the web runs directly over a gravure roll surface. This wide ranging parametric study illustrates the effect of the operating parameters on the final film thickness. Key findings are that speed ratio, fluid properties and cell shape and size can significantly influence the final film thickness. For a fixed roll speed it is observed that as the web speed is increased the gravure bead becomes unstable. This results in streaking on the web, and gives an upper limit to the speed ratio.

To Tricia

ACKNOWLEDGEMENTS

Firstly, I would like to express my sincere thanks to my supervisors, Prof. P.H. Gaskell and Prof. M.D. Savage, for their advice, support and encouragement over the last four years. I would also like to thank Dr. M. Wilson, Dr. H.M. Thompson and Dr. J.L. Summers for their help with numerical methods and other computational matters.

Thanks to Luciano Bellon and Paul Banks for their manufacturing skills, practical assistance and the endless supply of biscuits! Mr. P. 'Go' Moussalli and Mr A. Bates have provided me with many useful discussions about the industrial relevance of this work, and Mr. B. Wilde has provided help beyond the call of duty in setting up the pilot coating apparatus.

I would like to thank all my colleagues and friends in the School of Mechanical Engineering, the EFM research group and around the University for making my time here so enjoyable.

Special thanks go to my parents, brothers and grandparents for their constant support during my studies, and finally to Tricia for her encouragement and patience throughout.

Finally I would like to record my gratitude to the University of Leeds for supporting this research through a scholarship, and the School of Mechanical Engineering and DuPont for providing additional funding.

Contents

List of Figures

List of Tables

NOMENCLATURE

Most of the symbols used in this thesis have different meanings in different chapters while others are only relevant to short sections of text. Below are listed some of the symbols which have a general meaning, however specific definitions will depend on the context. A convention used throughout the thesis is that, unless otherwise indicated (and except for Re, Ca, S), quantities in upper case are dimensional while those in lower case are dimensionless.

Ca	Capillary number
H_0	Minimum gap width
H_1, H_2, H^∞	Outlet film thickness
H_i	Inlet film thickness
$H(X), h(x)$	Gap width
H_U, h_u	Gap at upstream meniscus
H_D, h_d	Gap at downstream meniscus
R_1, R_2	Roll radius
R_U, r_u	Radius of upstream meniscus
R_D, r_d	Radius of downstream meniscus
Re	Reynolds number
S	Speed ratio
U_1, U_2	Speed
Q	Flux
U, V, W, u, v, w	Velocity components
X, Y, Z, x, y, z	Cartesian coordinates
X_0	X position of the minimum gap
μ	Dynamic viscosity
ρ	Density
σ	Surface tension
θ_C	Static contact angle
θ_D	Dynamic contact angle

Chapter I

Introduction

Contents

1.1 Introduction

Liquid film coating is simply the process of replacing one fluid (usually air) on a solid surface by a liquid. The range of coated products in everyday use is vast – paper, photographic products, packaging materials, magnetic media (for example floppy disks; video cassettes) and aluminium sheets, to name but a few. The coated web or substrate range from being very flexible (thin plastic sheet) to being stiff (such as wood, board or metal).

Generally speaking, to produce coated films economically, three requirements need to be met :

- The film is evenly coated on the substrate to provide a product that meets with customer specification.
- The coated film is thin to minimise the drying load (as after coating the web the solvent — either aqueous or organic — needs to be removed by evaporation) and to minimise the solvent inventory in the process.
- The production rate of coated films needs to be high such that capital equipment costs can be minimised.

It is relatively easy to meet any two of these requirements, but it is becoming increasingly important from an economic and environmental perspective to meet all three. This has lead to a great deal of fundamental research in the area of wet coatings, predominantly in the last 20 years.

Of central importance to coating operations is the 'surface tension' of a fluid and the 'contact line' where the liquid meets a stationary or moving boundary. These are discussed in the following sections.

1.1.1 Surface Tension

Across a liquid–gas interface (as we are concerned only with single layer coatings in this thesis) is a steep gradient in density, where the properties change from those in

the bulk liquid to those in the bulk gas. At the interface the molecules are attracted more strongly to neighbouring molecules than those in the bulk, as illustrated in figure 1.1. This results in the surface layer acting with a tension along it. Mathematically this layer is assumed to have zero thickness.

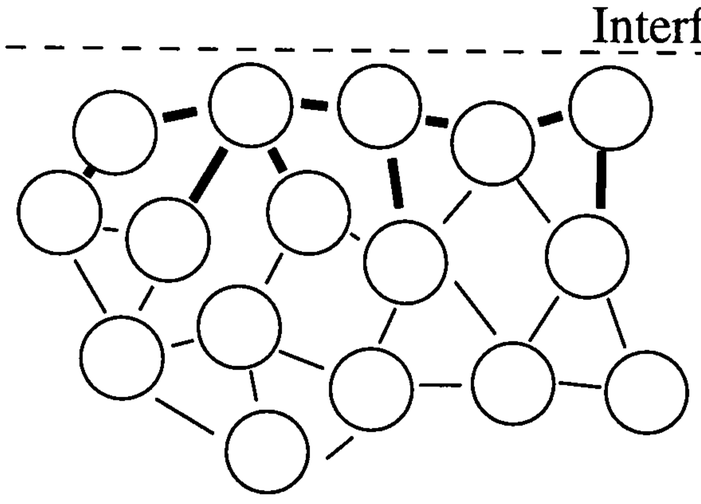

Figure 1.1: Surface tension of a liquid at an interface with a gas. The thicker lines represent a greater attractive force causing a tension at the surface.

Surfactants are commonly added to aqueous coating fluids to reduce the static surface tension. The partially hydrophobic/hydrophilic nature of a surfactant molecule means that they preferentially reside at the interface. As the intermolecular forces between the surfactant molecules is less than that between water molecules, the surface tension is reduced. The dynamic surface tension is caused by a concentration gradient of surfactant along the interface. This is generated when a new interface is formed, for example at a contact line, and fluid from the bulk comes onto the surface. It will take a small, but finite, time for the dispersed surfactant molecules to diffuse to the interface and an equilibrium to be established. Tricot (1997) presents a thorough review of this phenomenon.

1.1.2 The contact line

The contact line is a three phase boundary where two immiscible fluids meet at a solid boundary. The contact line is referred to as 'static' where the relative motion is zero, and 'dynamic' where the point of apparent contact moves relative to the

solid.

The static contact line can be quantified by a 'static contact angle', θ_c. For the liquid/gas system common in many coating flows this is the angle the liquid makes with the solid (measured through the liquid, as shown in figure 1.2). It can best be understood from a balance of forces given by the Young (1805) equation, shown in figure 1.2, where σ_{sg}, σ_{lg} and σ_{sl} are the surface tensions of the solid–gas, liquid–gas and solid–liquid interfaces. The horizontal forces balance when

$$\sigma_{sg} = \sigma_{sl} + \sigma_{lg} \cos\theta_c \tag{1.1}$$

where θ_c is the contact angle. The work of adhesion of the liquid to the solid is defined (Atkins, 1998) as

$$W_{ad} = \sigma_{lg} + \sigma_{sg} - \sigma_{sl} \tag{1.2}$$

and equation (1.1) can be written as

$$\cos\theta_c = \frac{W_{ad}}{\sigma_{lg}} - 1. \tag{1.3}$$

A liquid with a strong adhesion to the solid will wet well (and completely if $W_{ad} > 2\sigma_{lg}$) whilst those with strong cohesive bonds within the liquid will not.

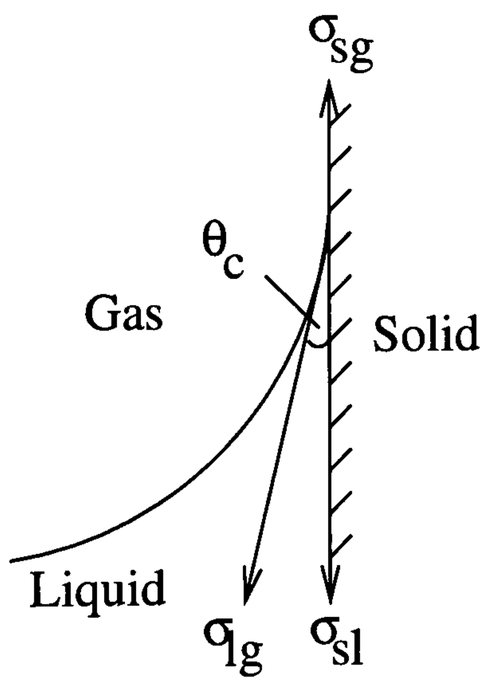

Figure 1.2: Balance of forces at the three phase boundary.

The physics at a contact line is still poorly understood, particularly when there is relative motion between the liquid and solid. In the modelling of this problem the jump from non–slip at the solid surface to the zero shear stress at the free surface gives rise to a stress singularity, and to calculate the flow field some property of the system must be relaxed. Commonly, the no–slip boundary condition at the wetting line is replaced by an explicit velocity distribution which increases from zero to the speed of the substrate over a distance given by the slip length; see Dussan (1979) for a comprehensive review of the physical arguments for the form the slip length expression can take. However, using this approach both the slip length and the dynamic contact angle, θ_D, need to be introduced into the model and have an (unknown) dependence on the speed and the fluid properties. A more recent theoretical approach by Shikhmurzaev (1993, 1994, 1996) is based on the flow near the contact line giving rise to a surface tension gradient along the two interfaces. Here the contact angle and slip length need not be imposed as part of the solution; however the model introduces several physical parameters, including a coefficient of sliding friction (in effect a slip length), which are difficult to interpret in physical terms, or to measure.

1.2 Classification of coaters

Coaters generally fall into one of two broad categories (Benjamin and Scriven, 1992) — self metered where the flux on the web depends on the fluid properties, geometry and operating conditions of the coater and pre–metered where the flux is set externally (for example *via* a selected pump rate) and all fluid is transferred to the web. Cross–sections through the metering region of common coating devices are shown in figures 1.3 (self metered) and 1.4 (pre-metered), some of which are discussed in more detail in the following sections.

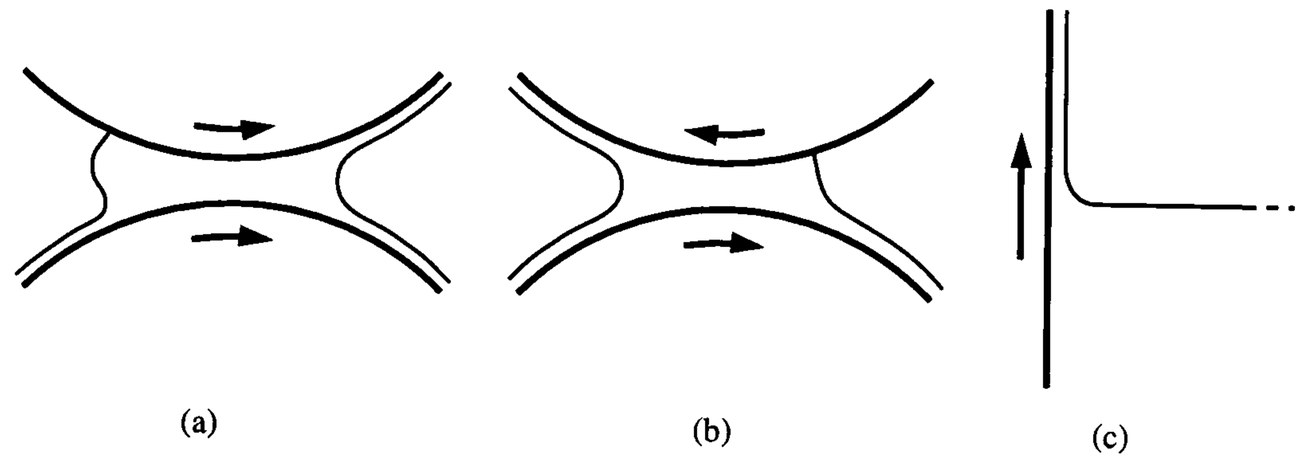

Figure 1.3: Examples of self metered coaters: (a) forward roll coater, (b) reverse roll coater, (c) dip coater.

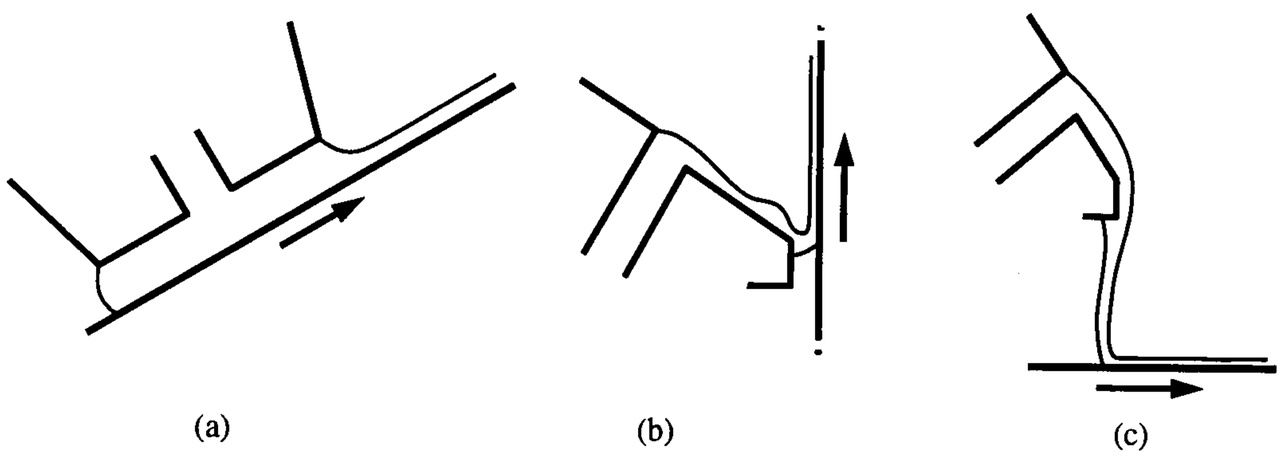

Figure 1.4: Examples of pre-metered coaters: (a) slot coater, (b) slide coater, (c) curtain coater.

1.3 Roll coaters

Roll coating is the process of depositing a thin layer of fluid on a web or substrate by using one or more rolls. Between each roll/web or roll/roll pair the speeds, roll radii, gap and fluid properties govern the film–split ratio and hence the thickness of the outgoing films. Roll coaters can be sub–classified, depending on the relative directions of the rolls, whether the rolls are rigid or if covered in a soft elastomer covering or possibly if the surface is patterned with gravure cells. These roll systems are reviewed below.

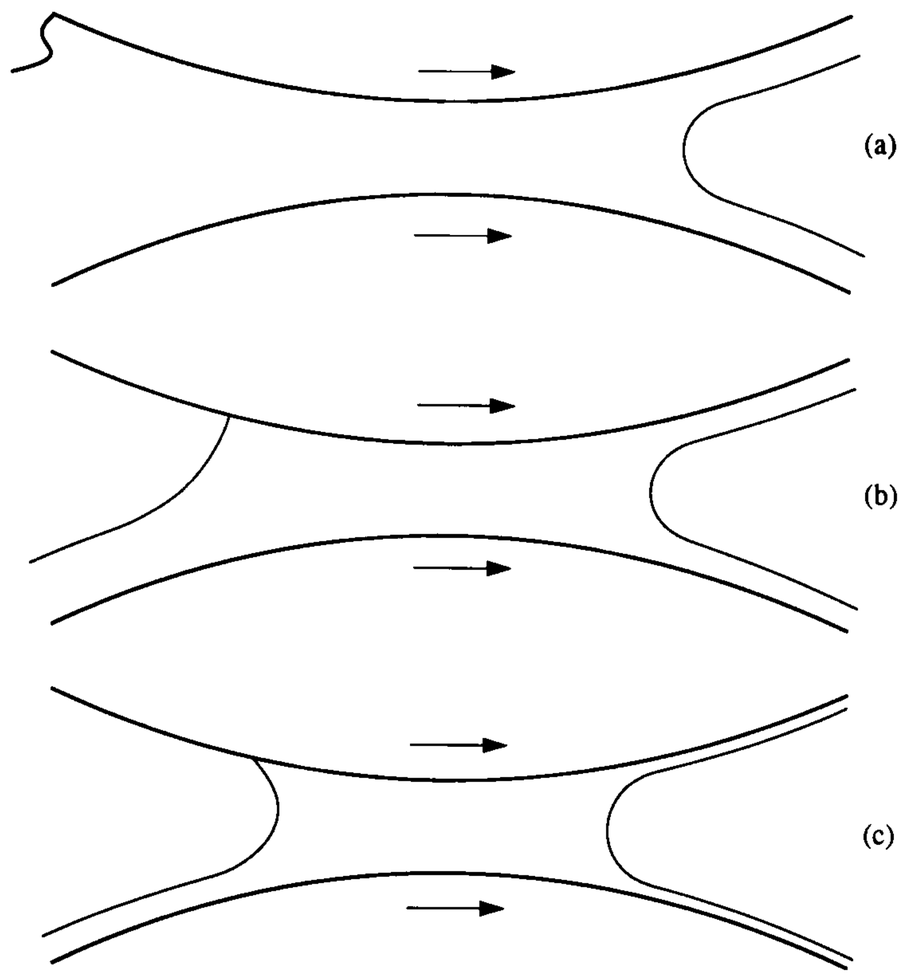

Figure 1.5: Classification of a forward roll coater based on the inlet film thickness: (a) fully flooded, (b) moderately starved and (c) ultra–starved.

1.3.1 Forward roll coaters

A forward roll coater consists, most simply, of a pair of counter–rotating rolls, such that the motion of the surfaces through the 'nip' is in the same direction. The 'nip' refers to the part of the coater where the two roll surfaces are in closest proximity. Forward roll coaters are generally used to coat films of between 25 μm and 60 μm thickness, at speeds of between 3 and 60 m/min for fluids of viscositys in the range 1–50 mPa s (Zink, 1979).

A forward roll coater can be further classified into fully flooded, moderately starved or ultra starved depending on the ratio of the inlet film thickness to the minimum gap, as illustrated in figure 1.5. This distinction was first observed experimentally by Malone (1992) and investigated computationally and analytically by Gaskell *et al.* (1995). The characteristic flow structures within the bead were found to be strongly dependent on the state of the inlet condition.

The speed ratio S for a forward roll coater is defined as $S = \frac{U_1}{U_2}$, as shown in figure 1.6.

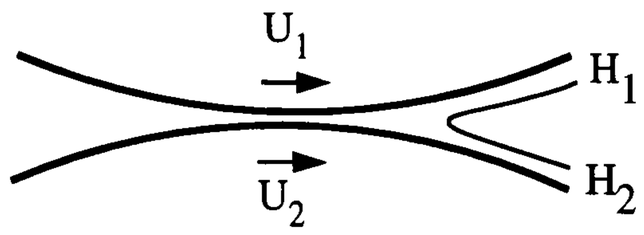

Figure 1.6: The location of the outgoing films H_1 and H_2 and the speeds of the rolls, U_1 and U_2 in forward roll coating.

The inlet flooded regime

The inlet flooded regime is the most extensively investigated of the three modes of operation, indeed it was not until 1992 that Malone highlighted the importance of the feed condition on the flow structures. In this regime of operation a rolling bank of fluid forms upstream of the nip, the inlet film being thicker than the gap so that some fluid rolls back into the reservoir.

Taylor (1963) was the first to suggest the flow in such a device could be split into two distinct regions – unidirectional flow through the nip and two–dimensional flow downstream of the nip where the film split occurs (figure 1.7). The flow in the nip can be modelled using Reynolds lubrication equation (1886) where the pressure distribution is determined subject to appropriate boundary conditions :

$$\frac{d}{dX}\left(H^3\frac{dP}{dX}\right) = 12\mu U\frac{dH}{dX} \tag{1.4}$$

where U is the characteristic speed, μ the viscosity, $H(X)$ the gap measured between the two roll surfaces, P the pressure and X the distance along the nip.

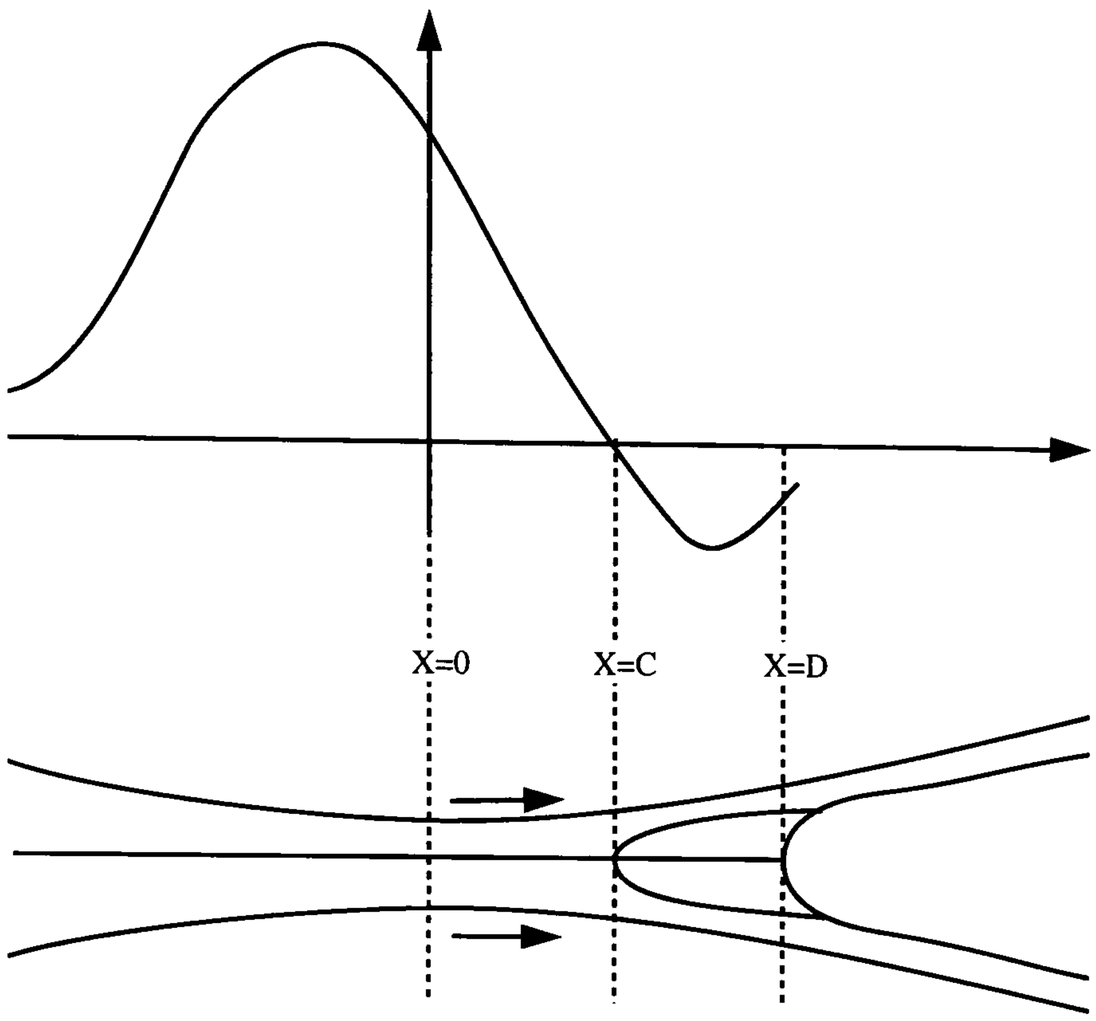

Figure 1.7: Pressure profile and flow structure in fully flooded forward roll coating.

Experimentally, Malone (1992) showed using a roll flat–plate arrangement that the pressure rises to a maximum and then falls to a minimum (below atmospheric pressure), before relaxing to capillary pressure at the meniscus (Decré *et al.* 1995).

The first boundary condition locates the upstream meniscus at $-\infty$ since it is far from the nip compared to a typical length scale in the Z direction. Three further boundary conditions are needed, two for the (2^{nd} order) Reynolds equation and one to locate the downstream meniscus.

The first is a condition stating that the pressure decays to ambient at the upstream interface, $P(-\infty) = 0$ where ambient pressure is taken as the reference pressure of zero.

The other two conditions at the downstream interface (located at $X = D$) are for P and $\frac{dP}{dX}$.

Reynolds (1886) suggested boundary conditions for the split of a liquid film, pos-

tulating that the capillary pressures are small and the pressure gradient is zero at $X = D$:

$$P(D) = \left(\frac{dP}{dX}\right)_{X=D} = 0. \tag{1.5}$$

These conditions are also known as the Swift–Stieber condition after the independent work of Swift (1931) and Stieber (1933), however such conditions do not predict the experimentally observed pressure profile, which has led others to propose alternatives.

Hopkins (1957) in a study of a lubricated sheet passing between two rolls proposed that the film split occurred at a stagnation point such that the flux divided in two. For equal speed rolls then the velocity and shear stress are zero at this point i.e.

$$U(D) = \left(\frac{dU}{dZ}\right)_{X=D} = 0. \tag{1.6}$$

These separation conditions (sometimes referred to at the Prandtl – Hopkins conditions due to Prandtl's (1904) work in this area) are often supplemented with the condition that the fluid pressure is constant through the recirculation region ($C \leq X \leq D$) and predicts the experimentally observed sub–ambient pressure loop.

Coyne and Elrod (1970,1971) derived a condition on pressure gradient by investigating a film smoothly separating from a flat plate and being dragged away by a nearby parallel plate. They assumed a quadratic velocity profile normal to the free surface and by matching the inlet and outlet flux found

$$\frac{dP}{dX} = \frac{6\mu U}{H^2}\left(1 - \frac{2H^{\infty}}{H_D}\right) \tag{1.7}$$

where H^{∞} is the outlet film thickness, H_D is the distance between the two roll surfaces at the film split point and the ratio $\frac{2H^{\infty}}{H_D}$ depends on capillary pressure. This condition was used to solve Reynolds equation in a two roll problem and the predictions found to be in good agreement with experimentally determined load carrying capacity and downstream meniscus location.

A second boundary condition that can be used to relate the film thickness to the height at the wetting point is due to Landau and Levich (1942). They modelled

the withdrawal of a plate from a bath and showed that radius of curvature of the meniscus is related to the film thickness by

$$H^{\infty} = 1.34RCa^{2/3}, \tag{1.8}$$

where R is the radius of the meniscus, although they did not explicitly determine the coefficient. The coefficient was determined later by Bretherton (1961) and Deryagin and Levi (1964). Ruschak (1976) and Wilson (1982) showed this expression to be valid as $Ca \to 0$. Ruschak (1982) showed it was only accurate for $Ca \lessapprox 0.01$ and proposed

$$H^{\infty} = 0.54RCa^{1/2} \tag{1.9}$$

to extend this range to $Ca \in [0.01, 0.1]$ using finite element calculations.

Flow rate and film split

The flow rate and film split ratio between the two rolls is important as these two parameters determine the final film thickness. Gatcombe (1945) in an investigation of flow between fully submerged rolls replaced the condition for pressure at the interface with $P(\infty) = 0$ and calculated that

$$\lambda = \frac{4}{3}, \tag{1.10}$$

where $\lambda = \frac{Q}{(U_1+U_2)H_0}$ and Q is the volumetric flux per unit length of roll. Benkreira *et al.* (1981) in a study of forward roll coating under typical operating conditions determined experimentally that

$$\lambda = 1.31. \tag{1.11}$$

Coyle (1984) and Coyle *et al.* (1986) using finite element methods with an inlet profile given by lubrication theory at the nip showed the film split ratio was given by

$$\frac{H_2}{H_1} = S^{0.65} \; S \in [0.1, 10]. \tag{1.12}$$

This is in good agreement with Benkreira *et al.* (1981) who determined

$$\frac{H_2}{H_1} = 0.87S^{0.65} \; S \in [0.03, 14.9] \tag{1.13}$$

for vertically aligned rolls. Decré *et al.* (1995) expressed the film split as

$$\frac{H_2}{H_1} = \alpha S^{\beta} \tag{1.14}$$

and found α to lie in the range 0.67 to 0.87, and β to lie in the range 0.52 to 0.73. Walker (1995) investigated the film split ratio and showed it to be dependent on (S, St, Ca, H_0/R) in order of decreasing importance which supports Decré *et al.*'s findings.

Ruschak (1985) modelled the withdrawal of rolls as flat plates such that

$$\frac{H_2}{H_1} = S^{2/3}, \tag{1.15}$$

whereas Savage (1982) used the separation conditions to derive

$$\frac{H_2}{H_1} = S^{1/2} \tag{1.16}$$

but later questioned the validity of using these conditions for $S \neq 0, 1$. Savage (1992) and Gaskell *et al.* (1998c) derived an alternate model based on $U = V = 0$ at the stagnation point giving:

$$\frac{H_2}{H_1} = \frac{S(S+3)}{(1+3S)} \quad 1 < S < 10. \tag{1.17}$$

Decré *et al.* (1995) showed equation 1.17 fitted the film split data well over a large range of speed ratios.

Moderately starved forward roll coating

As the inlet flux is reduced the rolling bank of fluid diminishes, as illustrated in figure 1.5. Malone (1992) using experiments, and later Gaskell *et al.* (1995) using finite

element analysis showed the flow domain can be characterised by two stagnation points in the nip between which the flow is essentially unidirectional.

The meniscus regime

Although used in industry for many years, this mode of operation escaped the coating community at large, until recently (Gaskell *et al.* 1995). Malone (1992), Gaskell *et al.* (1998a) and Wicks *et al.* (1995) experimentally showed the flow domain to consist of a small bead of fluid located between the two rolls and went on to elucidate the remarkable flow structures within the bead (figure 1.8). Thompson (1992) formulated a 'zero flux model' where the upper and lower rolls were replaced by flat plates and the menisci by vertical planes along which shear stress was zero. Neglecting the flux, he solved the biharmonic equation and produced streamline plots similar to those observed by Malone (1992). Gaskell *et al.* (1995) used a small flux model with arc–of–circle approximations for the radius of curvature of the free surface to show meniscus coating is a small capillary number regime with a completely sub–ambient pressure profile in which the capillary pressure plays a dominant role. Gaskell *et al.* (1995) also showed, using finite element calculations that there exist two modes of fluid transfer from one roll to the other (figure 1.8): ultra-starved where only a primary transfer jet exists and starved where a secondary jet is responsible for part of the transfer.

Gaskell *et al.* (1998a) confirmed experimentally the film split ratio shown in equation 1.15 for meniscus roll coating, and went on to include a gravity correction term in this equation, which gave better agreement with the experimental data.

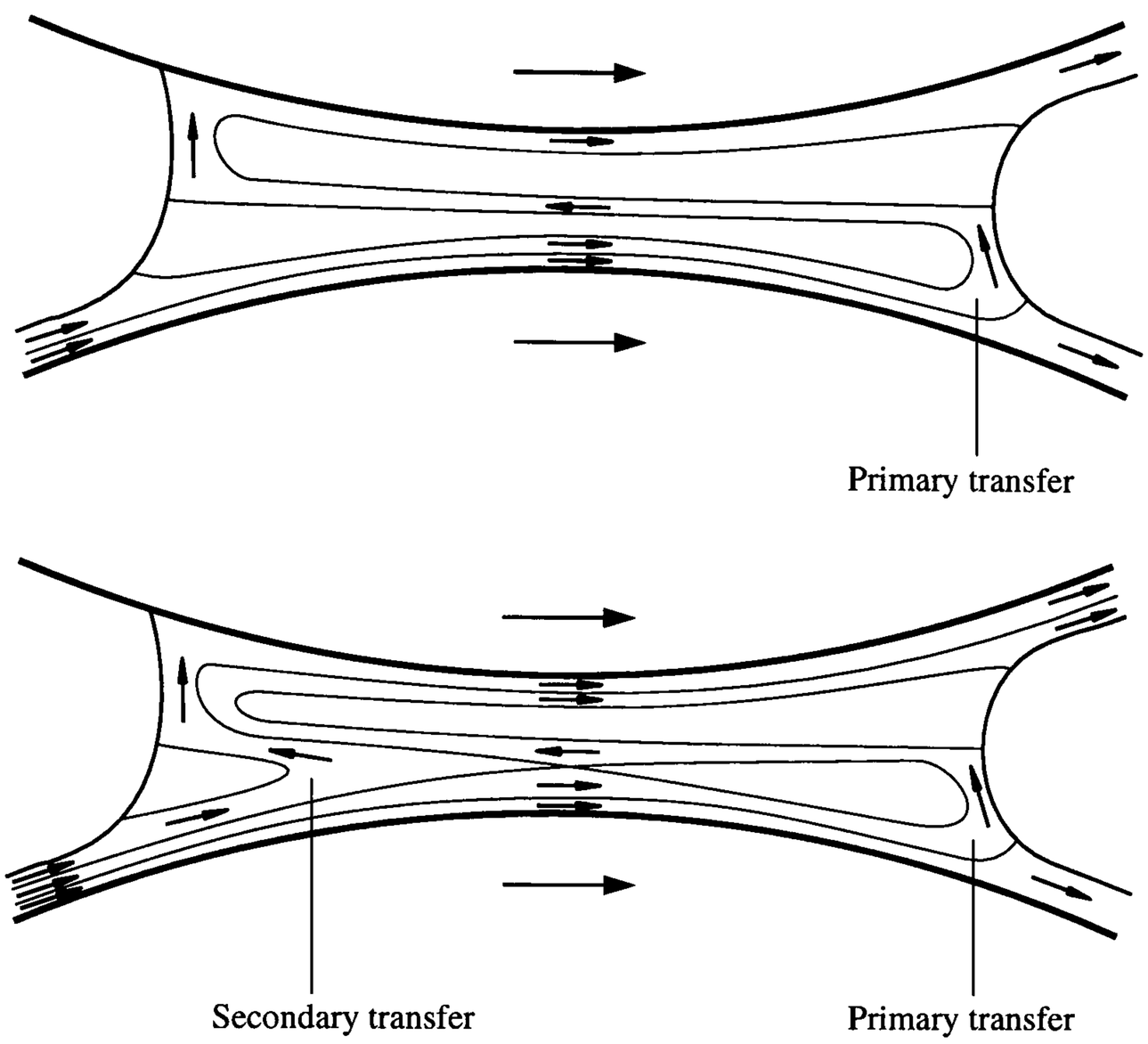

Figure 1.8: Transfer of fluid from the lower to the upper roll in ultra–starved and starved forward roll coating.

1.3.2 Reverse roll coating

A reverse roll coater is similar to a forward roll coater except that the direction of one of the rolls is reversed such that the two roll surfaces move through the nip in opposite directions, as shown in figure 1.9. Reverse roll coaters are used to coat films down to thicknesses of 25 μm at speeds of between 30–500 m/min with fluids of viscosities over a range of 0.01 to 50 Pa s (Richardson 1996).

The work of Richardson (1996) highlighted two regimes, inlet flooded and inlet starved where the incoming film is the same order or smaller than the gap width, respectively.

The speed ratio S is defined as $S = \frac{U_1}{U_2}$, as shown in figure 1.9.

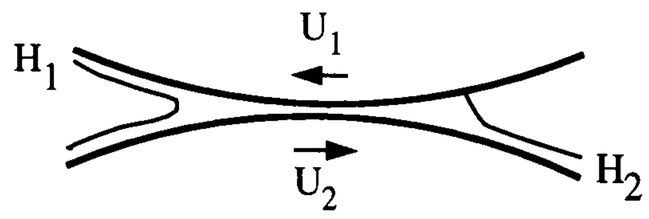

Figure 1.9: The location of the outgoing films H_1 and H_2 and the speeds of the rolls, U_1 and U_2 in reverse roll coating.

Inlet flooded

Broughton *et al.* (1950) performed an experimental study on an inlet flooded reverse roll coater and derived an empirical relationship for the lower film thickness as a function of the gap and speed ratio.

Lubrication models were formulated by Cheng and Savage (1978), Ho and Holland (1978), Greener and Middleman (1981) and Benkreira *et al.* (1982) which all gave expressions for the non–dimensional film thickness $h_2 = h_2/H_0$ of the form:

$$h_2 = A(1 - S) \quad A \in [1.23, 1.33], \quad \text{(valid for } S < 1\text{)}. \tag{1.18}$$

More accurate finite element based models were formulated by (for example) Coyle (1984), Coyle *et al.* (1990a) and Richardson (1996) which highlighted the structures in the flow field. Coyle *et al.* (1990b) asserted that lubrication theory does not predict the flow accurately enough, however Richardson (1996) applied the visco-capillary boundary condition (the Landau–Levich condition combined with a simple model for the shape of the interface) at both the upstream and downstream interface. This was based on a earlier model of Fukazawa *et al.* (1992), who applied this condition at just the downstream interface. In this way Richardson (1996) derived a model that predicted key transitions in the flow structure for $S < 1$, which are in close agreement with those obtained using finite element calculations.

Meniscus regime

Malone (1992) was the first to identify a meniscus regime in reverse roll coating. Richardson (1996) performed an exhaustive computational study and identified two different means of transfer from the lower to the upper roll, ultra-starved where transfer is *via* one jet, and starved where fluid is also transferred *via* a second jet.

1.3.3 Deformable roll coating

Deformable roll coaters are used in both forward and reverse modes, to coat films that are generally thinner than those of their rigid counterparts. A deformable roll pair most commonly consists of one steel and one elastomer covered roll. The rolls can be operated with a positive gap or with a negative gap where the rolls are in interference at rest, as shown in figure 1.10. Previous research in this area has been concerned only with deformable forward roll coating systems.

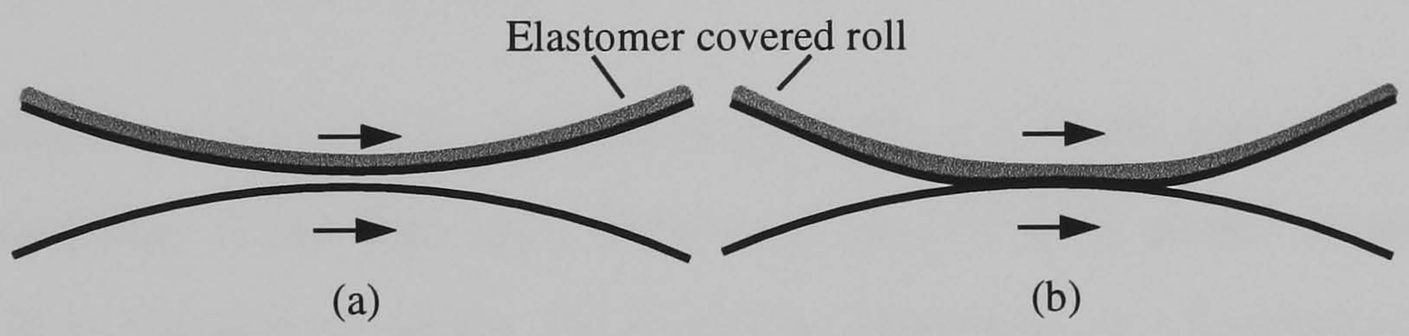

Figure 1.10: A deformable forward roll coater set with (a) a positive gap and (b) a negative gap.

Coyle (1988a) studied a deformable roll system and measured the sensitivity of the film thickness to a range of parameters – fluid properties, roll speeds and load — for a typical range of operating conditions. Adachi *et al.* (1988) considered flow between a roll and a flat–plate covered with a deformable layer; Cohu and Magnin (1995) performed similar experiments to Coyle (1988a) but showed the thickness of the deformable layer could affect the flux on the roll surfaces.

Coyle (1988b) formulated a one dimensional model (a Hookean spring model) for the solid where the deformation of the solid is directly proportional to local pressure of

the fluid, although this is strictly valid only for thin deformable layers with Poisson's ratio not equal to 0.5. The results for film thickness as a function of fluid viscosity, roll velocity, load and Youngs modulus of elasticity compared qualitatively with his experimental findings, but consistently over–predicted the film thickness.

Later, Carvalho and Scriven (1995) (again using a Hookean spring model for the deformable layer) considered two-dimensional flow between a rigid and deformable roll. They confirmed the experimental findings of Carvalho (1995) who showed for equal roll speeds the film thickness on the deformable roll was 10% higher than that on the rigid roll. They attributed this to the modified curvature of the deformable roll local to the downstream meniscus.

Recently Young (1998) has refined and extended the theoretical work of Carvalho, Scriven and Coyle to provide results for incompressible layers (Poissons ratio equal to 0.5) and more negative gaps and to consider the stability of such a system.

1.3.4 Multiple roll coaters

Often in practice a roll coater consists of more than a single pair of rolls. With a full understanding of the film split between a pair of rolls under all possible feed conditions it is possible to derive the final film thickness as a function of the parameters at each nip. Benjamin (1994) studied the double fed forward film split where each roll surface enters the nip with a film. Later, for a series of rolls with each nip operating in forward mode, Benjamin *et al.* (1995) derived an expression relating the final film thickness to the feed film thickness and speed ratio of all the gaps. Each film split was modelled by a power–law relationship $\frac{h_{i+1}}{h_i} = \alpha_i (S_{i+1,i})^{\beta i}$ with the parameters α_i, β_i depending on factors such as strength and direction of gravity, roll diameters and fluid rheology.

The equivalent system of reverse mode rolls proved more difficult to analyse as the expression for the film split ratio in such an arrangement is more complex. Wilson (1997) derived a lubrication model for a three roll arrangement, with the central roll having a film on both incoming surfaces. He concluded that no simple model could be derived to analyse multiple reverse roll coaters.

1.3.5 Gravure roll coaters

In the 1870's the first continuous gravure printing (intaglio) process was developed whereby an image was transferred from an inked patterned roll to a web (paper in this case). Over the next 20 years the gravure printing method developed into the gravure coating method as a substitute for plain roll coating, having the advantage of speed and accuracy in terms of the laid down film (Larkin, 1984). It is just this property that has ensured the continued use and development of gravure coating for the last 100 years. Gravure coaters can be operated at speeds of up to 15 m/s and are generally used with low viscosity fluids to give a final wet coat thickness of between 1 and 10 μm.

A gravure roll is a roller that has had a regular pattern of small depressions ('cells') cut into the surface. The pattern can be continuous in nature, for example a trihelical groove which runs around the cylinder, or it may consist of discrete cells. The cells can be one of a range of shapes (see section 2.3.2), and are generally made by one of two approaches. The older of the two is to take a copper plated cylinder and knurl the roll with a hard steel mesh. The roll is then nickel plated giving it a smooth surface. Recently laser engraved ceramic rolls have gained in popularity. Here a ceramic powder is sprayed through a hot flame onto a rotating roll to which it sticks. The built up layer of ceramic can then be etched using a laser and finally the surface is ground back to leave cells of a given volume. These rolls offer the advantage of good wear resistance so that the cell volume remains constant over a long period of operation.

Gravure coaters fall into one of two categories: offset or direct as shown in figure 1.11. For both cases the rotating gravure roll first picks up fluid which fills the gravure cells, for example by rotating in a reservoir. In direct gravure coating, a doctor blade held against the roll removes excess fluid from above the lands, a more detailed review of this process can be found in section 7.1.2. The action of the web (moving in the opposite direction to the roll) causes a proportion of the fluid to be removed from the cells. In offset gravure coating the fluid picked up by the gravure roll is metered by the action of the deformable roll. A fraction of the film on the

deformable roll is then coated onto the web, again moving in the opposite direction to the roll.

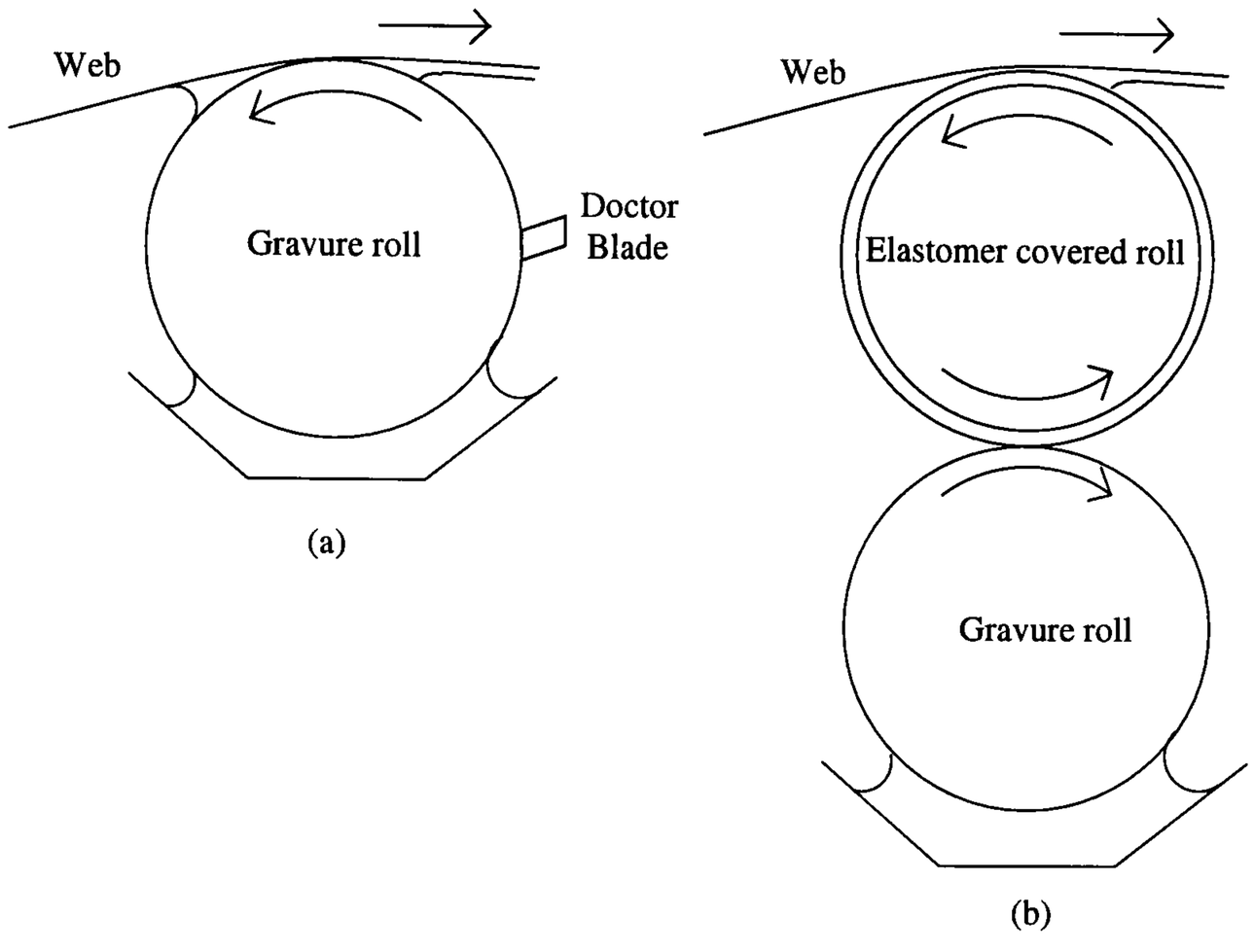

Figure 1.11: A cross–section through (a) a direct and (b) an offset gravure coater.

The web can also be driven in the same direction as the roll – this is termed forward gravure coating. The expression 'offset gravure' or 'direct gravure' used throughout this thesis always refers to the reverse mode of operation.

Offset gravure coating

Offset gravure coaters are used to coat films of around 10 μm thickness. They can coat substrates of a variety of thicknesses and offer good control over the final film thickness by varying the speed ratio and the nip pressure (Rees, 1995). The offset gravure coater shown in figure 1.11 can be split into two distinct regions (i) the nip region where fluid is transfered from the gravure roll to the deformable roll and (ii) the coating bead where fluid is transferred from the deformable roll to the web.

Nip region

The flow in the nip region is complex and is dominated by an interaction between a (rough) gravure roll and an elastomer covered roll. Rees (1995) showed the transferred film to be a function of nip pressure, the gravure pattern, the speed ratio and the magnitude of the roll speeds. Hanumanthu and Scriven (1996) studied flow between a gravure roll an a deformable roll. By using a transparent elastomer layer they were able to visualise the nip flow and concluded that past analyses of smooth rolls indicated trends that could be applied to the gravure system.

Coating bead

The region where the fluid is transferred from the roll to the web is commonly referred to as a kiss coater. Pearson (1985) examined a kiss coater operating in forward mode, and derived an expression for film thickness as a function of the operating parameters. Rees (1995) studied the (reverse mode) kiss coating bead experimentally and observed two distinct regimes, in keeping with the experiences of coating practitioners. When the speed of the web is slower than the roll ($S < 1$) then only a fraction of fluid is transferred to the web. However when $S > 1$ all the fluid is transferred to the web and the film thickness depends on the relative speed of web to roll and the thickness of film on the incoming roll surface.

Rees (1995) used a lubrication model to predict the amount of fluid left on the roll but was unable to calculate the fraction transferred to the web as he assumed an infinite bank of fluid upstream of the nip. Later Storey (1996) extended the analysis with more realistic boundary conditions and derived an expression for the final film thickness H_2 on the roll,

$$\frac{H_2}{R} = \frac{6}{5} Ca (1 - S)^2 \left(\frac{\sigma}{T\beta} \right) \quad (S < 1) \tag{1.19}$$

where R is the roll radius, Ca the capillary number based on the roll, S the speed ratio, σ the surface tension, T the web tension and β the wrap angle. As $S \rightarrow 1$, $H_2 \rightarrow 0$ in accordance with experimental observations. Further details of the

lubrication models derived by Rees and Storey can be found in Gaskell *et al.* (1998b). Storey also extended his work to a full two dimensional solution using finite elements, with a fully flexible web. The fluid flow proved to be rich in the flow structures and features observed in other coating devices used in reverse mode.

The foil bearing

The geometry of the kiss coating bead is similar to that of a foil bearing, and for this reason a brief review is presented here. Typically a foil bearing has a large angle of wrap with the minimum gap between the roll and web as small as 1 μm. The domain is infinite as it is lubricated only by air, with no wetting lines present.

Eshel and Elrod (1965, 1967) studied foil bearings with a high degree of wrap ($>$ 180°) and divided the domain into three : a convergent entrance region, a central region of constant gap and a divergent exit region. They used a numerical method to solve the lubrication equations in the entrance and exit regions.

Barlow (1967a) used shell theory to derive a general set of equations for the behaviour of a foil that included bending stiffness, foil inertia and fluid compressibility. Barlow (1967b) went on to present solutions for a reduced set of equations, Licht (1968) confirmed many of these findings in an extensive experimental study. More recently Stahl *et al.* (1974) used a finite difference scheme to solve the time dependent problem of the foil passing over a non–circular roll. The results were confirmed experimentally by Vogel and Groom (1974). Heinrich and Connolly (1992) used a finite element method to solve the equivalent problem in three dimensions.

Direct gravure coating

Direct gravure coating is one of the most difficult coating operations to study experimentally due to the extremely small length scales associated with the coating bead. Little is known about the actual mechanism that transfers fluid from the cells onto the moving web. Previous studies of gravure coating have concentrated on the emptying characteristics of the cell as a function of operating parameters.

Pulkrabek and Munter (1983) looked at the transfer of fluid from a trihelical roll to a web operating in the forward mode. They identified two coating defects: (i) 'multi-line pickout' where a line refers to a single groove on the roll surface. Here uneven ridges of fluid, similar to those encountered in ribbing (see section 1.6.2) are deposited on the web; (ii) flashing where transfer from a line does not occur, leaving an uncoated portion on the web. Patel and Benkreira (1991) examined the effect of the load on the doctor blade on the amount of fluid removed from the roll surface. Later, Benkreira and Patel (1993) investigated experimentally the amount of fluid transferred to a web for three gravure patterns and found the thickness of the final coated film was one third of the characteristic volume of the cell. Benkreira and Cohu (1998) studied forward mode gravure coating and showed the film thickness on the web was between 0.15 – 0.2 of the characteristic volume of the cell.

Rees (1995) proposed meniscus evacuation as a possible mechanism by which fluid was removed from a gravure cell. He used a pair of contra–rotating rolls, one with an elastomer layer on the surface and the second with coarse cut gravure cells, and observed the cells to be partially emptied by the dragging action of the meniscus as a cell passed beneath it. As a first step to modelling the problem Rees formulated a model for an inlet flooded slot coater with a time varying domain. He considered a moving step as it passed under the free surface (both facing forward and backwards) and a rectangular groove passing through the domain, as illustrated in figure 1.12. He observed the meniscus dipped slightly into the cell as it passed through the domain but no fluid was removed from the cell.

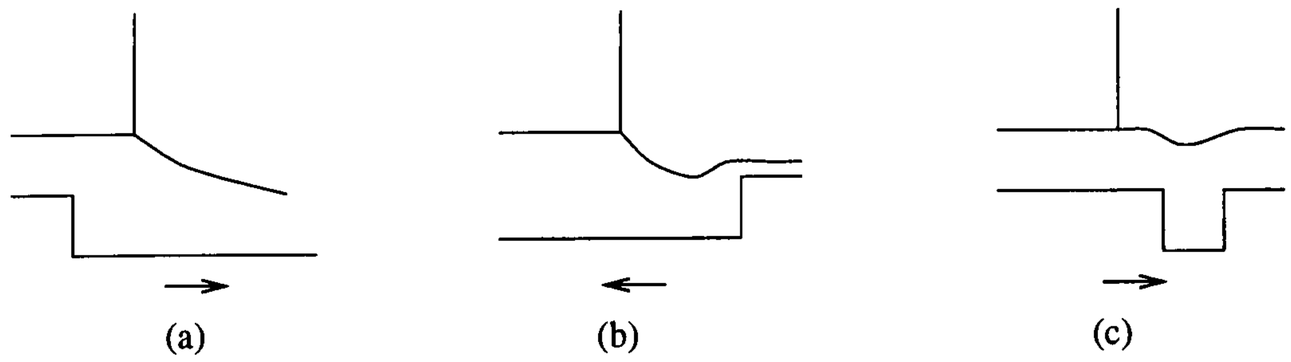

Figure 1.12: The three studies by Rees (1995) of (a) a forward step, (b) a reverse step and (c) a groove moving under a free surface pinned to a corner.

Schwartz *et al.* (1998) considered a two–dimensional time dependent flow based on lubrication theory to model a series of cells as they passed under a pinned meniscus. The free surface shape settled down to continuous periodic profile which dipped into the gravure cell. They proposed that the difference in the fluid volume between a full and partially emptied cell gave the flux. However, it would appear that by specifying the initial shape of the meniscus and the outlet boundary conditions, the flux is actually being imposed.

Powell (1999) recently considered a time dependent two dimensional free surface flow at the downstream meniscus, shown in figure 1.13. He imposed a Poiseuille–Couette flow at the outflow which caused the meniscus to dip into the cell and a portion of the fluid to be 'evacuated' into the coating bead.

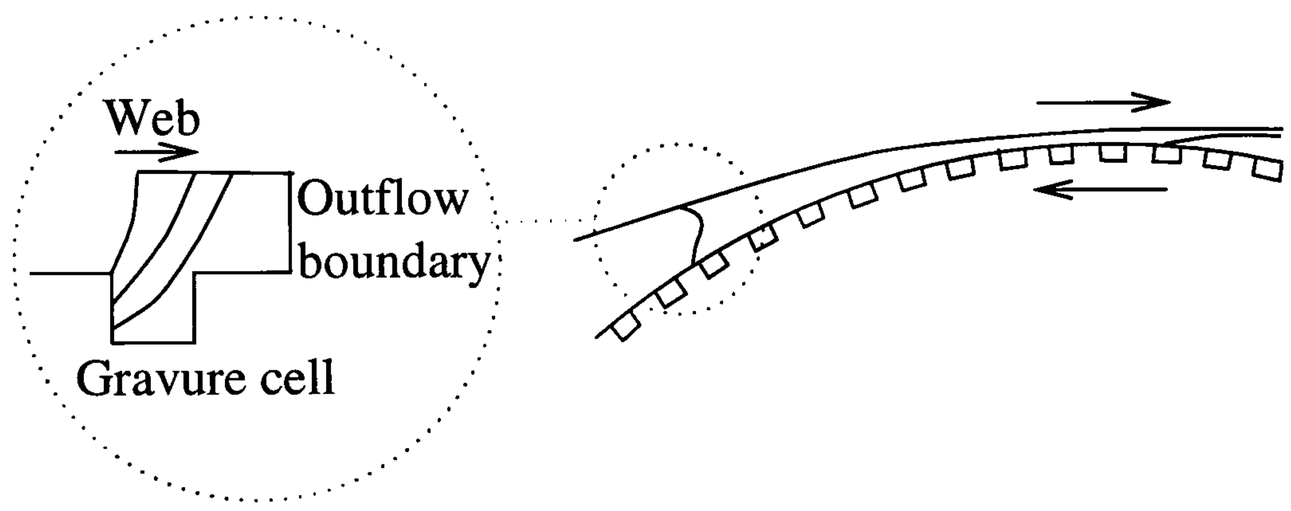

Figure 1.13: The evolution of the meniscus at the downstream interface in direct gravure coating as studied by Powell (1999).

1.4 Slot coating

The slot coater is a pre–metered device commonly used in industry as it can deliver a film within tight tolerances. It can also be arranged to coat several layers of fluid simultaneously. The fluid is fed through a narrow feed slot between two lips where it enters the coating bead to form a uniform film at the outlet. The slot coater can be used to coat films as thin as 10 μm at speeds of 6 – 600 m/min with fluids of viscosities in the range 1 mPa s to several thousand Pa s (Durst and Vagner, 1997).

Coyne and Elrod (1969) analysed the flow in the downstream region and derived the asymptotic behaviour at large distances from the coater. Later they developed a boundary condition based on a quadratic velocity distribution tangential to the meniscus. Ruschak (1976) analysed the parameter bounds under which the slot coater is able to produce films of uniform thickness, although his model was only valid for low flow rate and web speeds. Higgins and Scriven (1980) derived similar results but included viscous effects in the analysis. They also showed the necessity of a 'backing box' to apply a slight vacuum, used to stabilise the upstream meniscus position when the minimum gap exceeds twice the wet film thickness.

Silliman and Scriven (1980), Saito and Scriven (1981), Carter (1985) and Thompson (1992) used the finite element method to calculate the flow at the downstream end of the domain, with the meniscus pinned on the corner of the plate. Durst and Wagner (1997), Grald *et al.* (1994) Sartor (1990) and Daniels (1998) went on to study the whole domain and obtain full numerical solutions. Sartor also conducted an experimental investigation with which his numerical predictions compared well, and in addition investigated the effect of changing the geometry on the stability of the slot coater using numerical, analytical and experimental techniques.

The assumption that the meniscus remains pinned on the downstream corner is generally made in the literature. Sartor (1990), in his experimental study, showed the meniscus could detach and climb the corner of the slot face or regress into the gap. Daniels (1998) was the first to computationally model a slot coater with the meniscus free to retreat towards the feed point. He also considered the stability of this flow. Further work on the effect of meniscus climb is presented in chapter 5.

1.5 Blade and knife coating

Knife coating is a cheap and compact technique whereby an excess film is metered from the web by a rigid knife held close to the supported web (Coyle, 1997). Speed of operation for knife coaters vary between 3–120 m/min, viscosity is in the range 1–10 Pa s and wet coat thicknesses are usually in the range 50–2500 μm (Zink, 1979).

The thickness of the final coated film is strongly dependent on the gap between the knife and the web, which makes the final film thickness sensitive to any variations in the substrate thickness. The knife coater also has a tendency to cause streaking on the web.

Blade coating systems are similar, in principle, to knife coaters, but the rigid knife is replaced by a flexible blade which is clamped at one end. The elasto-hydrodynamic blade coater can be used to form thin coatings with less sensitivity to the mechanical tolerances associated with fixed gap roll and blade coaters (Pranckh and Coyle (1997)). Saita and Scriven (1985) were the first to elucidate the transition from (inflexible) knife coating to (flexible) blade coating.

In blade coating there is an elasto-hydrodynamic interaction between the flexible blade and the hydrodynamic stresses generated in the fluid beneath it. For a smooth roll, as the load holding the blade against the roll is increased the wet film thickness falls dramatically as the blade only deforms slightly. This results in a narrow minimum gap which ultimately determines final film thickness. As the load is increased further the blade begins to bend causing the exerted pressure at the blade tip to decrease, which can result in a thicker doctored film. Additional increases in the load causes the channel to become divergent which results in a slight thinning of the film (Pranckh and Scriven, 1990).

At very high coating speeds (up to 15 m/s) typically found in the paper industry (Aidun and Triantafillopoulos (1997)) the inertia of fluid entering the metering region can give rise to significant pressures on the blade (Kahila and Eklund (1978)), which determine the coat weight (Triantafillopoulos and Altung (1991)). This, together with the absorbent surface of the paper, makes the study of high speed paper coating a difficult one.

Blade coaters running at this speed are susceptible to significant wear over a period of operation, which changes the 'bevel angle' — typically between 25° and 50° as illustrated in figure 1.14(a). Roper and Attal (1993) and Ramp (1983) pointed out that running a bevelled blade on its 'toe' (figure 1.14(b)) or its 'heel' (figure 1.14(c)) can cause web breaks or coating defects.

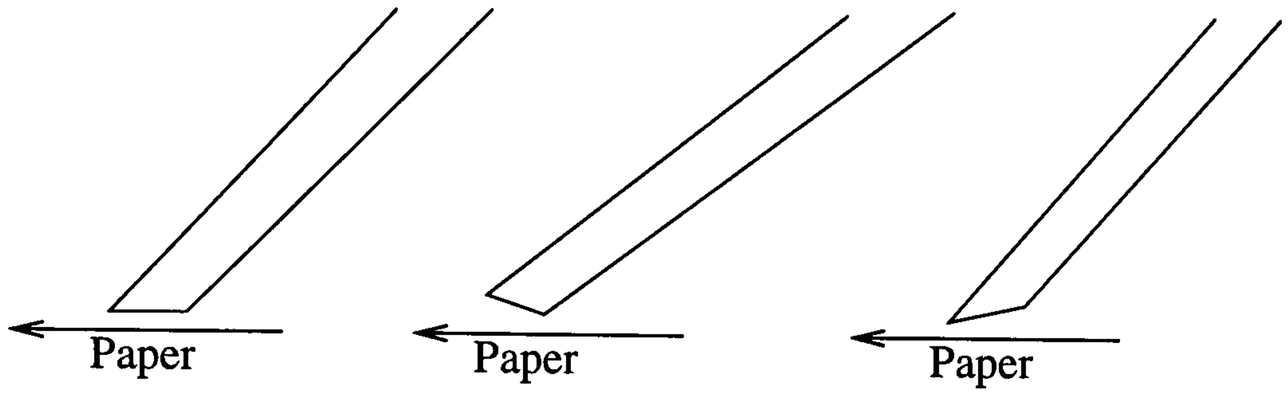

Figure 1.14: A schematic of a bevelled blade running (a) parallel, (b) on the toe and (c) on the heel.

1.6 Instabilities in coating flows

Coating processes are all susceptible to instabilities or defects in one form or another. The onset of these instabilities limit the range of parameters that may be used on the coater. Commonly, the term 'instability' is used to refer to a periodic variation in the film thickness on the web, whilst a defect tends to be spaced irregularly and may only affect a small part of the coated film.

1.6.1 Air entrainment

Air entrainment is often characterised by a series of small air bubbles and craters on a coated film and is caused by air being entrained into the fluid at the wetting line. Wilkinson (1975) and Bolton and Middleman (1980) studied the entrainment of air into a bath of fluid by a partially submerged rotating roll. They obtained empirical correlations that related the speed of the web and the fluid properties to the onset of air entrainment, and showed that the process of entrainment was linked to the formation of a cusp on the surface. Innes *et al.* (1998) studied the source of air entrainment in roll coating systems with various feed mechanisms. For the case of coating with a hydrostatic head positioned above the rolls (as studied in chapter 3) they showed that the critical speed for the onset of air entrainment into the reservoir (i.e. under the side baffle) could be increased by a factor of 2.5, by the

judicious use of a vacuum box positioned where the web passed into the reservoir.

Burley and Kennedy (1976), Blake and Ruschak (1979), Burley and Jolly (1984) and O'Connell (1989) investigated air entrainment by plunging a dry tape into a bath of fluid. They showed that as the contact angle approached 180° V-shaped cusps were formed on the interface. Bourgin and Tahiri (1995) studied air entrainment in a high speed curtain coater.

1.6.2 The ribbing instability

Often when a thin film is spread onto a moving substrate, instead of forming a smooth layer it forms a non–uniform film. The surface is characterised by a sinusoidal variation across the width of the web and is most commonly termed ribbing, but also referred to as corduroy, rake-line or phonographing. The ribbing instability has been observed in forward roll, reverse roll, slot, offset and direct gravure coatings, and can occur when the fluid bead is bounded between an upper and lower solid boundary. Most commonly, ribbing is observed in forward and reverse roll coating, with the former being most susceptible. A great deal of experimental, analytical and computational effort has gone into investigating the conditions for the onset of ribbing.

Despite the two–dimensional flow in the region of the downstream meniscus a common approach has been to use the rectilinear lubrication equations to model the base flow. Pearson (1960) introduced a linear stability analysis but did not supply the necessary boundary condition to locate the interface. Savage (1977b) and Fall (1978) used the boundary condition of Coyne and Elrod (1970) to model flow near the meniscus, and developed linear stability analyses for the study of a roll–flat plate arrangement and a wide angled spreader geometry, respectively. Using a similar approach, Savage (1984) analysed the stability of a equal speed forward roll coater and later, Carter and Savage (1982) examined the unequal speed case. Fall (1985) included the time dependent response of flow in the roll–flat plate arrangement to obtain growth rates of the instability as a function of wavenumber. Castillio and Patera (1997) studied the evolution of a coating flow from the unstable

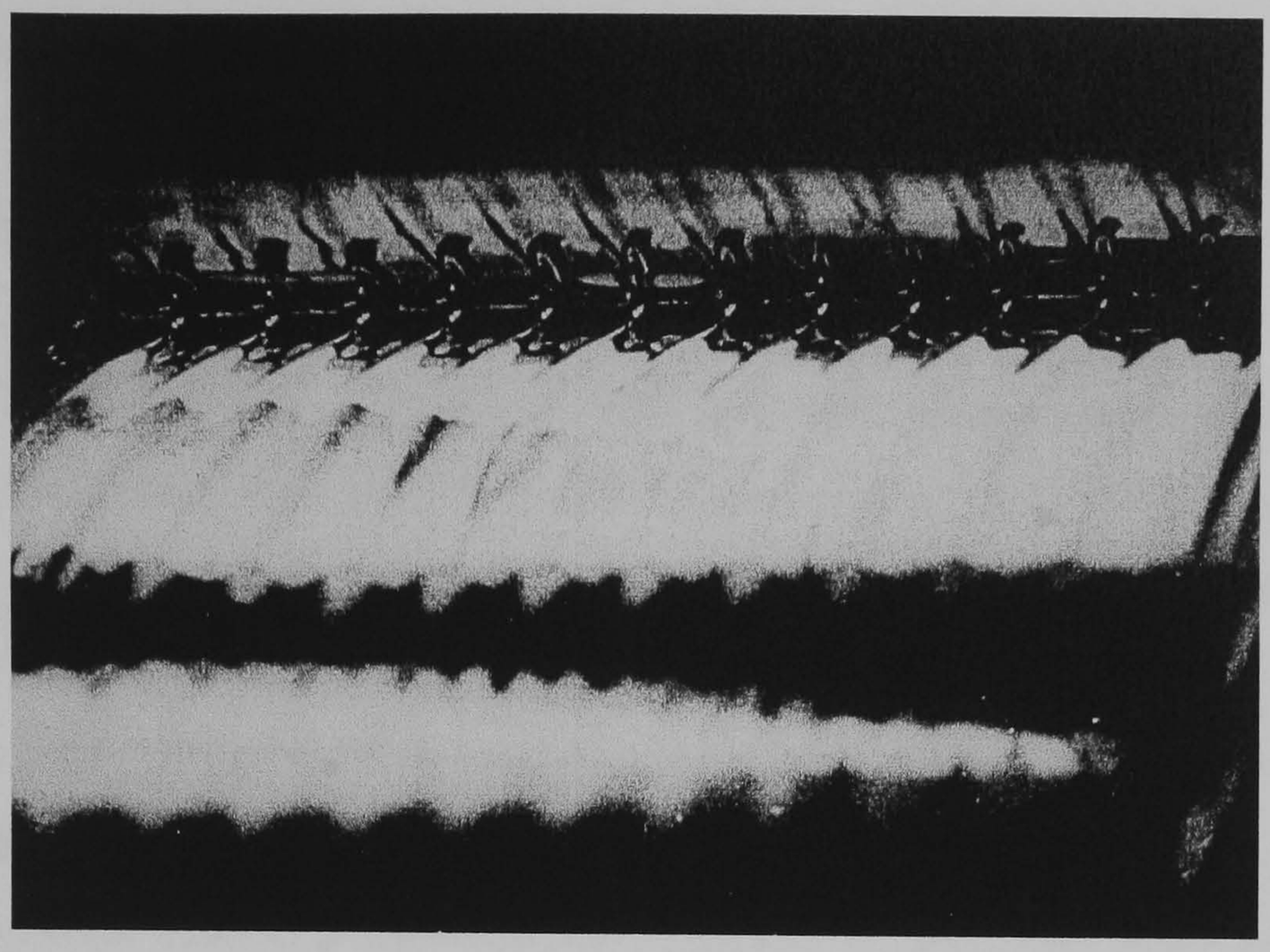

Figure 1.15: A ribbed film as it leaves the nip of a forward roll coater (Dowson and Taylor (1979)).

two-dimensional case to a stable three-dimensional case in forward roll coating using a numerical technique.

Coyle (1984) and Coyle *et* al. (1990b), based on work of Bixler (1982) used an alternative approach of perturbing a two–dimensional steady state solution for the flow obtained from the finite element method. Daniels (1998) used this approach to predict the onset of ribbing in forward, reverse and slot coating.

An approximate way to determine the stability of the downstream meniscus using a stability hypothesis or criterion was developed by Pitts and Greiller (1960) and Savage (1977b) where the response of the interface to a small disturbance in its position was calculated.

Hasegawa and Sorimachi (1993) showed that the careful positioning of a taut wire at the downstream meniscus can delay the onset of ribbing, a detailed experimental investigation by Decré *et al.* (1996) also highlighted that the position of the string in the nip could substantially affects the film split ratio. Coyle (1997) attributed the stabilising effect of the wire to the reduction in destabilising pressure gradient at the meniscus caused by the interface being pinned to the wire at a larger distance

from the nip. An alternate explanation for this is offered in chapter 5.1.

1.6.3 The cascade, herringbone or seashore instability

The cascade instability is restricted to the reverse roll coating mode. It is characterised by periodic cross–web disturbances with each resembling an irregular saw tooth pattern in the transverse direction. The onset of the cascade instability was first mapped in the $Ca - S$ plane by Booth (1970) and later by Coyle (1984). Coyle also suggested a mechanism for the formation of this instability in which the downstream meniscus is pulled upstream of the nip and the outlet film thickness is of the same order as the gap. The outgoing film attempts to re-attach itself to the upper roll as shown in figure 1.16 causing an oscillatory motion due to the periodic attachment and detachment of the free surface.

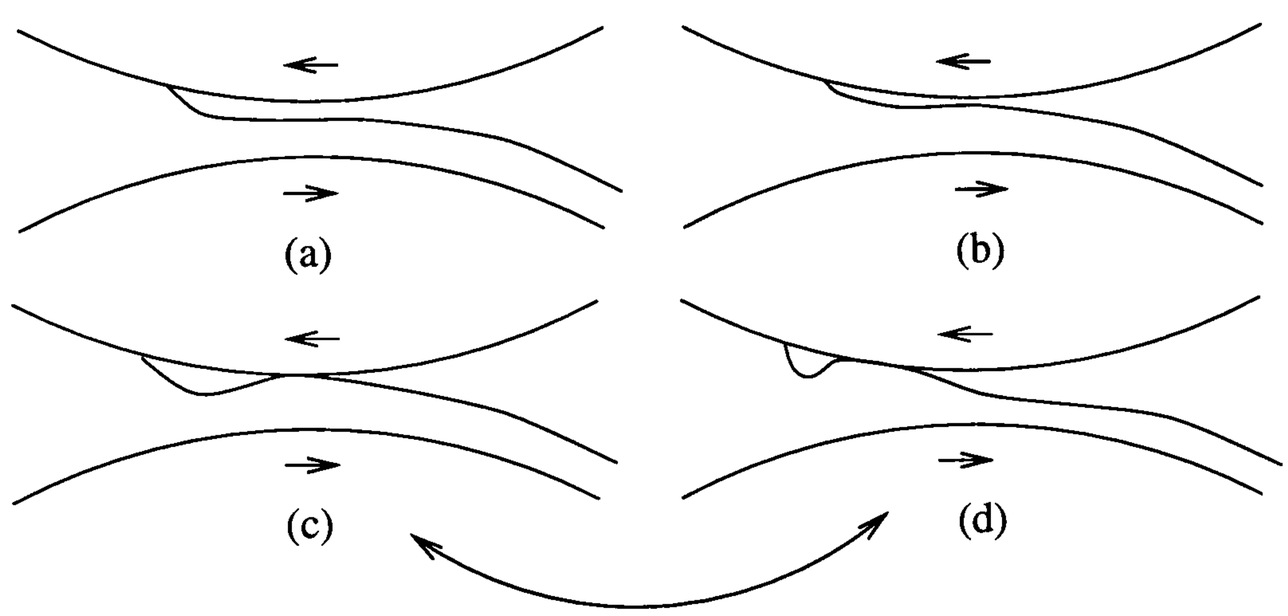

Figure 1.16: Coyle's (1984) mechanism for the onset of cascade. As the speed of the upper roll is increased the wetting line is pulled through the nip causing a thickening of the film (a). As the speed is increased further, the film thickness approaches that of the gap (b), eventually causing attachment at a second wetting line (c) and trapping an air pocket. This travels through the nip (d) causing a defect on the final film. The motion between (c) and (d) is oscillatory.

1.6.4 Bead–break instability

The 'bead–break' instability arises in both forward and reverse meniscus roll coating and was first observed by Malone (1992) in the forward mode. By fixing the lower roll speed and gradually increasing the upper roll speed he observed that at a critical speed ratio the upstream meniscus became unstable and accelerates and collides with the downstream meniscus. Further work on this instability is presented in chapter 4.

1.6.5 Pinholing

Pinholing is observed just downstream of the film formation. It is characterised by small pits where the film thickness varies rapidly from the mean film thickness to zero, see figure 1.17. Often a film may de-wet from the edge as it 'beads up', but also a film can spontaneously rupture away from the edges creating a dry patch of web with new edges (Padday, 1971). The event that precedes the formation of a pinhole is a local thinning of the film. This can be caused by (Kheshgi (1997)): evaporation; electrostatic forces; drainage due to gravity; capillary driven flows from sharp edges or surface tension gradients caused by particulates or surfactants dropping onto the film. The apparent contact angle that the fluid makes with the film can be used as an index of whether the liquid is wetting or non-wetting and capable of pin-holing (Frenkel (1946), Mohanty (1981)). Further details of pin-holing can be found in Kheshgi (1997).

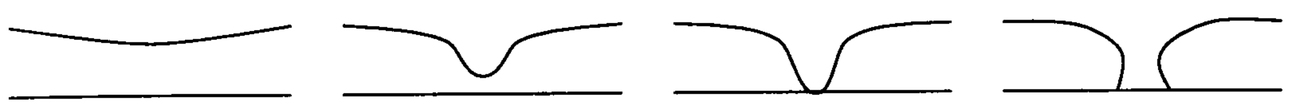

Figure 1.17: The formation of pinholes: (a) A local thinning of the film occurs which is aided by molecular attraction from the surface (b) once the minimum thickness is less than approximately 1×10^{-6} m (Kheshgi (1997)) (c). The film can now recede from the new edges (d).

1.6.6 Streaks

The origin of streaks on the final coated film is often uncertain. They can be caused by particulates in the feed solution passing through the coating head to give point imperfections. Depending on the chemistry of the coating fluid, particulates may be formed in the coating liquid (for example a time hardening compound) which may then remain trapped in a recirculation causing a streak on the final film. For this reason it is important to try and minimise the residence time distribution of the fluid by reducing the size of any recirculation region. This also helps to prevent the entrapment of bubbles of air which can also produce streaks. Particular care should be taken at the startup of a coater as often surfaces become wet with the coating fluid that would not normally do so in the course of normal operation.

1.7 Outline of this thesis

This thesis describes a number of coating flow problems that have been investigated using a combination of analytical, computational and experimental methods.

Chapter 2 describes the experimental apparatus used in this study into coating flows, and gives a general overview of the experimental techniques adopted.

Chapter 3 describes an experimental investigation of reverse roll coating where the nip is fed from a reservoir of fluid positioned above the rolls and contained by an arrangement of baffles. The depth of the fluid above the nip is considered as an extra variable in the problem. A comparison with theoretical work presented by Gaskell *et al.* (1999b) is found to be in close agreement.

Chapter 4 describes the bead–break instability in forward meniscus coating. This instability gives an upper bound for the ratio of the doctor roll to applicator roll speed, with all other parameters held constant. A series of experimental flow visualisations clearly show the transition of the stable bead to an unstable state. A lubrication model for the base-flow is used together with a perturbation in the location of the upstream meniscus to predict the onset of bead–break. These predictions

are compared with experimental data, and found to be in good agreement. Finally, a study is made into the operability of a meniscus coater used in a typical industrial situation.

In chapter 5, a series of experiments illustrate 'meniscus climb' up the front face of a knife. This arrangement is typical of that used in blade coating, but is geometrically similar to the front face of many slot coaters, or when doctoring a gravure roll. To study the arrangement of the knife a finite element method is used to solve the Navier–Stokes equations that govern Newtonian flow. Experimentally, a simple method is shown that can be used to prevent meniscus climb and eliminate the associated eddy structure within the flow. Finally, a series of images taken from experiments show the meniscus retreating away from the corner prior to the onset of the ribbing instability.

In chapter 6, a range of models for flow in the nip of a kiss coater operating under the specific condition of the web moving in the opposite direction to the roll surface, and at a speed greater than the roll. Here all the fluid on the roll is transferred to the web, so the flux is zero at any station in the bead, however an upper bound on the speed ratio is given by the onset of the ribbing instability. Two simple models are derived for the stable bead, and a perturbation hypothesis for the prediction of stability are applied to these. Both the predictions of the stable bead and the stability model are tested against experimental results.

Chapter 7 describes an experimental study into direct gravure coating that identifies the key parameters controlling the transfer of fluid from the gravure cells to the web. The study highlights striking new results that both fluid properties and the web-to-roll speed ratio control the final film thickness on the substrate. These variables can be exploited when operating a gravure roll coater. The upper limit of the speed ratio is determined experimentally; at this point the gravure bead is seen to break up into a number of smaller, unsteady beads which result in streaking on the web. Finally, some evidence is given for the physical mechanisms that control the gravure action.

Finally chapter 8 summarises the main conclusions drawn from the work, and recommends avenues for future investigations.

Chapter II

Experimental Methods

Contents

2.1 Introduction

Careful experimental work in the field of coating has provided valuable insight into the physics of the associated industrial processes, see for example Schweizer (1988) – slide coating; Malone (1992), Gaskell *et al.* (1998a) – forward meniscus roll coating; Decré (1994), Decré *et al.* (1995) – forward flooded roll coating; Coyle (1990a,b) – reverse coating; Clarke (1995) – curtain coating. The apparatus used to investigate such flows is, by necessity of the small length scales involved, designed within tight tolerances and a with high degree of controllability so that accurate data can be collected. This chapter describes the experimental apparatus and general methods followed when investigating the coating flows encountered in this thesis.

2.2 The high precision twin roll apparatus

This rig was originally commissioned by Lodge (1994). The twin roll apparatus used in the experimental investigations of 'reverse fed hydrostatic coating', the 'bead–break instability' and 'meniscus climb' is shown in figure 2.1. It consisted of two cantilever mounted rolls and associated bearing housings fixed on an aluminium alloy frame. This allowed good visual access to the nip, important for flow visualisation studies. The upper bearing and roll was located on a micrometer driven slideway to allow ease of alteration of the gap between the two rolls. The whole bearing support frame could be mounted so that either the two rolls were vertically or horizontally aligned, or through the use of a separate bracket such that the axis of the two rolls was set at 45° to the horizontal. The diameter of both the rolls was 50.48 mm, with a length of 100.0 mm.

2.2.1 Design of the rolls

Each roll and bearing housing formed a single unit which could be removed from the bearing support frame. This allows the extremely high tolerance in the concentricity of the roll within its housing ($\pm 5\mu$m) and the parallelism between the two rolls ($\pm 10\mu$m) to be maintained. Stainless steel was used throughout for the manufacture

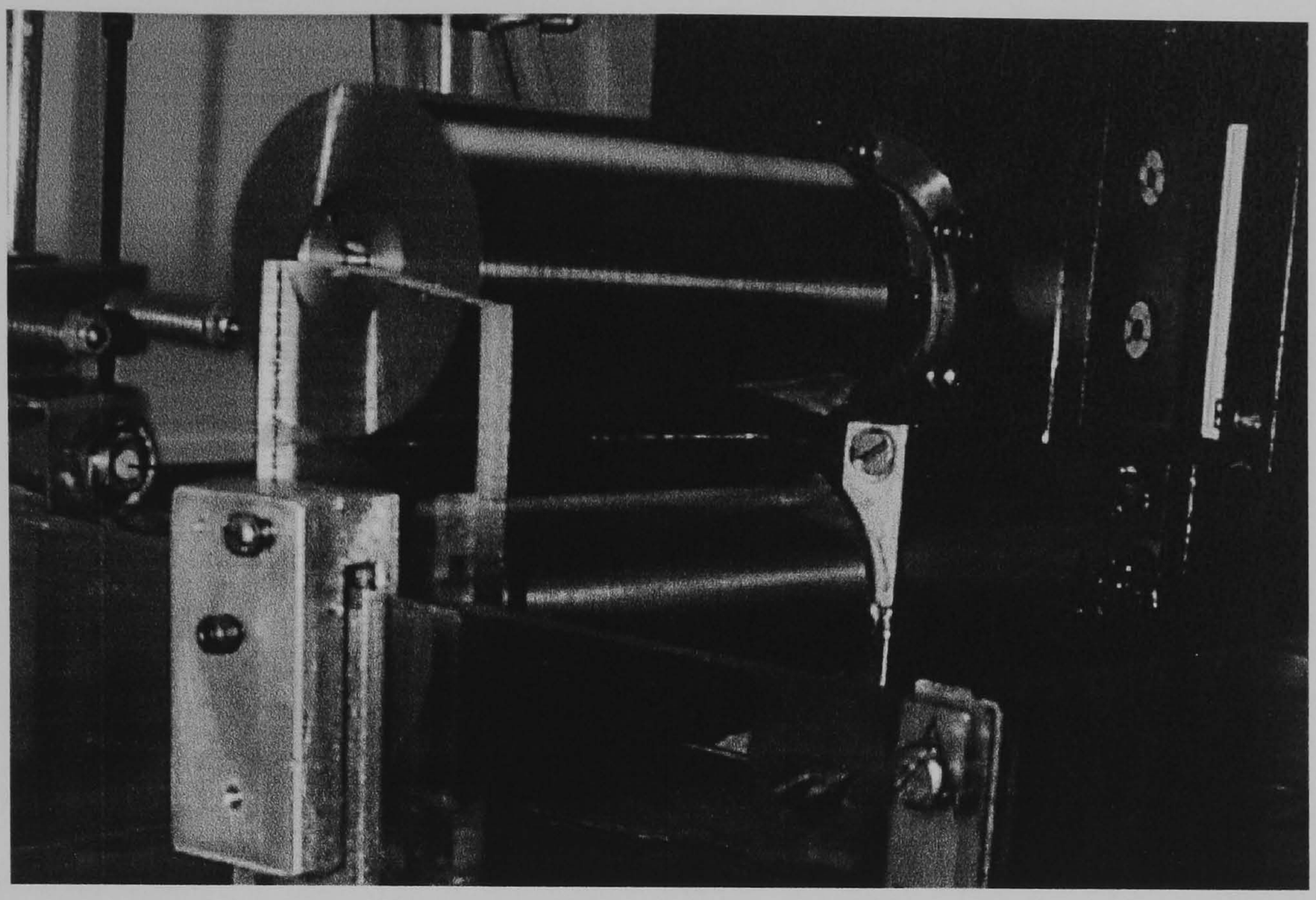

Figure 2.1: A photograph showing two cantilevered rolls mounted on an alloy frame in the high precision twin roll apparatus.

of the rolls and housings, with roll surfaces ground to a finish of $r.a. < 0.8$ μm. A third hollow roll was manufactured out of Perspex, shown in figure 2.2 and mounted in a bearing housing, this allowed visualisation of the coating bead from above. Great care was taken during the manufacture of this roll to prevent deformation of the material due to external forces applied during machining. Perspex is sensitive to environmental conditions and the size needs to be checked at regular intervals.

2.2.2 Design of the flat plate

A flat plate could be fitted above the lower roll in place of the upper roll on the twin roll apparatus. The flat plate was manufactured out of 15 mm gauge plate and was ground on all surfaces to a finish of $r.a. < 1.2$ μm. The plate had a width of 50 mm and a length of 100 mm. The plate could be moved in the X-direction on a slideway such that either corner of the plate could be imposed on the coating flow, as illustrated in figure 2.3. Two plates were used giving a selection of four corner angles of $90°, 70°, 50°$ and $30°$.

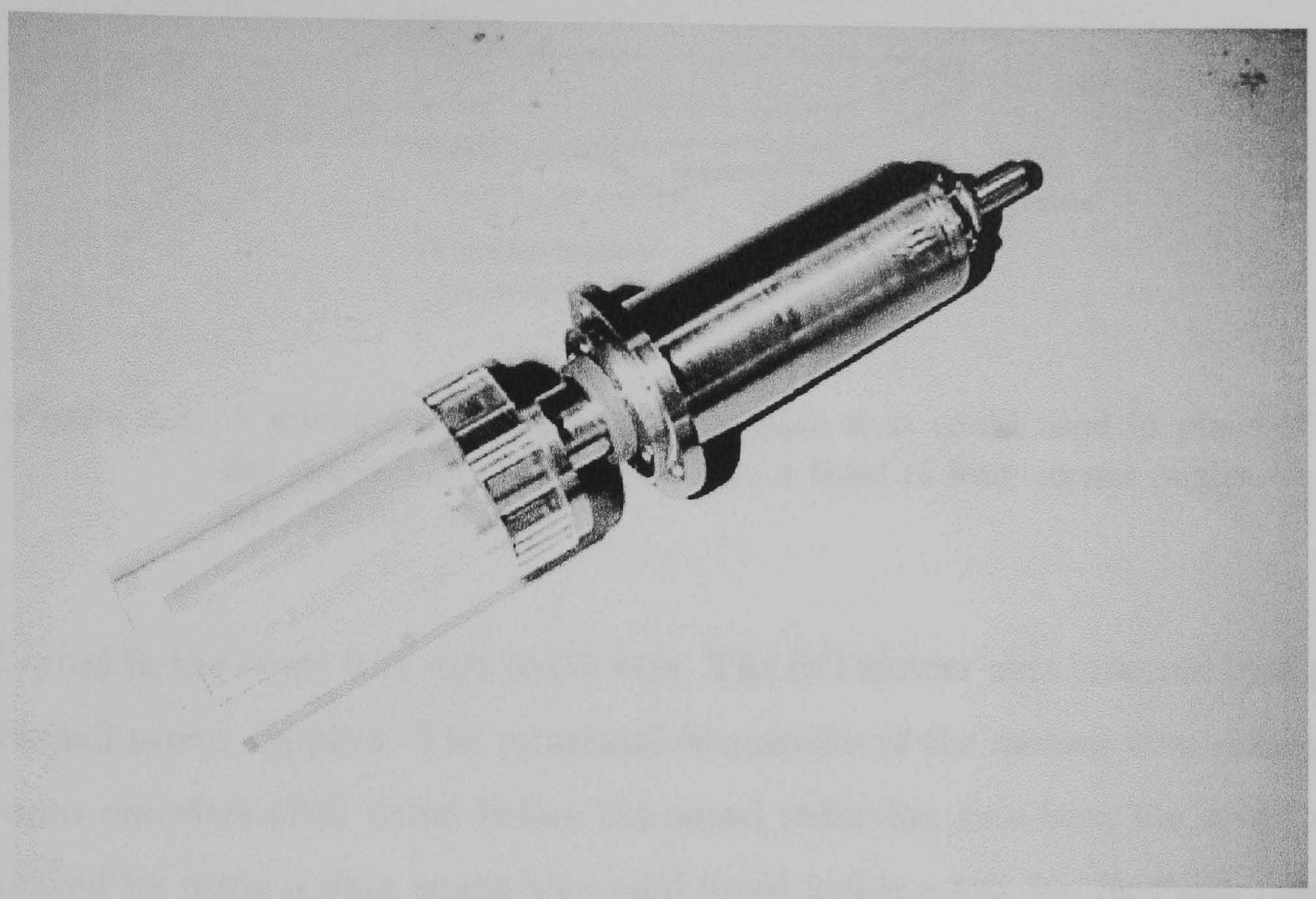

Figure 2.2: A photograph showing a roll and associated bearing housing designed to maintain concentricity and parallelism between rolls when fitted on the frame.

Setting the gap

The gap between the two rolls or roll–flat plate needed to be set accurately. Although the top roll was mounted on a slide driven by a micrometer, it was found that using feeler gauges to set the gap gave better repeatability. Malone (1992) estimated an error of $\pm 25\mu$m using feeler gauges and went on to describe the use of a thin flexible sheet as a gauge material, which was not as sensitive to horizontal misalignment, and gave an estimated error of $\pm 10\mu$m. Tests here showed that, with carefully aligned feeler gauges, the gap settings using either of these methods were within an error of $\pm 10\mu$m.

2.2.3 Drives

The rolls were driven by a pair of permanent magnet DC motors (1/17 hp Bodine) fitted to the rear of the frame, coupled with a small universal joint. Two gear-boxes were available for each drive with a 30:1 or an 18:1 reduction giving a peripheral

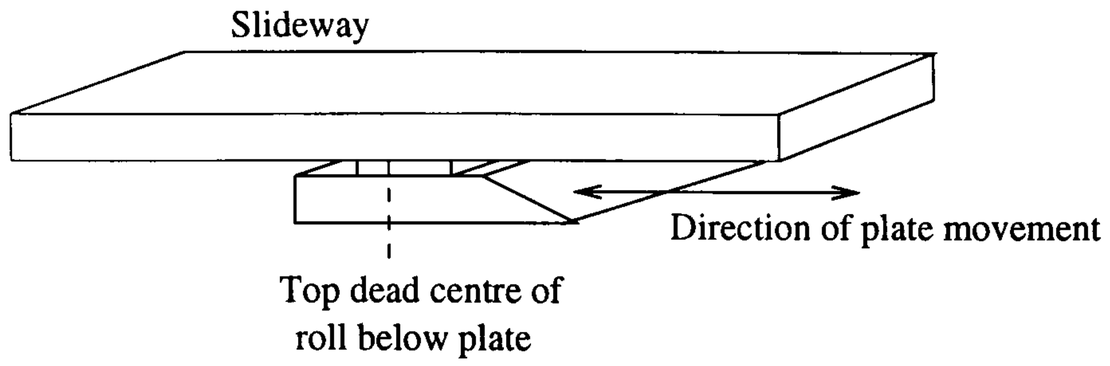

Figure 2.3: A schematic showing the flat–plate that could used in place of the upper roll. Two plates give a total of four corner angles — $90°, 70°, 50°$ and $30°$.

roll speed in the range 0.01 m/s to 0.3 m/s. The DC motors were powered by a pair of Farnell power supplies. The rotational frequencies of the motors were measured by opto–encoders (RS) fitted before the speed reduction gear-box, the speed was displayed by using a data acquisition card fitted inside a PC. No feedback control was employed due to the high stability of the power supplies and the relatively constant load on the motors.

2.2.4 Fluid supply

Reservoir for vertically aligned rolls or flat–plate

The lower roll was immersed in a bath of fluid, the depth of which could be altered by changing the height of fluid in the reservoir. Fluid was metered onto the roll by viscous lift. The semi–empirical work of Innes (1993) showed that the thickness of film on the roll surface is given by an equation of the form

$$H_i = aCa^b, \tag{2.1}$$

where a and b are two constants which need to be determined experimentally, H_i is the film thickness, Ca is the capillary number of the roll defined as $Ca = \frac{\mu U}{\sigma}$ where U the speed of the roll, μ the viscosity and σ the surface tension of the coating fluid, respectively. The thickness of a film on a rotating roll is not constant as there is a variation due to the effect of gravity (*e.g./* Tharmalingham and Wilkinson (1978)). In this thesis all film thicknesses are quoted as average film thickness equal to the

ratio of flux to roller speed.

Reservoir for horizontally aligned rolls

With the two rolls aligned horizontally (illustrated in figure 3.3) a specially constructed reservoir was made out of Perspex to feed the coating fluid. This was located against the top surface of the rolls with a small vertical force applied (5 N) to help minimise air entrainment under the side baffles. The distance between the two side baffles was 50 mm, and the reservoir allowed a maximum height of 75 mm of fluid above the top of the roll surface.

The fluid circuit

Figure 2.4 illustrates the layout of the apparatus in relation to the fluid supply. Temperature affects the physical properties of the fluid, most significantly the viscosity (see section 2.7). In order to maintain a constant temperature over the course of the experiments a large reservoir of fluid was kept within the system so that the temperature remained to within $\pm 0.5°C$ of the average temperature. In addition to this, a small refrigeration unit was constructed and controlled by a PID controller (Cal 2000), which could be switched into the circuit when environmental conditions dictated, permitting a temperature control of $\pm 0.1°C$.

2.3 The industrial pilot coating apparatus

A second experimental facility was used to perform the gravure and kiss coating experiments described in chapters six and seven. This facility was designed by Harding (1993) in conjunction with ICI (now DuPont).

Figures 2.5 and 2.6 show a photograph and a schematic of the pilot apparatus, respectively. The apparatus can be divided into two major units, the coating head and the web handling facility. The pilot unit was capable of running under conditions close to those found on industrial scale equipment.

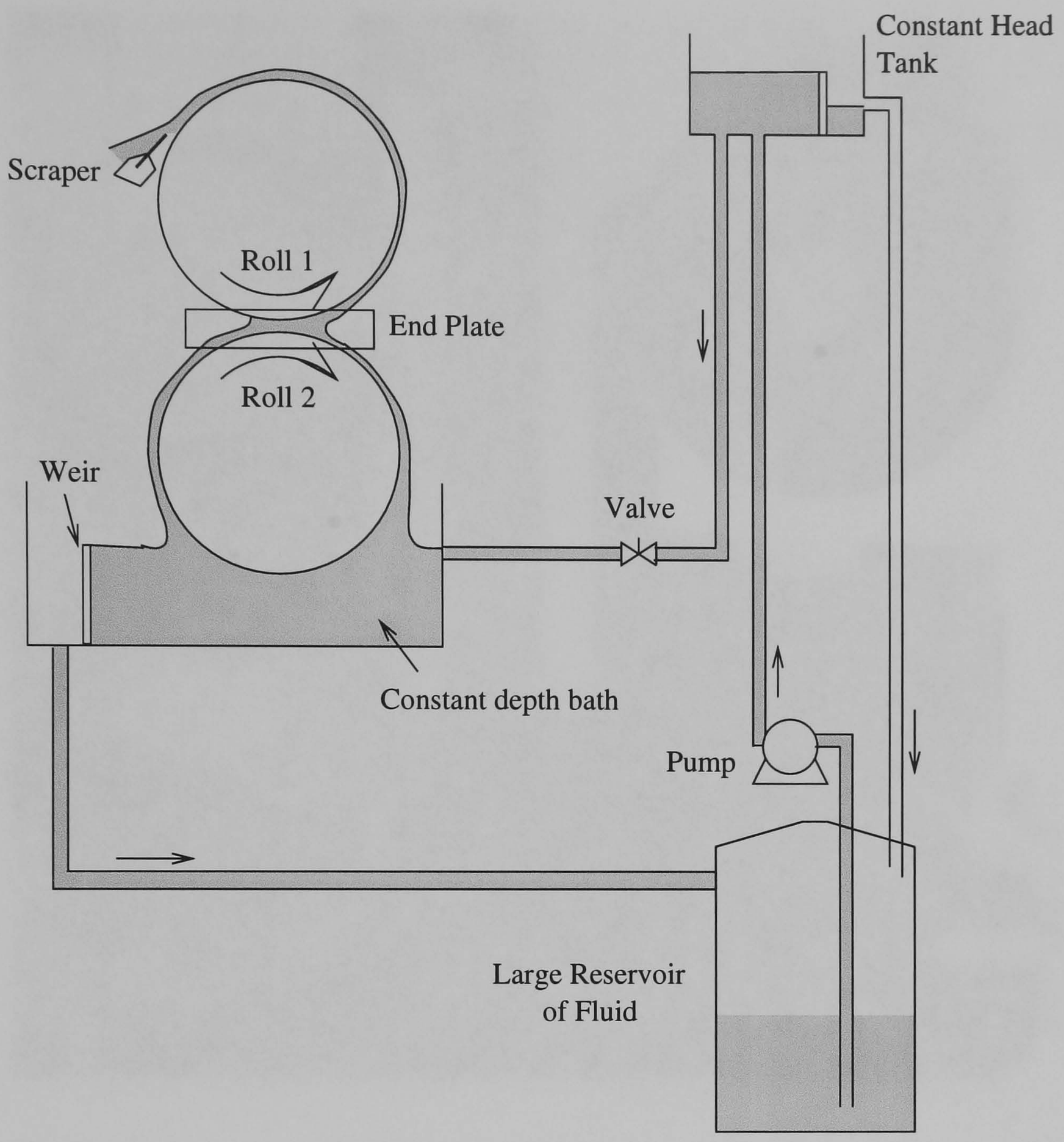

Figure 2.4: A schematic of the experimental set–up showing the arrangement of the fluid feed to the reservoir.

Table 2.1 shows the operating range of the coating head and web handling facility. The front panel contains all the necessary controls for the apparatus: potentiometers for setting the speeds of the upper and lower rolls, and the speed and tension of the web; the start and stop buttons for the rolls and web, and an emergency stop button to bring everything to a rapid halt. Also on the front panel was a switch that controlled a solenoid valve used to open or close the nip. LED displays indicated the actual speed of the rolls and web, and the tension of the web.

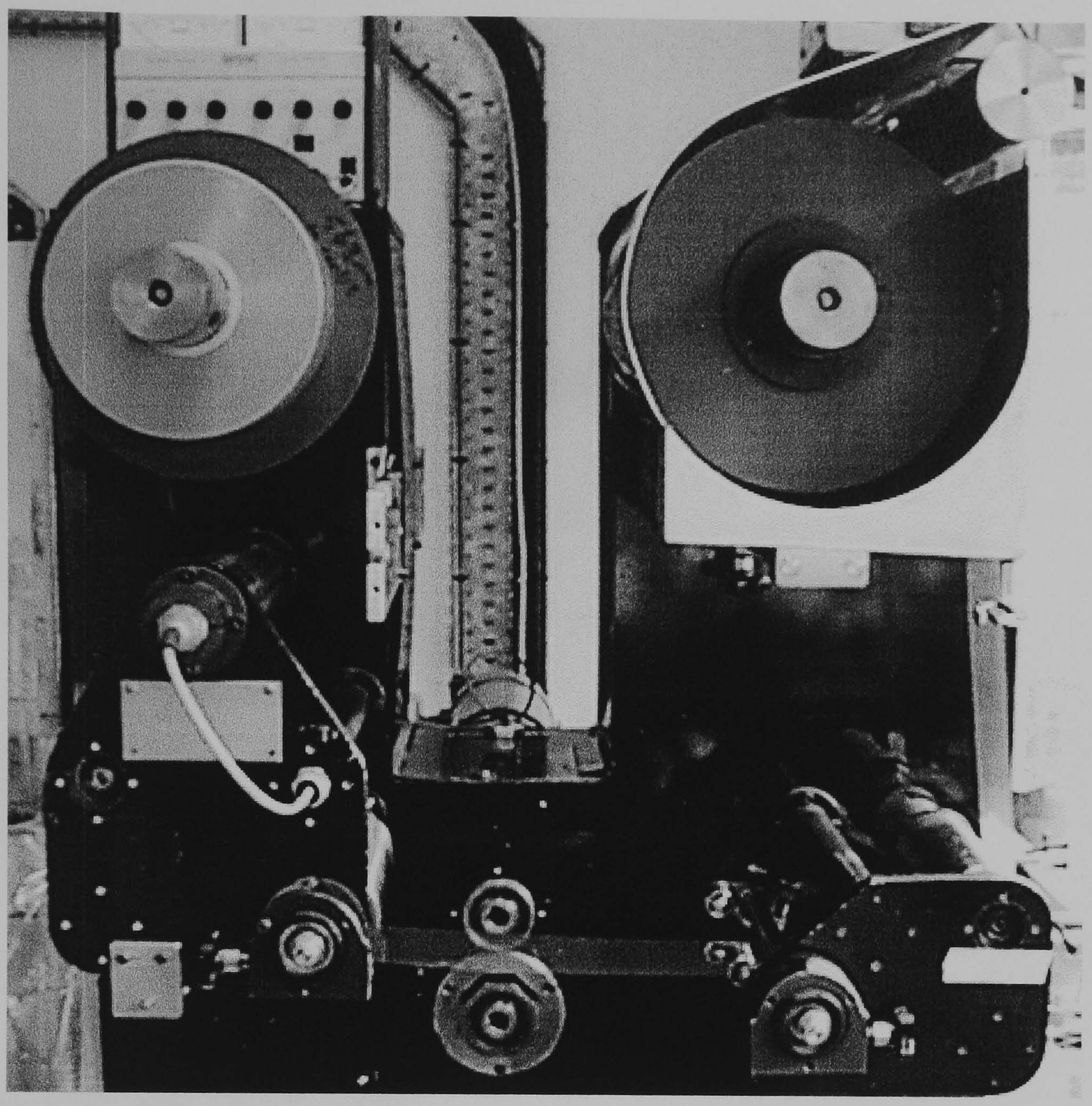

Figure 2.5: Photograph of the pilot coating unit. No coat head was installed on the apparatus, and the drive couplings for the rolls can be clearly seen.

2.3.1 The coating heads

Two coating heads were available for use on the pilot rig, a simple single roll head for studies of direct gravure coating, and a more complex double coat head for studies into offset gravure coating.

Either head could be mounted beneath the web on a V-block to ensure reproducible alignment. The roll shafts were keyed into the drive couplings and driven by two 0.5 kW motors controlled using tachometer feedback. The rolls had dimensions of 100 mm diameter and 200 mm length.

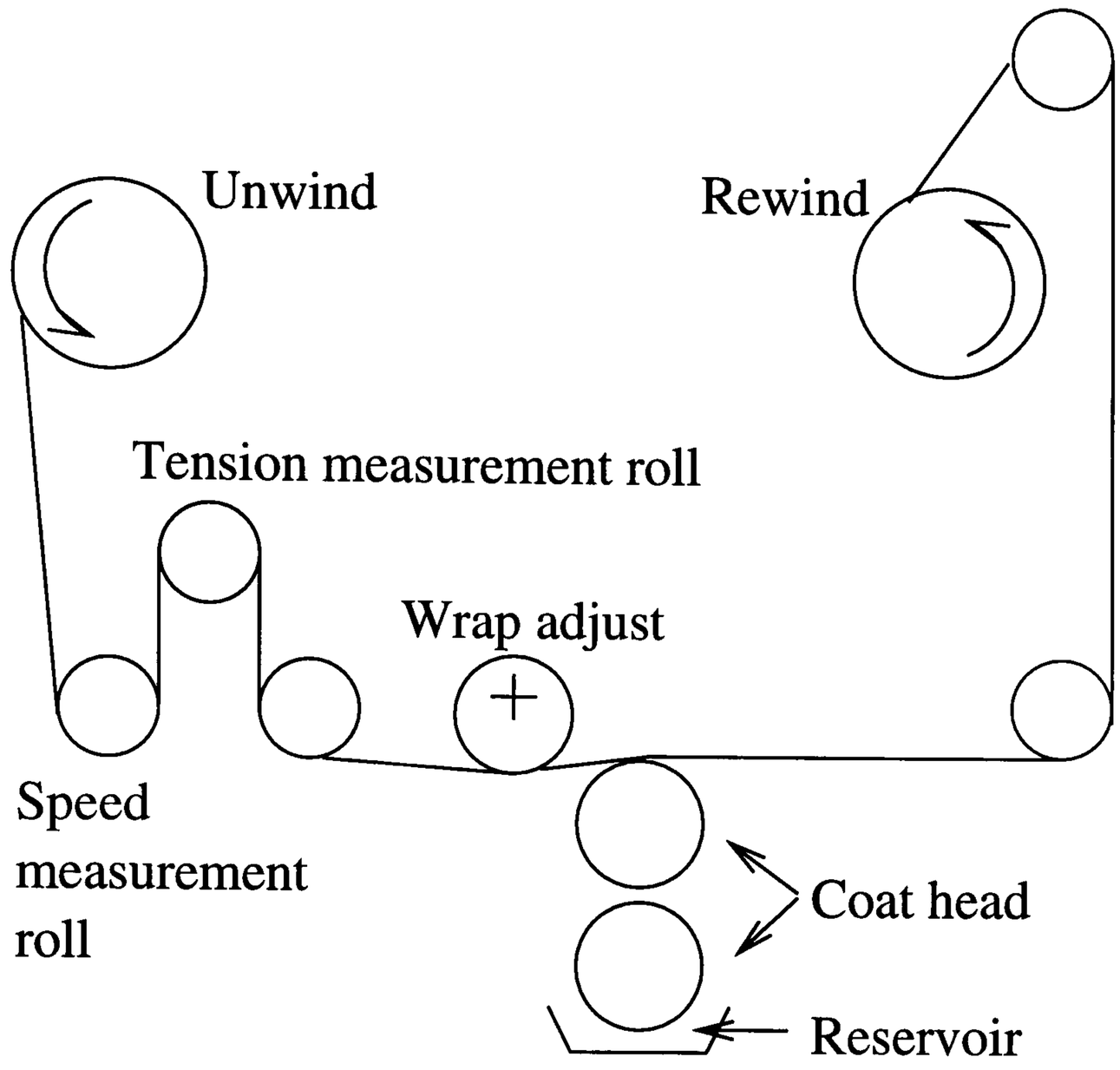

Figure 2.6: Schematic of the pilot coating unit showing the layout of the web handling facilities in relation to the coat head.

The single roll coating head

Shown in figure 2.7 is a photograph of the single head. The single roll is mounted between two side plates, such that when the head was installed on the pilot rig it sat with the top of the roll approximately level with the tensioned web. The roll sat in a reservoir of fluid so that as it rotated it supplied coating liquid to the nip region between the web and roll by viscous lift. In direct gravure coating the roll

	Minimum speed m/min	Maximum speed m/min	Minimum tension N	Maximum tension N
Lower roll	1	75	–	–
Upper roll	1	75	–	–
Web	2	75	25	250

Table 2.1: Operating limits of the pilot coating apparatus.

is metered by using a doctor blade positioned after the reservoir and before the coating bead. The position of the clamp that held the doctor blade could be varied vertically, and the angle of the blade could be set by rotating the clamp within the mount as can be seen in figure 2.7. The blade was made out of 250 μm thick melinex strip. Typically, in industrial situations, a doctor blade is offered up to the roll and preloaded with a small force against it. However, during the course of experiments described in chapter seven, it was found that a more controllable way of setting the doctor blade was by applying a known load to the blade, which remained constant over the course of the experiments, more details of this can be found in section 7.2.4.

Due to the much larger fluxes involved in the pilot scale apparatus, a simplified handling circuit was used. Fluid was merely pumped into the reservoir at approximately the same rate as it was removed by the coated web. The reservoir of feed liquid was large which helped maintain a constant temperature ($\pm 0.5°C$) over the course of the experiments.

The twin roll coating head

Shown in figure 2.8 is a photograph of the double roll head mounting. The upper roll was located between the two side plates, the lower roll mounted on an inner carriage and guided by two slideways to ensure vertical motion. Five pneumatic actuators beneath the inner carriage were used to move the lower roll up to the upper roll, to nip the two together. Straddle mounting the rolls in this way is more suited to coating operations when the rolls are in contact, such as in deformable or offset gravure coating, because of the large forces imposed on the bearings. Rees (1995) estimated the final runout of the rolls to be 10 μm.

The force nipping the two rolls together could be controlled by the pressure of air supplied to the actuators (in the range 100 KPa to 1100 KPa) which together with the total area of pistons (4.02×10^{-3} m^2) gave a nip force per unit length of roll in the range of 2000 N/m to 22000 N/m. To control the gap between the two rolls, two bolts at either end of the frame could be adjusted to limit the travel of the inner carriage. In the experiments described in chapter six, the travel was not limited in

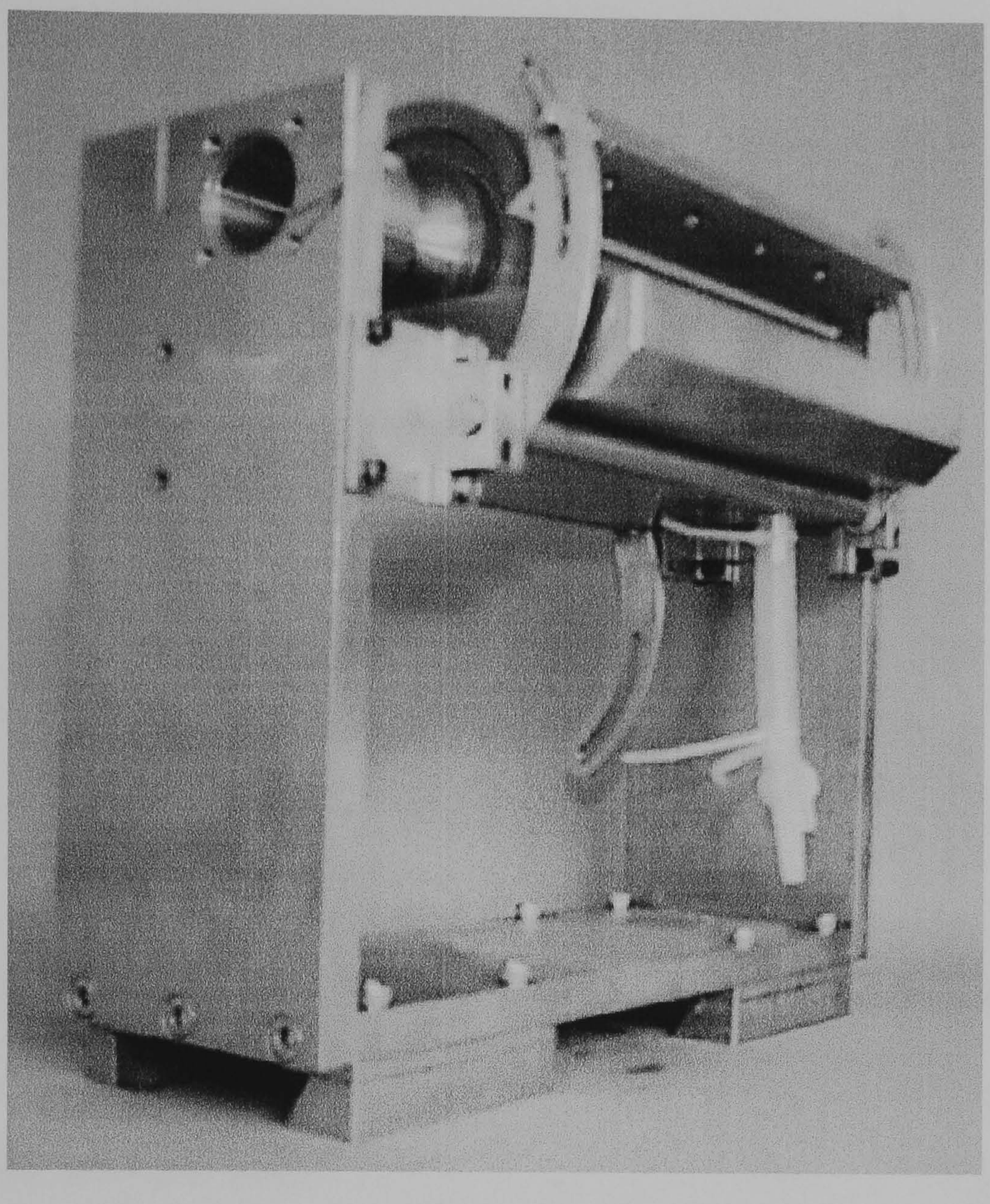

Figure 2.7: The single roll head used in studies of direct gravure coating. A reverse angle doctor blade is shown here, positioned against the gravure roll.

any way so that the applied force between the two rolls was known. Young (1998) developed a third head for use in exploring deformable coating, with micrometer wedges to control the gap setting to a higher tolerance than possible using the two bolts.

The lower roll was mounted in a reservoir of fluid so that as it rotated it picked up a film of fluid by viscous lift, the depth of the reservoir was such that the nip region of the offset gravure system was always fully flooded.

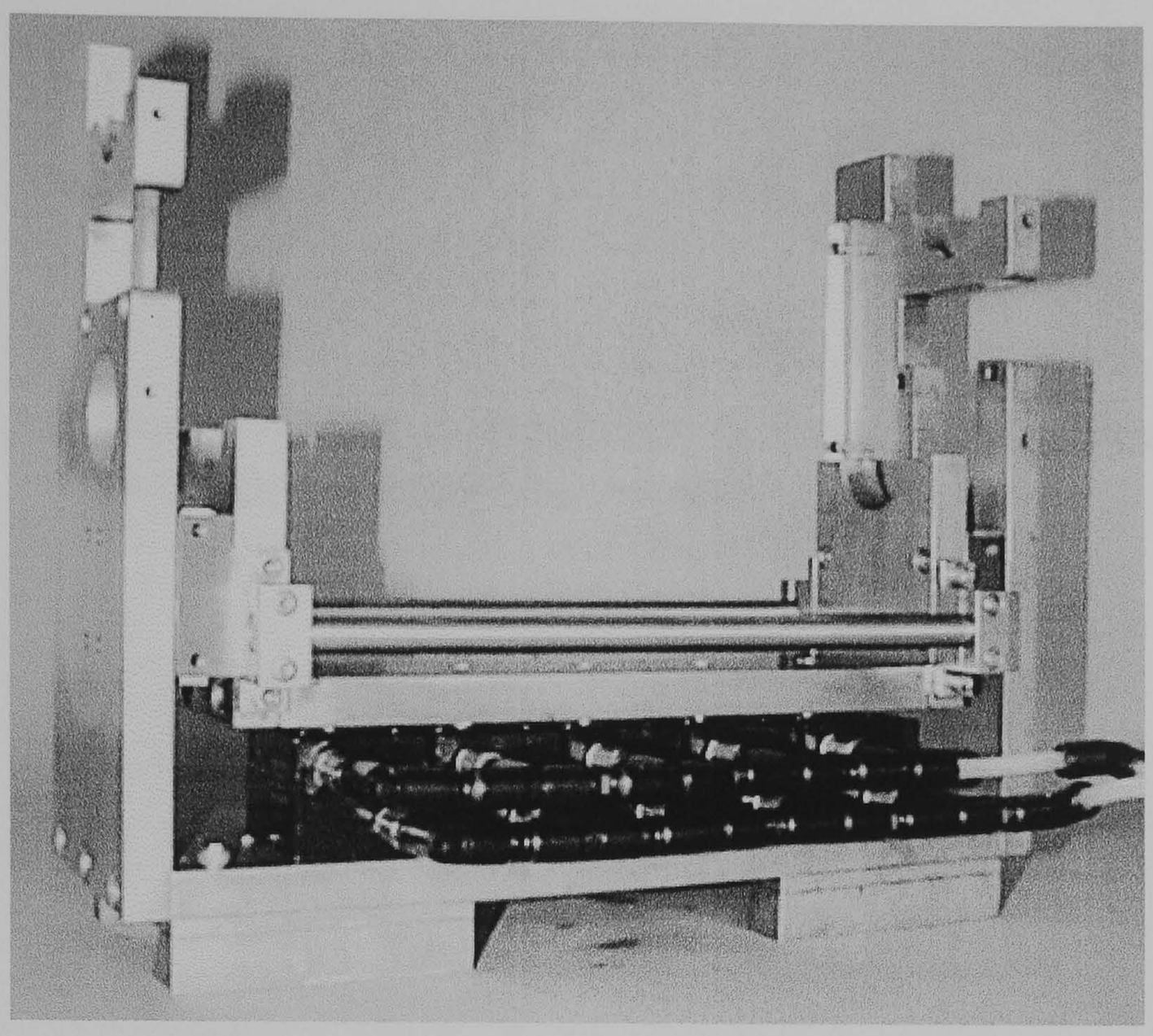

Figure 2.8: The double roll head mounting used in the investigation of offset gravure and kiss coating.

2.3.2 The gravure rolls

A range of gravure rolls were available for use with the coating heads. The gravure pattern on a roll is usually specified by (i) its cell count per unit length – historically in lines per inch (lpi), (ii) the cell volume per unit area of roll m^3/m^2 (equivalent to the film thickness this volume would give if it were spread on a smooth roll of the same area), (iii) the shape of the cells and (iv) the mesh angle (the angle at which a line of cells lies relative to the direction of the motion of the roll). Mechanically engraved rolls can be produced with cell shapes classified as quadrangular, pyramidal or trihelical (see figure 2.9). Recently, laser engraved ceramic rolls have gained in popularity due to the low roll wear rate, although the wear rate of the doctor blade may be correspondingly higher, Moussalli (1998). A range of cell shapes are available, ellipsoidal or hexagonal (illustrated in figure 2.10), or more complex hybrid cells, such as QCH cells – which are lines of hexagonal cells linked by small channels, similar to those found in trihelical rolls.

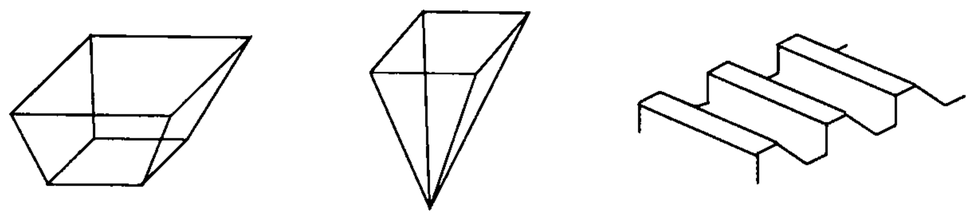

Figure 2.9: Typical cell shapes of mechanically etched rolls, left to right — quadrangular, pyramidal, trihelical.

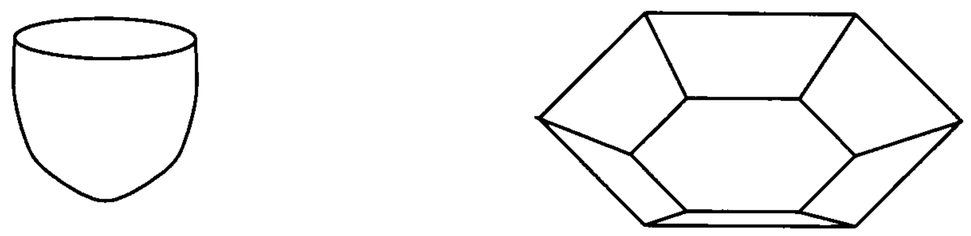

Figure 2.10: Typical cell shapes of laser engraved rolls, left to right — ellipsoidal, hexagonal.

Other non–dimensional parameters that can be used in the classification of rolls are the effective wetted area (i.e. the area of cell opening per unit area of roll) and the aspect ratio of the cell (cell width/cell depth). Table 2.2 lists the gravure rolls which were available for this study, and their relevant parameters. Shown in figures 2.11 to 2.13 are a series of height profiles of one of the roll surfaces (here the 300 lpi laser engraved roll). The three dimensional profiles shown were taken from a resin cast of the roll surface using a form talysurf, and the data manipulated in the Windows based Talymap program (both supplied by Taylor–Hobson). The figures show respectively, a three dimensional projection of the surface, a view from above the roll (used to estimate the cell area), and a height profile passing through the centre of a row of cells. Also shown in figure 2.14 is a magnified photograph of the roll surface. The profile data for the six cell patterns has been collated on figure 2.15 and 2.16 to show the actual shape and size of the cells and the relative shape and size of the cells (non–dimensionalised with respect to the maximum cell depth), respectively.

Roll type	Cell count lpi	Volume m^3/m^2	Effective wetted area	Aspect ratio
Laser engraved	60	31×10^{-6}	0.5	2.21
Laser engraved	100	26×10^{-6}	0.43	1.87
Laser engraved	200	10×10^{-6}	0.21	3.2
Laser engraved (hexagonal)	300	4×10^{-6}	0.73	6.7
Quadrangular	60	40×10^{-6}	0.86	3.74
Quadrangular	200	13.5×10^{-6}	0.68	6.7

Table 2.2: Details of the gravure rolls. Unless otherwise stated laser engraved roll cells were ellipsoidal. The mesh angle was 60° in all cases.

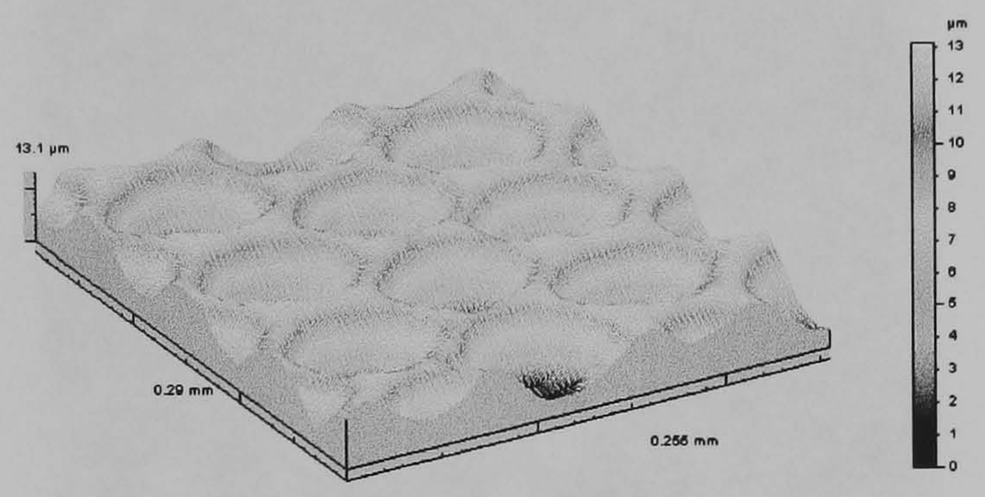

Figure 2.11: Projection of the roll surface for the 300 lpi laser engraved gravure pattern.

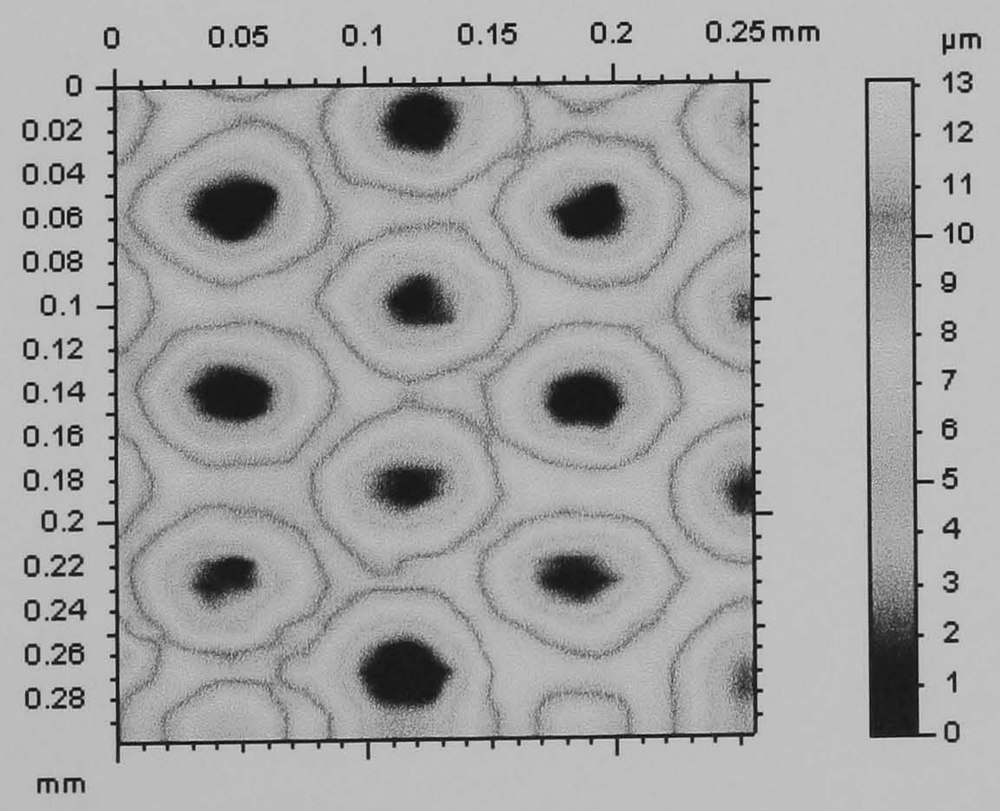

Figure 2.12: Top view of the roll surface for the 300 lpi laser engraved gravure pattern.

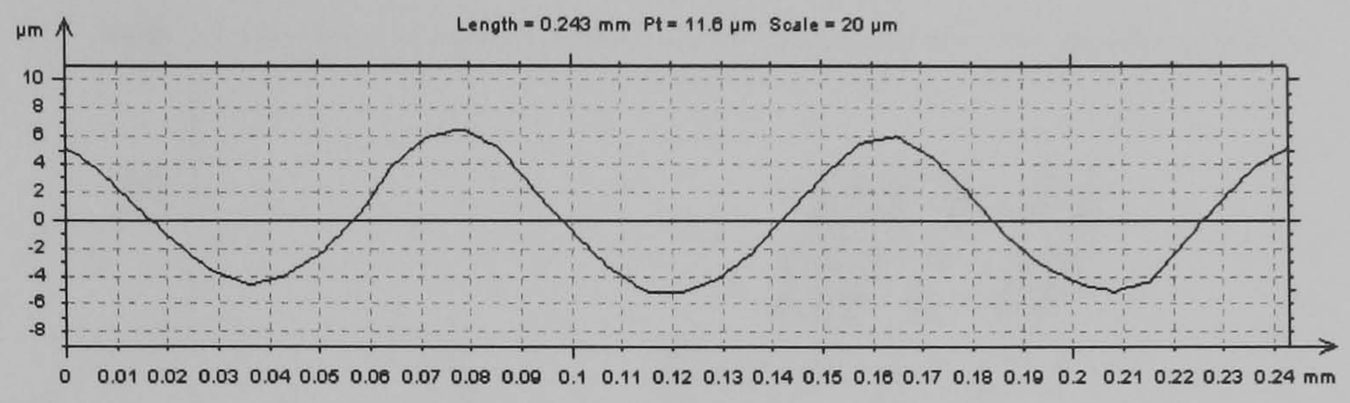

Figure 2.13: Cell profiles for the 300 lpi laser engraved gravure pattern.

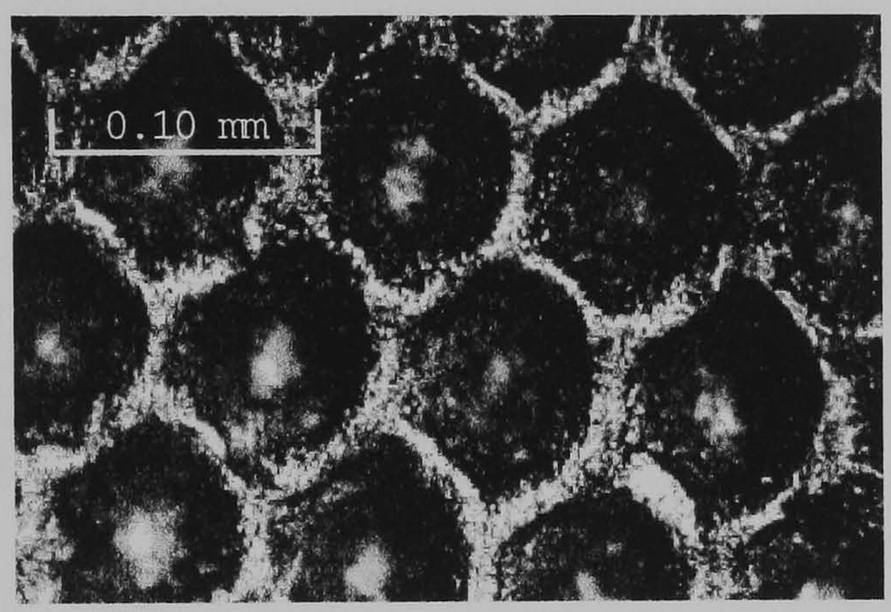

Figure 2.14: Photograph of the 300 lpi laser engraved gravure pattern.

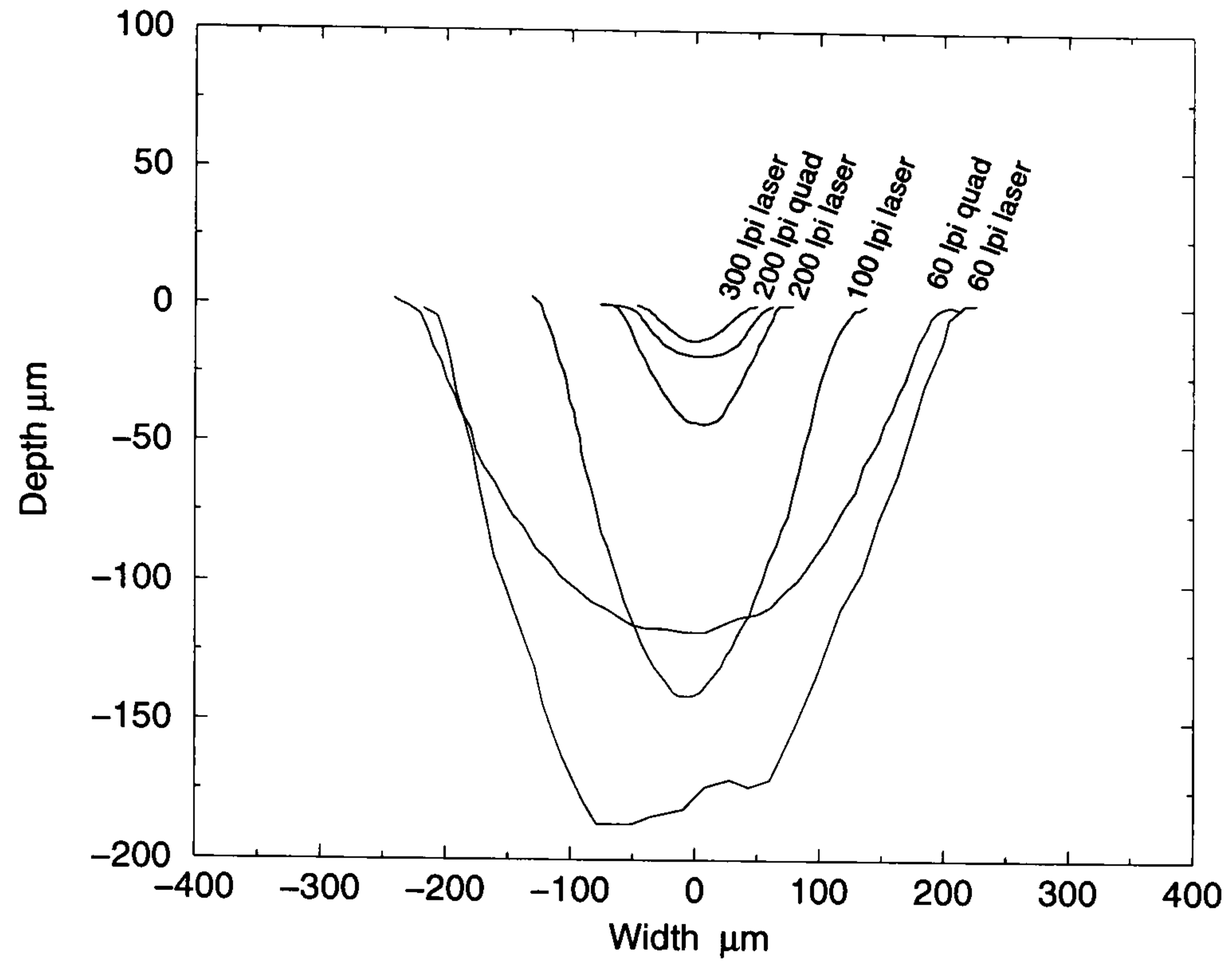

Figure 2.15: The shape of the gravure cells for the six different rolls shown in table 2.2.

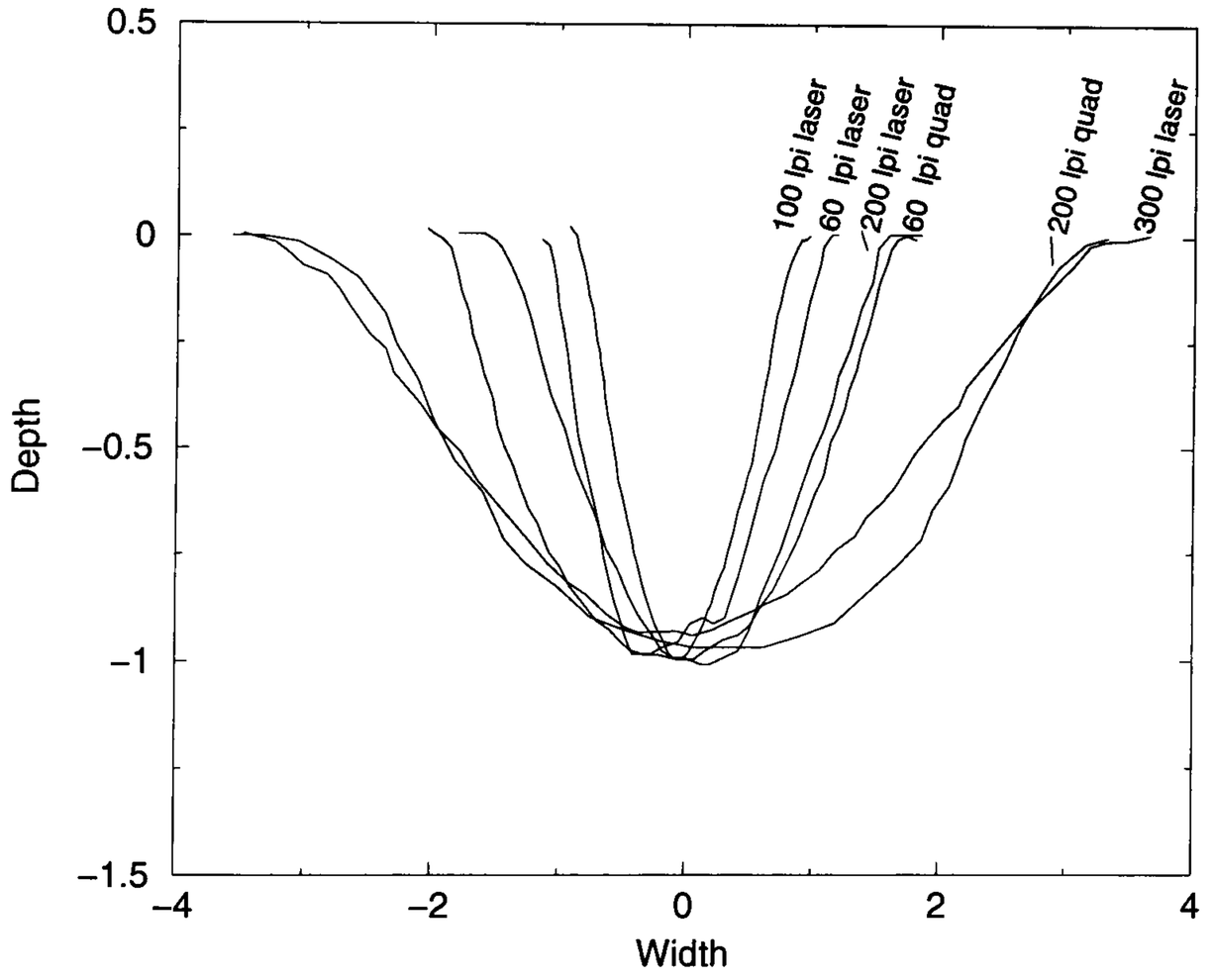

Figure 2.16: The aspect ratio (cell width per unit depth) of the gravure cells for the six different rolls shown in table 2.2.

2.3.3 Web handling facility

To provide a well defined set of conditions for the experiments, both the speed and the tension of the web needed to be controlled. This was achieved using two separate drives for the unwind and rewind reels of film. After leaving the unwind roll the web passed around a roll attached to a tachometer which was used to control the speed of the takeup roll. The web then passed over an idle roll mounted on a pair of load cells, this was used to control the speed of the unwind roll such that the tension of the web was maintained at its set point.

The web speed displayed on the control panel was checked by using a hand held tachometer held against the web. The load cell response was checked statically, by hanging known weights onto the roll. This also allowed the linearity to be confirmed.

The other parameter associated with the web is the 'wrap angle' — defined as the angle made by the web beneath the horizontal as shown in figure 2.17. This was controlled by using a roller mounted on an eccentric journal bearing, and required careful calibration. A flat bar of known thickness was positioned on top of the coating roll and under the 'wrap' roll. The wrap roll was rotated about its offset axis so that the bar was level (checked with a long spirit level). An accurate clock for measuring vertical displacements was then set beneath the wrap roll so that the height of this roll in relation to the height of the coating roll was known for a given angular position of the external journal. This, together with the distance between the axis of the wrap roll and the coating roll enabled the wrap of the roll to be calibrated.

Rees (1995) reported considerable difficulty in controlling the speed and tension of the web, due to feedback problems in the control circuits which caused wild variations in the web tension. To correct this the control circuits were re–tuned to give, primarily, only proportional feedback.

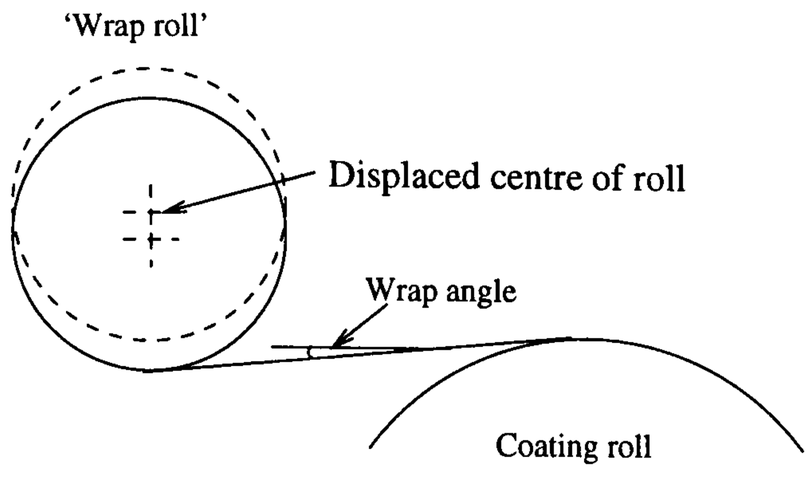

Figure 2.17: Mechanism for adjusting the wrap angle of the web by using an eccentric roll. Rotating the roll on the left around an offset centre altered the angle of the web passing over the coating roll.

The web

A polyethylene terathalate (PET) web in a range of thicknesses – 23, 36 and 50 μm was available for study. The width of the web was 100 mm, and a reel had a typical length of 2000 m. This gave tensions in the range 250 N/m to 2500 N/m when used on the pilot coating apparatus. The 50 μm thick web had a very thin (less than 1 μm) aluminium coating on one side. The web (trade name 'Melinex') had a small quantity of filler on the surface to prevent problems such as slippage and telescoping of the wound reels. This filler had the effect of making the web slightly hazy, and for this reason is not used in the production of the thicker films (175 μm) used for optical products.

Each roll of web was used only once in the experiments so that the surface properties from one test to another remained as constant as possible.

2.4 Flow visualisations

There are a multitude of techniques available for the investigation of fluid flows, e.g. particle image velocimetry or laser doppler anenometry, although perhaps none are more visual than those of dye injection or streakline photography. Flow visualisations can provide valuable information on the flow topology, for example the location of saddle points, recirculations, and meniscus positions in coating flows which can

be used to verify analytical and computational predictions as well as providing a visual stimulus for mathematical modelling. The basic features of any apparatus for visualising flows are a controllable rig, a light source, some method of highlighting streamlines within the flow and an image capture device.

2.4.1 Light source

Workers such as Schweizer (1988), Clarke (1995), Decré (1994) and Decré *et al.* (1995) describe the use of a laser sheet to section the flow – i.e. the illumination of a small width of the bead to reduce out of plane effects when capturing an image of the flow. A static laser sheet has a typical thickness of 0.1 mm and can be used to study areas with a characteristic length of a few cm. Dynamic light sheets, where a narrow beam of light is swept over the area at a high frequency, can also be used. However, due to the small gap width (in roll coating), or equivalent dimension in other coating systems, the static sheet is more practical in studies of this type (Decré, 1997). Further details on static and dynamic light sheets can be found in Thiery *et al.* (1996).

In the studies of interest in this thesis, a less exacting method of lighting the bead has been employed. A 150 W halogen light source fitted with fibre optic guides has been used to illuminate the region. Although the light section created with the fibre optic guides was wider than that generated using a laser, a precise dye injection system kept the image of the flow in one plane.

2.4.2 Highlighting the flow

There are a range of methods that can be used to highlight streamlines within the flow. Tracer techniques include adding small particles to the flow or generating small hydrogen bubbles in aqueous bases solutions. More details of these methods, and criteria for successful operation can be found in Merzkirch (1974) and Adrian (1991). Tracer techniques, combined with some means of recording the particles position, can also be extended to measuring the velocity within the flow (Particle Image Velocimetry), for examples of this used in the study of coating flows see

Malone (1992) or Wicks *et al.* (1995). Here, a simple dye injection system was employed.

The simplest apparatus for dye injection purposes is merely a hypodermic needle fitted to a syringe filled with a coloured dye. However, a number of practical problems can occur with such a system including the uneven expression of dye from the syringe, sticking of the plunger (perhaps due to an incompatibility between the fluid and the material of the syringe body or plunger) and the need for frequent refilling. Figure 2.18 shows an improved apparatus for dye injection developed by Lodge (1994). A pressure vessel approximately half filled with dye was pressurised to typically 2×10^5 Pa. The base of the vessel was fitted with a valve and a flexible tube which attached to a hypodermic needle. The hypodermic needle was fitted on a bracket with a micrometer which was used to adjust the depth of immersion of the needle into the fluid. This enabled specific streamlines to be highlighted within the flow. The colourant used in these experiments was an oil soluble blue dye (grasol blue) which was dissolved in a small quantity of the test fluid to minimise any surface tension gradients within the fluid (Schweizer 1988).

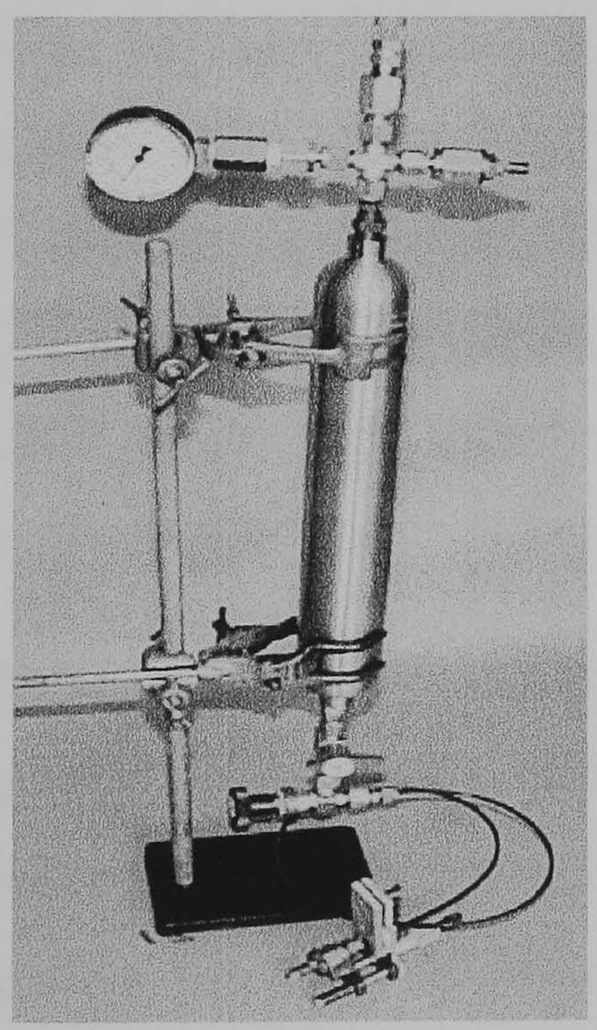

Figure 2.18: The dye injection apparatus developed by Lodge (1994) consisting of a pressurised reservoir of fluid connected to a hypodermic needle.

2.4.3 Capturing the image

Two mediums were available for taking images, either using a CCD (charged coupled device) camera or still photographs onto film.

Images taken using a CCD camera can be recorded onto VHS or S-VHS video tape, a convenient archival format that can easily be digitised onto a computer using a frame grab board. Another advantage of using a CCD camera connected to a video recorder is that slow flows can be recorded at a typical frame rate of 50 Hz. However, on the (interlaced) PAL system used in the studies described in this thesis, for any given frame half the information was from the last time step and half from the current time, which gave an effective frame rate of 25 Hz. More recently, digital cameras and frame grab boards capable of capturing a complete image at a give time directly to computer memory have become more affordable.

Taking still photographs of coating flows can render much higher quality images than the pixelated output from a CCD camera, although careful setting of the exposure time and aperture setting is required. Photographic film with a high speed (ASA) rating sensitive to low light levels is available, which proved useful when photographing the positions of the menisci in direct gravure coating, since they are very small and don't contrast well with the surroundings. Fast films suffer from a large grain size (the 1600 ASA film used in the study of direct gravure coating had a grain size of 25 nm). Still photographs can be 'scanned' to give an image in a digital format, for inclusion into reports.

Except for in chapter 7, CCD cameras have been used for visualising the flows described in this thesis — a grey–scale Panasonic WV BP310/B and a colour Panasonic WV K9152. Both cameras had facilities for turning off any autogain or black offset, and to fix the shutter settings at a given value, in accordance with Decré (1997). The images were recorded onto S-VHS video cassettes using a JVS HRS4700EK video recorder, and displayed on a JVC TM1500PS monitor. The small size of the light sensitive CCD array (typically 1/3 inch) meant that the overall magnification of the microscope used to image flows typical of those observed in coating processes only needed to be relatively low, enabled a large working distance between the apparatus

and CCD camera. A monocular microscope (Meiji Technol Co.) was used with a $\times$ 0.7–4.5 zoom, and an optional $\times$0.5 or $\times$0.25 magnification lens. A graticule was fitted within the microscope to facilitate interpretation of the images. The camera and microscope were mounted on a three way table to allow the position and the focus to be easily varied.

2.4.4 Digital image processing

Images recorded onto S-VHS video tape were captured for digital manipulation using a frame grab board. The one used here formed an integral part of a Silicon Graphics 'Indy' workstation. Basic manipulation of the images included adding lines to define the roll boundaries, the removal of reflections, the addition of a scale and marking the position of, for example, the top dead centre of rolls. Many computer packages also allow standard dark room procedures to be performed on the image, for example increasing the contrast of parts of an image, although no editing of the flow field has been performed on the images shown in this thesis so as not to inadvertantly provide misleading information.

2.4.5 The viewing window

The final requirement for capturing an image is an undistorted view of the flow field. At the edge of the rolls the fluid forms a secondary meniscus in the X-Y plane due to the surface tension of the fluid, thus distorting the image of the flow field. To counter this a transparent end plate was pressed against the edge of the rolls producing a viewing window, as described by Malone (1992). The position of the end plate window is shown in the schematic of the high precision appraratus in figure 2.4.

One problem with using a viewing window at the edge of the rolls is that it can affect the shape of the menisci in the immediate vicinity of the plate, hence it was important to focus some distance from the edges of the rolls (typically 5 mm). However, Malone (1992) found that distortion of the menisci only became excessive at high roll speeds and small gaps, which were beyond the scope of the current

experimental studies.

Decré (1994) and Decré *et al.* (1995) used an alternate technique where the meniscus, illuminated using a laser sheet, was viewed at an oblique angle to the roll axes, and subsequently resolved back into the lab frame of reference using computer software, hence removing the need for a viewing window. This technique was only used to provide information on the meniscus profile.

2.4.6 Aligning the camera

The high precision twin roll apparatus

The camera was aligned with the centre of the gap in the high precision apparatus in one of two ways:

- The camera was positioned so that it was focussed on the machining centre of a roll (which lay along the axis of the roll). The camera was then moved in the Z direction to the nip region, with the position X_0 (the top dead centre of the roll) lying along the line from the machining centre.

- A small bead of fluid was trapped between the two vertically aligned surfaces, and the gap between the plate and roll increased so the bead became elongated, as illustrated in figure 2.19. The fluid bead naturally positioned itself centrally about the axis of the roll, which allowed the centre to be clearly defined by eye.

Comparisons between the two methods using two rolls, showed either method capable of aligning the camera to the nip centre within $\pm 10\mu$m.

The industrial pilot coating apparatus

In all the flow visualisation experiments performed on the pilot unit, the liquid bead was viewed directly from above, through a transparent web. In this way it was possible to measure the positions of the upstream and downstream menisci relative

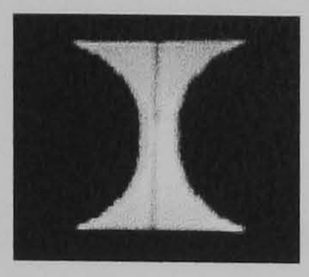

Figure 2.19: A small bead of fluid trapped between the upper and lower rolls used for determining the location X_0.

to the top dead centre of the roll. To accurately define the location of the top dead centre of the roll a calibration piece was designed and constructed. This is shown in figure 2.20. The calibration piece replaced the top roll, and hung vertically between the two bearings. A mark on the top of the piece defined the axis of the roll.

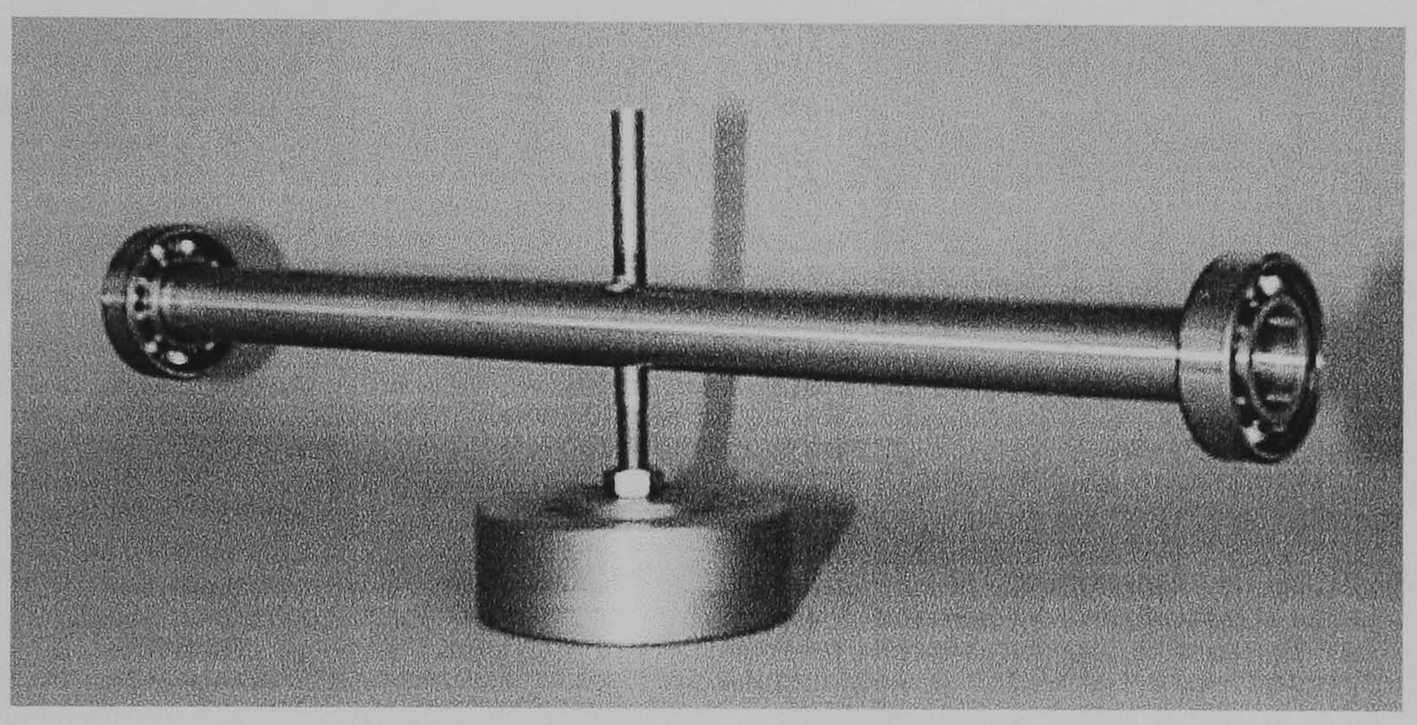

Figure 2.20: The calibration piece used to align the camera with the top dead centre of the roll in offset or direct gravure.

2.5 Flux measurements

The measurement of the film thickness is important in coating flows. A range of film thickness measurement devices are available. Although the flux measurements throughout this thesis have been made using the scraping technique, some of the other methods that could be suitable for use in the lab environment are also briefly reviewed.

2.5.1 Infra-red absorption

Any liquid has a peak wavelength of light at which it absorbs, for water it is at 1.94 μm. The film thickness can be determined by shining a beam of light through the liquid and clear web and measuring the amount absorbed when compared to a reference beam of light with a different wavelength. Malone (1992) extended the method to non-aqueous based solutions, but experienced difficulties finding suitable dyes, and with spurious reflections off the roll surface. Schweizer (1997) highlighted that this technique was difficult to calibrate. Patel (1989) used such a technique to measure film thicknesses in direct gravure coating.

2.5.2 Laser indexing

Laser indexing measures the distance to a plane by one of two methods. Either the beam is shone directly down on the surface and the specular reflection is measured, or the beam is shone at an angle down to the surface and the position of the reflected beam measured. When used on wet coated surfaces the plane of reflectance is not the top interface of the fluid, but some mid–plane within the liquid, which requires the arrangement be calibrated. This method can also be sensitive to the slope of the surface, Decré (1997).

Patel (1989) used a similar device to this, a fine parallel beam of light is generated which is scanned across the workpiece, as illustrated in figure 2.21 to generate the spatial dimensions of the piece. Patel was not able to get agreement with this system and one using infra-red absorption, and concluded it to be an inaccurate method, although no data was presented for comparison against a third method, for example, scraping.

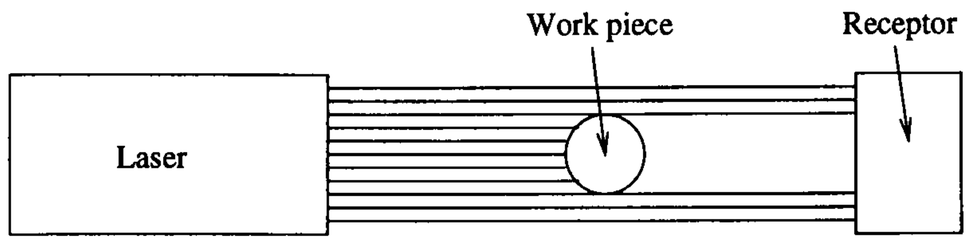

Figure 2.21: The laser scan micrometer used by Patel (1989) to measure film thicknesses.

2.5.3 Capacitance techniques

Capacitance techniques have been used by a number of authors (Malone (1992), Patel (1989), Innes (1993) and Adachi *et al.* (1988)) to measure film thicknesses. The gap between the probe and the conducting surface acts as a capacitor – in this case the non–conducting oil film and the air act as capacitors in series, but with proper calibration this allows the film thickness to be determined.

2.5.4 Scraping

Fluid may be removed from a roll surface by using a doctor blade pressed against the roll or web, such that the fluid runs away from the scrape off point and can be collected over a fixed time period. The film thickness is given by the simple formula

$$H = \frac{W}{\rho T L U} \tag{2.2}$$

where H is the film thickness, W is the weight of the fluid, T the time of scraping, L the width of the blade and U the peripheral speed of the roll.

The design of the scraper blade needs to be such that it removes the maximum possible film from the roll surface. Malone (1992) used a single scraper blade and found up to 2μm could be left on the surface. Innes (1996) used a twin scraper blade to remove more of the film, it was estimated, by using absorbent pads after the scraping that a maximum film of 0.5μm remained on the surface.

To scrape the fluid film from the web in direct gravure coating, a windscreen wiper blade fitted inside a special mount was used. The blade was pressed up against the web as it passed over an idle roll and the fluid collected beneath it. Figure 2.22 shows the blade and holder. Estimates made using absorbent pads positioned after the blade showed that the maximum remaining film on the web after scraping by a correctly positioned blade was less than 0.1μm.

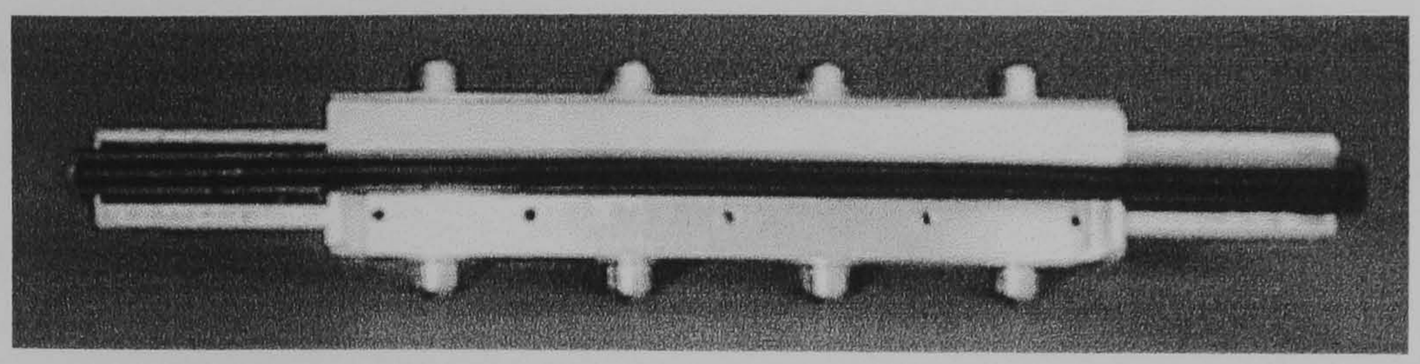

Figure 2.22: The modified wiper blade used to scrape fluid from the web.

2.6 The laser ranging device

The use of a laser ranging device to measure the web deflection as it passed over a fluid bead was first investigated by Rees (1995). Accordingly, as part of the investigation into direct gravure coating described in chapter 7, a system based on an Anritsu KL–132A laser ranging device was developed to measure the web deflection. The ranging head was mounted on a slideway so that it could traverse from the upstream to the downstream menisci of the bead. The device used a 30 – 60 μm diameter beam to reflect off the surface, and gave a measurement range of $\pm 800\mu$m either side of the centre line. The accuracy of the laser ranging device was $\pm 0.4\mu$m and the frequency of measurement was 16 kHz, the output (a -5 V to +5 V signal) was acquired by a computer fitted with an analogue to digital conversion data acquisition board (Amplicon PC226). Custom written software was developed to aid the data acquisition.

The position of the laser ranging device in relation to the top–dead centre of the roll also needed to be recorded. To do this a linear variable differential transformer (LVDT) connected to the slide–way was used to measure the position.

Due to the high sensitivity of the laser ranging device, the run–out of the roll could mask the web deflection, particularly when repeat readings were averaged. To prevent this occuring the movement of the slideway was triggered at the same point of the rolls rotation in each experiment, by using an opto–transducer and a small reflective mark on the roll shaft. Once triggered, the opto–transducer released an electro–magnet, and a small falling weight moved the laser ranging device smoothly across the region of interest.

Figure 2.23 shows a photograph of the laser ranging device mounted on the slideway. Also in the picture can be seen the LVDT on the left, and the electromagnet release in the bottom right.

Static tests were made using the laser ranging device to measure the thickness of the Melinex web. This was used to confirm that the plane of reflectance was from the top surface of the web. This was tested with the web positioned on a reflective metal surface, a liquid surface and in free air.

Figure 2.23: The laser ranging device mounted on a slideway to enable it to measure the web deflections.

2.7 Fluid selection and measurement of properties

Typical fluids used in the coating industry range from very dilute aqueous solutions of low viscosity which are essentially Newtonian in nature, to high viscosity fluids that exhibit complex visco–elastic behaviour. Selection of fluids for use in the laboratory is limited by health and safety considerations. A suitable range of fluids that are Newtonian and safe are light organic oils – Shell Tellus R5, Shell Tellus R10 and a more viscous oil – HVI 160, in addition to water and glycerine. In addition for some of the direct gravure coating experiments described in chapter seven a mixture of water and glycerine was used to give low viscosity aqueous coating solutions

typical of those found in industry.

Two proprietary surfactants were available to alter the surface tension of the aqueous solutions – Synperonic-N (supplied by DuPont) and Lodyne S103 (supplied by Ciba-Geigy). These were added in an approximate quantity of 5 ml per litre of coating solution. The solutions were used for a maximum period of 3 hours to minimise any effect of evaporation on the physical properties.

2.7.1 Viscosity

The viscosity of the fluids used in the experiments was measured using a range of Oswald (capillary tube) viscometers, one of which is illustrated in figure 2.25. Shown in figure 2.24 is an example of the variation of viscosity with temperature of Shell Tellus R5 oil, under normal operating conditions a change in temperature of 1°C lead to a 3% change in viscosity.

Temperature was measured for each experiment and the exact value of viscosity was then interpolated using a fitted function relating the viscosity to the temperature — for the example shown in figure 2.24 a linear interpolation gives

$$\mu[Pas] = -0.27 \times 10^{-3} T[^{\circ}C] + 0.0129.$$

This allowed for a correction to the capillary number to be made. Later a small refrigeration unit controlled by a Cal 2000 controller was used to maintain a steady temperature of $\pm 0.1^{\circ}$C, and this correction was not necessary.

Rees (1995) showed that the viscosity of the light organic oils (R5 or R10) could change with time, presumably due to evaporation of the lighter components, so it was important to contain, as much as possible, the fluid in a closed circuit. Viscosity measurements were made before and after the experiments described in this thesis and showed no variation due to the relatively short times the fluids were in use.

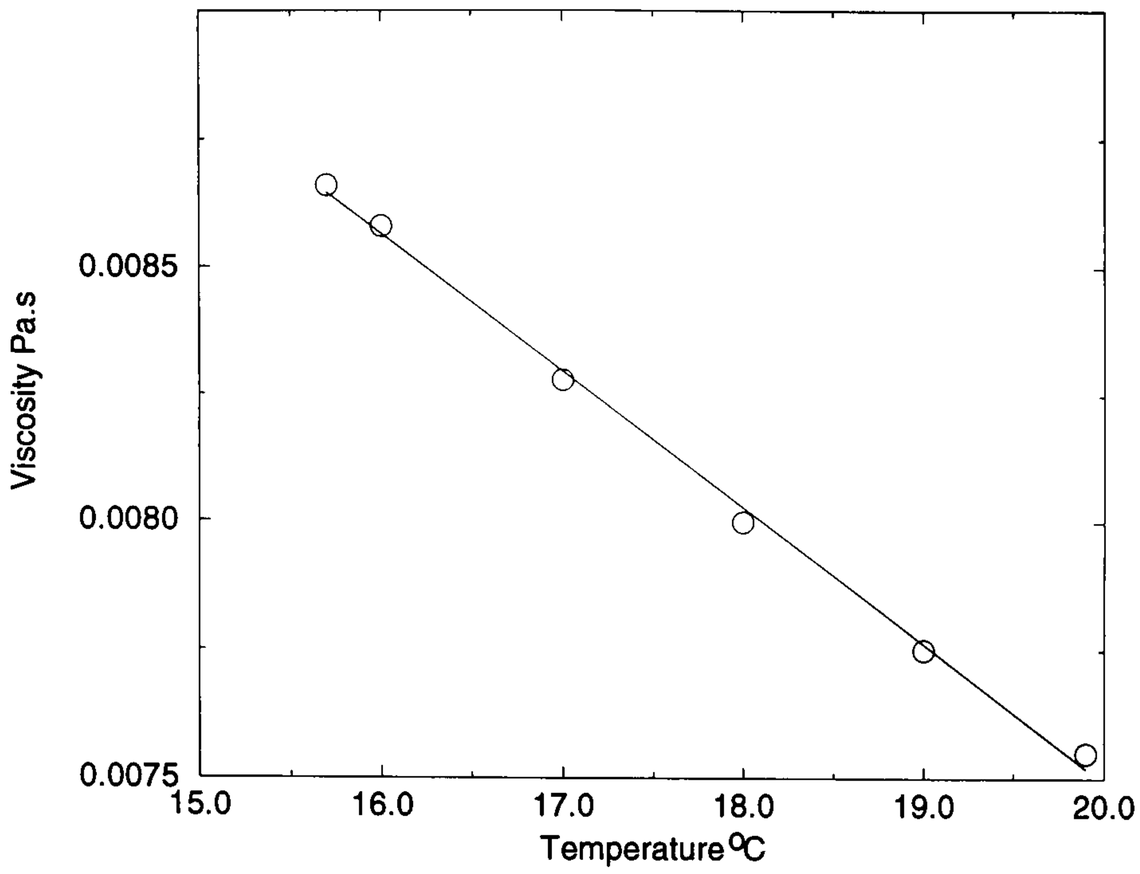

Figure 2.24: Viscosity of R5 oil as a function of temperature. ∘ experimental points, — fitted function: $\mu[Pas] = -0.27\times10^{-3}T[^{\circ}C]+0.0129$.

2.7.2 Surface tension

Surface tension was measured using a 12 mm diameter du Noüy platinum ring on an accurate torsion balance (White), illustrated in figure 2.25. The ring was cleaned thoroughly before each measurement by gently flaming using a Bunsen burner. The accuracy of the device could be checked using doubly distilled water which has a recorded surface tension of 72.3×10^{-3} N/m at 20°C.

2.7.3 Density

The density of the fluid was measured using a density bottle illustrated in figure 2.25. The mass of the bottle before and after filling was recorded and related to the fluid density using the known volume of the bottle.

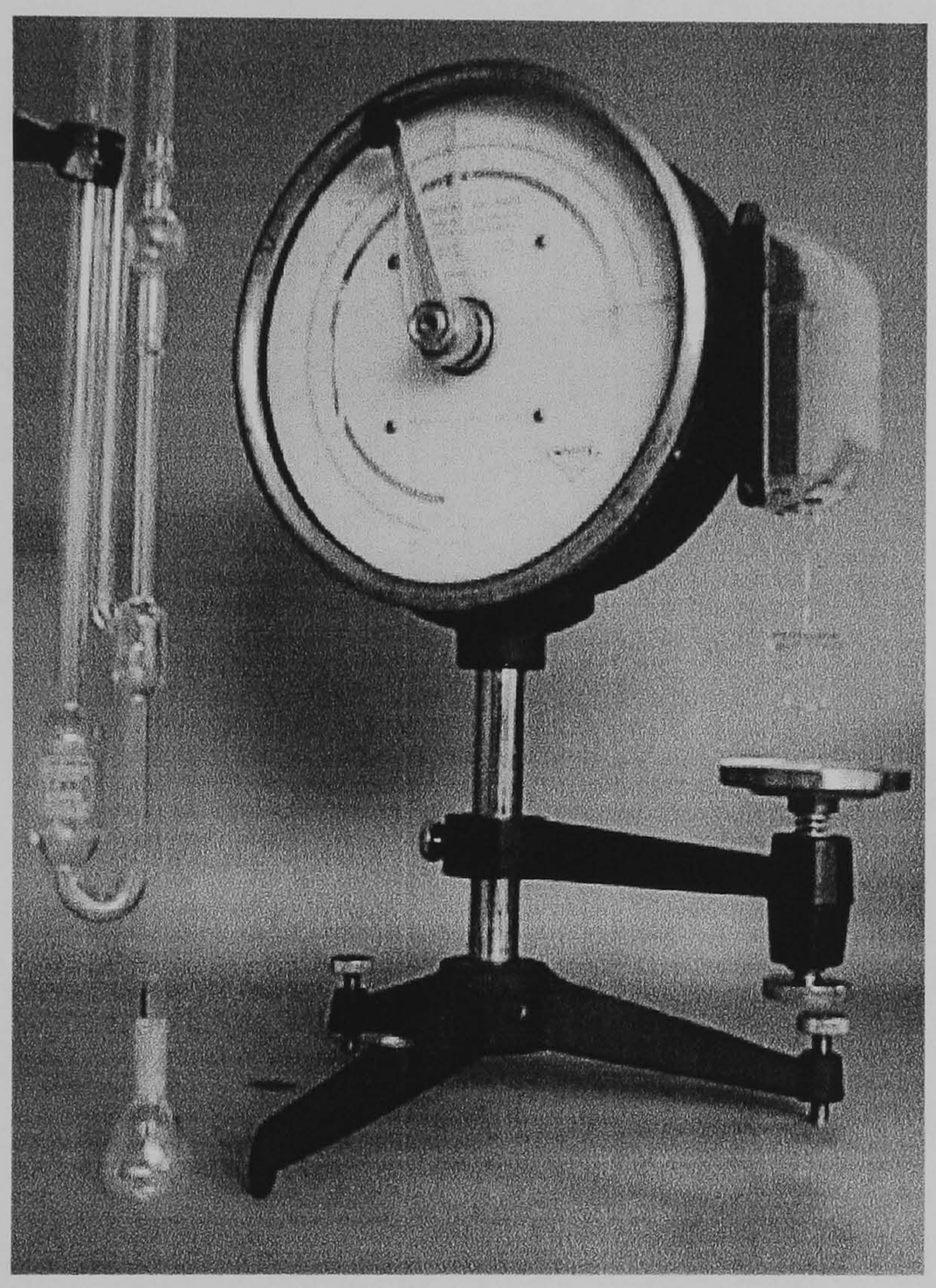

Figure 2.25: The equipment used to measure the fluid properties – the torsion balance (right), the capillary tube viscometer (left) and the density bottle (bottom left).

Chapter III

Reservoir fed reverse roll coating

Contents

3.1 Introduction

Reverse roll coating systems are used throughout industry for the application of thin liquid films due to their versatility. Products include, for example, magnetic media, adhesive tapes, films and foils (Coyle (1997)). Booth (1970) classified the most common reverse roll coating systems as either 'pan-fed' or 'nip-fed' and identified eight different variants, each distinguished by the particular form of feeding mechanism employed.

Figure 3.1 shows examples of both pan-fed and nip-fed reverse roll systems where the web is wrapped around a rigid backing roll over which there is a deformable elastomer covering. In both cases, the flow in the gap between the applicator and metering rolls determines the final coated thickness, H_{app}, on the web as essentially all fluid between the deformable roll and the applicator roll is transferred, by a 'wiping' action, to the web (Coyle (1997)). For this reason, most previous experimental and theoretical studies of reverse roll coating systems have focussed on the flow in the metering gap.

Ho and Holland (1978), studied a simple system with the rolls aligned horizontally and the web emerging vertically upwards from the metering gap. They developed a model based on lubrication theory to predict how the film thickness on the web depends on the metering gap and the ratio of the roll speeds; their predictions agreed reasonably well with their experimental data. Although they included a gravity term in their analysis they showed, for the experimental arrangement employed, that it was small and could be neglected.

Greener and Middleman (1981) examined the simplified model system shown in figure 3.2 with the rolls side-by-side and half submerged in the coating liquid. They modified Ho and Holland's lubrication model by applying a different boundary condition near the film splitting meniscus at a location marking the onset of two-dimensional recirculating flow, and also neglected gravity. Their film thickness predictions exhibited the same trends as their experimental data over the speed ratio range $(0.25 \leqslant S \leq 1.75)(S = U_{web}/U_{app})$, although there were significant discrepancies between the actual data values.

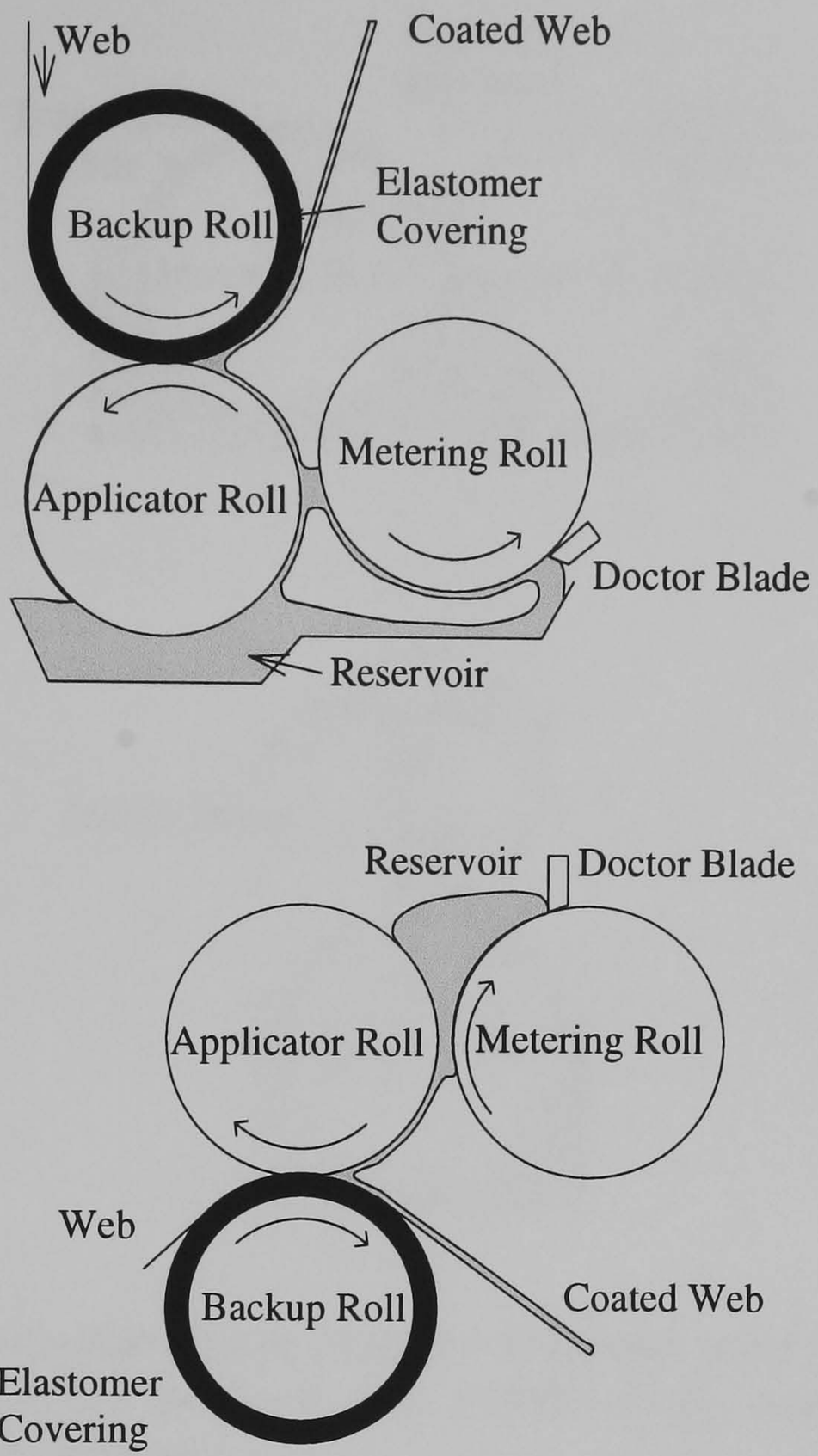

Figure 3.1: Examples of pan–fed (top) and nip (bottom) fed reverse roll systems.

Coyle *et al.* (1990a) later examined Greener and Middleman's (1981) model system both experimentally and computationally *via* finite element solutions of the Navier–Stokes equations in which the flow near the film splitting meniscus was modelled much more accurately. Accordingly, they proposed that the discrepancies between theory and experiment reported by Greener and Middleman (1981) could be partially explained by the latter's neglect of gravity since when the roll speeds are low there is a large body of liquid above the gap which must be accounted for. Coyle *et al.* (1990a) concluded that this model system, though simple, is not a good representation of flow in the metering gap of a reverse roll coater because of the absence of a dynamic contact line which can be of crucial importance, particularly for large values of S. They went on to show that gravity, acting in a direction opposite to

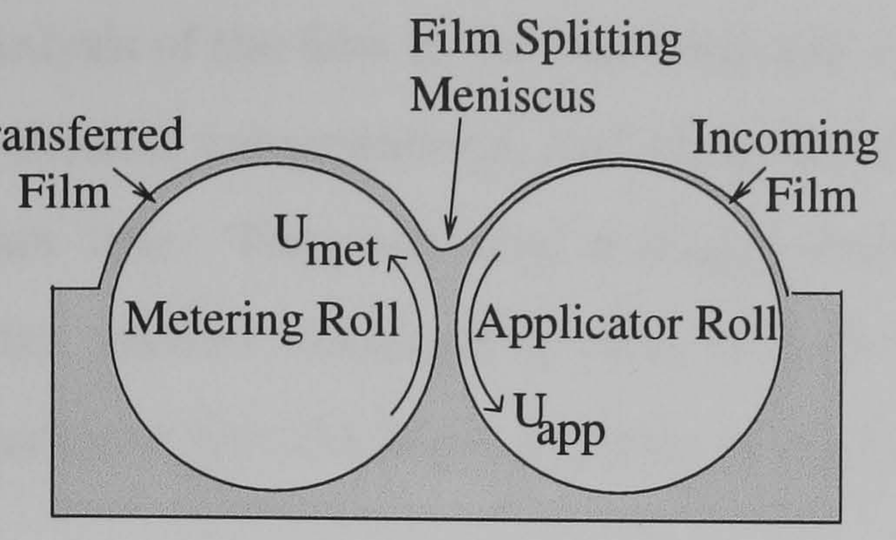

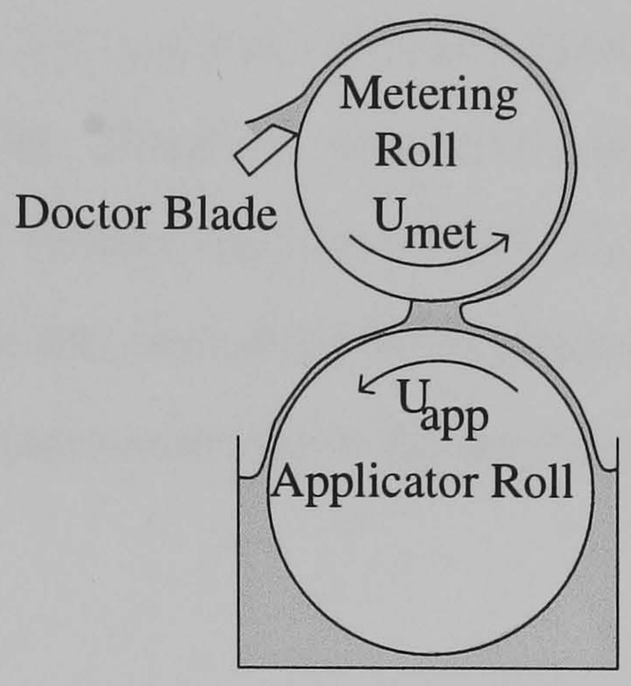

Figure 3.2: The simplified model system of Greener and Middleman (1981) also studied by Coyle *et al.* (1990a) (top), and Benkreira *et al.* (1981) (bottom).

that of the motion of the metering roll can decrease the transferred film thickness (see figure 3.2), as gravity increases flow down through the gap.

Benkreira *et al.* (1981) performed a detailed series of experimental measurements of the flow rates and film thicknesses for a system with rolls in vertical alignment, as shown in figure 3.2, which is a more realistic model of the true metering flow situation found in practice. Their results for both Newtonian and non-Newtonian coating liquids were summarised in the form of empirical relationships obtained by correlating their experimental data. Benkreira *et al.* (1982) subsequently developed a lubrication model for this flow situation and predictions from this model were found to agree well with their earlier experimental data.

However, it was the work of Coyle *et al.* (1990b) that lead to a major step forward in the understanding of the metering flow in reverse roll coating systems. They

performed a detailed analysis of the flow in the metering gap using a combination of experiments and finite element computations, including the effects of both menisci and the dynamic contact line. They reported a large number of important new results and, in particular, showed conclusively that at high speed ratio and high capillary numbers the metered film thickness deviates strongly from the predictions of lubrication theory.

Unfortunately Coyle *et al.* (1990b) were unable to derive a model based on lubrication theory as they did not have an appropriate boundary condition to use at the downstream meniscus. However, later Richardson (1996) used the condition of Fukazawa *et al.* (1992) (based largely on the work of Landau and Levich, 1942) to derive just such a model, including both menisci, that showed similar trends to that of Coyle *et al.*'s computational results for low capillary number at speed ratios greater than one.

3.2 Motivation

In this chapter a variant of nip-fed reverse roll coating is studied in which the nip region between the applicator and metering rolls is fed by a large reservoir of coating liquid located *directly above*, as shown in figure 3.3. In the industrial situation a web is wrapped around a rigid applicator roll and its coating thickness, H_{web}, is determined by the competition between the metering action of the reverse roll configuration and the influence of gravity in the form of the hydrostatic head provided by the reservoir. This process is similar to that shown in figure 3.1 but with two important differences: (i) the web is wrapped around the applicator roll (roll 2) so that there is no subsequent transfer to a web wrapped around a back-up roll; (ii) the height of the reservoir, H_R, above the point of minimum separation of the two roll surfaces is used as a further operating variable, rather than simply requiring the inlet to be flooded.

The aim of the present work is to provide a fundamental understanding of the influence of the reservoir on this process and in particular to determine how it affects the coated film thickness, H_{web}, and the position of the contact line.

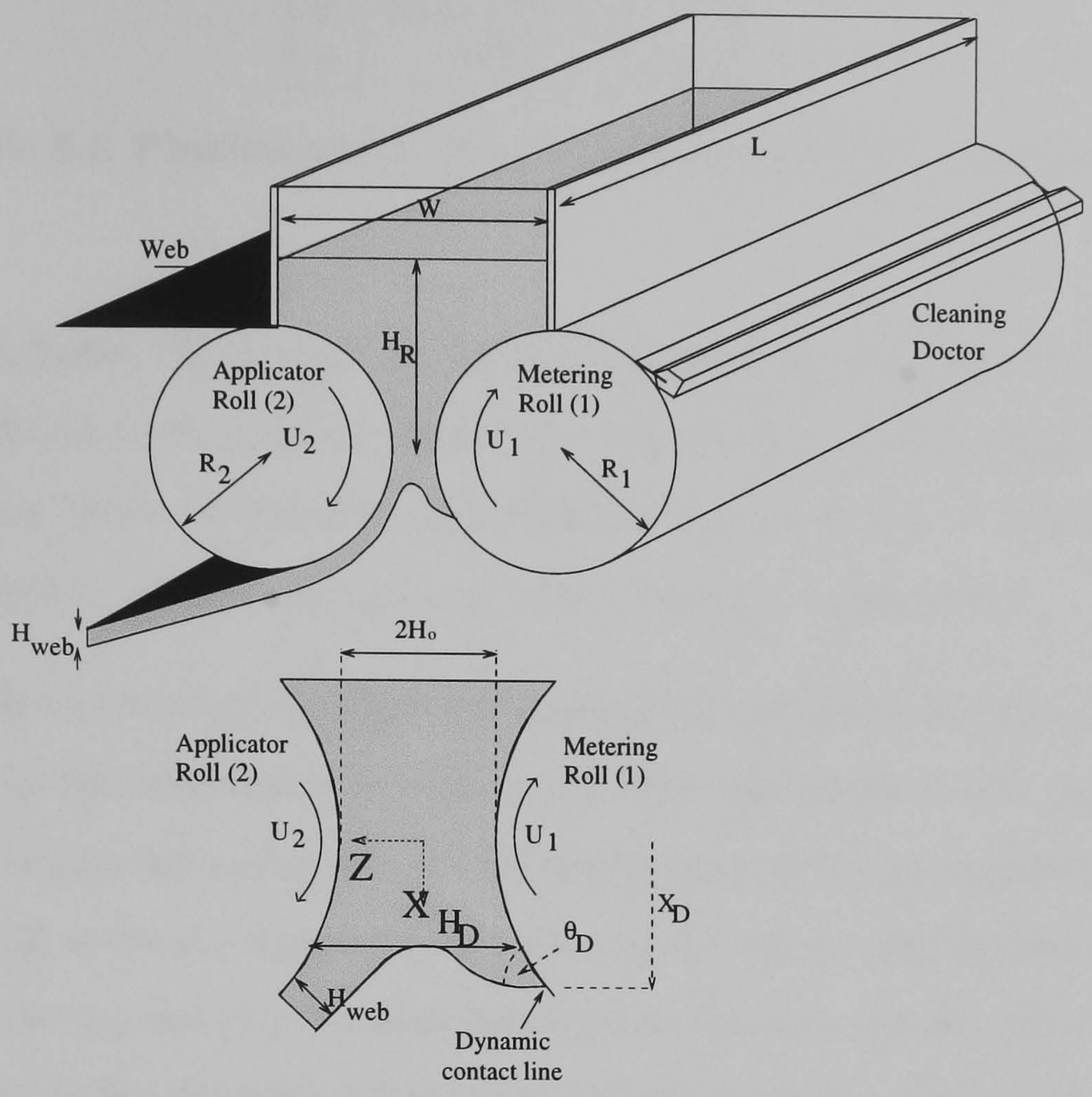

Figure 3.3: Reservoir fed reverse roll coating: roll arrangement and geometrical parameters.

3.3 Experimental method

The experimental results presented in the following sections were performed on the precision twin–roll apparatus described in section 2.2. Briefly it consisted of two horizontally aligned rolls (of diameter 50.48 mm) with a Perspex reservoir mounted directly above, as illustrated schematically in figure 2.4. The reservoir allowed a maximum height of 75 mm of fluid above the centre of the rolls, and the width, W, between the side baffles was fixed at 50 mm.

Fluid was supplied to the reservoir from a constant head tank, with an in–line weir used to regulate the level. A large reservoir of fluid ensured that changes in ambient temperature did not significantly alter the fluid properties. A Newtonian mineral oil (HVI–160) was used as the working fluid, with the properties shown in table 3.1.

μ	61.5×10^{-3}	Pa s
σ	33.5×10^{-3}	N/m
ρ	862	kg m^{-3}

Table 3.1: Physical properties of the fluid used in the experiments.

The film thickness, H_{web}, was measured by scraping the fluid from the roll over a fixed time period, as outlined in section 2.5. A second doctor blade was also installed to remove any fluid entrained on the metering roll surface as it passed under the side baffle, and so prevent disturbance to the dynamic contact line.

Dye injection was used to highlight the topological features of the flow. To highlight the motion in the reservoir a hypodermic needle was inserted into the fluid bulk, close to the stagnation point, and moved slowly upwards in the negative X direction (see figure 3.3) to leave a stream of dye. Flow in the nip was highlighted by injecting dye into (i) the top reservoir to show streamlines descending from the top eddy, and (ii) upstream of the dynamic contact line (as illustrated in figure 3.4). The latter flooded the nip with dye, although after a short period of time entrainment of clear fluid within the coating bead carried away any dye not trapped in the eddy, giving a dark recirculation contrasting with the clear coating fluid.

Lighting of the reservoir was achieved using a 150 W halogen light source fitted with twin flexible light guides, and the fluid sectioned by injecting the dye into only a narrow band (typically 5 mm away from the end of the roll).

To illuminate flow in the nip the light source was positioned to light the whole bead from one end. Any dye injected into the nip showed up as a dark line (where the light was not transmitted) against a light background. The menisci were also illuminated in this way to enable the position to be measured, however using this method is impractical for determining, for example, the contact angle since the error associated with looking through a finite length of fluid distorted this measurement which needs to be made very close to the wetting line. Figure 3.4 illustrates the positioning of the light source to highlight various aspects of the flow for the hydrostatic fed reverse flow coating.

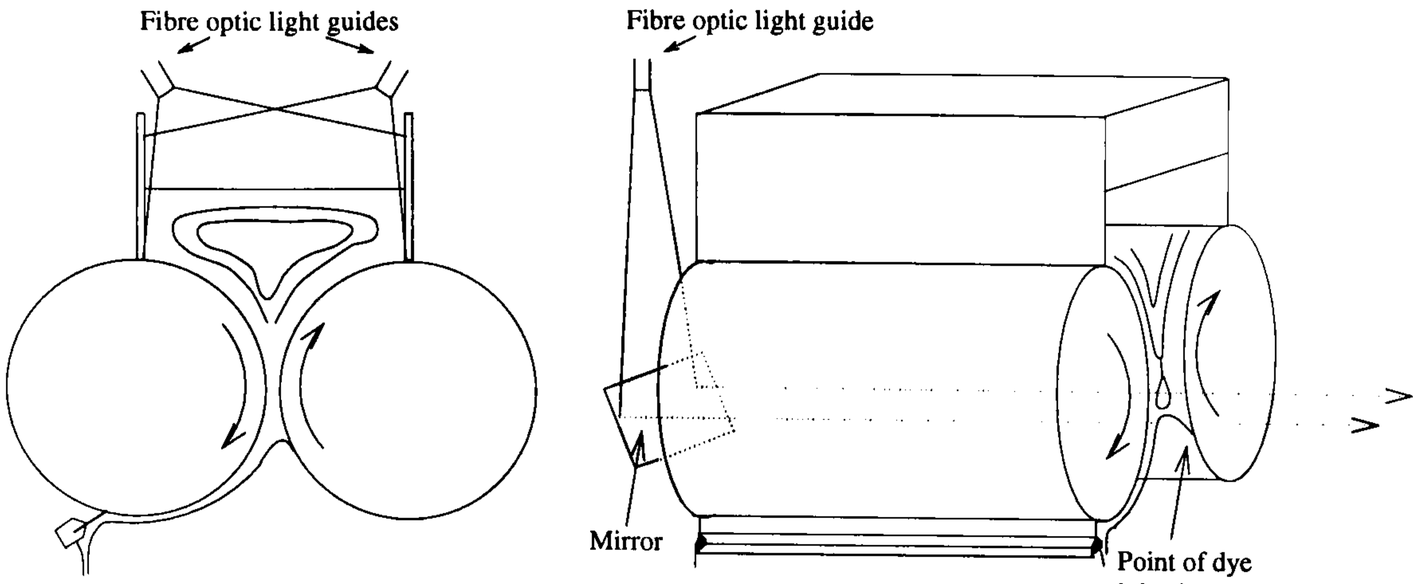

Figure 3.4: Light source arrangement to highlight (left) the top eddy and (right) the flow in the nip region.

3.4 Results and discussion

Experimental results were obtained by keeping the applicator roll speed, U_2, constant at $U_2 = 0.1175$ ms^{-1} (corresponding to $Ca_2 = 0.216$) and varying the metering roll speed, U_1, between 0.01175 ms^{-1} and 0.205 ms^{-1} (corresponding to $0.0216 \leqslant Ca_1 \leqslant 0.38$) giving speed ratios over a large range, namely $0.1 \leqslant S \leqslant 1.75$. Results were collected for each of three different reservoir heights of liquid, H_R =32.5 mm, 40 mm and 55 mm. In each case the nip width, $2H_0$, was kept constant at 250 μm. The effect of roll radii was not considered due to the constraints imposed by the apparatus available.

Figure 3.5 shows the effect of increasing speed ratio on the coated film thickness. As the speed ratio is increased, with all other parameters held constant, the film thickness at first decreases, until $S \approx 1$ after which point the film thickness starts to increase.

The above behaviour is best understood by examining the corresponding variation in the wetting line position — see figure 3.6. As speed ratio increases, the wetting line at first moves in towards the nip. At the point where the film thickness starts to increase with increases in speed ratio the wetting line is located at the point of minimum separation between the rolls. Further increasing the speed ratio causes the wetting line to migrate upstream of the nip.

The film thickness can be related to the distance between the two roll surfaces at the film split point, H_D, (as shown in figure 3.3) using the work of Landau and Levich (1942). Starting with their relationship :

$$\frac{H_{web}}{R_D} = 1.34 Ca_2^{2/3}, \quad Ca_2 < 0.01, \tag{3.1}$$

where R_D is the radius of curvature of the meniscus at the film split point, and using a model to relate R_D to the gap thickness at film split, H_D:

$$R_D = (1 + \cos\theta_D)(H_D - H_{web}) \tag{3.2}$$

gives an explicit relationship for the ratio H_{web} to H_D

$$\frac{H_{web}}{H_D} = \frac{(1 + \cos\theta_D)1.34 Ca_2^{2/3}}{1 + (1 + \cos\theta_D)1.34 Ca_2^{2/3}}. \tag{3.3}$$

Equation (3.3), although strictly valid for low capillary numbers only, suggests that for a given applicator roll speed, U_2, (hence constant Ca_2) the film thickness is a function of the roll separation at the film split point, H_D, — a larger separation at film split results in a thicker film. The actual film split split location, and hence H_D, is a function of both roll speeds and the fluid properties. A more detailed model would be required to accurately predict the wetting line position as a function of the parameters of the system, the interaction between the capillary and hydrodynamic forces playing a key role in this.

Consider now the effect of increasing U_1, hence the speed ratio, on the position of the meniscus:

- As U_1 increases the meniscus is pulled towards the nip and H_D decreases due to the convergent nature of the geometry. Equation (3.3) indicates that a reduction in H_D (for a given Ca_2) results in a thinner film, H_{web}, as shown in figure 3.5.

- As the meniscus is pulled upstream of the nip, due to further increases in the metering roll speed, H_D now increases due to the diverging nature of the

geometry. Equation (3.3) indicates that an increase in H_D (for a given Ca_2) results in a thicker film, H_{web}, as observed in figure 3.5.

Similar behaviour in the metering gap of a reverse roll coater without a reservoir has been reported by Coyle *et al.* (1990a), who also pointed out that the contact line migrating upstream of the nip is intimately linked to the onset of the cascade instability.

From figure 3.5 it is evident that changes in the height of fluid in the reservoir, H_R, also affect the web film thickness. The experimental data presented in figure 3.5 shows that the deepest reservoir level used in this study, $H_R = 55$ mm, gives the thickest film for low speed ratios, yet at high speed ratios $S > 1$ the thickest film is given by the shallowest reservoir $H_R = 32.5$ mm. A deeper reservoir of fluid (larger H_R) will result in a greater hydrostatic pressure which causes the wetting line to move in an increasing downstream (positive) direction. When the wetting line is located downstream of the meniscus this results in a thicker coated film as the gap separation at the film split point, H_D, is also increased. Conversely, when the wetting line is located upstream of the nip, increasing the hydrostatic head will result in a thinner coated film since the wetting line moves towards the point of minimum separation of the rolls and the distance between the rolls at the film split, H_D, reduces.

The height of the reservoir also affects the speed ratio for which the wetting line lies at the point of minimum separation between the rolls. This point is important as it corresponds to the point where the film thickness is a minimum, and an increase or decrease in speed ratio will result in a thicker coated film. Experimentally, it has been shown in figure 3.5 that if the hydrostatic head is increased then a corresponding increase in the speed ratio is required to locate the meniscus at the point of minimum separation in the gap. Again, this behaviour is due to the increased hydrostatic pressure forcing the meniscus in the (positive) X direction and delaying the point when the wetting line is located at $X_D = 0$.

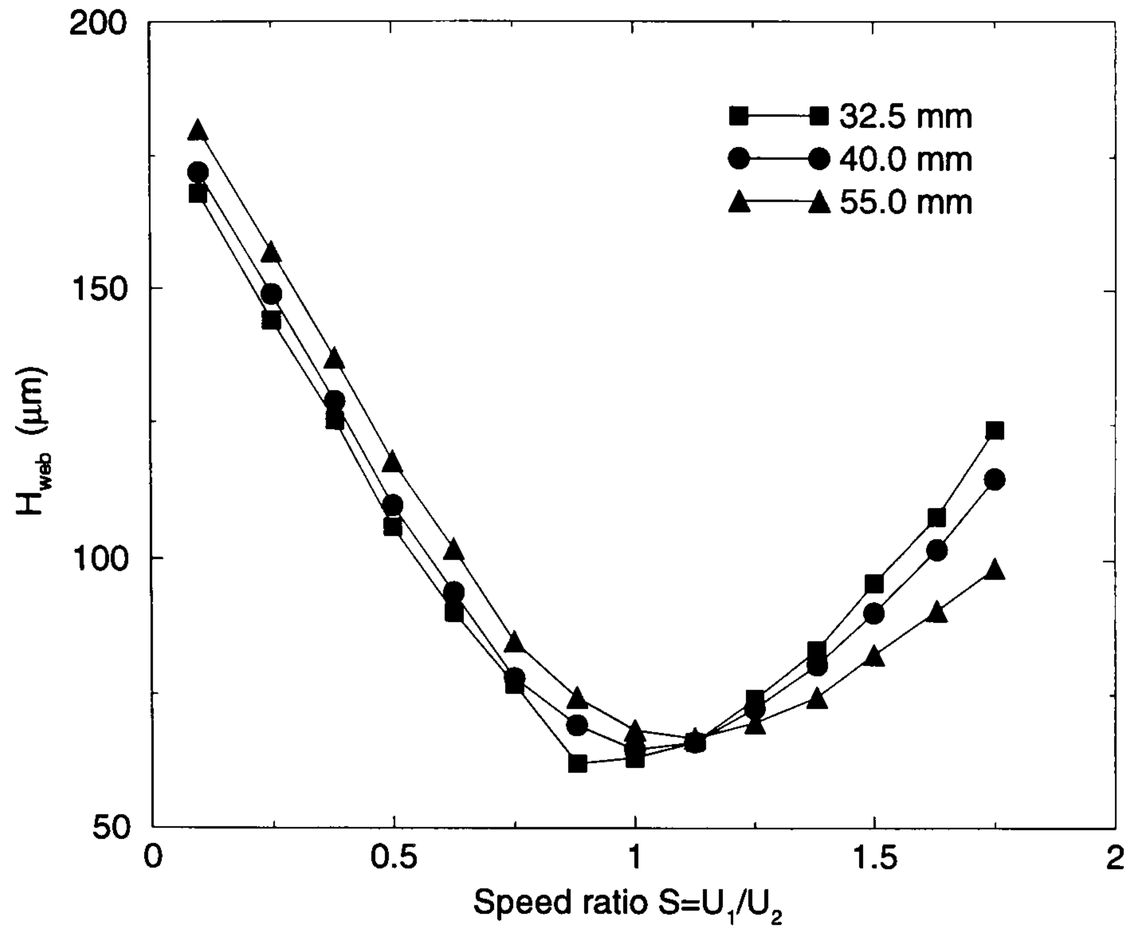

Figure 3.5: Experimental measurements of the coated film thickness on the applicator roll, H_{web} as a function of S: $Ca_2 = 0.216$; $2H_0 = 250$ μm; corresponding H_R as indicated.

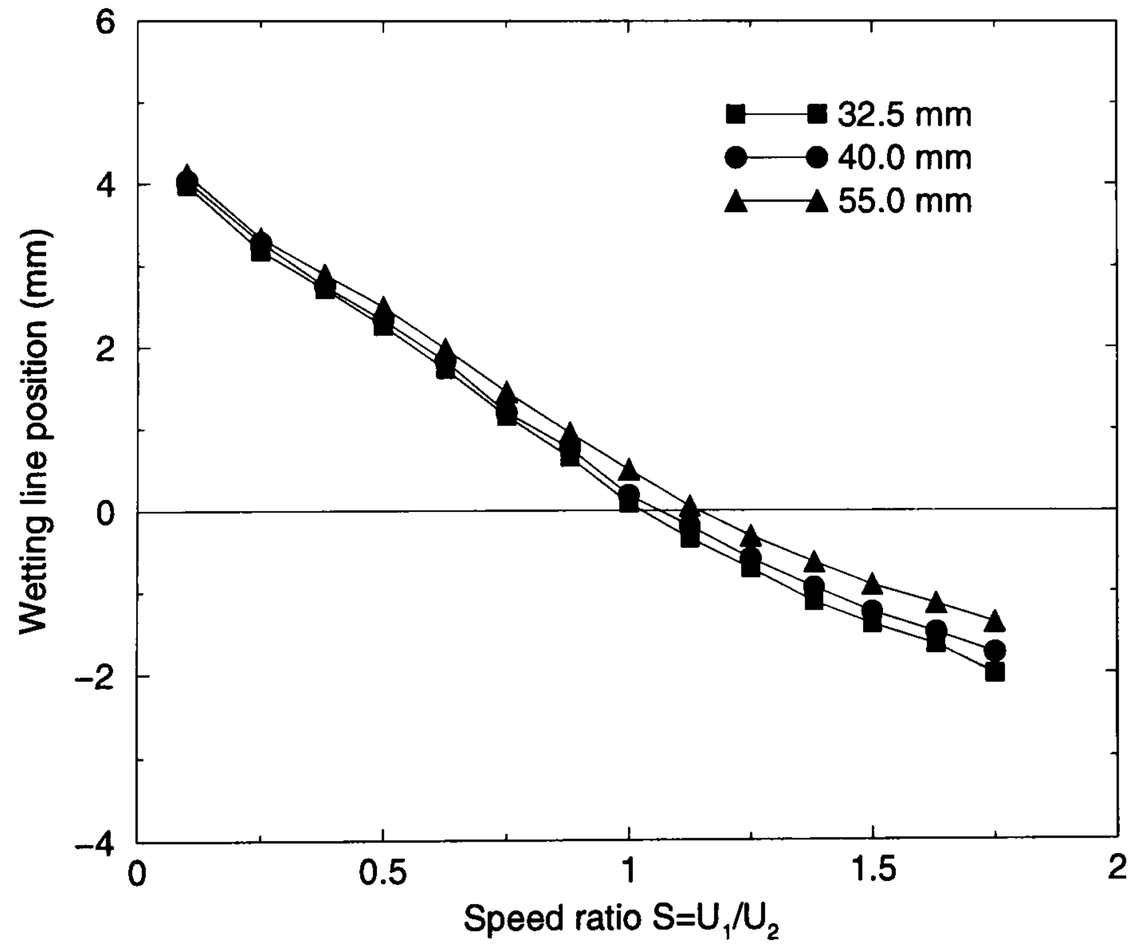

Figure 3.6: Experimental measurements of the position of the wetting line as a function of S: $Ca_2 = 0.216$; $2H_0 = 250$ μm; corresponding reservoir height.

Visualisations of the flow in the reservoir (for $H_R = 55$ mm) are shown in figures 3.7(a), (b) and (c) for $S = 0.1$, 0.5 and 1 respectively. It can be seen that the flow consists of a single, large recirculation in all cases and that the stagnation point at its centre is displaced towards the metering roll as its speed and hence S increases. When $S = 1$ (figure 3.7(c)), there is a slight asymmetry to the flow structure caused by the outgoing film on the applicator roll.

Figure 3.8 shows streamline plots from a solution to the Navier–Stokes equations, for the same set of conditions under which the experiments were run. The computational model was formulated and solved by Thompson, and these results are taken from Gaskell *et al.* (1999b). It is evident from comparing figures 3.7 and 3.8 that the predictions of the model and the experimental data are in excellent agreement, the computational model capturing the features observed experimentally very well indeed.

Figures 3.9(a), (b) and (c) for $S = 0.1$, 0.5 and 1, respectively, show visualisations in the reservoir for $H_R = 40$ mm. It is clear from a comparison with figure 3.7 that changes in the height do not significantly alter the main features of the reservoir flow.

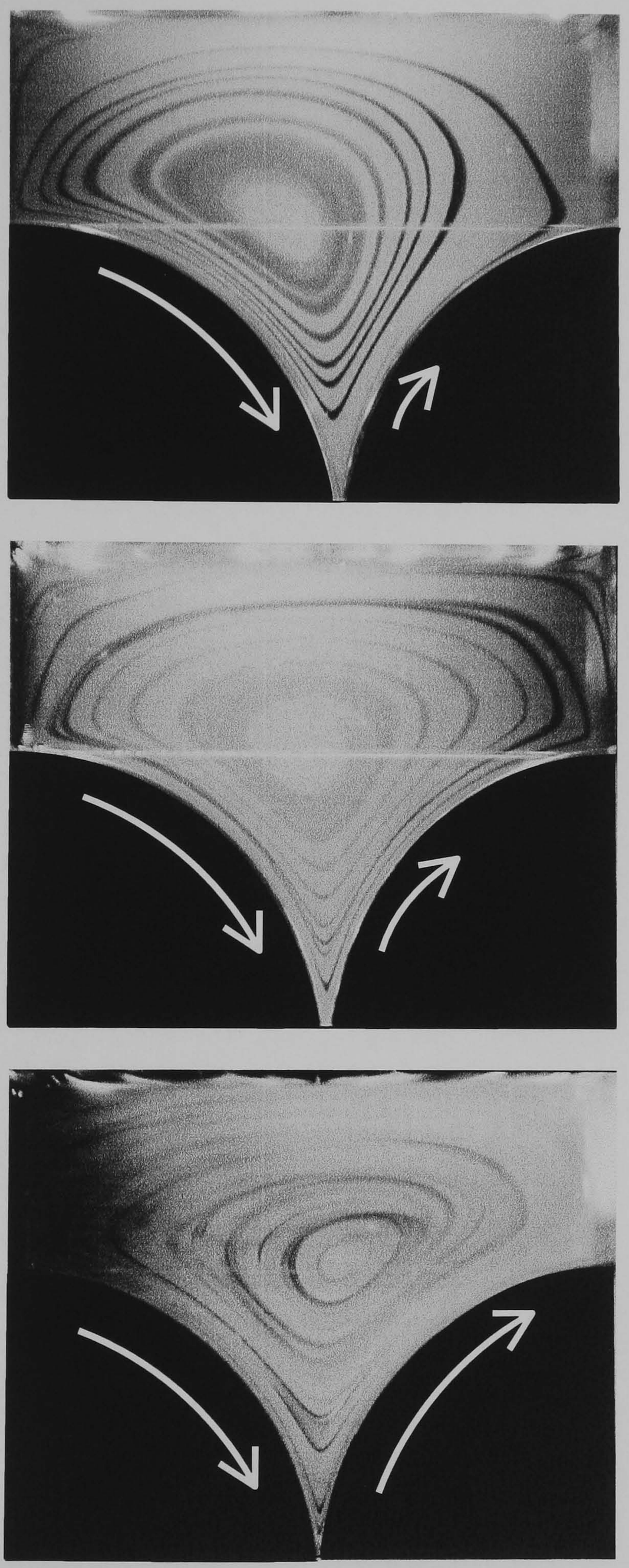

(a)

(b)

(c)

Figure 3.7: Dye traces illustrating the induced eddy flow in the reservoir for (a) $S = 0.1$, (b) $S = 0.5$, (c)$S = 1.0$. Here $Ca_2 = 0.216$, $2H_0 = 250\ \mu$m, $H_R = 55$ mm.

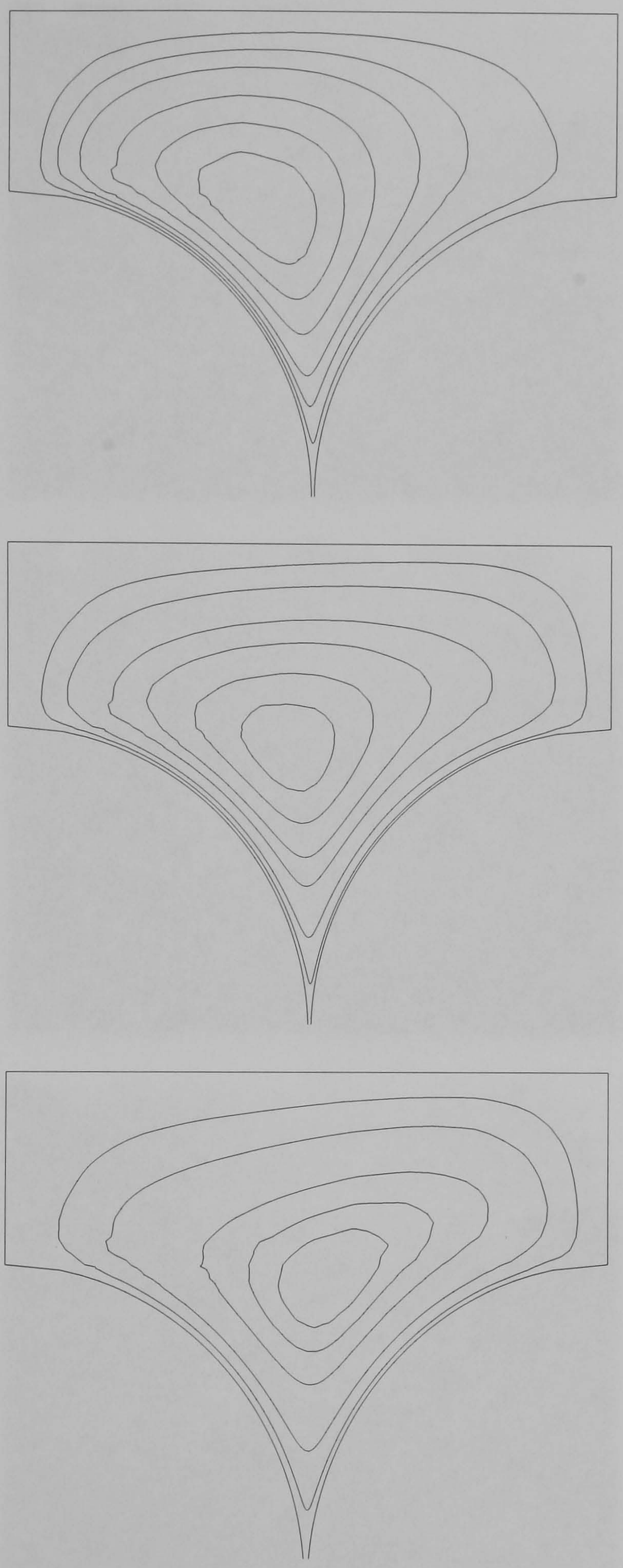

(a)

(b)

(c)

Figure 3.8: Corresponding numerical predictions of the eddy flow in the reservoir for (a) $S = 0.1$, (b) $S = 0.5$, (c)$S = 1.0$. Here $Ca_2 = 0.216$, $2H_0 = 250\ \mu$m, $H_R = 55$ mm.

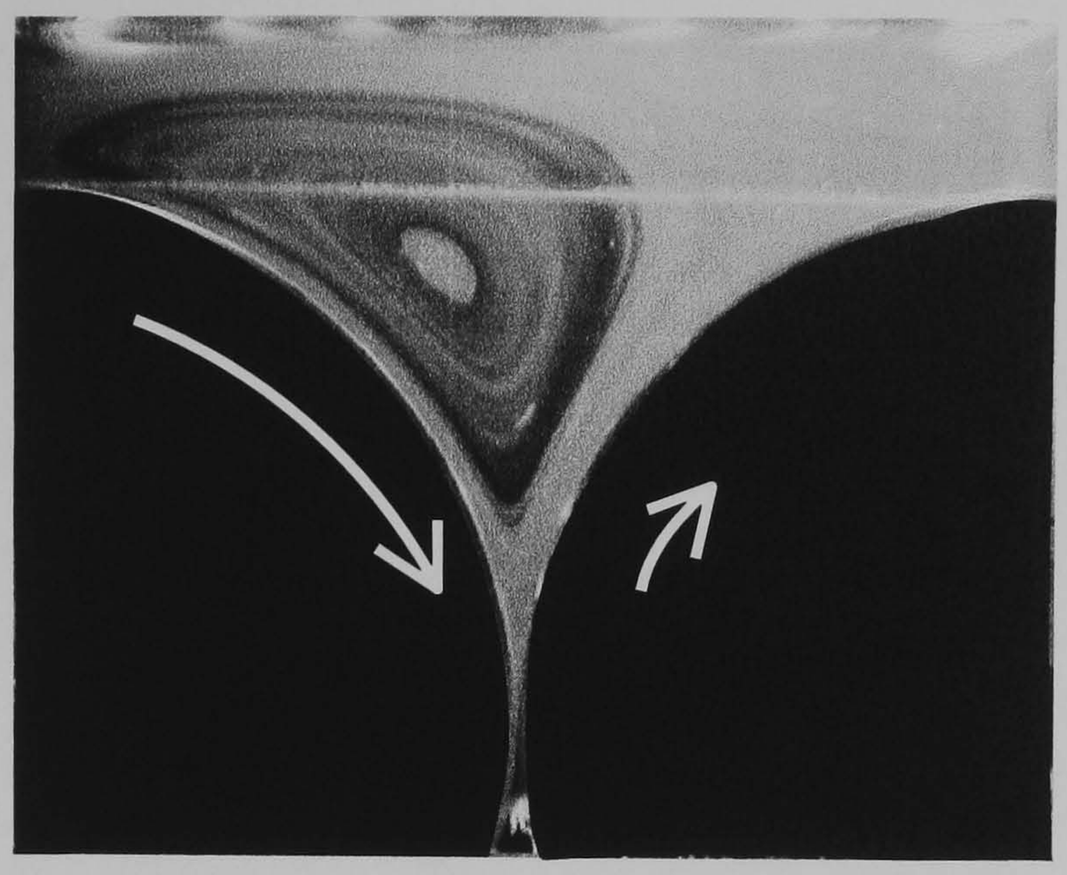

(a)

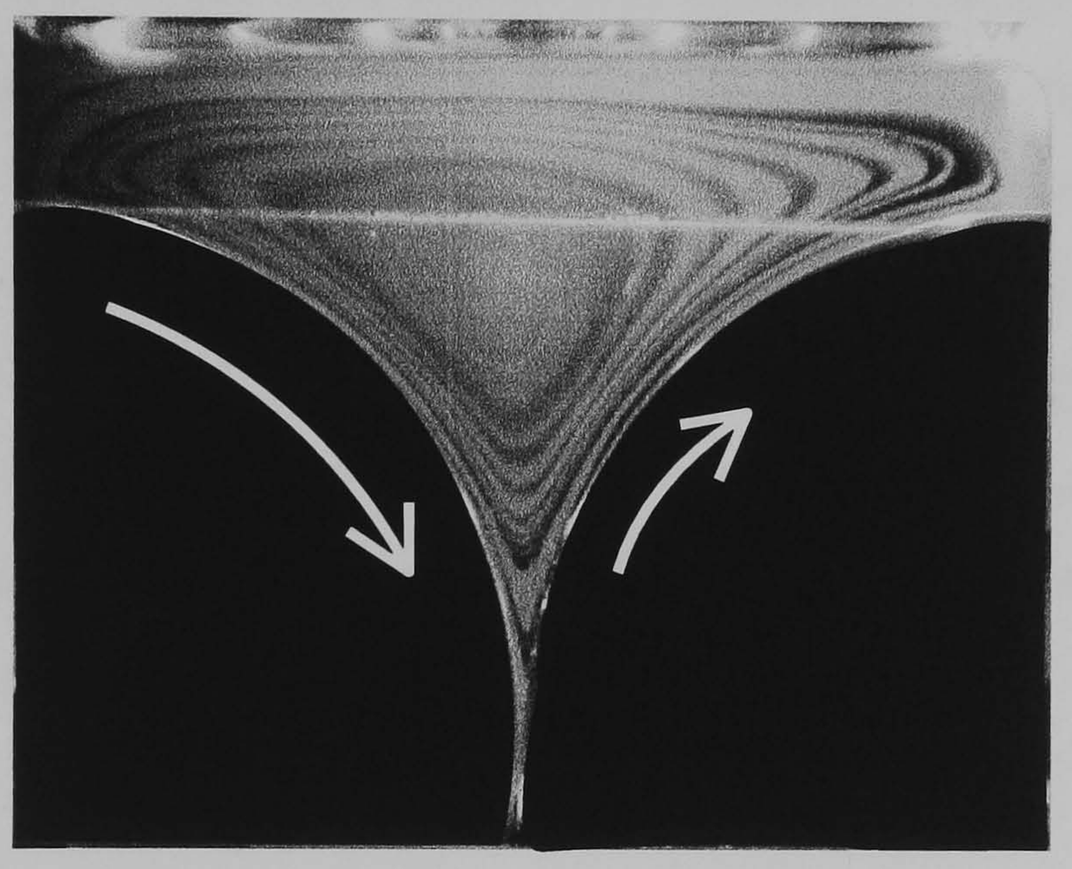

(b)

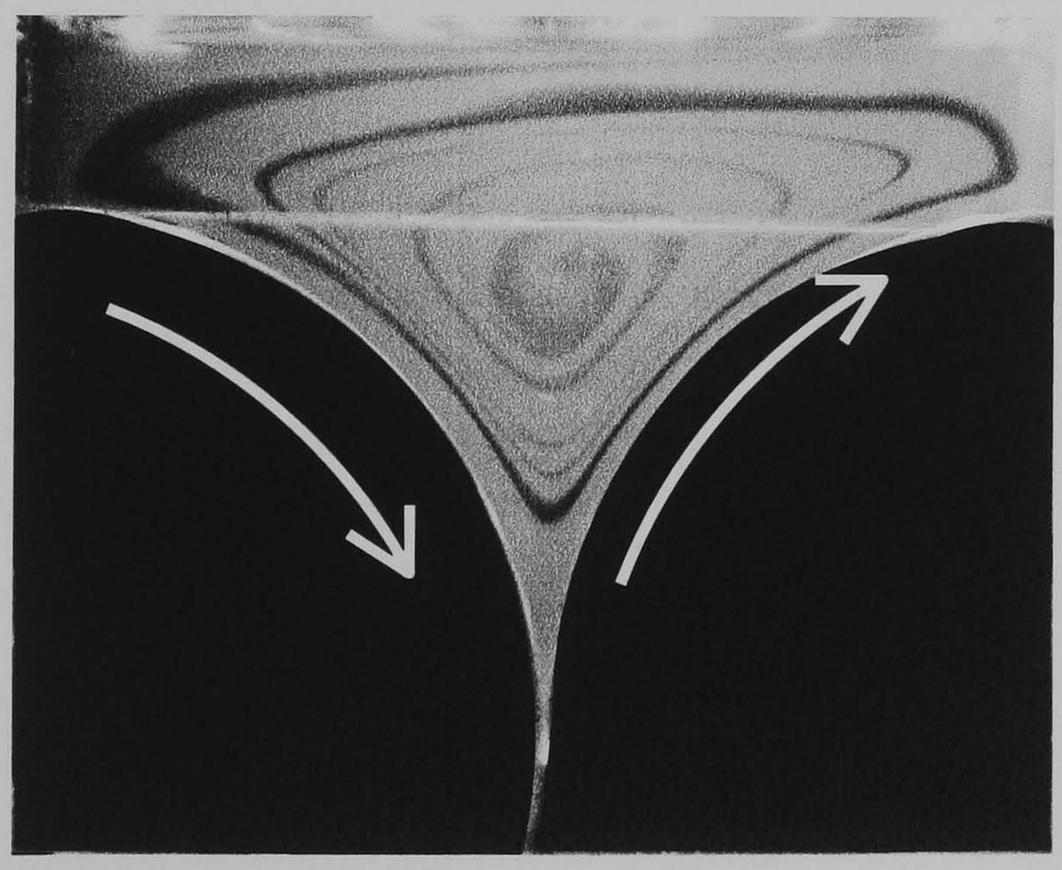

(c)

Figure 3.9: Dye traces illustrating the induced eddy flow in the reservoir for (a) $S = 0.1$, (b) $S = 0.5$, (c)$S = 1.0$. Here $Ca_2 = 0.216$, $2H_0 = 250$ μm, $H_R = 40$ mm.

Shown in figure 3.10(a), (b) and (c) are flow visualisations near the dynamic contact line when $H_R = 55$ mm and $S = 0.1$, 0.5 and 1, respectively. For $S = 0.1$ and 0.5 recirculations are clearly evident close to the contact line (the centres of which are darker due to entrapment of the tracer fluid) and the large recirculation in the reservoir is separated from the downstream by a nearly rectilinear flow region close to the nip. However for $S = 1$ (figure 3.10(c)) no recirculation region is discernible close to the contact line and the reservoir recirculation now penetrates into the nip region close to the contact line.

Figure 3.11 shows the corresponding numerical results generated using Thompson's finite element software for the same parameters as used in the experiments. Clearly there is good agreement between the topological features of the two. One shortcoming of the numerical model is the need to supply a value for the dynamic contact angle; here a constant value of 35° has been specified, although in practice as the metering roll speed is altered (to vary S) the contact angle would change. Unfortunately the value of the contact angle is difficult to estimate directly from images such as those shown in figure 3.10 since resolving very close to the contact line is not possible using the current lighting and imaging arrangement.

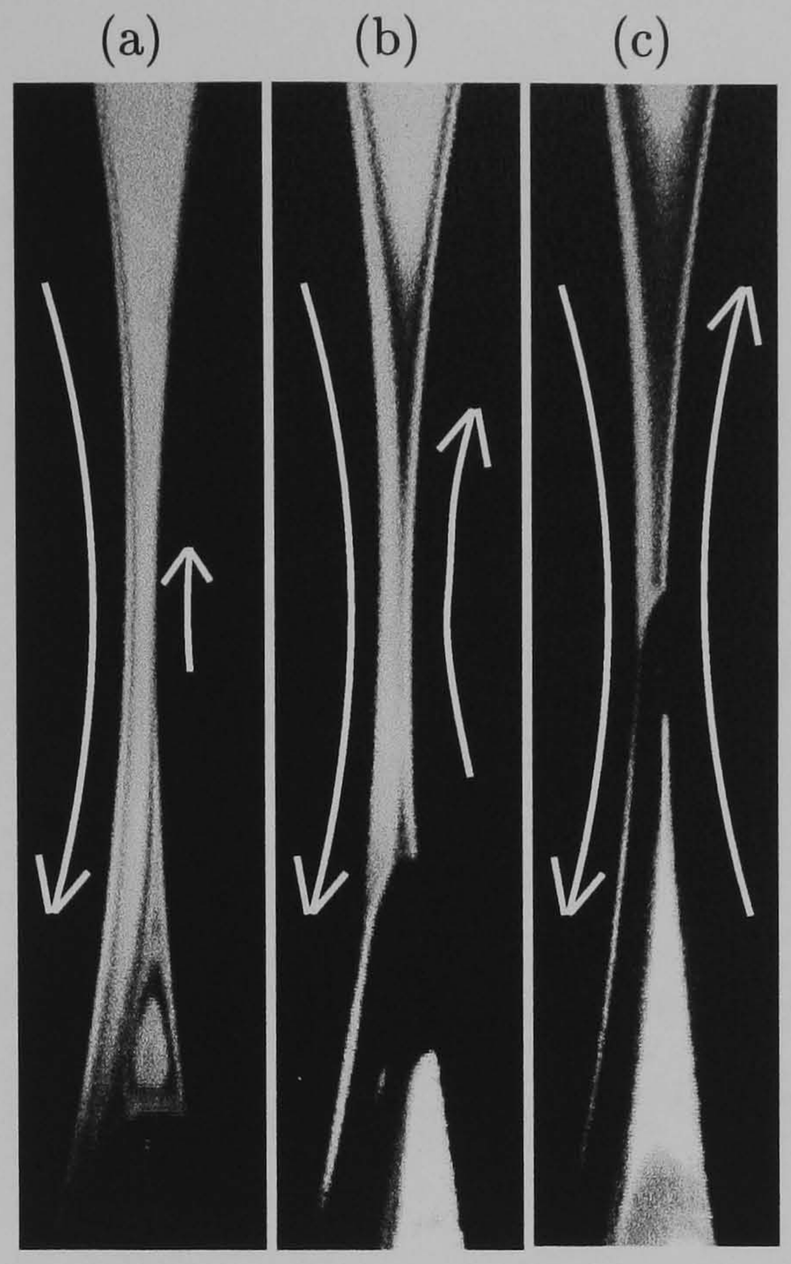

Figure 3.10: Flow structure close to the dynamic contact line for (a) $S = 0.1$, (b) $S = 0.5$, (c)$S = 1.0$. Here $Ca_2 = 0.216$, $2H_0 = 250$ μm, $H_R = 55$ mm.

Figure 3.11: Numerical predictions of the flow structure close to the dynamic contact line for (a) $S = 0.1$, (b) $S = 0.5$, (c)$S = 1.0$. Here $Ca_2 = 0.216$, $2H_0 = 250$ μm, $H_R = 55$ mm.

3.5 Summary

A number of conclusions may be drawn from this work:

- Experimental measurements show that the speed ratio and the depth of fluid in the reservoir can affect the web film thickness.

- When the meniscus is located downstream of X_0, either increasing the speed ratio or decreasing the depth of fluid in the reservoir results in a thinner film. However, when the meniscus is located upstream of X_0 the reverse is true.

- The flow structure consists of a large recirculation in the reservoir and, depending on the value of speed ratio, a possible eddy close to the downstream meniscus.

- Altering the depth of the reservoir does not significantly affect the main flow features.

Chapter IV

Bead–break in forward meniscus coating

Contents

4.1 Introduction

In the forward mode meniscus coating regime — illustrated in figure 4.1a, the inlet feed condition is starved and the fluid domain is bounded by the two roll surfaces and an upstream and downstream meniscus (relative to the incoming film). The capillary action of the two menisci play a crucial role in determining the pressure field within the bead of fluid which is entirely sub–ambient, Malone (1992).

Gaskell *et al.* (1998a) showed experimentally that fluid entering the coating bead in the form of a thin layer is transferred from one roll to the other prior to exiting as two films on the downstream side by means of one or more transfer jets, Gaskell *et al.* (1995). The latter also determined meniscus locations, flow structure, pressure profile and film thicknesses theoretically by means of a small flux, free boundary problem solved using the lubrication approximation and numerically using finite element methods.

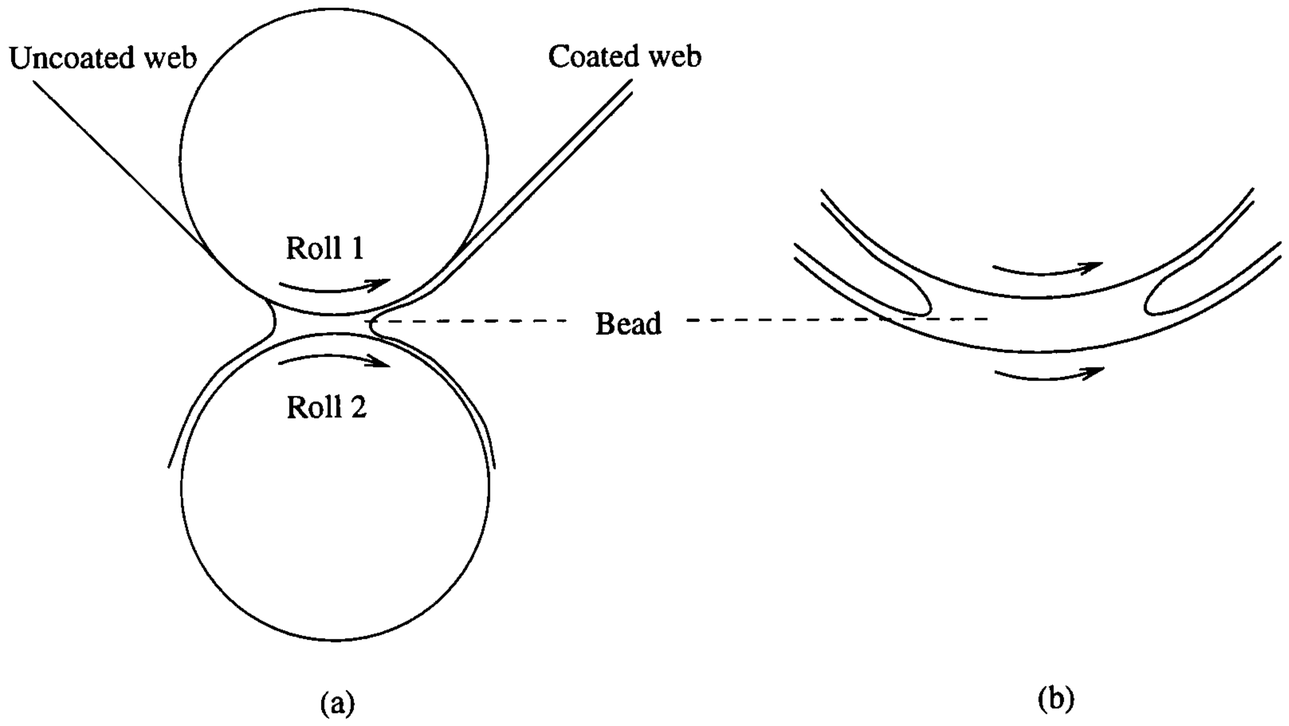

Figure 4.1: Cross–sectional scheme of (a) a forward mode meniscus roll coater of interest here and (b) the starved flow journal bearing arrangement.

The above work concentrated primarily on equilibrium flow conditions but Malone (1992) had showed earlier that bead–break can arise when the lower roll speed is kept constant while the speed of the upper one is increased. He found that in this case the upstream meniscus is observed to move inwards and pass through the nip with the cross–sectional flow remaining stable. Eventually, with the whole bead

lying downstream of the nip, a critical speed ratio is reached at which the meniscus loses stability — the bead rapidly contracts, and bead–break occurs when the two menisci collide.

Two dimensional 'bead flow' has also been observed in the journal bearing geometry shown in figure 4.1b, when a small quantity of viscous fluid is placed in the narrow gap between two non–concentric rotating cylinders, Rabaud *et al.* (1990), Rabaud and Hakim (1991). As well as the obvious difference in flow geometry between the meniscus coater and the journal bearing, the latter also has no contact line in the problem as there are thin films attached to both cylindrical surfaces. By varying the quantity of fluid, Michalland (1992), Michalland *et al.* (1996) were able to investigate experimentally the stability of both the upstream and downstream menisci. For co–rotating cylinders they established :

1. the presence of a ribbing instability on the downstream meniscus when the volume of fluid is 'large' and the menisci are located on either side of the nip;
2. two types of instability on the upstream meniscus when the volume of fluid is 'small' and the entire bead is located downstream of the nip. The first instability is a standing or propagating wave and this is followed by a steady state pattern of fingers separated by air columns.

Reinelt (1995) presented a mathematical model for viscous flow in this experimental setup, figure 4.1b, and analysed its stability to small amplitude, three–dimensional perturbations, periodic in the axial direction — achieving qualitative agreement between theory and experiment. However, the above workers did not analyse or report the presence of the bead–break instability in either the forward or reverse modes of operation.

4.1.1 Motivation

It is of practical interest to predict the parameter bounds imposed on the roll coating process by the bead–break phenomenon. Although the problem is just as relevant to co–rotating rolls this study is restricted to one of bead–break in a forward roll

coater for the case of one roll (roll 1) mounted vertically above the other (roll 2), see figure 4.2. This is achieved in two ways:

- Theoretically – use is made of the small–flux theory of Gaskell *et al.* (1995) describing the flow in the bead linked to a perturbation hypothesis used to determine the necessary conditions for the upstream meniscus to remain stable (*justification for this approach can be found in Gaskell* et al. *(1999a)*).

- Experimentally a systematic investigation is performed using a two-roll apparatus to collect meniscus location, flux measurements and associated bead–break conditions.

The theoretical predictions and experimental results are compared and the former used to map out the bead–break instability under conditions that may be encountered in practice.

4.2 Stable bead analysis

4.2.1 Downstream meniscus position

A mass balance for the system shown in figure 4.2 gives:

$$U_2 H_i = U_1 H_1 + U_2 H_2 \tag{4.1}$$

$$\text{or} \quad H_i = S H_1 + H_2.$$

The film thicknesses H_1 and H_2 can be written in terms of the radius of curvature of the downstream meniscus, R_D, using the relationship of Landau and Levich (1942):

$$H_1 = 1.34 R_D Ca_1^{2/3} \tag{4.2}$$

$$\text{and} \quad H_2 = 1.34 R_D Ca_2^{2/3}$$

which, together with equation (4.1), gives:

$$H_i = 1.34 R_D Ca_2^{2/3} (S^{5/3} + 1), \tag{4.3}$$

where Ca_2 is the capillary number based on roll 2, S the speed ratio and H_i the inlet film thickness as shown on figure 4.2. The radius of curvature of the downstream meniscus is now assumed to approximately equal to the semi-gap thickness $R_D = H(X_D)$, see figure 4.2, since the thicknesses of the inlet and the outlet films are small — $\frac{H_i}{H_0} \ll 1, \frac{H_1}{H_0} \ll 1, \frac{H_2}{H_0} \ll 1$ and assuming also the roll profiles near the nip are parabolic, R_D can be written as:

$$R_D \approx H_D = H_0(1 + x_d^2). \tag{4.4}$$

The dimensionless downstream meniscus position x_d is given by:

$$x_d = \left(\frac{2\lambda_i}{1.34 Ca_2^{2/3}(S^{5/3} + 1)} - 1 \right)^{1/2}. \tag{4.5}$$

The parameter x_d, and others used in this analysis – the inlet flux λ_i, the capillary numbers Ca_1 and Ca_2 and the speed ratio, S, are given by

$$x_d = \frac{X_D}{(2RH_0)^{\frac{1}{2}}}, \lambda_i = \frac{H_i}{2H_0}, Ca_1 = \frac{\mu U_1}{\sigma}, Ca_2 = \frac{\mu U_2}{\sigma}, S = \frac{U_1}{U_2}, \tag{4.6}$$

where R the roll radius, H_0 the semi-gap width, H_i the inlet film thickness, U_1 the upper roll speed, U_2 the lower roll speed, μ the viscosity and σ the surface tension of the liquid. The one other parameter that is required in this analysis is the contact angle the fluid makes with the moving roll, θ_D.

Equation (4.5) has been derived without any lubrication type flow calculations, but rather from a mass balance over the system and the use of the relationship of Landau and Levich (1942).

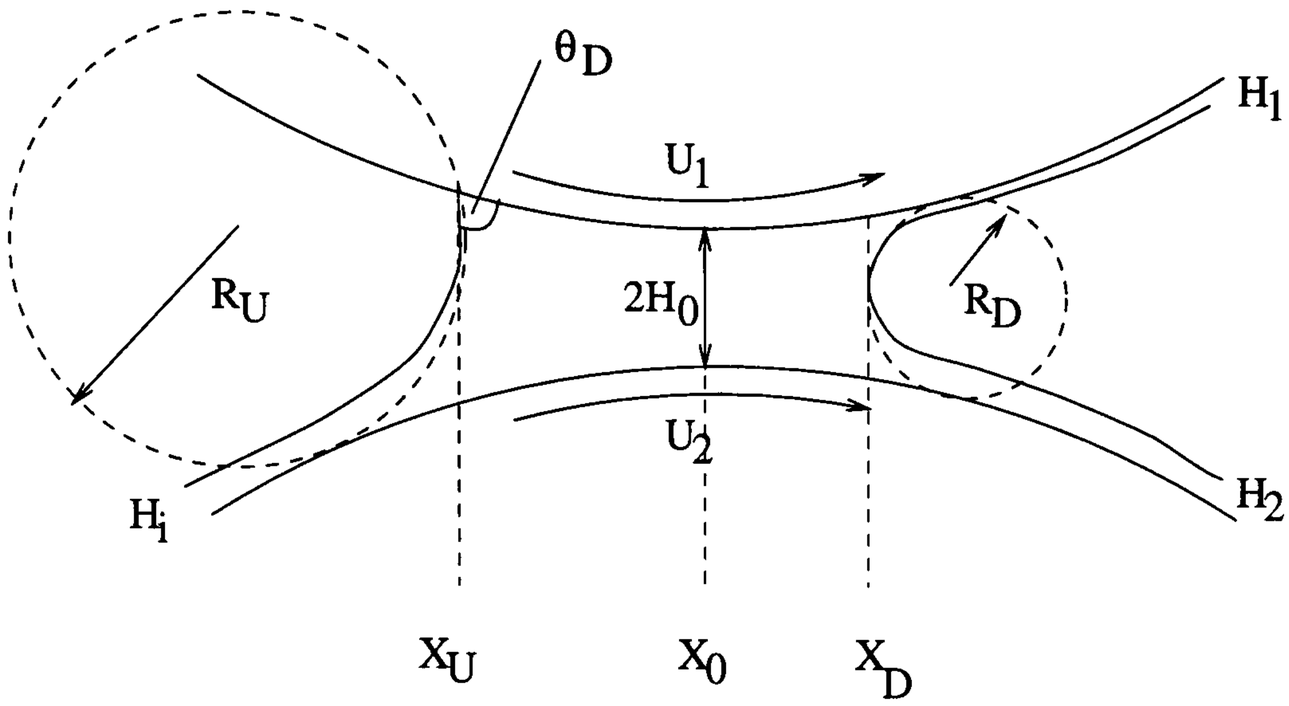

Figure 4.2: A cross-section of the bead located between the two rolls showing the geometric parameters of the system.

4.2.2 Upstream position

In the nip region the equation of fluid motion is the X-momentum equation in which pressure is assumed to be a function of X only,

$$P_X = \frac{dP}{dX} = \mu \frac{d^2U}{dZ^2}. \tag{4.7}$$

Integrating twice with no-slip boundary conditions, $U(-H) = U_2$, $U(+H) = U_1$ on the roll surfaces gives the velocity distribution

$$U = \frac{P_X}{2\mu}(Z^2 - H^2) + \frac{U_1 - U_2}{2H}Z + \frac{U_1 + U_2}{2}. \tag{4.8}$$

Integrating across the gap, between the upper and lower rolls, gives the flow rate per unit width

$$Q_i = \int_{-H}^{H} U dZ = -\frac{2}{3}\frac{P_X}{\mu}H^3 + (U_1 + U_2)H, \tag{4.9}$$

which after integration and rearrangement gives

$$P = \frac{3\mu}{2}(U_1 + U_2)\int \left(\frac{H - \frac{Q_i}{U_1 + U_2}}{H^3} \right) dX + C. \tag{4.10}$$

At both menisci, where the radius of curvature at the downstream meniscus is given by equation (4.4) and at the upstream meniscus approximated by (Fukazawa *et al.* (1992))

$$R_U = \frac{2H_U}{1+\cos\theta_D}. \tag{4.11}$$

the fluid pressure is balanced by the capillary pressure, i.e.

$$P + \frac{\sigma}{R} = 0. \tag{4.12}$$

This gives rise to two boundary conditions

$$P_U + \frac{\sigma(1+\cos\theta_D)}{2H_U} = 0\,, \quad P_D + \frac{\sigma}{H_D} = 0. \tag{4.13}$$

To solve equation (4.10) it is convenient to define a meniscus pressure function

$$G(X) = P(X) + \frac{\sigma}{R_U(X)}, \tag{4.14}$$

which is identically zero when $X = X_U$, together with a number of non-dimensional variables:

$$\begin{aligned}
h &= \frac{H}{H_0}, \\
\lambda &= \frac{Q_i}{H_0(U_1+U_2)} = \lambda_i \frac{2}{1+S}, \\
Ca &= Ca_2 \frac{1+S}{2}, \\
p &= \frac{2PH_0^2}{\mu(U_1+U_2)(2RH_0)^{1/2}}, \\
g &= \frac{2GH_0^2}{\mu(U_1+U_2)(2RH_0)^{1/2}}.
\end{aligned} \tag{4.15}$$

These along with the transformation $x = \tan\alpha$ allow equations (4.10) to (4.14) to be written in the form

$$p = 3\int(\cos^2\alpha - \lambda\cos^4\alpha)d\alpha + c, \tag{4.16}$$

$$p_u = -\frac{2^{1/2}(1+\cos\theta_D)}{4Ca\left(\frac{R}{H_0}\right)^{1/2}}\cos^2\alpha_u,\ p_d = -\frac{2^{1/2}}{2Ca\left(\frac{R}{H_0}\right)^{1/2}}\cos^2\alpha_d. \tag{4.17}$$

$$\begin{aligned} g(\alpha) = \left(\frac{2H_0}{R}\right)^{1/2} \frac{1}{4Ca}[(1+\cos\theta_D)\cos^2\alpha - 2cos^2\alpha_d] \\ -(\sin 2\alpha_d - \sin 2\alpha + 2\alpha_d - 2\alpha) \\ +\frac{3}{4}\lambda\left(\frac{\sin 4\alpha_d - \sin 4\alpha}{8} + \frac{3}{2}(\alpha_d - \alpha) + \sin 2\alpha_d - \sin 2\alpha\right) \end{aligned} \tag{4.18}$$

where θ_D is the contact angle and $\alpha_d = \tan^{-1} x_d$.

Since the zeros of $g(\alpha)$ correspond to the zeros of $G(X)$, they give the possible locations of the upstream meniscus when $g(\alpha_u) = 0$ in equation (4.18). A plot of $g(\alpha)$ against α for various speed ratios, as shown in figure 4.3, reveals that the graph either crosses the α axis twice, touches it, or lies entirely below it, depending of the magnitude S. The contact angle, θ_D was given a value of 50° taken from the experiments described in section 4.4.

Hence

$S < S^c, g = 0$ has two solutions – α_1, α_2

$S = S^c, g = 0$ has a double root $\alpha_1 = \alpha_2$ since $\frac{dg}{d\alpha} = 0$ also

$S > S^c, g = 0$ has no solutions

Two key questions naturally arise as a consequence of figure 4.3:

- For $S < S^c$, which of the two solutions of $g(\alpha) = 0$ is stable and observed in practice ?
- Since $g(\alpha) = 0$ has no solutions for $S > S^c$, then does S^c and $\frac{dg}{d\alpha} = 0$ correspond to the onset of instability ?

These questions are addressed below.

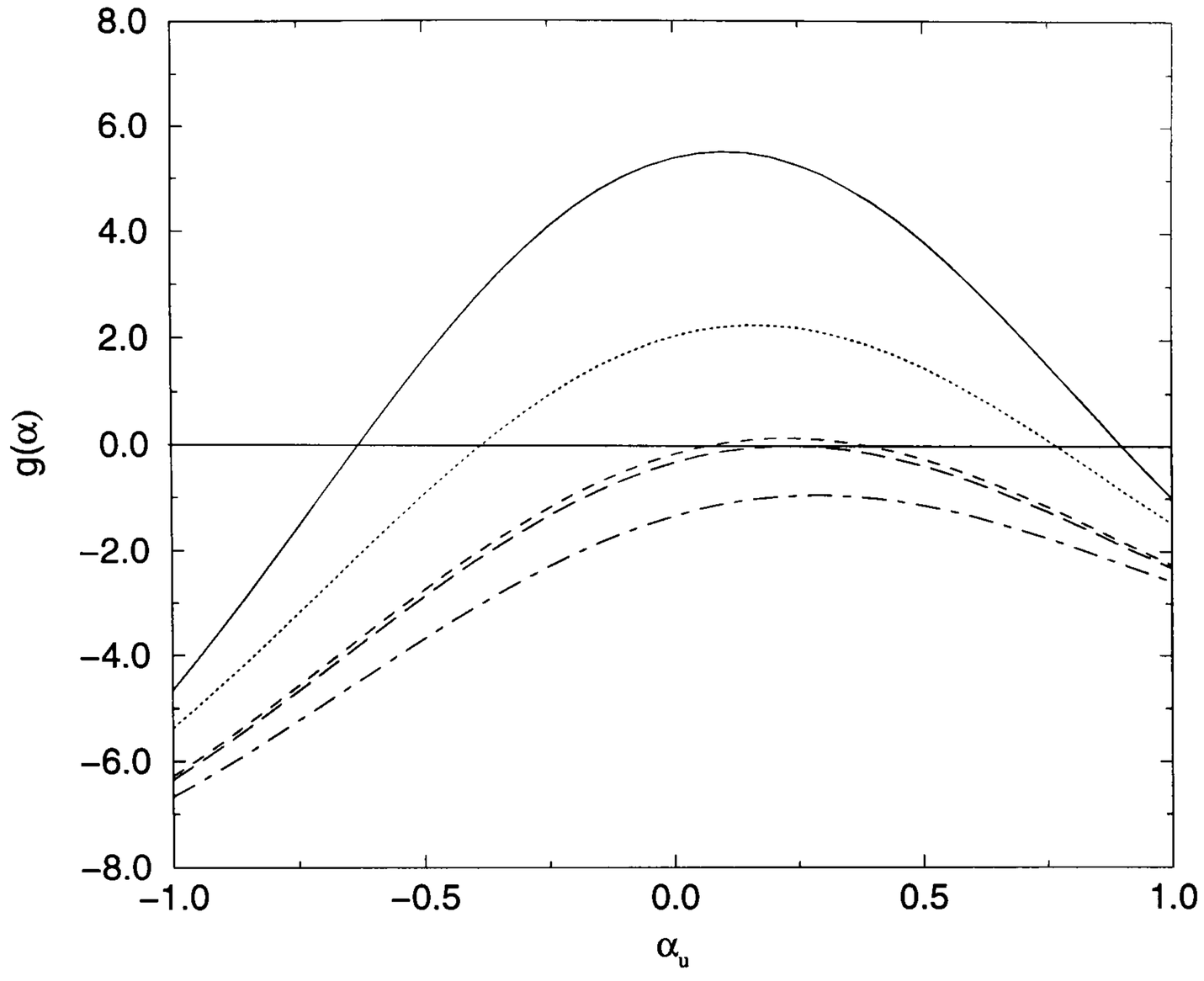

Figure 4.3: $g(\alpha)$ as a function of α_u and speed ratio S. $Ca_2 = 0.01$, $R/H_0 = 100$, $\lambda_i = 0.1$, $\theta_D = 50°$. S= — 0, $\cdots$0.5, – – 1.0, — — 1.071, – - – 1.5.

4.3 Stability hypothesis

Figure 4.4 shows a cross–section of the bead with the upstream and downstream menisci at X_U and X_D respectively.

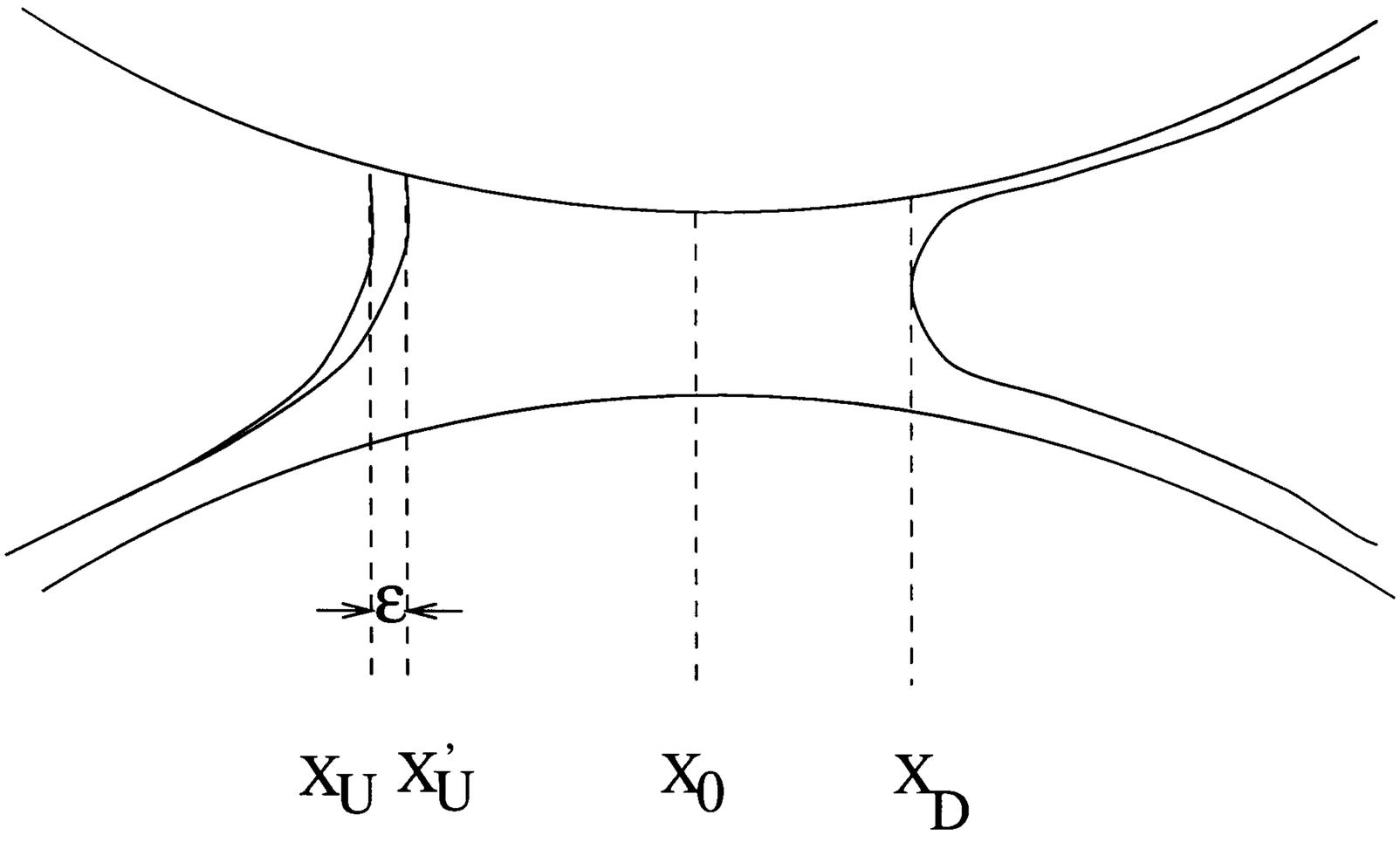

Figure 4.4: A cross–section of the bead showing a perturbation to the upstream meniscus.

The balance of fluid and capillary pressure at the upstream meniscus is given by

$$P + \frac{\sigma}{R_U} = 0 \text{ at } X = X_U. \tag{4.19}$$

The hypothesis used here is a local analysis which considers the stability of the upstream meniscus by its response to a small perturbation in its position. The contact angle is assumed to remain constant. Here the upstream meniscus is perturbed by a small distance, ϵ, such that its new position is given by

$$X_U' = X_U + \epsilon. \tag{4.20}$$

The restoring force, $F_{X_U'}$, acting on the interface in the negative X direction is given by

$$F_{X_U'} = \left(P + \frac{\sigma}{R_U}\right)_{X_U'}$$

$$= \left(P + \frac{\sigma}{R_U}\right)_{X_U} + \epsilon \frac{d}{dX}\left(P + \frac{\sigma}{R_U}\right)_{X_U} + O(\epsilon^2) \tag{4.21}$$

$$= \epsilon \frac{d}{dX}\left(P + \frac{\sigma}{R_U}\right)_{X_U} + O(\epsilon^2). \tag{4.22}$$

Using equation (4.11) this gives

$$F_{X'_U} = \epsilon \frac{dP}{dX} + \epsilon \frac{d}{dX}\left(\frac{\sigma(1+\cos\theta_D)}{2H_U}\right) \tag{4.23}$$

$$= \epsilon \left(\frac{dP}{dX} - \frac{\sigma(1+\cos\theta_D)}{2H_U^2}\frac{dH_U}{dX}\right) \tag{4.24}$$

The sign of $F_{X'_U}$ will determine whether the perturbation will diminish, remain neutrally stable (the onset of bead–break) or grow (i.e. bead–break will occur) accordingly as:

$$\begin{aligned} &F_{X'_U} > 0 \text{ the perturbation decays} \\ &F_{X'_U} = 0 \text{ the perturbation remains neutrally stable} \\ &F_{X'_U} < 0 \text{ the perturbation grows.} \end{aligned} \tag{4.25}$$

In forward meniscus roll coating, where $\lambda_i \ll 1$, the pressure gradient throughout the bead is positive (Gaskell *et al.* (1998)) :

$$\frac{dP}{dX} > 0 \tag{4.26}$$

so, from equation (4.23), when the upstream meniscus is located upstream of X_0 then $\frac{dH_U}{dX} < 0$ and $F > 0$, i.e. the the interface will always remain stable to disturbances.

On the other hand, when the upstream meniscus is located downstream of X_0 then $\frac{dH_U}{dX} > 0$ and the interface may now become unstable; hence

$$X_U > 0 \text{ is a necessary condition for instability.} \tag{4.27}$$

Non-dimensionalising 4.23 with respect to the quantities given in equation (4.15), yields

$$F_{X'_U} = \left(P + \frac{\sigma}{R_U}\right)_{X'_U} = \epsilon \frac{H_0}{\mu(U_1+U_2)R}\left(\frac{dg}{d\alpha}\right)_{\alpha_u} \cos^2\alpha_u \tag{4.28}$$

and for stability

$$\left(\frac{dg}{d\alpha}\right)_{\alpha_u} > 0. \tag{4.29}$$

Expanding and substituting for the non-dimensional variables gives

$$\frac{dP}{dX} = \frac{\sigma(1+\cos\theta_D)}{2H_U^2}\frac{dH}{dX} > 0 \text{ at } X = X_U \text{ for stability.} \tag{4.30}$$

So, consequently, instability arises when

$$\frac{\sigma(1+\cos\theta_D)}{2H_U^2}\frac{dH}{dX} > \frac{dP}{dX} \text{ at } X = X_U, \tag{4.31}$$

or, in dimensionless terms,

$$Ca_2\sqrt{\frac{R}{H_0}}(1+S) < \frac{\sqrt{2}(1+\cos\theta_D)\tan\alpha_u}{3(1-2\lambda\cos^2\alpha_u)} \text{ at } \alpha = \alpha_u. \tag{4.32}$$

When conditions are neutrally stable then $\alpha_u = \alpha_u^{crit}$ and equation (4.32) is an equality

$$Ca_2\sqrt{\frac{R}{H_0}}(1+S) = \frac{\sqrt{2}(1+\cos\theta_D)\tan\alpha_u^{crit}}{3(1-2\lambda\cos^2\alpha_u^{crit})} \text{ at criticality.} \tag{4.33}$$

Note that α_u is dependent upon Ca_2, $\sqrt{\frac{R}{H_0}}$, S and λ_i so this inequality has to be interpreted in conjunction with the steady state solution $g(\alpha_u) = 0$ as given by equation (4.18).

A plot of α_u^{crit} is shown in figure 4.5 together with the two real roots of equation (4.18), α_u^1 and α_u^2 that correspond to the predicted upstream meniscus position. The figure clearly shows that where a bead exists the smaller of the two real roots, α_u^2 is stable to perturbations, hence the one observed in practice. Figure 4.5 also shows that when $S > S^{crit}$ no stable bead exists, with the point $S = S^{crit}$ being the neutral stability point.

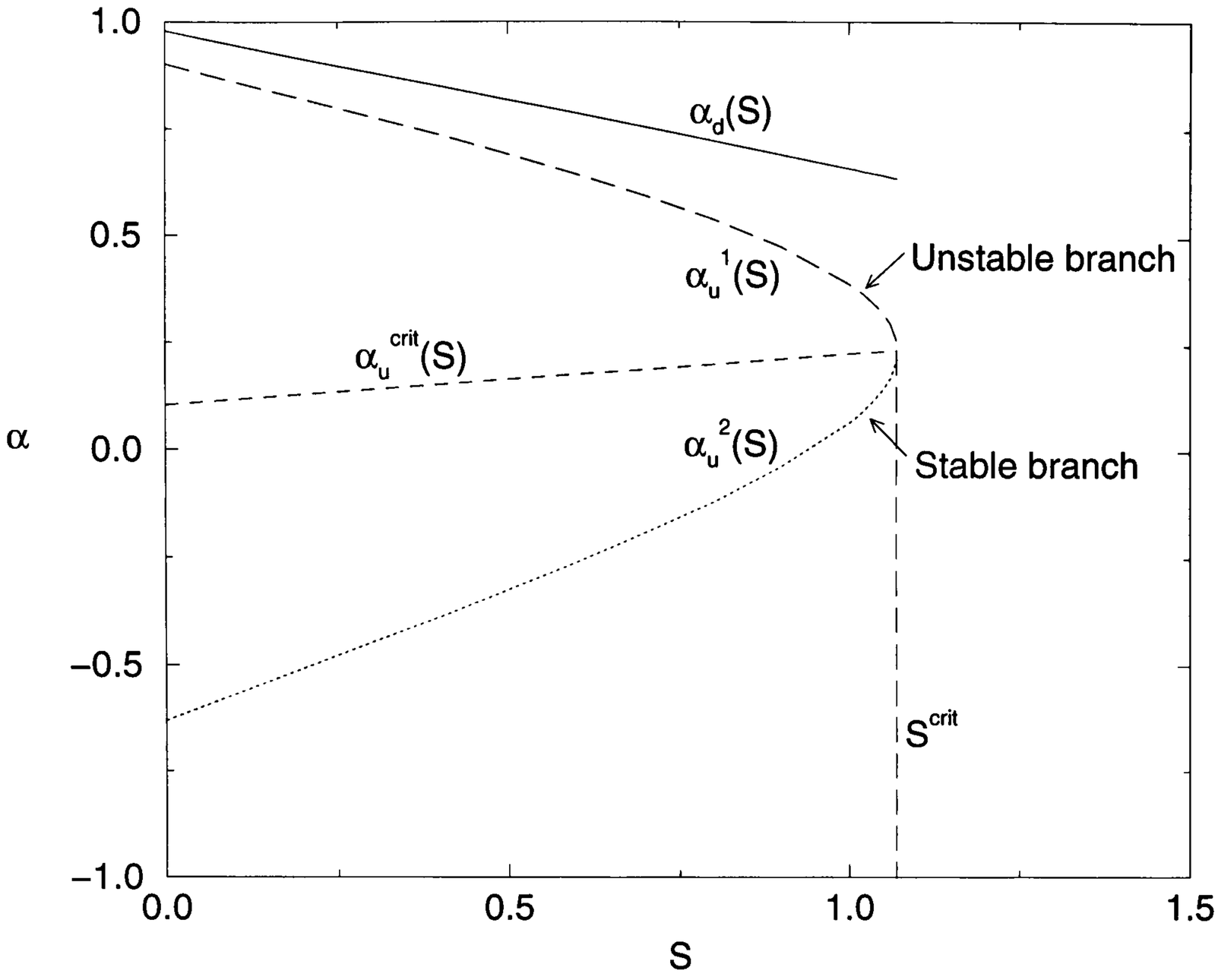

Figure 4.5: Menisci positions as a function of S, $Ca_2 = 0.01$, $R/H_0 = 100$, $\lambda_i = 0.1$, $\theta_t = 50°$. — α_d, $\cdots$ α_u^1(larger root), — — α_u^2(smaller root), – – α_u^{crit}.

4.4 Experimental techniques and methods

Experimental work has been carried out on a high precision coating apparatus designed specifically to allow ease of access for visualisation purposes, and precision machined for low roll runout ('wobble') and high axial alignment. Further details of the apparatus can be found in section 2.2 and a general schematic layout is shown in figure 2.4.

The fluid bead was visualised using a monocular microscope attached to a CCD camera. The bead was back lit using twin fibre optic light guides rendering the bead white and the surroundings black. Images of the bead were recorded on a S-

VHS video recorder and stills were captured from this onto a computer *via* a Silicon Graphics video board.

Menisci positions were recorded by moving the camera on a calibrated slideway. The position X_0 was found by trapping a small bead of fluid between the two stationary rolls and increasing the gap until a thin bead was formed, as described in section 2.4.6.

4.4.1 Investigation of the base-flow

Investigation of the baseflow of meniscus coating is important as the steady–state solution forms the basis of a predictive model for the onset of the bead–break instability. Gaskell *et al.* (1998a) show experimental data of menisci positions in forward roll coating. Here further results are taken for comparison with the analytical predictions described in section 4.2.

The inlet film in the experiment was metered onto the roll by viscous lift and the metered film thickness was a function of capillary number Ca_2. From viscous lifting theory (Innes, 1993) the semi-empirical relationship

$$H_i = aCa_2^b \tag{4.34}$$

can be used to fit experimental data for a roll immersed to a given depth in the reservoir. Figure 4.6 shows the experimental data and the fitted function over the range $0.005 \leqslant Ca_2 \leqslant 0.05$ with the values $a = 1.23 \times 10^{-3}$ m and $b = 0.665$ fitted by regression. The depth of immersion of the lower roll in the reservoir was 30 mm. Varying the depth of immersion of the roll simply alters the values of the constants in this equation.

The fluid used in the experiments was a light silicone oil (Shell Tellus R5) with properties given in table 4.1 — fitting the viscosity as a function of temperature, as shown in figure 2.24, allowed correction for any variation over the course of the experiments.

Maintaining a constant inlet film thickness over a range of Ca_2 by varying the depth

μ	$-0.27 \times 10^{-3}T + 0.0129$	Pa s, T[°C]
σ	30.5×10^{-3}	N/m
ρ	842	kg m^{-3}

Table 4.1: Physical properties of the fluid used in experiments.

of roller immersion is impracticable with the current experimental arrangement, although for a given Ca_2 the inlet film can be calculated from equation 4.34. A study of the baseflow involved setting the semi–gap width H_0 and fixing Ca_2 (hence fixing H_i) and measuring the meniscus positions over a range of speed ratios. This was repeated for three different Ca_2 values and two gap settings.

For visualisation purposes, a series of images of the steady state bead were recorded under varying speed ratio S with all other parameters remaining constant.

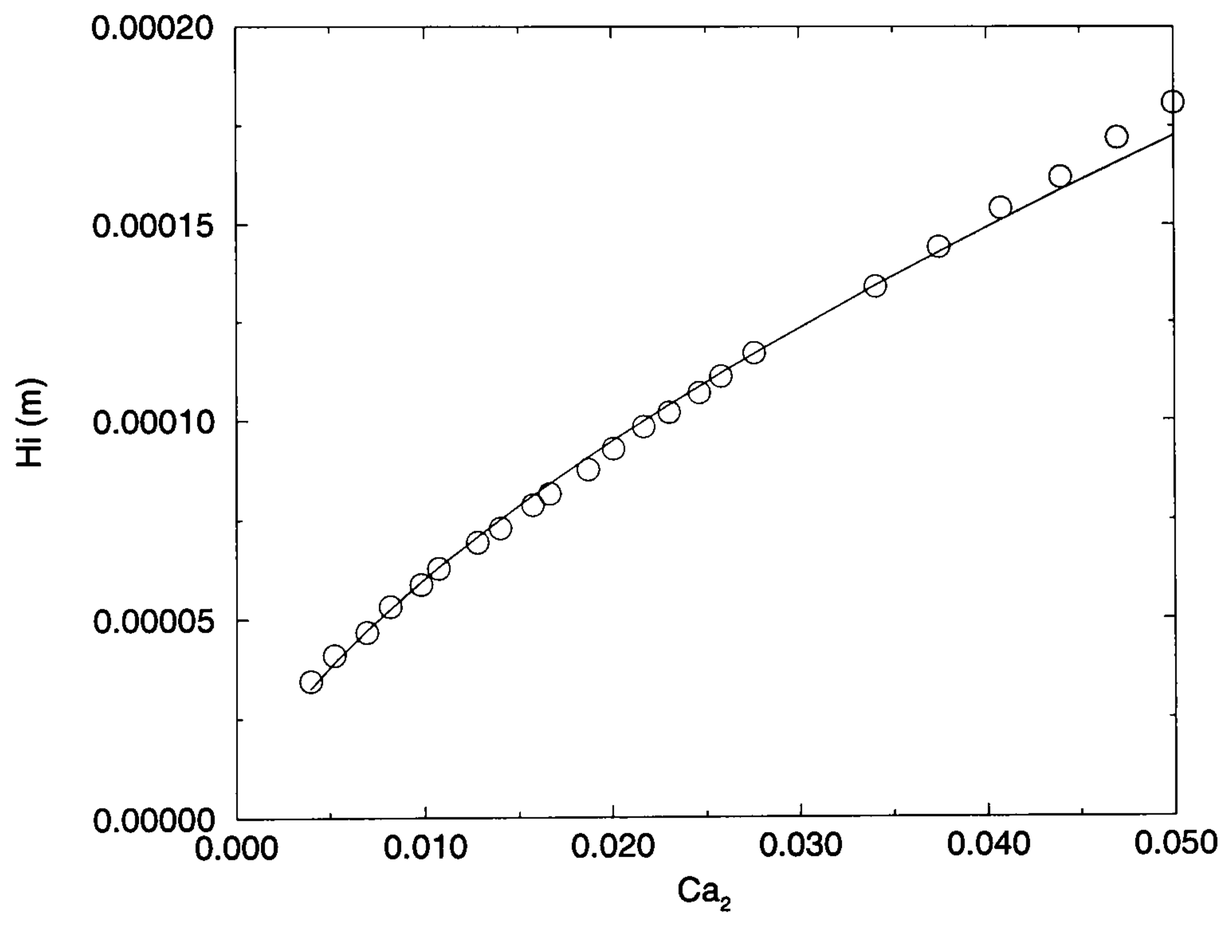

Figure 4.6: Inlet film thickness H_i as a function of Ca_2. ∘ experimental points, — fitted function.

4.4.2 Experimental results and discussion of the baseflow

The location of the upstream and downstream meniscus positions as a function of speed ratio, S, for $R/H_0 = (100, 200)$, 33 μm $< H_i <$ 128 μm and $0.004 < Ca_2 < 0.032$ are shown in figures 4.8 to 4.13. Data for $0 < S < 0.75$ is not shown on figures 4.8 or 4.11 as a consequence of a minimum speed for smooth operation of the drive to roll 1.

For a given set of parameters, as S in increased from zero the downstream meniscus is initially observed to move outwards from the nip. At $S = 0$ the bead makes two static contact angles with roll, one at the upstream interface and one at the downstream, as observed in figure 4.14 and shown schematically in figure 4.7. The radius of curvature of the downstream meniscus is given by an expression analogous to equation (4.11):

$$R_D = \frac{2H_D}{1 + \cos\theta_C}. \tag{4.35}$$

When the top roll is set in motion, the outgoing film of thickness H_1, effectively means that the downstream contact angle jumps from θ_C to 0°, and for the radius of curvature to remain the same the downstream meniscus moves outwards. The upstream static contact angle now takes a dynamic value, which is dependent on, among other things, the speed U_1. As the speed ratio is increased further, the downstream meniscus is observed to move towards the nip (i.e. in the negative X direction).

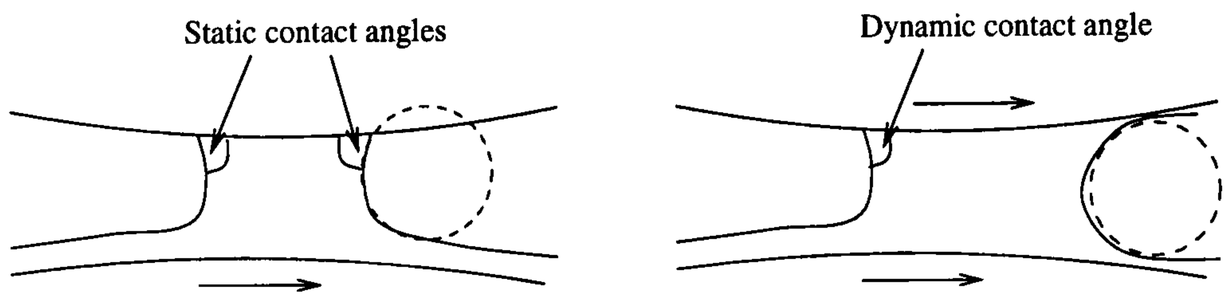

Figure 4.7: The jump in downstream meniscus position and the change in contact angle at the upstream meniscus caused by increasing speed ratio from (a) $S = 0$ to (b) $S > 0$.

As S increases, the upstream meniscus is also observed to move towards the nip (in the positive X direction), the combination of movement of the two menisci as the speed ratio is increased causes a reduction in the overall length of the bead.

The upstream meniscus was observed to advance through the nip prior to bead bead–break in all cases although this is not explicitly shown on figures 4.8 or 4.11.

Shown on figures 4.8 to 4.13 are the predicted upstream and downstream meniscus positions from solution of equations (4.5) and (4.18). The value of the contact angle θ_D at the upstream interface, necessary for solution, is taken as an average value of 50° from the images discussed in the next section. The agreement between the measured and predicted meniscus positions is good in all cases, with the experimental and analytical trends in close agreement. The greatest discrepancy is at $S = 0$, which, as discussed earlier, is due to the change in contact angles at the upstream and downstream menisci.

4.4.3 Visualisations of the steady state bead

Figure 4.14 shows a series of stable images of the fluid bead where the speed of roll 2 is held constant and the speed ratio varied in steps. No manipulation of the image was performed on the flow-field itself, though dotted lines were added to indicate the edge of the rolls and arrows used to indicate the direction in which the rolls are moving.

The visualisations show graphically the response of the meniscus positions to the increases in speed ratio, as discussed in the previous section. This figure was also used to determine an approximate value of the contact angle, θ_D with an average value of 50° was estimated from the figures. It would be more accurate to represent the contact angle as a function of the speed of roll 1, since it is a dynamic contact line with a relative motion of the roll to the fluid. However the error associated with measuring the dynamic contact angle as a function of roll speed directly from images such as these shown in figure 4.14 is relatively large. Representing the contact angle as an average value also gives a good indication of how well the model performs with only one value of contact angle used to model parameter space.

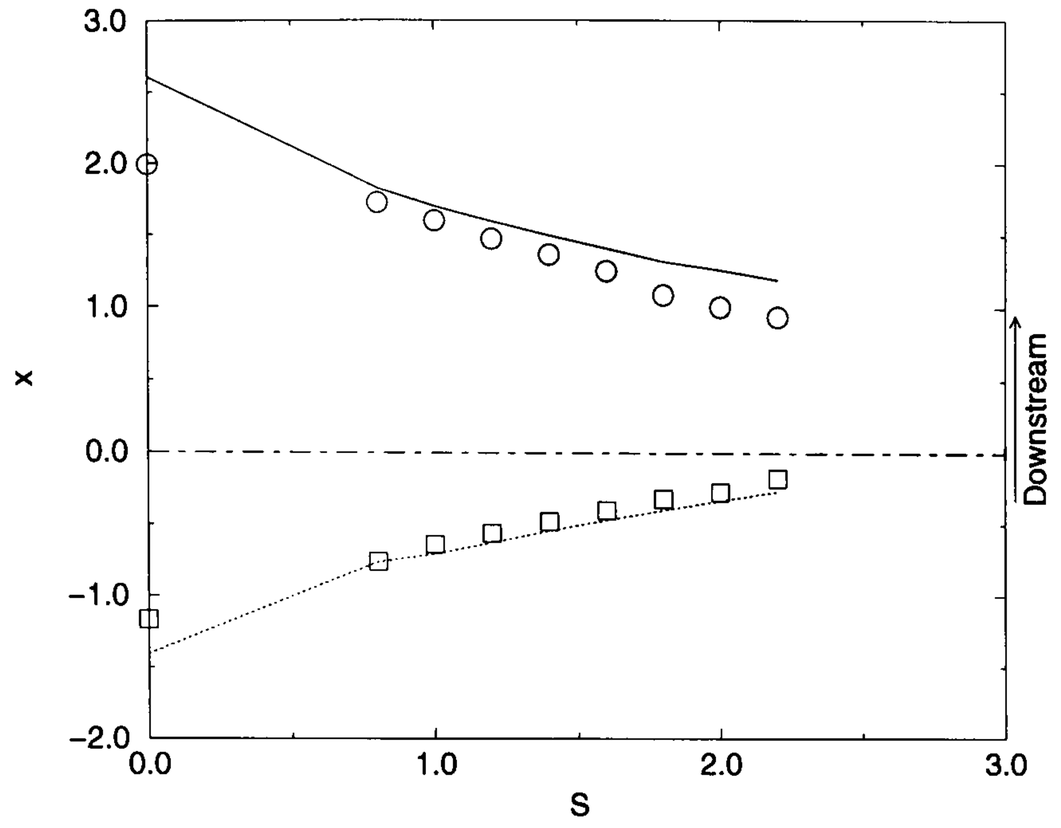

Figure 4.8: Stable menisci positions. $Ca_2 = 0.0042$, $R/H_0 = 200$, $\lambda_i = 0.137$, $\theta_D = 50°$. — x_d calculated,∘ x_d experimental, $\cdots$ x_u calculated,□ x_u experimental.

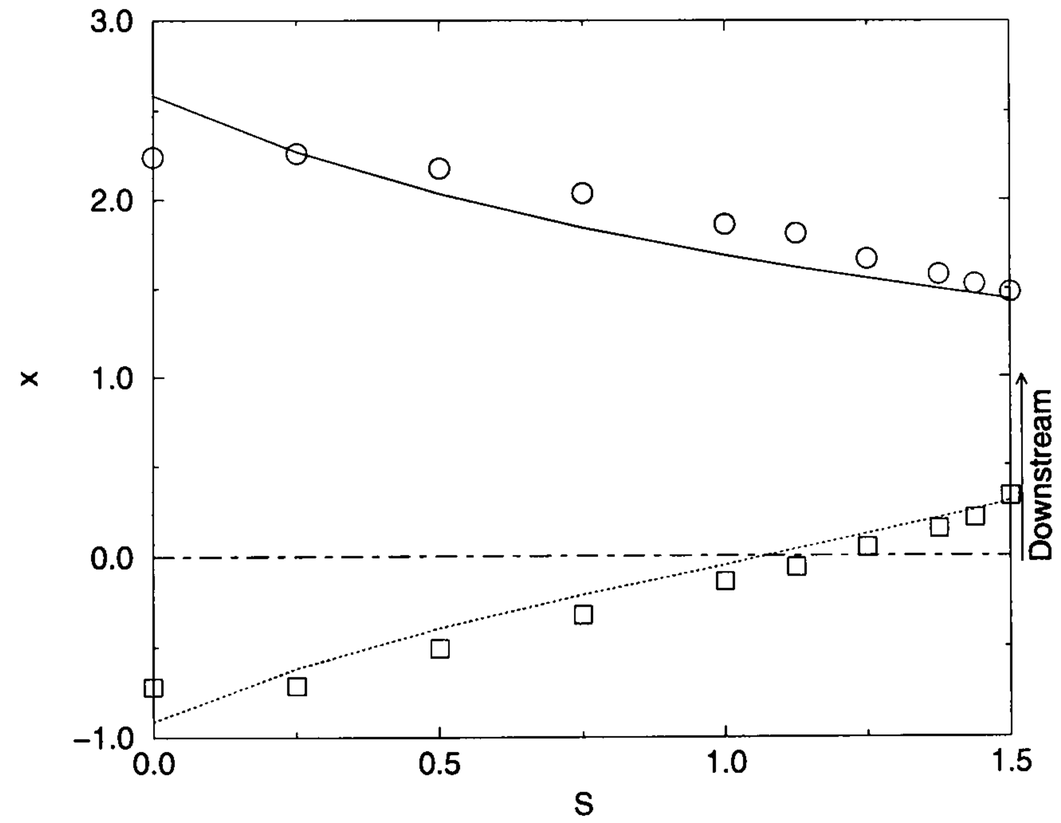

Figure 4.9: Stable menisci positions. $Ca_2 = 0.0162$, $R/H_0 = 200$, $\lambda_i = 0.33$, $\theta_D = 50°$. — x_d calculated,∘ x_d experimental, $\cdots$ x_u calculated,□ x_u experimental.

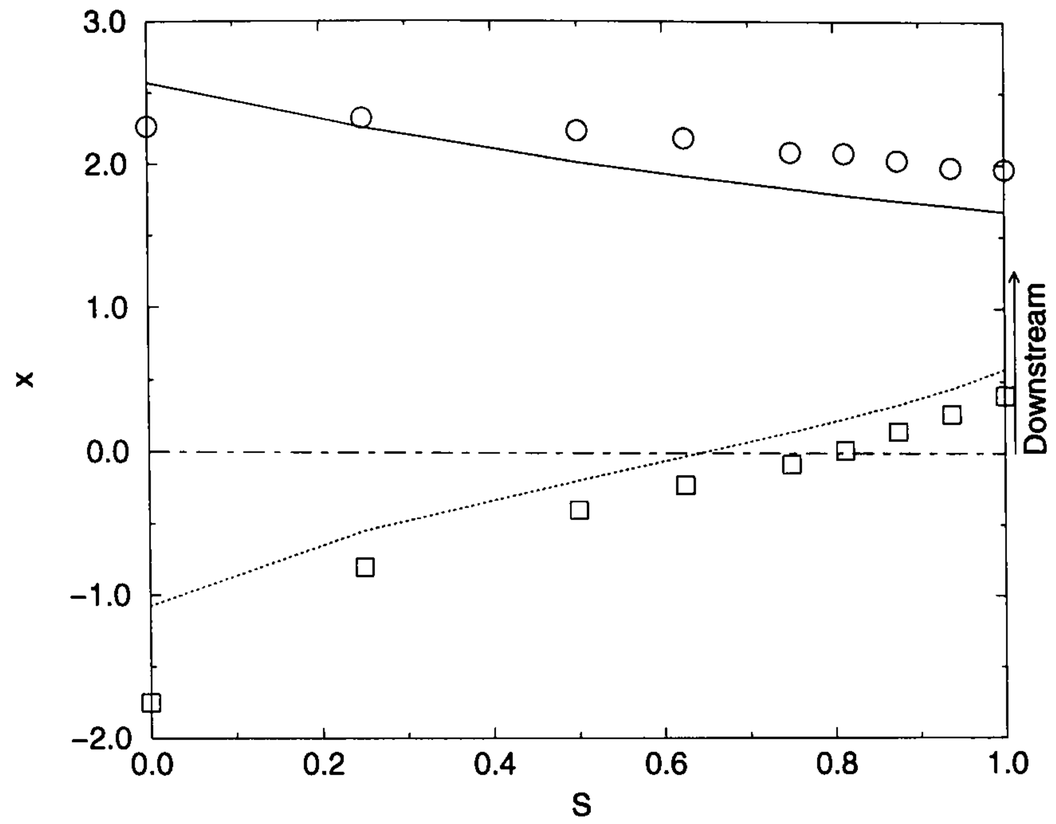

Figure 4.10: Stable menisci positions. $Ca_2 = 0.0318$, $R/H_0 = 200$, $\lambda_i = 0.512$, $\theta_D = 50°$. — x_d calculated,∘ x_d experimental, $\cdots$ x_u calculated,□ x_u experimental.

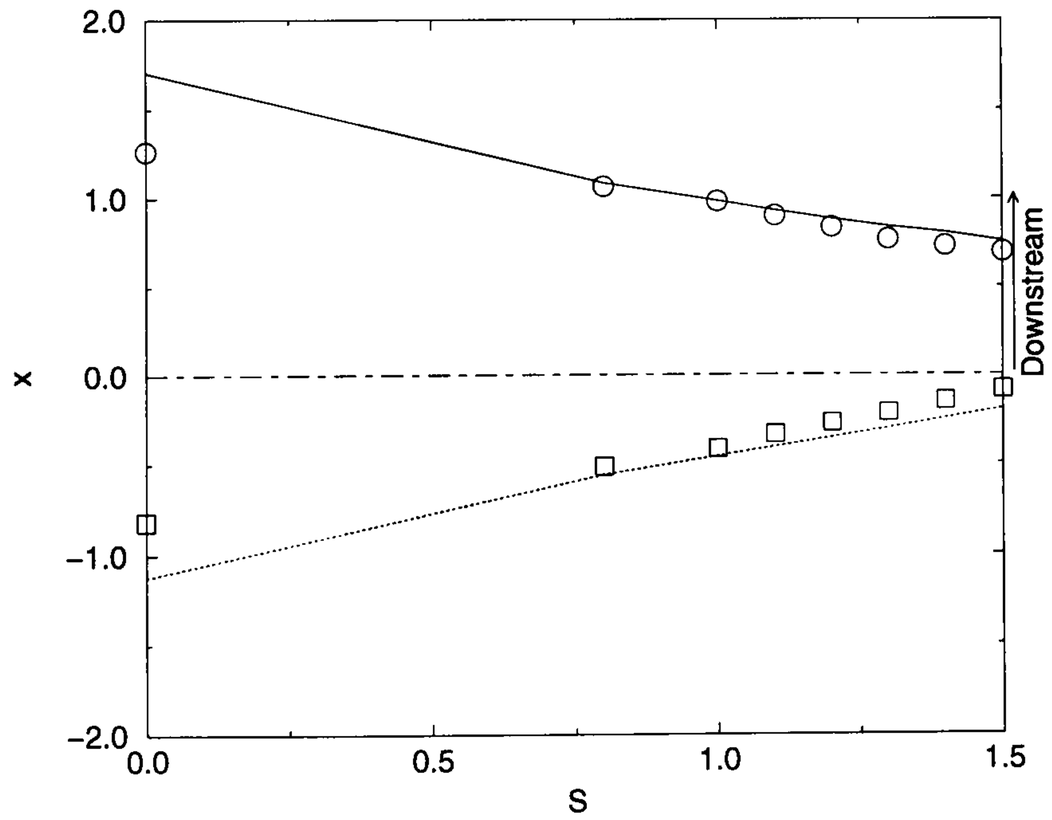

Figure 4.11: Stable menisci positions. $Ca_2 = 0.00403$, $R/H_0 = 100$, $\lambda_i = 0.0663$, $\theta_D = 50°$. — x_d calculated,∘ x_d experimental, $\cdots$ x_u calculated,□ x_u experimental.

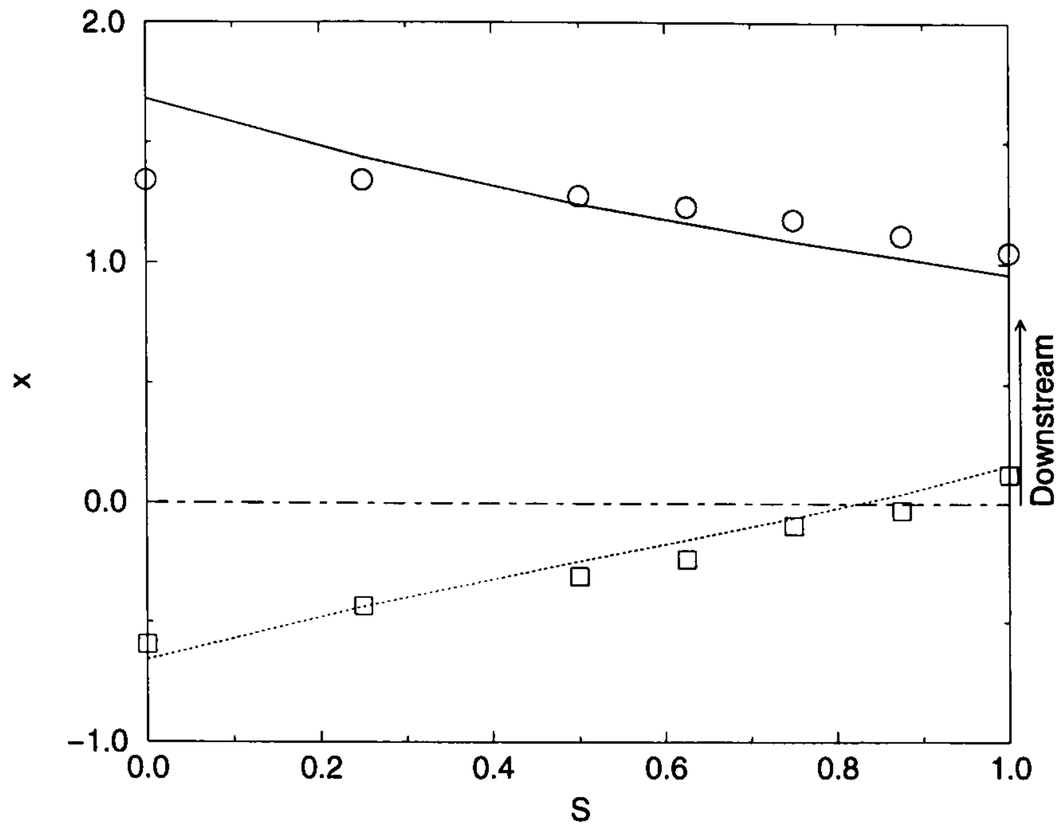

Figure 4.12: Stable menisci positions. $Ca_2 = 0.0159$, $R/H_0 = 100$, $\lambda_i = 0.166$, $\theta_D = 50°$. — x_d calculated,∘ x_d experimental,$\cdots$ x_u calculated,□ x_u experimental.

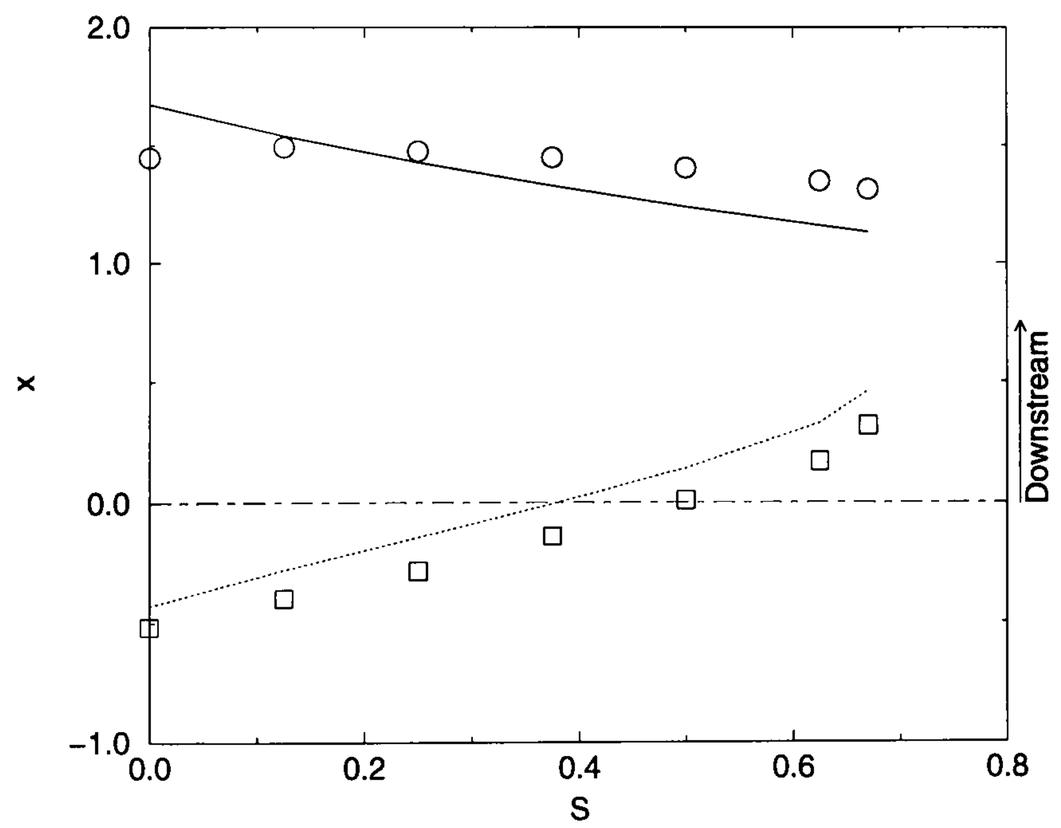

Figure 4.13: Stable menisci positions. $Ca_2 = 0.0318$, $R/H_0 = 100$, $\lambda_i = 0.256$, $\theta_D = 50°$. — x_d calculated,∘ x_d experimental, $\cdots$ x_u calculated,□ x_u experimental.

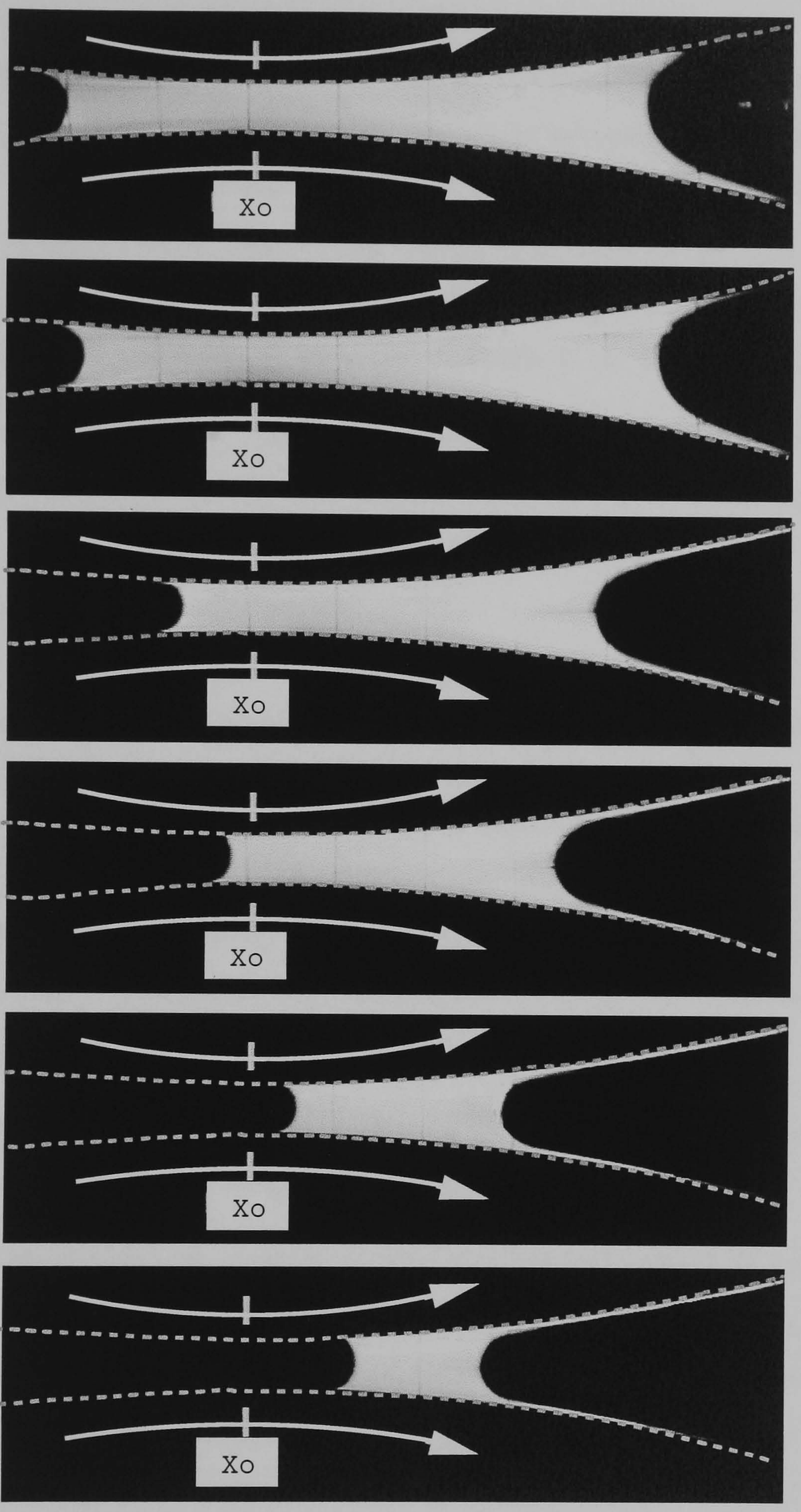

Figure 4.14: Images of stable bead as speed-ratio (S) is increased. From the top downwards S=0, 0.4, 0.6, 0.8, 1.0, 1.05; $Ca_2 = 0.012$, $R/H_0 = 100$, $\lambda_i = 0.12$.

4.4.4 Investigation of the bead–break instability

The point of onset of the bead–break instability was determined by fixing the lower roll capillary number Ca_2 and increasing the upper roll speed in incremental steps until bead–break was observed. When bead–break occurred the transmission of light along the bead was broken and the image observed to go from light to dark. This was repeated for nine values of Ca_2 and two half-gap settings (H_0). A series of images taken at 0.5 s intervals show the evolution of the bead–break instability.

A second set of experiments were run without the end-plate to aid visualisation of the bead. The curvature of the meniscus rendered the transmitted light as a line, however the onset of bead–break still caused the transmission of light to be interrupted.

Experimental results and discussion of the onset of bead–break

Figures 4.15 and 4.16 shows the critical speed ratio , S^{crit}, at the onset of bead–break as a function of Ca_2 for two different gap settings. It should be noted that the inlet film thickness H_i is not constant but varies as a function of Ca_2 as given by equation (4.34). The figures show that as Ca_2 increases, the critical speed ratio at which bead–break occurs decreases exponentially.

The onset of bead–break was found to occur, within experimental error, at the same value of speed ratio with or without the presence of the end-plate.

Also shown on figures 4.15 and 4.16 are the predictions for the onset of the bead–break *via* a solution to equation (4.33), with the inlet film thickness related to Ca_2 *via* equation (4.34). The agreement between the experiments and the analytical results is good, the biggest discrepancy occurring at Ca_2. This could be due, in part, to the change in the value of the contact angle, θ_D as the value of Ca_1 is increased.

Figure 4.17 shows the evolution of the bead–break instability in time. A stable bead (at $S = 1.05$) is shown representing time, t, zero. The stop clock was simultaneously started with a step increase in the speed ratio (achieved by altering the upper roll

speed) from $S = 1.05$ to $S = 1.08$, and subsequent images are shown at 0.5 s intervals. The left–hand interface is referred to as the upstream interface (in relation to the incoming film) and the right–hand interface as the downstream one.

The sequence of images clearly shows that the downstream meniscus position remaining constant, with the upstream interface accelerating rapidly and touching the downstream interface before the bead breaks.

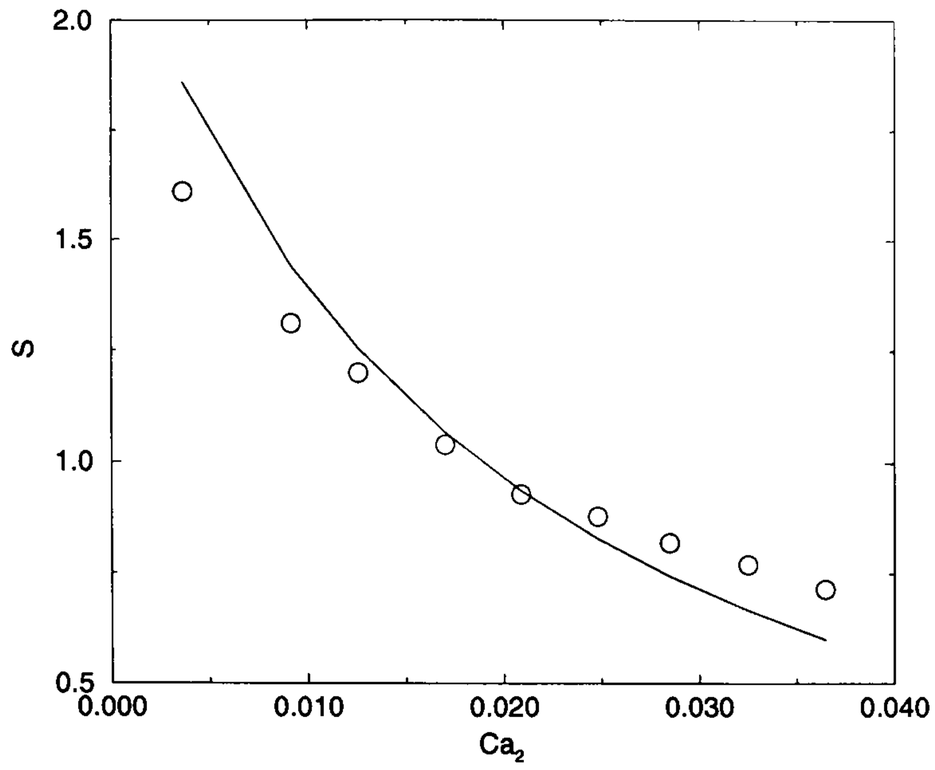

Figure 4.15: S^{crit} as a function $f(Ca_2, H_i)$ $R/H_0 = 100$. ∘ experimental points, — theoretical prediction.

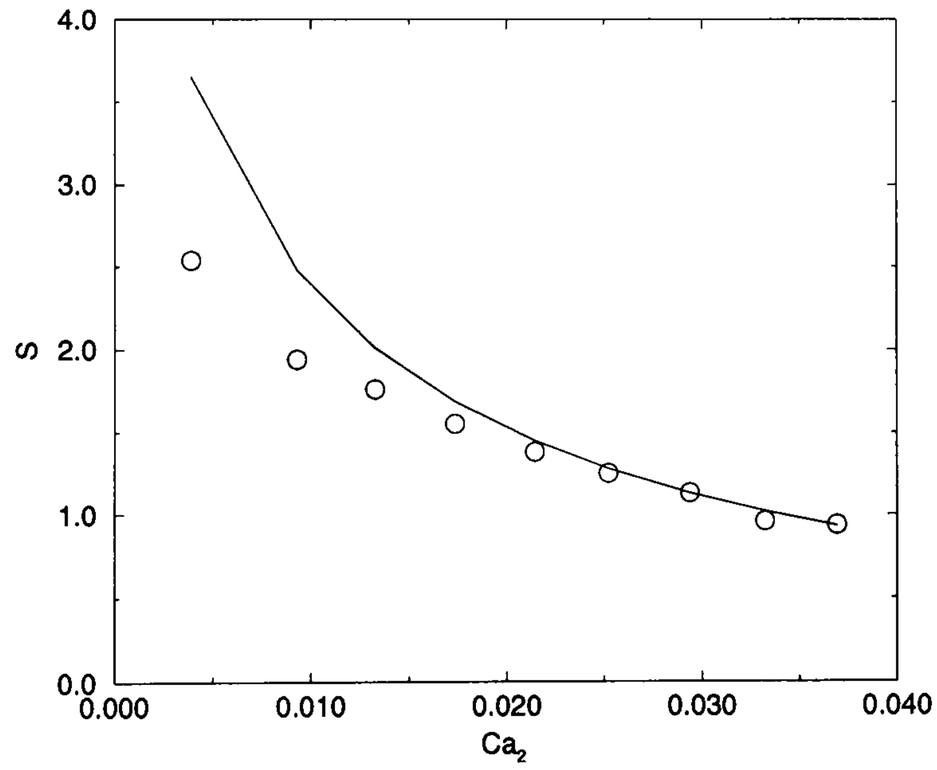

Figure 4.16: S^{crit} as a function $f(Ca_2, H_i)$ $R/H_0 = 200$. ∘ experimental points, — theoretical prediction.

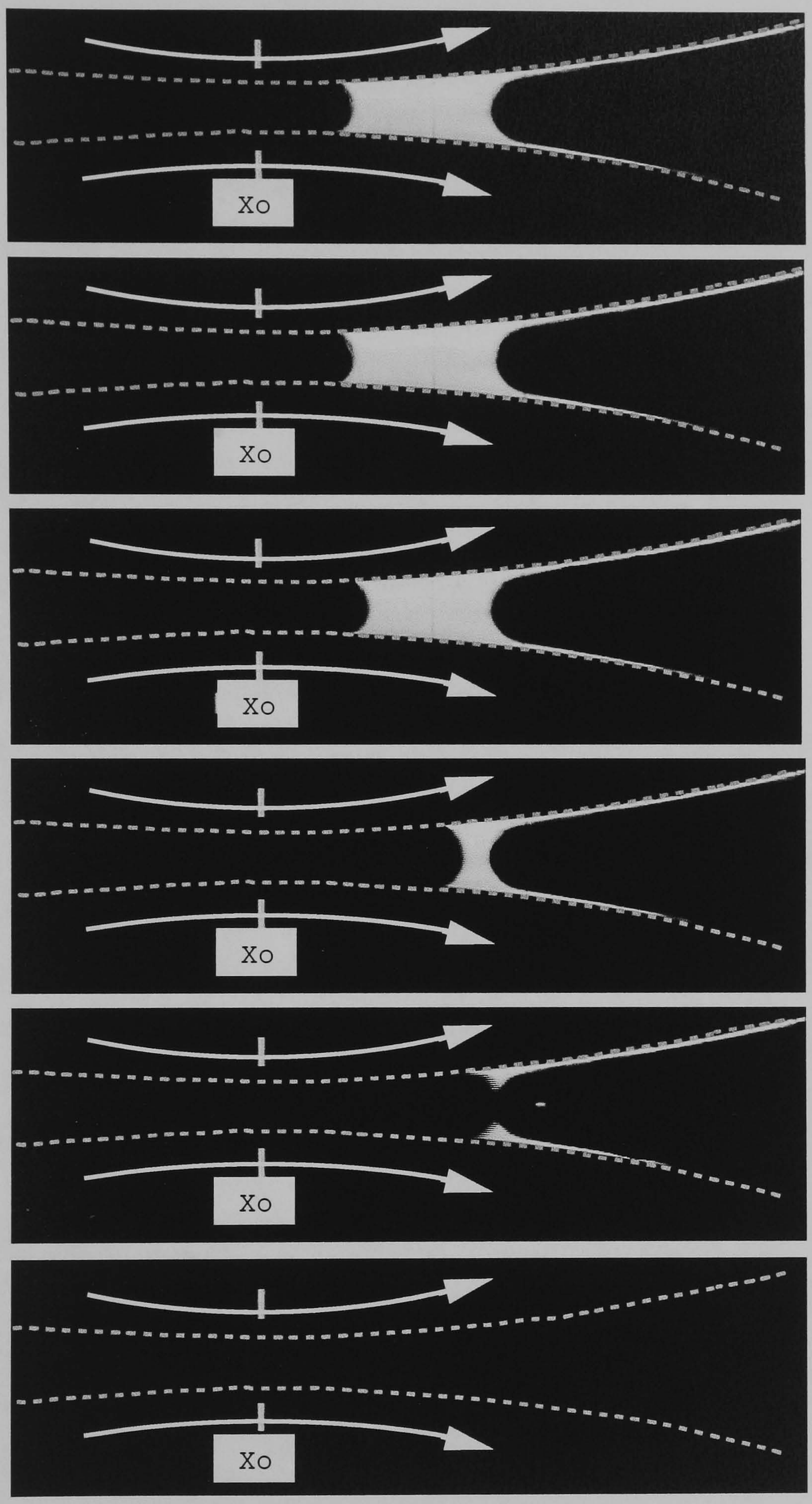

Figure 4.17: Sequence of images of unstable bead showing evolution of instability. From the top downwards time = 0, 0.5, 1.0, 1.5, 2.0, 2.5 s ;$S = 1.08$, $Ca_2 = 0.012$, $R/H_0 = 100$, $\lambda_i = 0.12$.

4.5 Further discussion

4.5.1 Analytical and experimental results

Analytical and experimental results for both the baseflow and the onset of bead–break were found to be in close agreement over the range of parameters investigated. Indeed the agreement between theory and experiments is excellent considering the fact that the value θ_D is taken as an average value from the range of experiments conducted here. The largest discrepancy between theory and experiments are at low S, which is in-part due to the change in contact angle, as discussed in above.

4.5.2 Bead–break as a design criterion

Optimising a meniscus roll coater with respect to some variable (for example web speed or film thickness) first requires specification of a number of parameters specific to the system. When choosing the conditions under which to run a meniscus roll coater one wants to operate with the slowest possible speed for the lower roll, U_2 to prevent air entrainment in the bath, and a high upper roll speed, U_1 to give a fast throughput and a thin film. This necessitates running at a high speed ratio, i.e. close to the point of bead–break, allowing the conditions under which bead–break occurs to be used as a guide for the operating parameters. Two cases that may occur in practice are considered here for optimisation :

1. A constant inlet film thickness on the lower roll (i.e. $\lambda_i = const$). A situation like this could arise if a third roll positioned below roll 2 was used to doctor the inlet film onto roll 2. Of course this second roll pair would also be subject to instabilities and would need analysing for potential defects.

2. The inlet film is a function of Ca_2 i.e. $H_i = f(Ca_2)$, for example the inlet film could be metered *via* viscous lift as in the experiments described here (see figure 4.6 and equation (4.34)).

Key parameters in the study of an industrial meniscus coater are H_1, the outgoing film thickness and U_1, the linespeed of the coater. Prior to any analysis it is first

necessary to relate H_1 to the other parameters in the system. The film split ratio for forward meniscus roll coating is based on an analysis by Landau and Levich (1942) and was first derived by Ruschak (1982) — later it was verified experimentally by Innes *et al.* (1998):

$$\frac{H_1}{H_2} = S^{\frac{2}{3}}. \tag{4.36}$$

Although the relationship of Landau and Levich (1942) given in equation (4.2) is strictly only valid for ($Ca \rightarrow 0.01$) the studies of the stable bead shown in section 4.2 show it is a good approximation up to ($Ca \rightarrow 0.03$).

This can be used together with a mass balance over the system,

$$H_i = SH_1 + H_2 \tag{4.37}$$

to derive a relationship $H_1 = f(H_i, S)$:

$$H_1 = H_i \left(\frac{S^{\frac{2}{3}}}{S^{\frac{5}{3}} + 1} \right). \tag{4.38}$$

It is convenient to non-dimensionalise this using $\bar{h}_i = \frac{H_i}{2R}$ and $\bar{h}_1 = \frac{H_1}{2R}$ such that for the case of constant inlet film thickness

$$\bar{h}_i = \frac{2H_0\lambda_i}{2R} = \lambda_i \left(\frac{H_0}{R} \right). \tag{4.39}$$

For the case $H_i = f(Ca_2)$

$$\bar{h}_i = \frac{aCa_2^b}{2R} \text{ (note a has units of length).} \tag{4.40}$$

Figure 4.18 shows a plot of $\frac{H_1}{H_i}$ as a function of S, as derived in equation (4.38). One notes that there is a maximum value of $\frac{H_1}{H_i} = 0.51$ at $S = \left(\frac{2}{3}\right)^{\frac{3}{5}} = 0.787$. This is the speed ratio that corresponds to the maximum film thickness on the upper roller for a given inlet film thickness. When $S < 0.787$, decreasing the upper roll speed will result in a thinner film on this roll; whilst when $S > 0.787$, decreasing the roll speed will result in a thicker film on the upper roll. This is important when assessing the effect of parameter changes on the final product specification. It should be noted

that the flux on the upper roll ($flux \propto \frac{H_1}{H_i} S$) decreases with a reduction in S, as shown in figure 4.19, which could be important when considering dryer performance (although the capacity of a dryer needs to be represented by more than just flux).

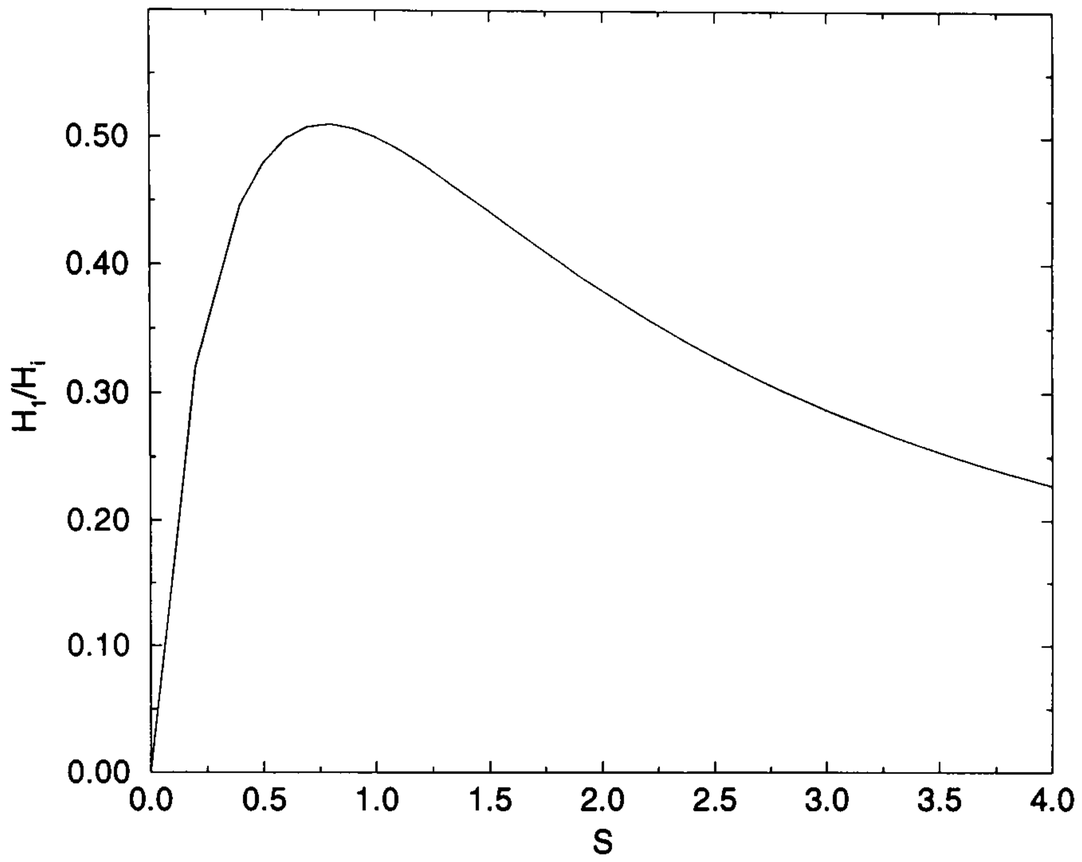

Figure 4.18: Ratio of outlet film thickness (roll 1) to inlet film thickness as a function of speed ratio.

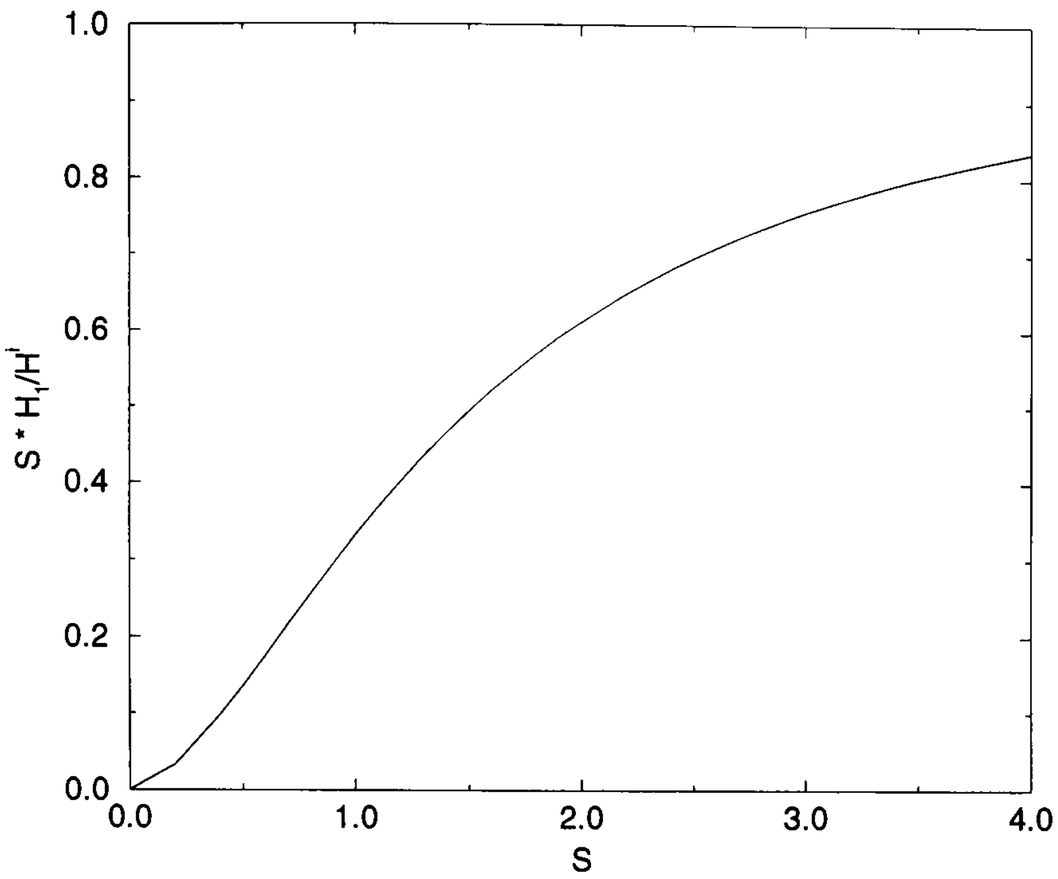

Figure 4.19: Dimensionless flux on upper roll as a function of speed ratio, S.

Results for $\lambda_i = const.$

When the inlet film thickness is constant, S^{crit} decreases monotonically with increasing Ca_2 as shown in figure 4.20. There is a maximum (lower) roll speed of U_2 above which no bead can be supported for any (upper) roll speed, U_1. It is also clear that, by increasing λ_i, the thicker film stabilises the bead and allows the speed ratio, S, to be increased. Figure 4.21 shows Ca_1^{crit} as a function of Ca_2. There is a maximum value of Ca_1^{crit} (i.e. upper roll speed) for a given inlet film thickness. Finally the film thickness on the upper roll (here expressed as λ_1) at criticality is shown in figure 4.22. Under the conditions of criticality, as Ca_2 increases the film thickness on the upper roll rises to a maximum corresponding to the value $S = 0.787$ which, as described in section 4.5.2, is the point where either an increase *or* a decrease in the speed ratio results in a thinner outgoing film H_1.

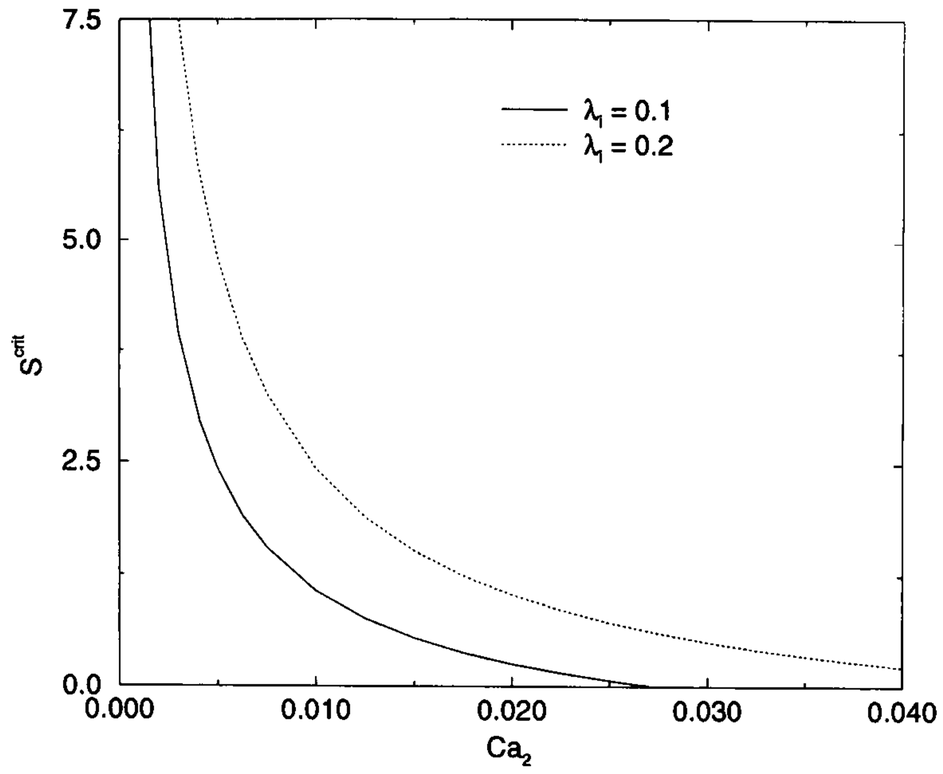

Figure 4.20: S^{crit} as a function of Ca_2 for a constant inlet film thickness, $R/H_0 = 100$, $\theta_D = 50^o$.

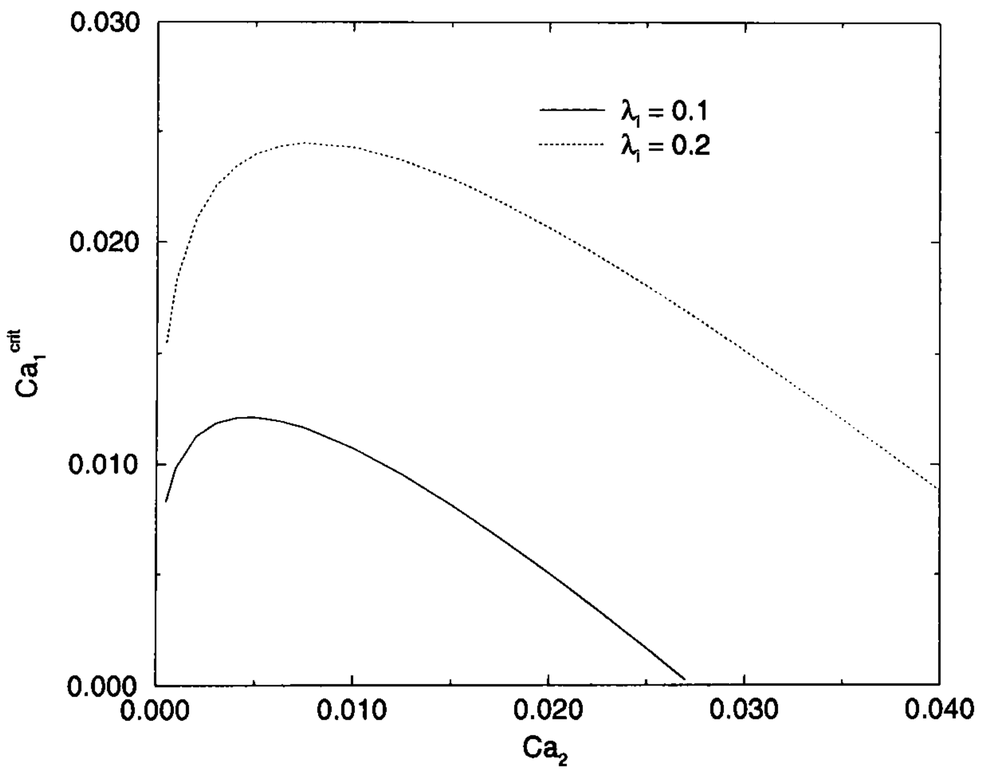

Figure 4.21: Ca_1^{crit} as a function of Ca_2 for a constant inlet film thickness, $R/H_0 = 100$, $\theta_D = 50^o$.

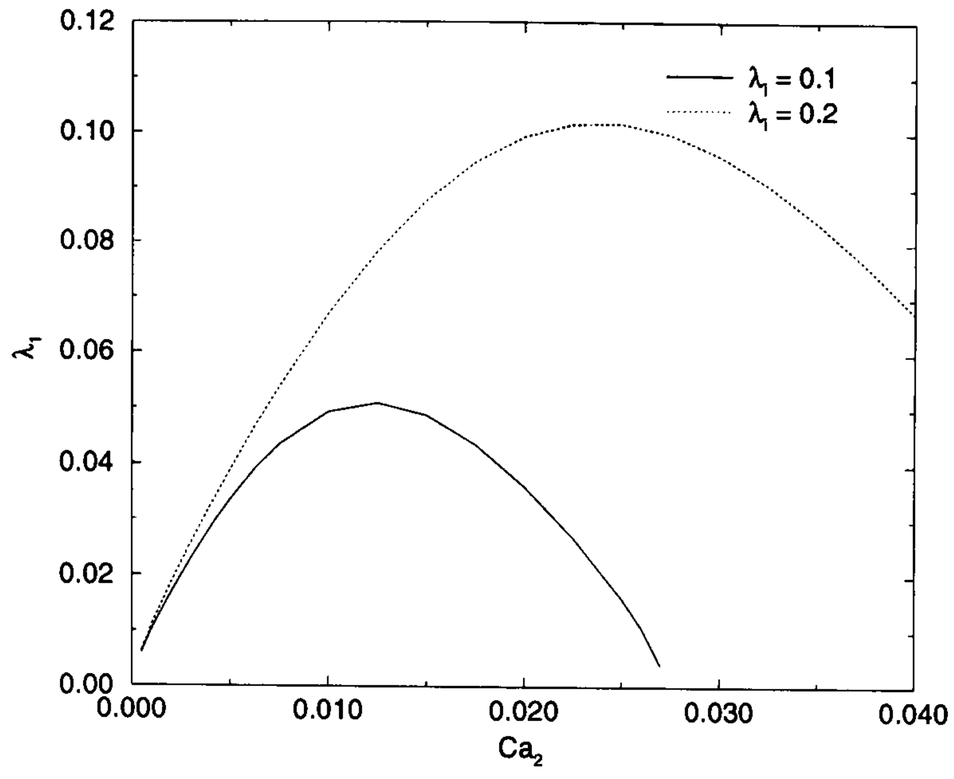

Figure 4.22: λ_1^{crit} as a function of Ca_2 for a constant inlet film thickness, $R/H_0 = 100$, $\theta_D = 50^o$.

Results for $H_i = f(Ca_2)$

Here the inlet film thickness is assumed to vary with Ca_2 (lower roll speed) as given by equation (4.40). The constants a,b need to be determined for the particular system. Here they are taken from our experiments, $\frac{a}{2R} = 0.0246$ and $b = 0.665$, and consequently figures 4.23 - 4.26 will need to be recalculated for different conditions.

Figure 4.23 shows a graph of the critical speed ratio as a function of Ca_2 as calculated from equation (4.33). Similarly the critical capillary number, $Ca_1^{crit} = S^{crit}Ca_2$ can be plotted as in figure 4.24. Using figure 4.24 it is possible to determine the minimum speed of the lower roll, to reduce air entrainment in the bath, for a given upper roll speed (which controls the production rate of the film). A series of curves for differing values of $\frac{R}{H_0}$ allow the effect of gap setting to be seen (here only two are shown for clarity).

The film thickness, H_1, is also of importance to the coating practitioner, as, together with the solids content of the coating fluid, it controls the dry film thickness. Figure 4.25 shows a plot of $\frac{H_1}{H_i}$ under critical conditions, as derived from equation (4.33).

Finally the dependence of H_1^{crit} on Ca_2 can be explicitly calculated using equation (4.40) as illustrated in figure 4.26.

At the point where the two curves for differing values of $\frac{R}{H_0}$ cross in figure 4.26, the corresponding values of S^{crit} can be read off directly from figure 4.23 at the relevant value of Ca_2 (here $Ca_2 = 0.035$). They are seen to lie on opposite sides of the value of S corresponding to the maximum transfer to the upper roll shown in figure 4.18.

To operate a safe margin away from the critical point the speed ratio needs to be reduced i.e. U_2 needs to be increased. Consequently an increase in Ca_2 (hence a decrease in S), necessary to operate a safe margin away from the point of criticality will result in a reduction in $\frac{H_1}{H_i}$ for the case $\frac{R}{H_0} = 100$ since it lies to the left of the maximum, but an increase in $\frac{H_1}{H_i}$ for the case $\frac{R}{H_0} = 200$. The actual film thickness H_1 can be related to the inlet film thickness at this particular value of capillary number using equation (4.40).

To summarise the design methodology :

- Specify a linespeed (Ca_1) and an initial value for R/H_0 then find the corresponding lower roll speed using figure 4.24.
- The film thickness of the final coated film can be found from figure 4.26.
- This process can be repeated to assess the influence of R/H_0 on the final film thickness for a given upper roll speed.
- The influence of reducing the speed ratio (by increasing U_2) on the final film thickness can be calculated, to operate a safe margin away from the point of criticality.

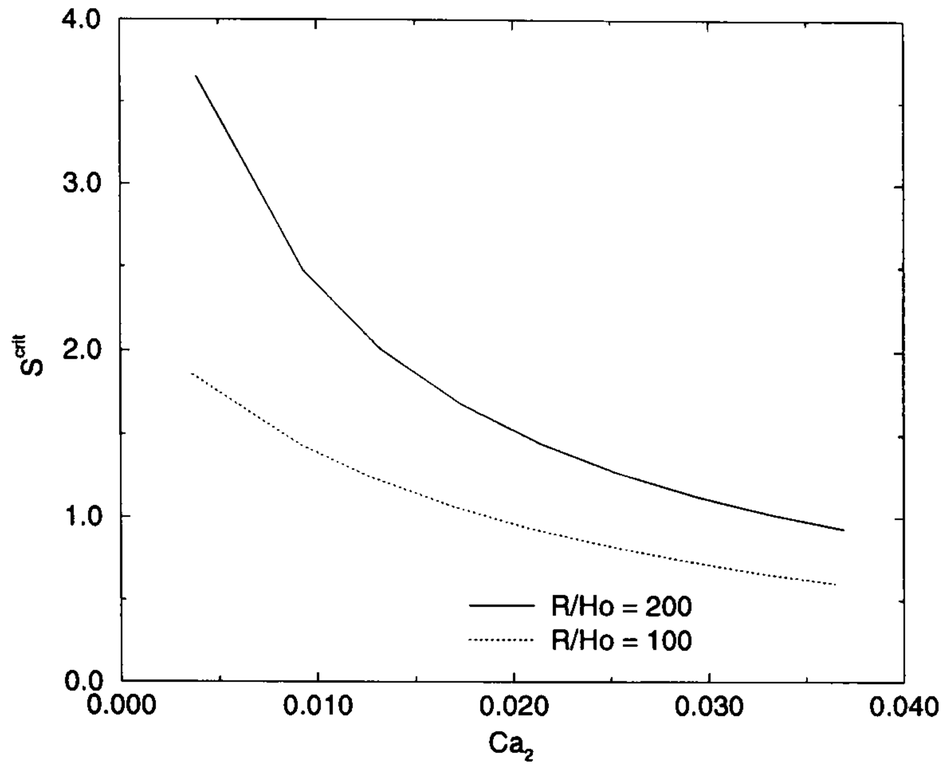

Figure 4.23: S^{crit} as a function $f(Ca_2, H_i)$.

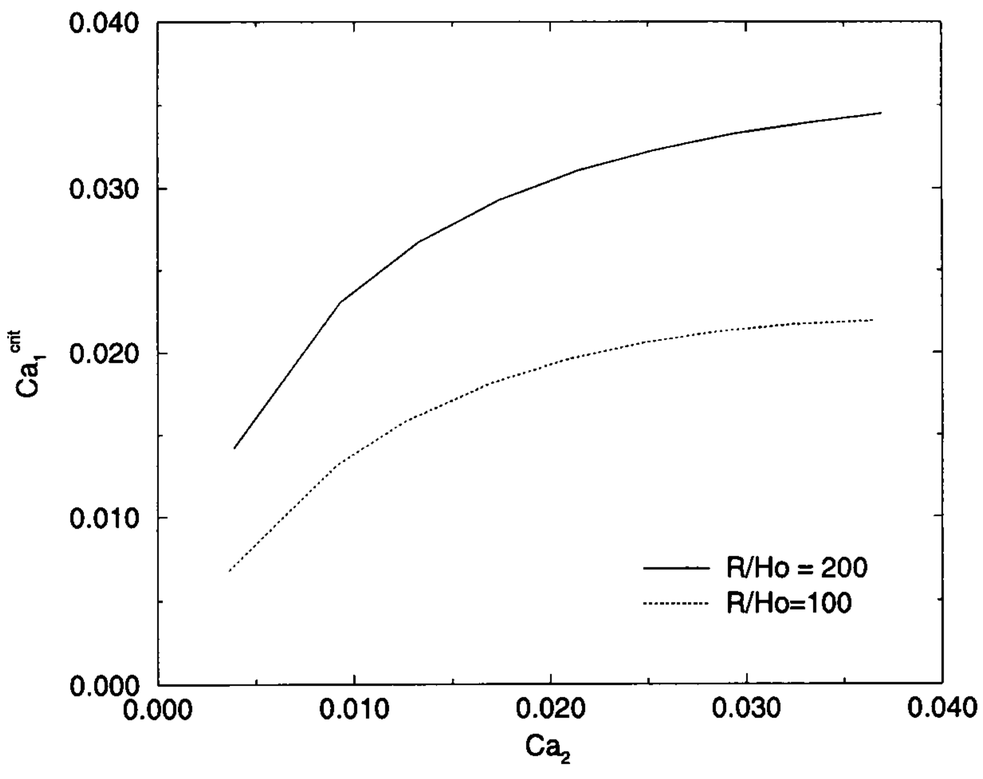

Figure 4.24: Ca_1^{crit} as a function $f(Ca_2, H_i)$.

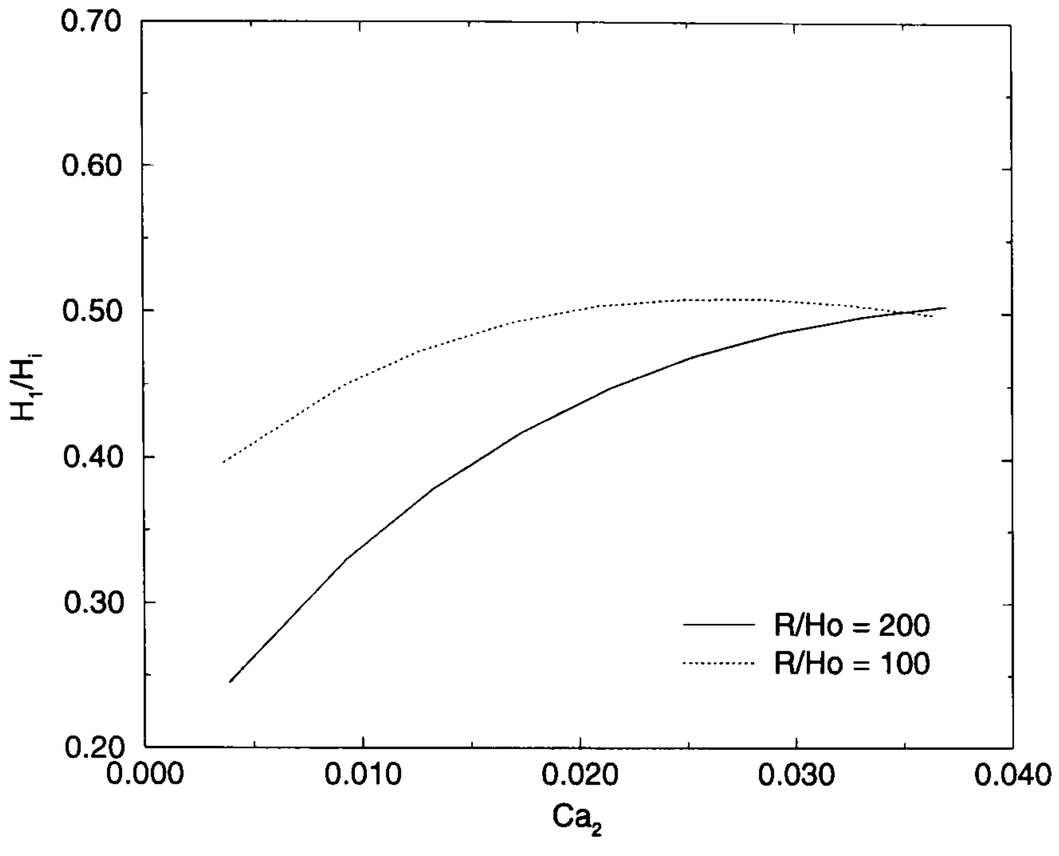

Figure 4.25: $\frac{H_1}{H_i}$ as a function$f(Ca_2, H_i)$ at the onset of bead–break.

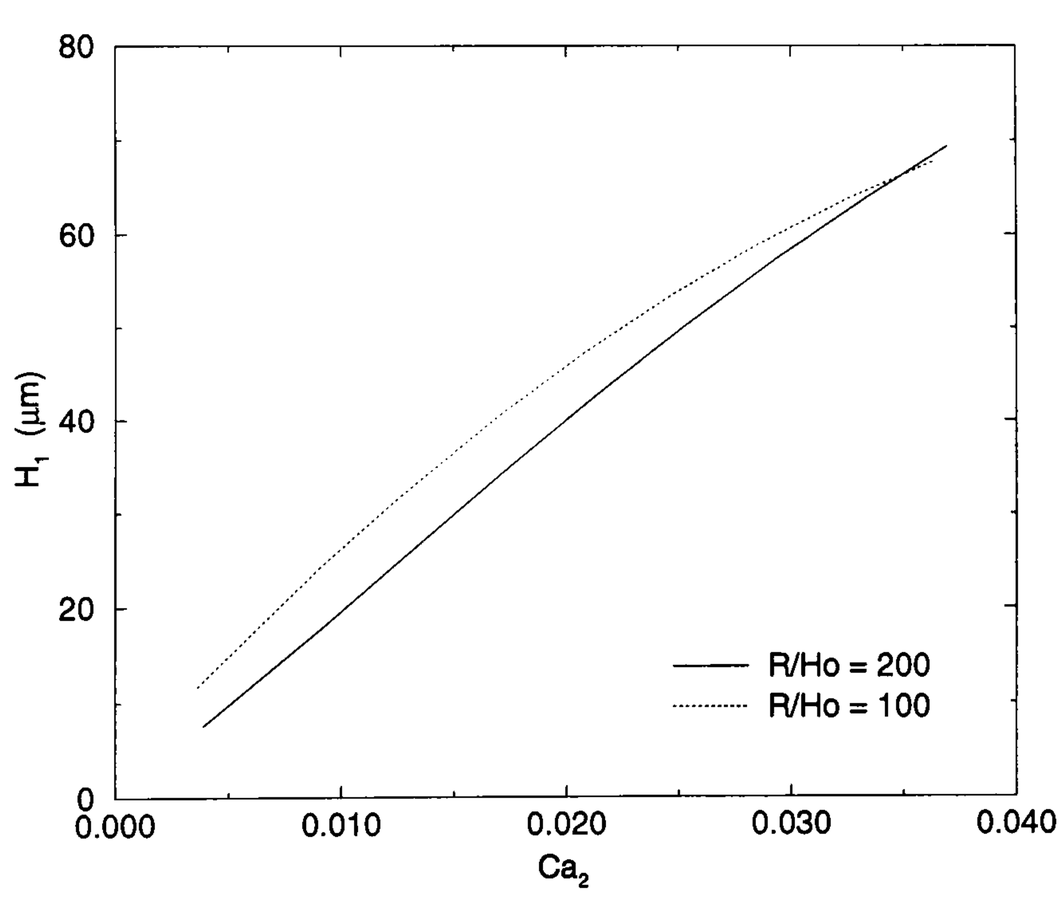

Figure 4.26: H_1 as a function of $f(Ca_2, H_i)$ at the onset of bead–break.

4.6 Summary

A number of conclusions may be drawn from this work:

- The model based on a perturbation hypothesis of a stable flow accurately predicts the onset of the bead–break instability, shown by a comparison with the experimental data.

- For a fixed inlet film thickness the critical speed ratio for the onset of bead–break was shown to decrease monotonically as the speed of roll 2 is increased.

- Increasing the inlet film thickness stabilises the coating bead.

- The bead–break instability may be used as a design criterion for the specification of the operating parameters.

Chapter V

Meniscus climb in knife coating

Contents

5.1 Introduction

Knife coating is a low cost versatile technique for doctoring a liquid film (Coyle (1997)). Figure 5.1a illustrates the actions of just such a device — a substrate passes over a roller of radius R, with the knife positioned a minimum distance H_0 away from the substrate. Fluid entrained on the substrate is doctored by the knife, giving a final film of thickness H^∞ on the substrate. Upstream of the knife a rolling bank of fluid forms with run-back of the residual fluid.

The knife coater described above has similarities with several other coating geometries — a flexible blade coater (figure 5.1b) a roll–flat plate (figure 5.1c), the face of a slot coater (figure 5.1d) and the doctor blade used in direct gravure coating to remove the fluid from lands of an engraved roller (figure 5.1e).

The blade coater (figure 5.1b) is essentially a knife coater where the blade is made out of a flexible material such that the shape of the fluid domain is dominated by an interaction of the hydrodynamic stresses developed in the liquid and the material properties (see, for example, Pranckh and Coyle (1997)).

The principle difference between the knife (figure 5.1a) and the roll–flat plate arrangement (figure 5.1c) is that a narrow knife is replaced by a much longer plate, with the developing flow in the entrance having no affect on the velocity field at the point of film formation. Sullivan *et al.* (1987) describe studies of a knife coater of length only ten times the gap between the roll and the knife where the flow–field is fully developed.

The slot coater is a pre–metered device where final film thickness is determined by the flow rate of the feed pump, whilst the knife coater is self metering. The feed point in a slot coater is generally located far enough upstream of the slot face to prevent entrance conditions affecting the coated film.

The doctor blade in a gravure coater is perhaps the most complex of the systems described here. A flexible blade is held against a rotating gravure (etched) roller (Booth, 1970), with the interaction between the hydrodynamic forces and the flexible blade determining the final shape of the flow domain. The dynamics of the process

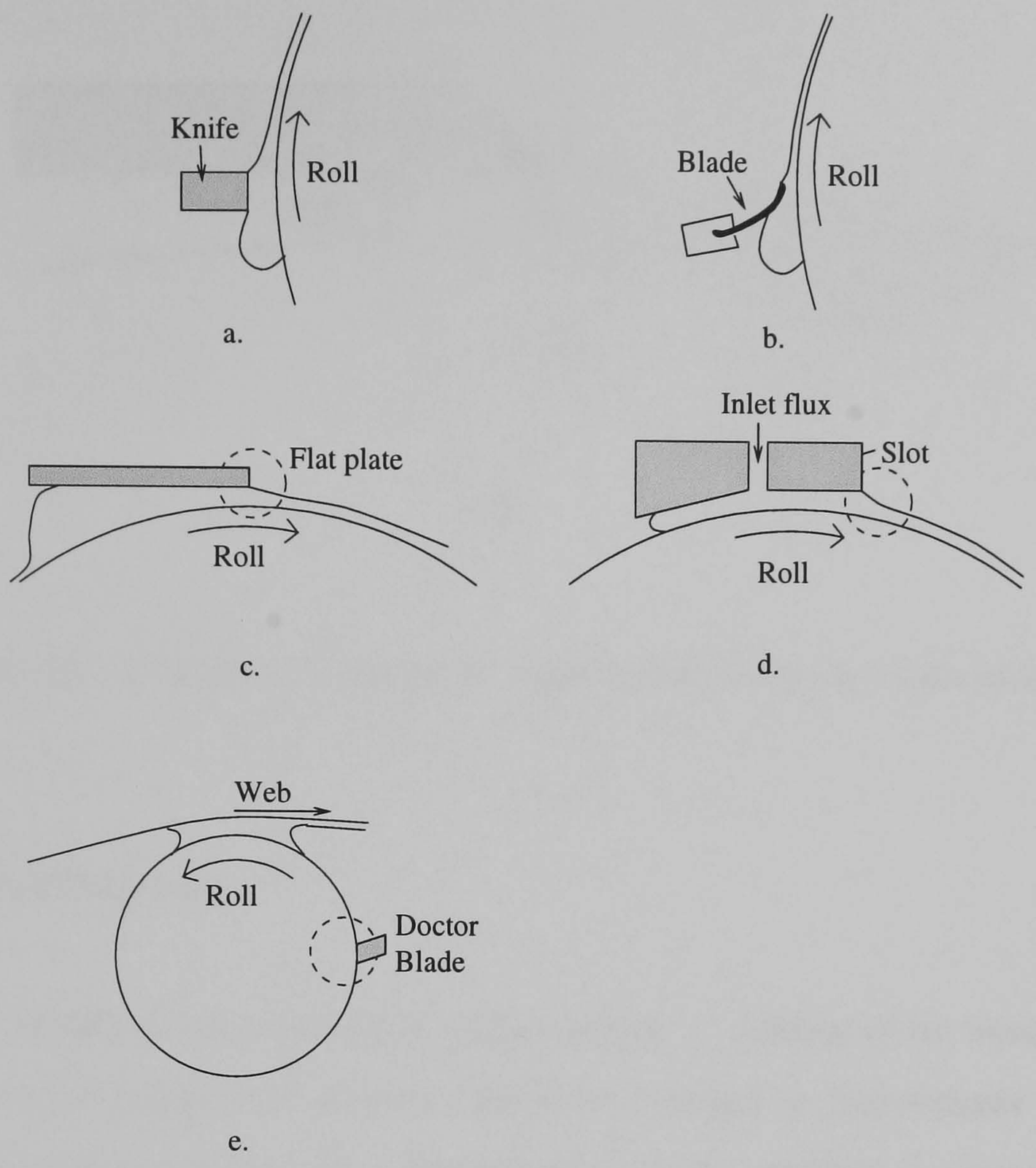

Figure 5.1: A knife coater (a), and other coating equipment with a similar geometry — (b) a flexible blade coater, (c) a roll–flat plate arrangement, (d) a slot coater and (e) a gravure coater.

are further complicated by the fact that the gravure roller is a rough surface.

Although not necessarily representing a specific industrial arrangement, the roll–flat plate geometry allows the study of the flow at the face of the knife uncomplicated by the specific characteristics of the coaters described above. One further simplification made in the computational and analytical study which follows is that the tip of the knife is located directly above the centre of the roll, at $X = X_0 = 0$ mm. Figure 5.2 defines the geometric parameters used in this study. Two further parameters are also defined: the length from the corner of the plate to the wetting line (along the face of the blade) L_{climb}; the height from the corner of the plate to the wetting line (measured in the Z direction) H_{climb}.

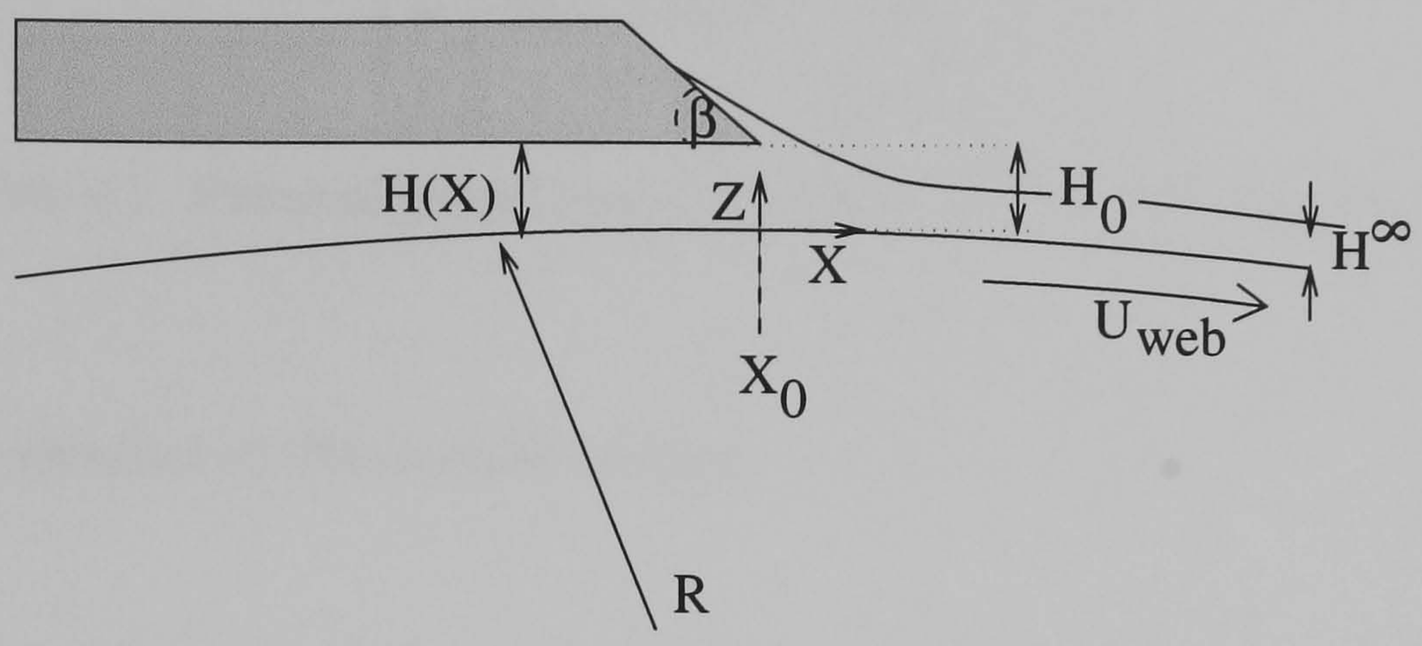

Figure 5.2: Definition of geometry used in the meniscus climb problem.

5.2 Motivation

Two types of defects are common in knife coating — ribbing which manifests itself as lines on a substrate, and streaks formed by bubbles or particulates trapped in closed recirculations causing local imperfections in the coating. A second source of streaks is due to the buildup of particles that are deposited on the knife tip causing the formation of a stalagtite, which can be attached to a substantial part of the knife across its width — see, for example, Branston *et al.* (1993) or Vodnick *et al.* (1993). The basic mechanism responsible for the formation of the stalagtites has not been clearly established. Engström and Rigdahl (1989) associate their formation with a vortex immediately downstream of the knife, whilst Isaksson *et al.* (1997) showed that the sub-ambient pressure downstream of the knife could be responsible for cavitation of the coating fluid, resulting in pressure pulses splashing the coating fluid onto the knife.

The aims of the investigation are two–fold:

- A theoretical and experimental study of the flow in which the meniscus is allowed to climb the face of the plate, with comparisons being made between the two, such that the theoretical work may be used with confidence
- Performing a series of experiments to identify the conditions that give rise to

μ	22×10^{-3}	Pa s
σ	33.5×10^{-3}	N/m
ρ	862	kg m^{-3}

Table 5.1: Physical properties of the fluid used in the experiments.

the formation of ribs in knife coating.

5.3 Experimental apparatus

The apparatus used in this study is described in section 2.2. Briefly, it consists of a roll rotating with peripheral speed U, partially immersed in a bath of fluid such that a film of coating liquid attaches to the roll surface by viscous lifting. The film is substantially thicker than the minimum point of separation between a horizontal flat plate placed in close proximity to the rotating roll, giving rise to a fully flooded nip. The plate is mounted horizontally above the roll on a slide–way to allow either face of the plate to be positioned above the centre of the roll by traversing the slide in the X direction. The use of two different plates gave a combination of four corner angles, $90°, 70°, 50°$and $30°$, allowing a study of the effect of the corner angle on the flow structure. The test fluid used was a silicone oil with properties shown in table 5.1.

Images of the flow field taken using a CCD camera were recorded onto S–VHS format video tape, with dye injection used to highlight the flow. Flux measurements were made by scraping the roll surface as discussed in section 2.5.

5.4 Computational method

A closed form theoretical solution to the problem cannot be found as the two–dimensional flow in the region close to the meniscus is of primary interest. Instead, the Navier–Stokes equations which govern incompressible Newtonian flow are solved numerically over the full domain.

A finite element (FE) formulation is used to approximate the Navier–Stokes equations over the domain of interest. The method is topologically very flexible, and well suited to problems of this type. Other approaches are also available — finite difference and finite volume techniques. Although both methods have been traditionally employed on fixed regular domains, recent advances have extended their use to irregular grids, through employing boundary fitted coordinates (Glaister (1995), Wang and Domoto (1994)). The boundary element or boundary integral method can also be used to solve free–surface flows, Kelmanson (1983), however the method is not easily applied to non–linear problems ($Re \neq 0$), although recent progress has been made in this area (Liao and Chwang (1996)).

The following section briefly describes the governing equations, the method for discretising the solution domain and the solution technique employed to solve the resulting non–linear systems. Interested readers are referred to Kistler and Scriven (1983), Thompson (1992) or Wilson (1997) for a fuller explanation.

5.4.1 The governing equations

Equations governing the steady flow of an incompressible fluid of constant density ρ and viscosity μ can be written in teems of the conservation of momentum and the mass for the system:

$$\rho \underline{U} \cdot \nabla \underline{U} = -\nabla P + \mu \nabla^2 \underline{U} + \rho \underline{G} \tag{5.1}$$

$$\text{and } \nabla \cdot \underline{U} = 0, \tag{5.2}$$

with $\underline{U}$ the fluid velocity, P the pressure and $\underline{G}$ the acceleration due to gravity. When written in non–dimensional form these equations become

$$Re \underline{u} \cdot \nabla \underline{u} = \nabla \cdot \underline{\underline{\sigma}} + St \underline{\hat{g}} \tag{5.3}$$

$$\nabla \cdot \underline{u} = 0 \tag{5.4}$$

where lengths have been scaled by H_0 — the minimum gap between the roll and the plate, velocities by the peripheral speed of the roll, U, and pressure and viscous

stresses by $\frac{\mu U}{H_0}$, with the Reynolds number $Re = \rho U H_0/\mu$ and the Stokes number $St = \rho g H_0^2/\mu U$. The unit vector $\hat{\underline{g}}$ indicates the direction in which gravity acts, and the dimensionless stress tensor, $\underline{\underline{\sigma}}$, for a Newtonian fluid is given by

$$\underline{\underline{\sigma}} = -p\underline{\underline{I}} + [\nabla \underline{u} + (\nabla \underline{u})^T]. \tag{5.5}$$

5.4.2 Discretising the domain

The fluid domain of interest is sub–divided into a number of elements, the position of which is identified by nodes located at points where the pressure and/or velocity is known, or needs to be determined. Within each element the variables are represented in terms of the nodal values by using interpolating functions. The velocity and pressure are given by

$$\underline{u}(x,z) = \sum_{k=1}^{K} \underline{\bar{u}}_k N_k(x,z), \qquad p(x,z) = \sum_{l=1}^{L} \bar{p}_l \psi_l(x,z). \tag{5.6}$$

The functions N and ψ_l are chosen to satisfy $N_k = 1$ at node k and $N_k = 0$ at all other nodes, and $\psi_l = 1$ at pressure node l and $\psi_l = 0$ at all other nodes, respectively.

The elements themselves need to be chosen carefully to prevent an ill posed problem, in particular the pressure is interpolated one order lower than the velocity so as to satisfy the Ladyzenskaya-Babuska-Brezzi stability condition (Babuska and Aziz, 1972). In this study V6/P3 elements are used (figure 5.3) as they are topologically well suited to the problem, although other elements are available (see Zienkiewicz, 1977). For this type of element N_k are 6 node biquadratic functions and ψ_l are 3 node linear functions.

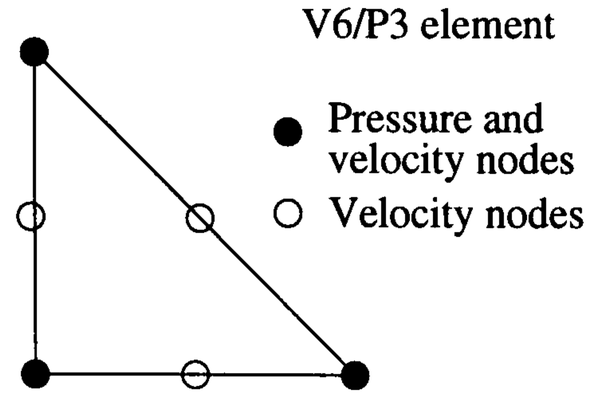

Figure 5.3: A V6/P3 element with velocities located at both corner and mid-side nodes, and pressure at corner nodes only.

5.4.3 Galerkin method

The finite element equations are derived by substituting equation (5.6) into (5.3) and (5.4), which results in an error – the residual – which needs to be minimised over the domain, subject to the boundary conditions. When the weighting functions are chosen to be the same as the integrating functions used to represent the unknown variables the method is known as the Galerkin method.

The momentum residuals are expressed as

$$\underline{R}_M^k = \int_\Omega [ReN_k(\underline{u} \cdot \nabla)\underline{u} - N_k \nabla \cdot \underline{\underline{\sigma}} - N_k St \underline{\hat{g}}] d\Omega = 0 \tag{5.7}$$

and the continuity residuals as

$$R_C^l = \int_\Omega \psi_l \nabla \cdot \underline{u} d\Omega = 0. \tag{5.8}$$

Equation (5.7) is simplified using the vector identity $N_k \nabla \cdot \underline{\underline{\sigma}} = \nabla \cdot (N_k \underline{\underline{\sigma}}) - \nabla N_k \cdot \underline{\underline{\sigma}}$, and after applying the divergence theorem gives

$$\underline{R}_M^k = \int_\Omega [ReN_k(\underline{u} \cdot \nabla)\underline{u} + \nabla N_k \underline{\underline{\sigma}} - N_k St \underline{\hat{g}}] d\Omega - \int_{\partial\Omega} \nabla N_k \underline{\underline{\sigma}} \cdot \underline{\hat{n}} ds. \tag{5.9}$$

In general the contribution to the momentum residuals from the boundary term ($\int_{\partial\Omega}$) will be zero along fixed boundaries where the velocity is known and zero at

any internal points reducing equation (5.9) to

$$\underline{\underline{R}}_M^k = \int_\Omega [ReN_k(\underline{u}\cdot\nabla)\underline{u} + \nabla N_k \underline{\underline{\sigma}} - N_k St\underline{\hat{g}}]d\Omega. \tag{5.10}$$

However, on the free–surface the boundary term contributions are non–zero and need to be retained and calculated.

5.4.4 The isoparametric map

The isoparametric map is a way of expressing the element in a local coordinate system, which greatly simplifies the evaluation of the interpolating functions from equation (5.6). Each element is mapped onto a standard triangle A_0, in coordinate space (ξ, η), as shown in figure 5.4.

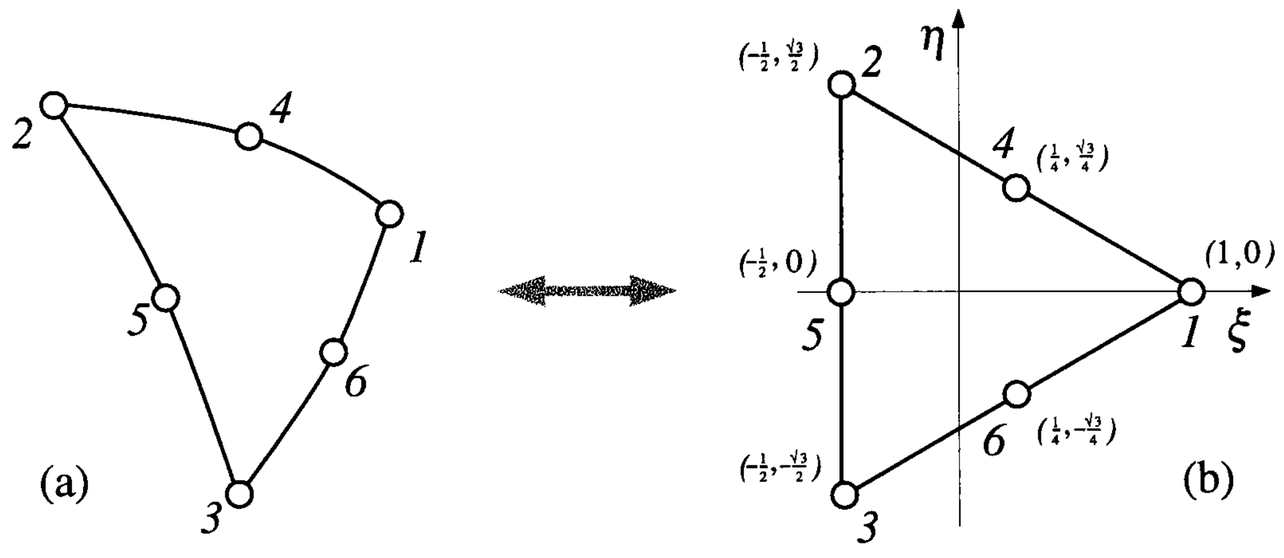

Figure 5.4: (a) A triangular element in global space. (b) The standard triangle in a local coordinate system with standard node numbering.

Under the node numbering system shown in figure 5.4 the interpolating functions N_k associated with each local node are given by

$$\begin{aligned} &N_1 = L_1(2L_1 - 1),\ N_2 = L_2(2L_2 - 1),\ N_3 = L_3(2L_3 - 1), \\ &N_4 = 4L_1L_2, \qquad N_5 = 4L_2L_3, \qquad N_6 = 4L_1L_3, \end{aligned} \tag{5.11}$$

while ψ_l associated with the corner nodes are

$$\psi_1 = L_1,\ \psi_2 = L_2,\ \psi_3 = L_3, \tag{5.12}$$

where

$$L_1 = \frac{1}{3}(1+2\xi),\ L_2 = \frac{1}{3}(1-\xi+\sqrt{3}\eta),\ L_3 = \frac{1}{3}(1-\xi-\sqrt{3}\eta). \tag{5.13}$$

The global coordinates of any point of an element's interior can now be found from the global coordinates of the nodes and the interpolating functions used for the dependent variables,

$$\underline{x} = \sum_{k=1}^{6} \underline{x}_k N_k(\xi,\eta), \tag{5.14}$$

where $\underline{x}_k$ are the global coordinates of the kth local node. Finally, the derivatives $\frac{\partial N_k}{\partial x}$, $\frac{\partial N_k}{\partial z}$ etc. in equation (5.6) need to be evaluated, but with N_k and ψ_l now defined in terms of local coordinates their relationship to the global coordinate system is given by

$$\begin{pmatrix} \frac{\partial}{\partial \xi} \\ \frac{\partial}{\partial \eta} \end{pmatrix} = \begin{pmatrix} \frac{\partial x}{\partial \xi} & \frac{\partial z}{\partial \xi} \\ \frac{\partial x}{\partial \eta} & \frac{\partial z}{\partial \eta} \end{pmatrix} \quad \begin{pmatrix} \frac{\partial}{\partial x} \\ \frac{\partial}{\partial z} \end{pmatrix} = \underline{\underline{J}} \begin{pmatrix} \frac{\partial}{\partial x} \\ \frac{\partial}{\partial z} \end{pmatrix}, \tag{5.15}$$

with the entries in the Jacobian, $\underline{\underline{J}}$, found from

$$\frac{\partial x}{\partial \xi} = \sum_{k=1}^{6} \underline{x}_k \frac{\partial N_k}{\partial \xi}, \quad \frac{\partial x}{\partial \eta} = \sum_{k=1}^{6} \underline{x}_k \frac{\partial N_k}{\partial \eta}. \tag{5.16}$$

Using this, the integrals shown in equation (5.10) can be evaluated element by element in a local coordinate system,

$$\int_\Omega f(x,\beta)d\Omega = \int_\Omega f(x,\beta)dxdz = \sum_{elements} \left(\int f(\underline{x}(\xi,\eta),\beta)|J|d\xi d\eta \right). \tag{5.17}$$

5.4.5 Numerical integration

To further simplify the integrals in equations (5.8) and (5.10) subsequently transformed into a local coordinate system (using equation (5.15)), a Gauss quadrature scheme is used which replaces the integral by a sum of weighted values at specific points, i.e.

$$\int_{A_0} f(\xi,\eta)|J|d\xi d\eta = \sum_{i=1}^{n} f(\xi_i,\eta_i)w_i, \tag{5.18}$$

where w_i are the weights for the n Gauss points. Thompson (1992) concluded that a 4–point scheme was sufficient for a study of the free–surface flow problem of a forward roll coater using V6/P3 elements, and for this reason they are adopted here. Figure 5.5 shows the positions of the Gauss points and the associated weights. Similarly the Gauss points for a 3–point scheme used in integration of a line element are also shown.

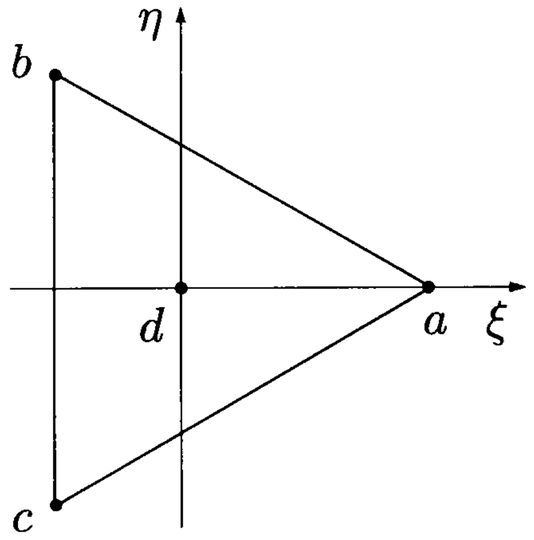

(a)

	ξ	η	w
a	1	0	$\frac{\sqrt{3}}{16}$
b	$-\frac{1}{2}$	$\frac{\sqrt{3}}{2}$	$\frac{\sqrt{3}}{16}$
c	$-\frac{1}{2}$	$-\frac{\sqrt{3}}{2}$	$\frac{\sqrt{3}}{16}$
d	0	0	$\frac{9\sqrt{3}}{16}$

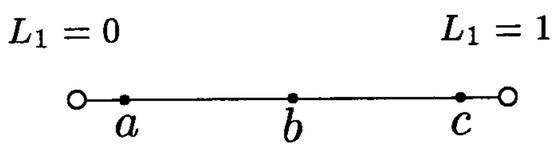

(b)

	L_1	w
a	0.11270167	$\frac{5}{18}$
b	0.5	$\frac{4}{9}$
c	0.88729833	$\frac{5}{18}$

Figure 5.5: Gauss points and corresponding weights in (a) a 4-point quadrature scheme for domain integrals, and (b) a 3-point scheme for boundary (line) integrals.

5.4.6 Iterative technique

The residual equations (5.8) and (5.10) require an iterative method to solve them as they are non–linear. Here, following Saito and Scriven (1980), the Newton-Raphson method is used as it exhibits rapid convergence as the solution is approached. Expressing the system of equations as

$$\underline{R}(\underline{\alpha}) = \underline{0} \tag{5.19}$$

and taking a Taylor expansion gives

$$R(\underline{\alpha}_{n+1}) \approx \underline{R}(\underline{\alpha}_n) + \left[\frac{\partial \underline{R}}{\partial \underline{\alpha}}\right]_{\underline{\alpha}=\underline{\alpha}_n} \Delta\underline{\alpha}_n = \underline{0} \tag{5.20}$$

where $\Delta\underline{\alpha}_n = \underline{\alpha}_{n+1} - \underline{\alpha}_n$. Hence at each iteration

$$\underline{\underline{J}}\Delta\underline{\alpha}_n \equiv \left[\frac{\partial \underline{R}}{\partial \underline{\alpha}}\right]_{\underline{\alpha}=\underline{\alpha}_n} \Delta\underline{\alpha}_n = -\underline{R}(\underline{\alpha}_n) \tag{5.21}$$

must be solved for the increments $\Delta\underline{\alpha}_n$.

As the solution is approached the convergence of such a scheme becomes quadratic, which provides a useful means of checking that the terms in the Jacobian have been evaluated correctly (Kistler and Scriven, 1983).

From an initial guess and after calculating the residuals, $\underline{\alpha}_{n+1}$ is updated by only a fraction of the new value. This is known as under–relaxation and can increase the radius of convergence. Once an initial solution had been obtained, successive solutions in moving through parameter space were found by zeroth order continuation in small steps (without under–relaxation).

The frontal method (Irons, 1970 and Hood, 1976) was used to minimise the storage requirements for the matrix $\underline{\underline{J}}$. This is based upon Gaussian elimination and well suited to many finite element problems. Further details of this method can be found in Wilson (1997), the implementation of the frontal method used in this study was developed by Gaskell (1990) and refined by Thompson (1992).

5.4.7 Post-processing

A convenient way of representing steady–state flows is *via* the use of streamlines. Coyle (1984) showed how the stream-function ψ can be found by solving the Poisson equation

$$\nabla^2\psi = \frac{\partial u}{\partial z} - \frac{\partial w}{\partial x}. \tag{5.22}$$

The Galerkin weighed residual approach is again used, resulting in a set of linear equations when the stream-function is specified everywhere on the boundary. The calculation of stream-function was performed using software written by Walker (1995).

5.4.8 Boundary conditions

The conditions at the boundary of the domain are illustrated in figure 5.6, and discussed below.

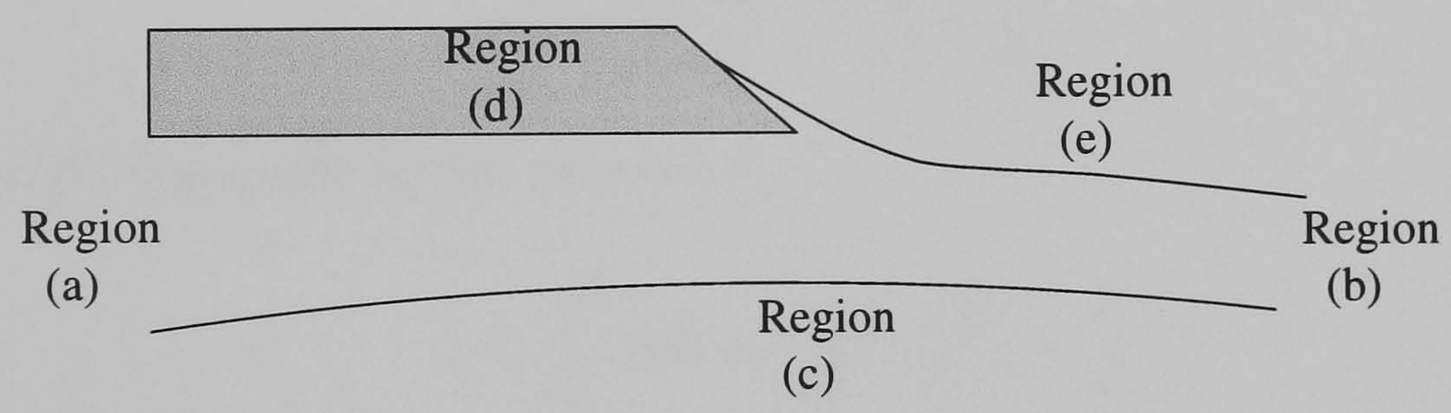

Figure 5.6: Location of the boundary regions described in section 5.4.8.

(a.) The inlet region. The flow is fully developed and is described by Reynolds equation and a continuity of flow equation:

$$\frac{d\bar{p}}{d\bar{x}} = \frac{d^2\bar{u}}{d\bar{z}^2}, \tag{5.23}$$

$$\frac{d\bar{u}}{d\bar{x}} + \frac{d\bar{w}}{d\bar{z}} = 0, \tag{5.24}$$

where the non–dimensional parameters used in this analysis are

$$\bar{p} = P\frac{H_0}{\mu U_{web}}\left(\frac{H_0}{2R}\right)^{1/2}, \qquad \bar{\lambda} = \frac{H^{\infty}}{H_0},$$
$$\bar{u} = \frac{U}{U_{web}}, \qquad \bar{w} = \frac{W}{U_{web}}\left(\frac{2R}{H_0}\right)^{1/2} \tag{5.25}$$
$$\bar{x} = \frac{X}{(2RH_0)^{1/2}}, \qquad \bar{z} = \frac{Z}{H_0}.$$

Note that these non–dimensional parameters are different from those used in the finite element analysis, and are represented by quantities with a bar over the letter.

Integrating equation (5.23) and applying the boundary conditions

$$\bar{u} = 0 \text{ on } \bar{z} = \bar{h},$$
$$\text{and } \bar{u} = 1 \text{ on } \bar{z} = 0,$$

gives

$$\bar{u} = \frac{d\bar{p}}{d\bar{x}}\left[\frac{\bar{z}}{2} - \frac{\bar{z}\bar{h}}{2}\right] + \frac{\bar{z}}{\bar{h}}. \tag{5.26}$$

The flux, $\bar{\lambda}$ is given by the expression

$$\bar{\lambda} = \int_0^{\bar{h}} \bar{u}d\bar{h} = \frac{d\bar{p}}{d\bar{x}}\left[\frac{-\bar{h}^3}{12}\right] + \frac{\bar{h}}{2}, \tag{5.27}$$

which together with equation (5.26) gives

$$\bar{u} = \frac{12}{\bar{h}^3}\left[-\bar{\lambda} + \frac{\bar{h}}{2}\right]\left[\frac{\bar{z}^2}{2} - \frac{\bar{z}\bar{h}}{2}\right] + \frac{\bar{z}}{\bar{h}}. \tag{5.28}$$

Substituting $\bar{h} = 1 + \bar{x}^2$ which describes $\bar{h}(\bar{x})$ for this particular geometry close to the nip, and

$$\bar{x} = \tan\alpha,$$

into equation (5.27), integrating and and applying the boundary condition

$$\bar{p}(-\infty) = 0, \tag{5.29}$$

which states the pressure in the liquid decays to atmospheric far upstream of the nip, as is the case where a rolling bank of fluid exists, gives

$$\bar{p} = 3(2 - 3\bar{\lambda}) \left[\frac{\alpha}{2} + \frac{\sin 2\alpha}{4} + \frac{\pi}{4} \right] - 3\bar{\lambda} \cos^3 \alpha \sin \alpha. \tag{5.30}$$

The $\bar{w}$ component of the velocity is an order of magnitude smaller than $\bar{u}$ and can be recovered from the continuity equation (5.24) — see Richardson (1996),

$$\bar{w} = \int -\frac{d\bar{u}}{d\bar{x}} d\bar{z} \tag{5.31}$$

and with the boundary condition $\bar{w}(\bar{z} = \bar{h}) = 0$, gives

$$\bar{w} = \frac{2\bar{x}(1 - 6\bar{\lambda} + \bar{x}^2)}{(1 + \bar{x}^2)^3} \bar{z}^2 + \frac{4\bar{x}(-1 + 3\bar{\lambda} - \bar{x}^2)}{(1 + \bar{x}^2)^4} \bar{z}^3, \tag{5.32}$$

The non–dimensional quantities in this lubrication analysis can be written in terms of required for the finite–element analysis as:

$$\bar{p} = p \left(\frac{H_0}{2R} \right)^{1/2}, \qquad \lambda = \bar{\lambda}, \tag{5.33}$$

$$\bar{u} = u, \qquad w = \left(\frac{H_0}{2R} \right)^{1/2} \bar{w}. \tag{5.34}$$

The (U,W) velocities in the inlet region are imposed by setting the relative values in the Jacobian. The pressure condition is imposed, following Coyle *et al.* (1986), by calculating the average pressure across the nip using the pressure shape functions ψ_l. The pressures along the inlet boundary and the flux are used to calculate a residual associated with the unknown λ.

(b.) Fully developed plug flow. At the outlet the velocity of the fluid is equal to that of the roll surface

$$\underline{u} = \hat{t}_1 \tag{5.35}$$

where $\hat{t}_1$ is the unit tangent to the lower roll surface.

(c.) A no–slip boundary. Here the fluid velocity is equal to that of the roll surface

$$\underline{u} = \hat{t}_1 \quad \text{at } z = 0. \tag{5.36}$$

(d.) A no–slip boundary Here the velocity of the plate is zero and so:

$$\underline{u} = 0 \quad \text{at } z = h. \tag{5.37}$$

(e.) A free–surface. Between the liquid and gas domain surface tension effects are important. Here a kinematic boundary condition applies, Kistler and Scriven (1984), which states that no fluid crosses the interface,

$$\underline{u} \cdot \hat{\underline{n}} = 0. \tag{5.38}$$

A second condition is that tangential shear stress is continuous and normal stress and surface tension balance, respectively

$$\hat{\underline{n}} \cdot \underline{\underline{\sigma}} = \frac{1}{Ca} \frac{d\hat{\underline{t}}}{ds}. \tag{5.39}$$

These conditions are used to find the two unknowns on the free–surface, the velocity and the location.

Equation (5.39) is included in the residual (equation 5.9) with the terms

$$\int_{d\Omega} \nabla N_k \underline{\underline{\sigma}} \cdot \hat{n} ds$$

replaced by

$$\int_{d\Omega} \nabla N_k \frac{1}{Ca} \frac{d\hat{\underline{t}}}{ds}.$$

The condition (5.38) is used to find the location of the free–surface *via* the spine method (Kistler and Scriven (1984)) described below.

5.4.9 Gridding

The primary difficulty in solving free–surface problems is parameterising the free–surface, since its location is not known *a priori*. One method used to solve problems of this nature is the 'spine' method which emerged as a natural development of the boundary support method (Ruschak (1980)). It was first used by Kistler and Scriven (1984) in a study of curtain and forward roll coating systems. Their method

is adopted here, with the free–surface position described in terms of 'spines', as illustrated in figure 5.8.

Gridding the domain with the meniscus free to climb

Each spine is defined by a fixed base point x_i^b and a unit vector $\hat{e}_i$ with the height h_i of the spine being the parameter that describes the free–surface position. Nodes are located along the spine by

$$\underline{x}_k = \underline{x}_i^B + w_j h_i \hat{e}_i \tag{5.40}$$

where w_j is the distribution function of the nodes.

The equations used to determine the spine heights are supplied by forming a weighted residual from the kinematic condition given by equation (5.38),

$$R_k^i = \int_{d\Omega} N_i \cdot \underline{u} \cdot \underline{\hat{n}} ds = 0. \tag{5.41}$$

Referring to figure 5.7 the nodes in region 2(i) have a weighting factor, w_j graded equally from $0 \rightarrow \frac{l_{fixed}}{l_{climb}+l_{fixed}}$ where l_{fixed} is the distance between the point b. — the corner of the plate and point a., defined by the intersection of a line that lies along the face of the plate through the corner and the roll. Here l_{climb} is the length from the corner of the plate to the wetting line taken along the face of the plate. Similarly, the weights in region 2(ii) are given by grading the weighting factor equally from $\frac{l_{fixed}}{l_{climb}+l_{fixed}} \rightarrow 1$. The first spine in the free–surface region has a base node located at the corner of the plate and direction, $\hat{e}_1$, so it lies along the face of the plate.

Subsequent base nodes are located along the roll surface and are graded in the $x-$direction to minimise computational effort such that

$$x_{i+2}^b = x_{i+1}^b + c_1(x_{i+1}^b - x_i^b), \tag{5.42}$$

with a typical value of $c_1 = 1.03$. Equation (5.42) requires the first two node positions to be specified. Alternatively, as in this study, the length of the domain

and number of nodes are specified and the first two node positions are calculated to meet these conditions.

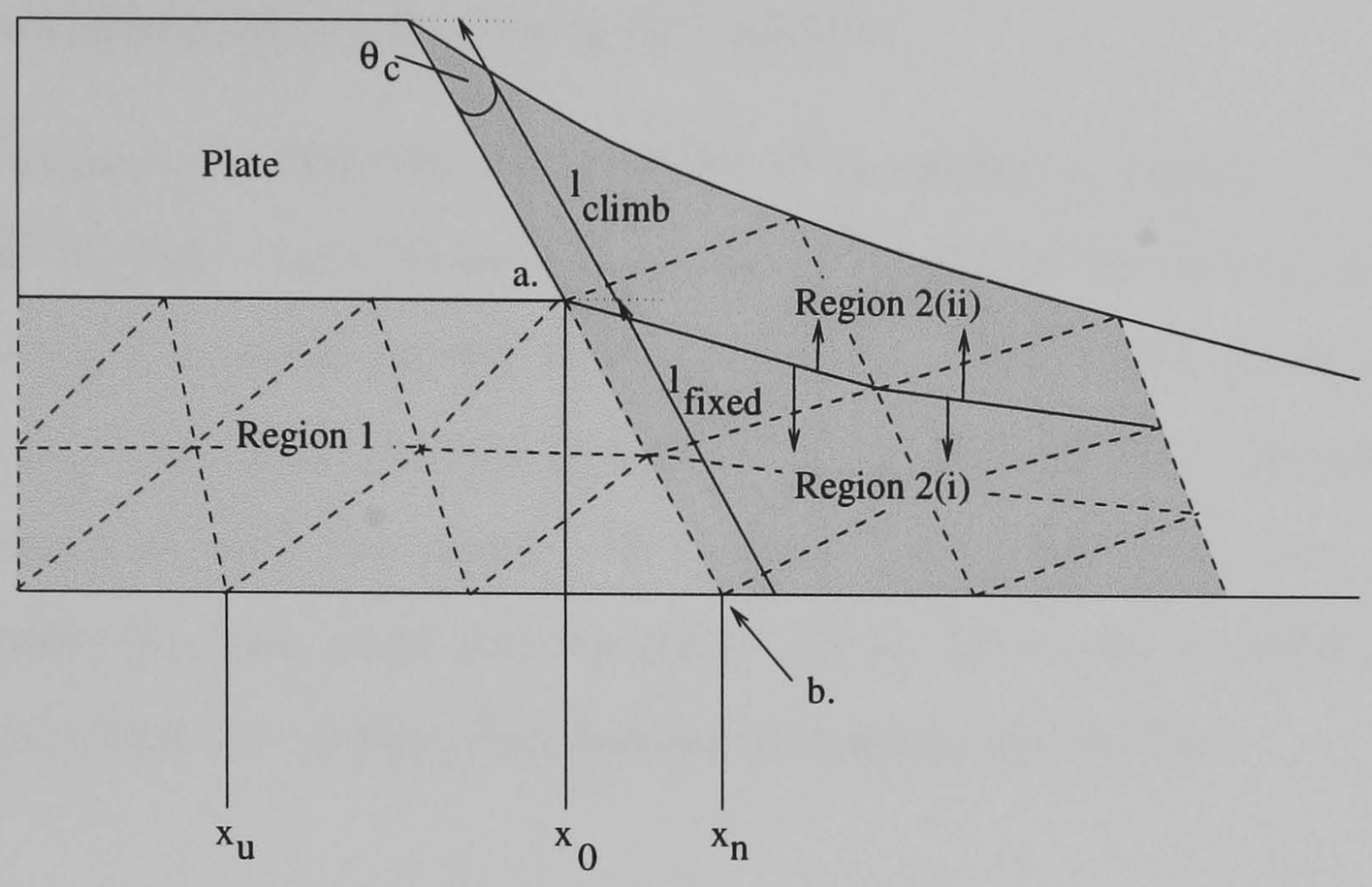

Figure 5.7: Location of the three regions : Region 1 fixed nodes, region 2 nodes located on spines — relative length of spines in region 2(i) and 2(ii) fixed by l_{climb}/l_{fixed}.

The direction vectors of the spines are graded such that the first spine lies parallel to the face of the plate, and the final spine is perpendicular to the tangent of the roll at the outlet.

A static contact angle, θ_c, must also be imposed in order to obtain a solution. The kinematic residual is automatically satisfied at the wetting line since the velocity is known, and this residual is replaced by

$$R^{h_1} = \underline{t} \cdot \underline{t}_w + \cos\theta_c = 0 \tag{5.43}$$

where R^{h_1} is the residual associated with the spine that passes through the wetting line, $\underline{t}$ is the tangent to the free–surface and $\underline{t}_w$ is the tangent to the wall. At this point there is an integrable stress singularity, and studies comparing the predictions of finite element calculations using the non–slip boundary condition with experiments seem to compare favourably, more information can be found in Kistler

and Scriven (1983). There is also a singularity in the vorticity at the sharp corner within the flow making a vorticity–streamfunction formulation difficult to implement. Here a UVP formulation has been used with the velocity already specified along the boundary, hence alleviating this problem.

All that remains is to describe the position of the nodes in region 1. Fixed spines are specified by base nodes located along the roll surfaces between $\underline{x}_u$ and $\underline{x}_n$. The direction of the spines are graded such that the first fixed spine is vertical and the last fixed spine lies parallel to the face of the plate, located such that the top–most node is coincident with the corner. The nodes along the fixed spine are equally spaced between the base node and the plate. Figure 5.9 shows a typical FE grid for a solution in which the contact line is able to migrate up the face.

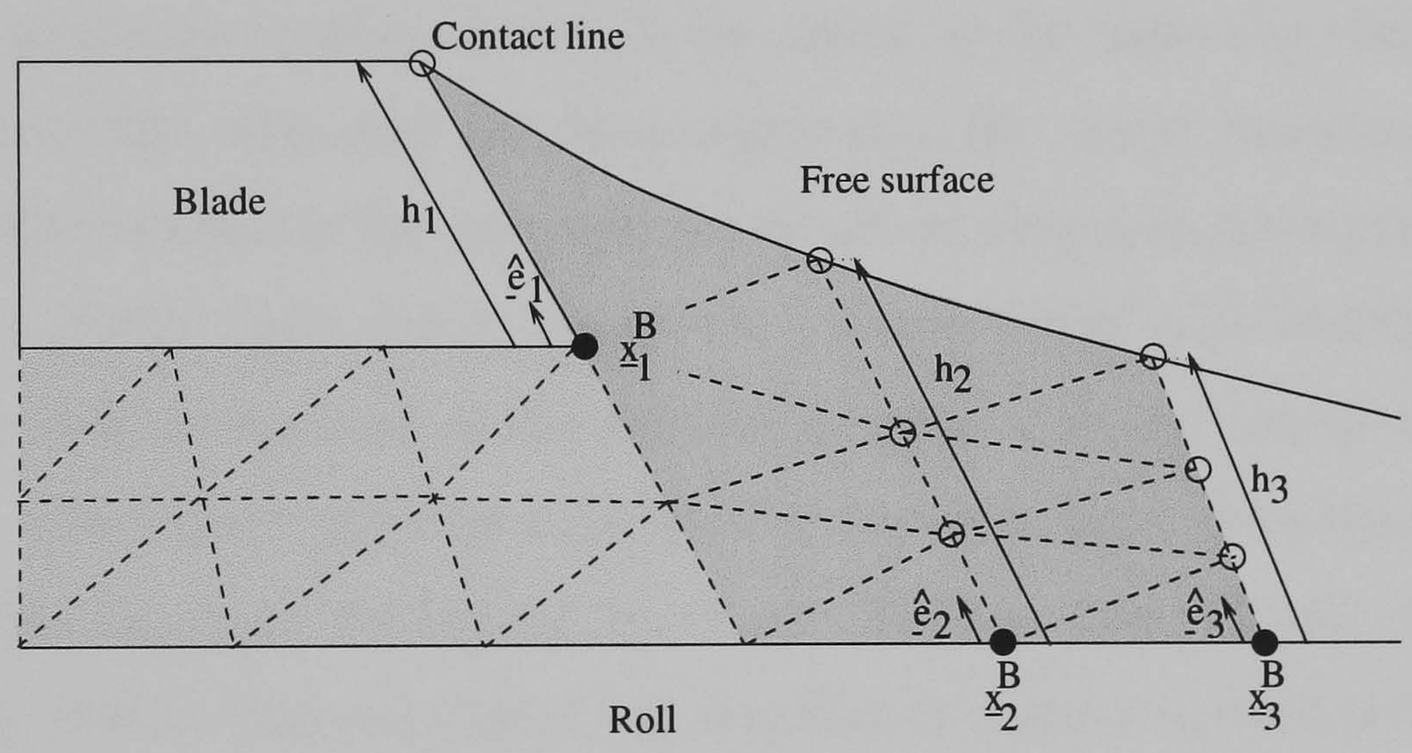

Figure 5.8: Details of the spine locations in the problem (• fixed base nodes, ∘ nodes located on spines).

Figure 5.9: A typical grid used in the solution of the problem, with the contact line free to migrate up the face.

5.4.10 Gridding the domain with the meniscus pinned on the corner

When the meniscus remains pinned to the corner of the plate the climb length is zero. Sartor (1990) identified the climb region in a slot coater experimentally, but only presented results for the case with the meniscus pinned on the corner. Silliman and Scriven (1980), Saito and Scriven (1981), Carter (1985) and Thompson (1992) studied the downstream end of the slot coater again with the meniscus pinned on the corner. The full slot problem with two free–surfaces, again using the assumption of zero climb, has been studied by Durst and Wagner (1997), Grald *et al.* (1994) and Daniels (1998). Daniels (1998) was the first to present numerical results with the downstream meniscus detached from the corner and free to advance or recede in the gap.

The study of the case with the meniscus pinned on the corner necessitates the use of a different grid to that described before, otherwise the cells in region 2(ii) (figure 5.7) would be forced to zero height and the numerical scheme would fail. Consequently for this situation the number of cells in region 2(ii) are set to zero with the cells in region 2(i) weighted between 0 and 1. Finally with the location of the wetting line now specified the contact angle is no longer imposed, but is determined as part of the solution.

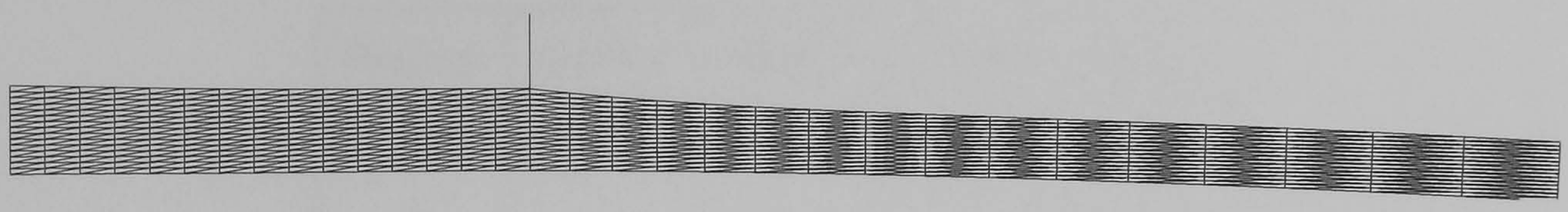

Figure 5.10: A typical grid used in the solution of the problem, with the contact line pinned on the corner.

5.4.11 Initial solution

An initial solution for the problem with the meniscus climbing the face was found by fixing the location of the contact line taken from experiment and under–relaxing the solution until a converged flow field was established. The free–surface position was then allowed to move to give the required solution.

An initial solution for the problem with the meniscus pinned on the corner of the plate was found merely by under–relaxing an initial guess for the free surface position, chosen to give a smooth profile.

5.4.12 Grid independence

It is important to verify the solution is independent of the mesh density. Four grids were used for this purpose, with the node densities shown in table 5.2. A maximum change in flux of 0.03% was recorded over the parameter range investigated, and a maximum change in climb length between grids 2 and 4 of 0.04% was calculated. From this study it was concluded that by using either grids 2 or 4 the solutions were grid–independent and sufficiently converged, the remainder of the solutions presented in this chapter were found using grid 4.

Region	Grid 1	Grid 2	Grid 3	Grid 4
X_1	15	15	31	21
Z_1	15	15	31	21
X_2	32	64	32	48
Z_2	16	32	16	24

Table 5.2: Node densities used in to assess grid independency. Refer to figure 5.11 for the definitions of X_1, X_2, Z_1, Z_2.

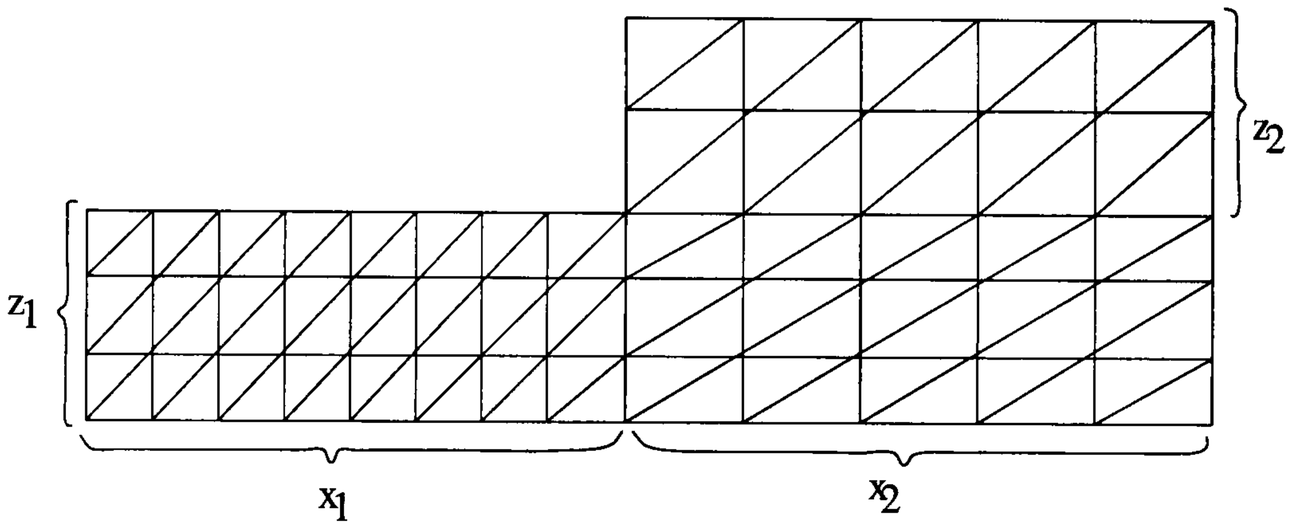

Figure 5.11: Density of nodes in the fixed and climb region of the grid.

5.5 Lubrication model

A model based on lubrication theory to predict the final film thickness H^∞ and pressure beneath the plate can be formulated. The analysis described in section 5.4.8 to formulate a boundary condition used in defining the boundary conditions for a full numerical solution needs just one condition to solve for all the variables. The simplest boundary condition to apply is to neglect curvature at the meniscus such that

$$\bar{p}(\bar{x} = 0) = 0. \tag{5.44}$$

Applying this boundary condition to equation (5.30) gives

$$\bar{\lambda} = \frac{2}{3} \tag{5.45}$$

and

$$\bar{p} = -2\cos^3\alpha \sin\alpha \tag{5.46}$$

for the case when the face of the knife is positioned directly above $x = 0$.

The assumption of zero pressure at $x = 0$ will become less valid as the meniscus climbs the face of the knife and the radius of curvature of the meniscus, and hence the sub-ambient pressure in the liquid, increases.

This limiting case of the knife positioned at $x = 0$ was highlighted by Coyle (1997), who derived a general model based on lubrication theory for knife coating.

5.6 Results and discussion

5.6.1 Comparison between experiments and theory

The principle aim of this section is to compare experimental data with the computational results so that a study of the features of the system can be made with confidence.

5.6.2 Flow visualisations

Figures 5.12 to 5.15 show a series of flow visualisations taken from experiments under identical conditions, but with the corner angle of the plate, β, at $90°, 70°$ and $30°$ respectively, and the tip of the plate located directly above the roll centre. For an angle $\beta = 30°$ the meniscus is seen to pin to the corner of the plate. When the plate angle is increased to $70°$ and then $90°$ the meniscus is observed to climb the face of the knife. Under these conditions a closed eddy is present in the region close to the contact line, shown in figure 5.15. Experimentally, dye injection was used to highlight the flow structure, whilst computationally appropriate streamlines were

plotted.

The comparison between the experimental flow visualisations, and the computations is good, with the latter predicting the flow features and meniscus shapes observed in practice.

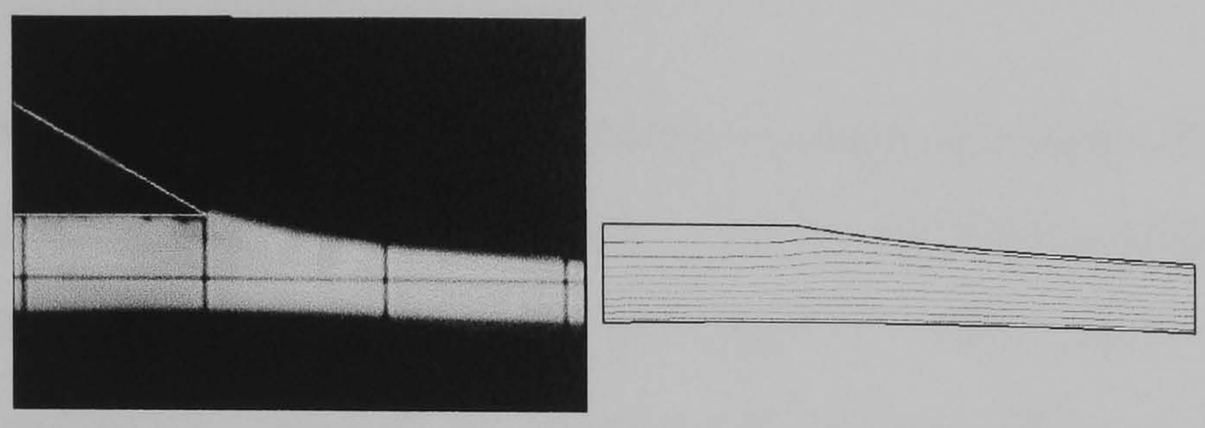

Figure 5.12: Comparison of the flow field observed from experiments and computed. Plate angle 30°. Conditions: $Ca = 0.06, R/H_0 = 100, \theta_c = 30°$.

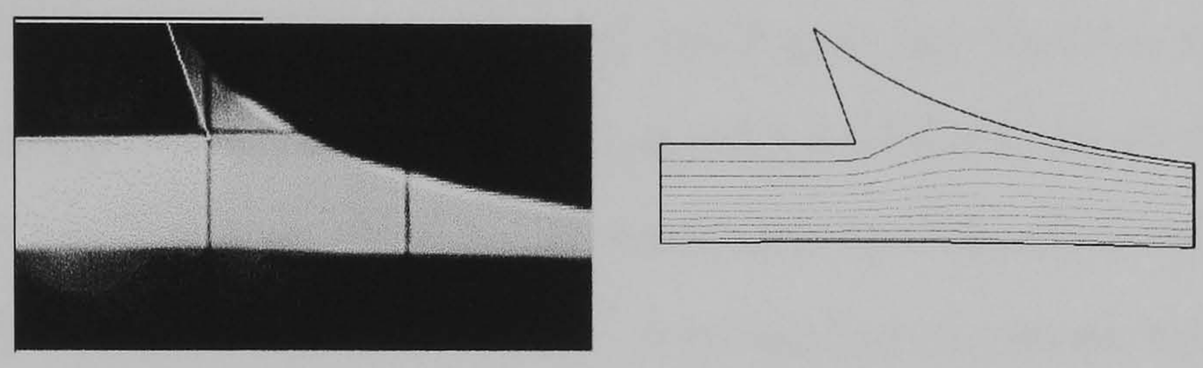

Figure 5.13: Plate angle 70°. Conditions as per figure 5.12

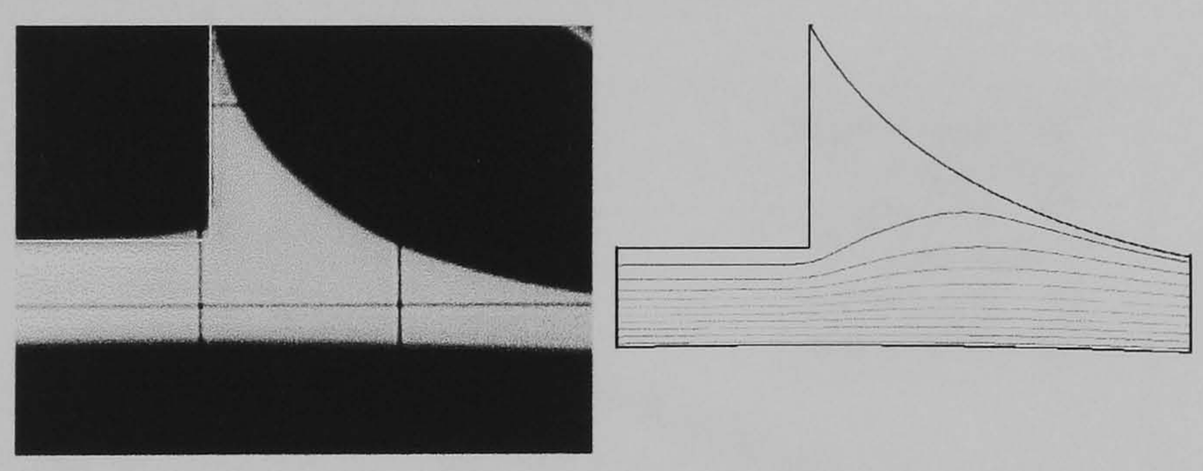

Figure 5.14: Plate angle 90°. Conditions as per figure 5.12

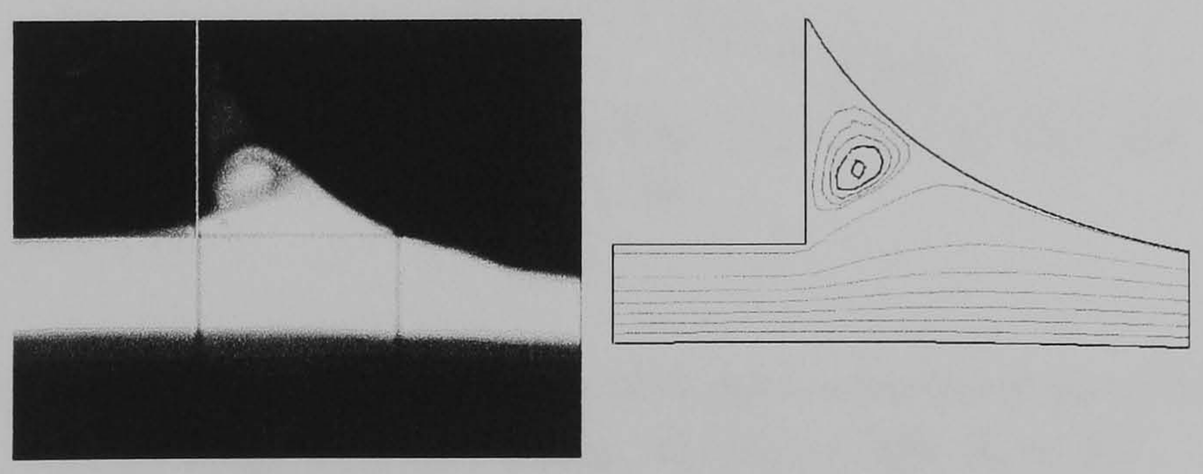

Figure 5.15: Dye used to highlight recirculation near the contact line. Plate angle 90°. Conditions as per figure 5.12

5.6.3 Climb length

Figure 5.16 shows the climb length (the distance measured along the knife from the corner to the wetting line) as the roll speed (hence capillary number) is increased for the three plates with tip angles $90°, 70°$ and $50°$. The climb length has been non–dimensionalised with respect to the gap, H_0, between the roll and knife at X_0. It can be seen for a given capillary number, as the corner angle β is reduced, the climb length along the knife decreases and the contact line approaches the corner. Similarly, as the capillary number is increased the climb length decreases as the meniscus is pulled downstream due to the increased roll speed.

The agreement between the experimental work and the theoretical predictions is reasonable, the biggest discrepancy occurring with a corner angle of $70°$. The reasons for this are still unclear and could be, in part, due to difficulties in setting the gap between the roll and plate (section 2.2.2), determining the exact termination of the flow domain or, indeed, something more fundamental.

With a corner angle of $30°$ the meniscus was observed to pin on the corner of the plate, and a climb length of 0 mm was recorded.

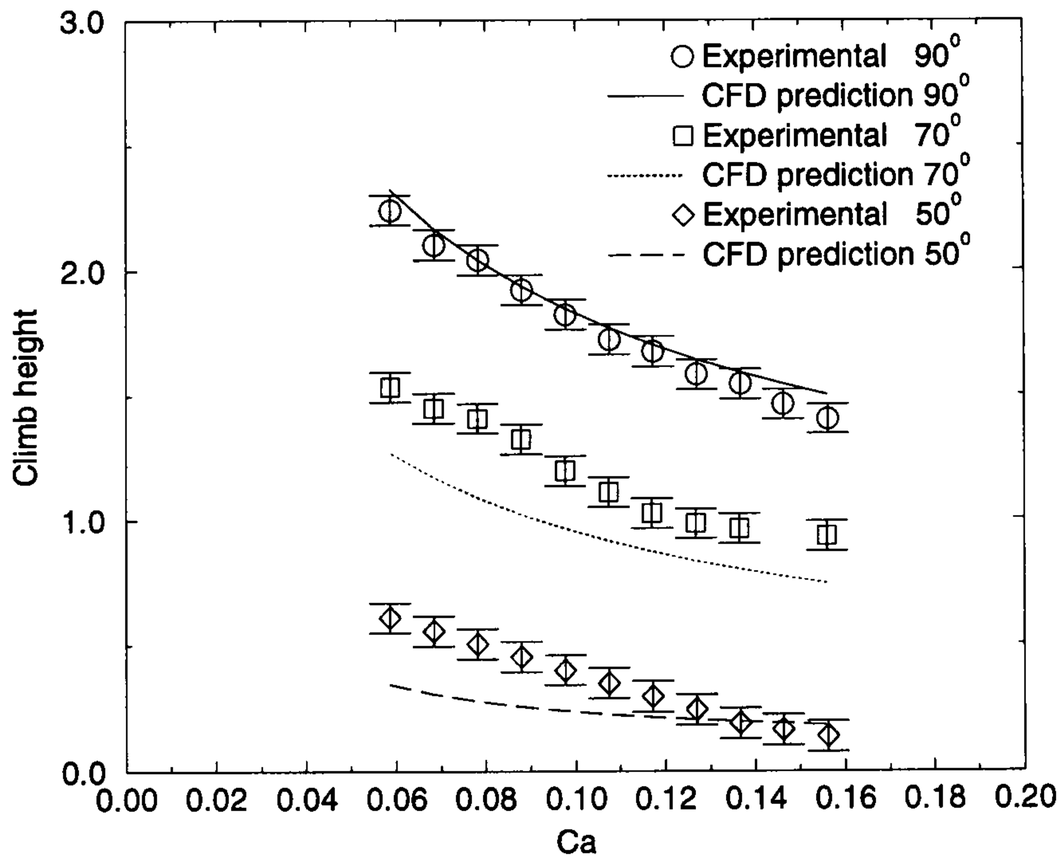

Figure 5.16: Comparison of experimental and numerical predictions for the climb length of the blade, $R/H_0 = 100$, $\theta_c = 35°$.

5.6.4 Flux measurements

Figures 5.17 and 5.18 show a comparison between experimental, numerical and analytical predictions for the flux as the capillary number is varied. The agreement between the three sets of results is excellent, with the analytical and computational predictions lying within the estimated error of the experiments.

As capillary number increases the flux remains almost constant showing that the sub-ambient pressure generated by the meniscus has only a small effect on the flow over the range of capillary numbers investigated here. Even when the meniscus is observed to climb the face of the plate, the dimensionless flux increases only very slightly from the pinned case.

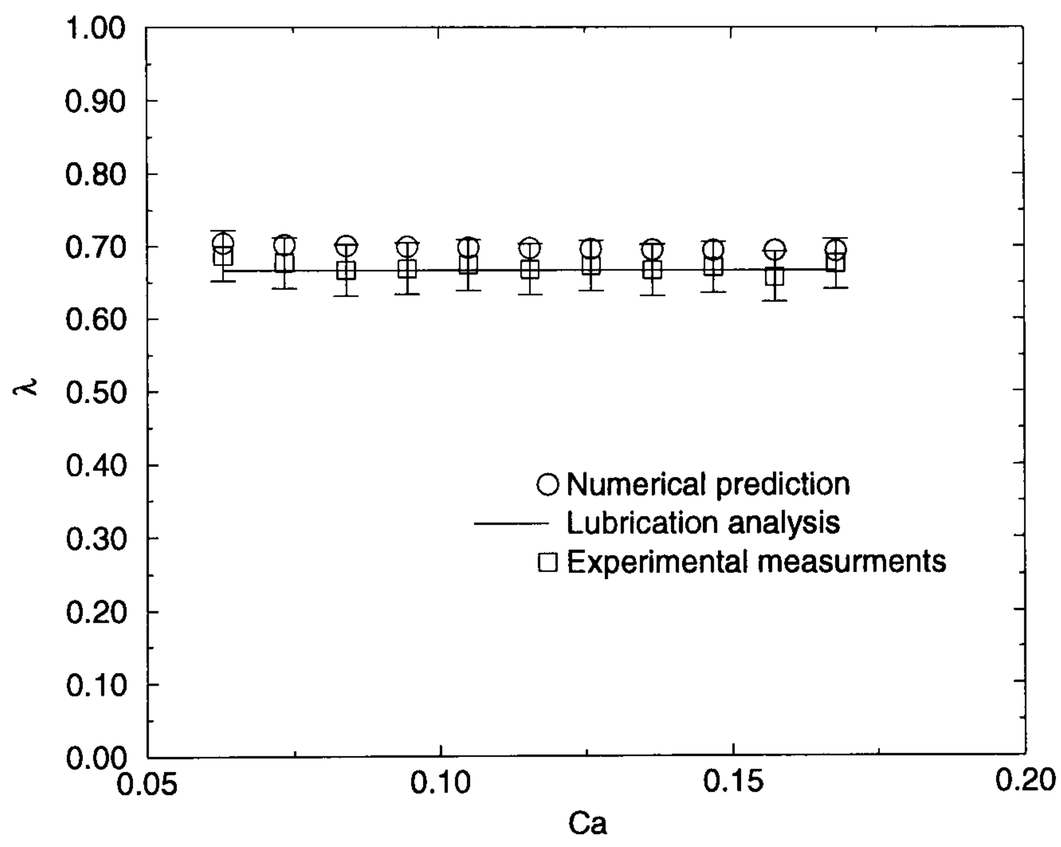

Figure 5.17: Comparison of experimental and numerical and analytical predictions for flux with a knife angle of 90°, $R/H_0 = 250$, $\theta_c = 35°$. The meniscus climbs the face of the knife.

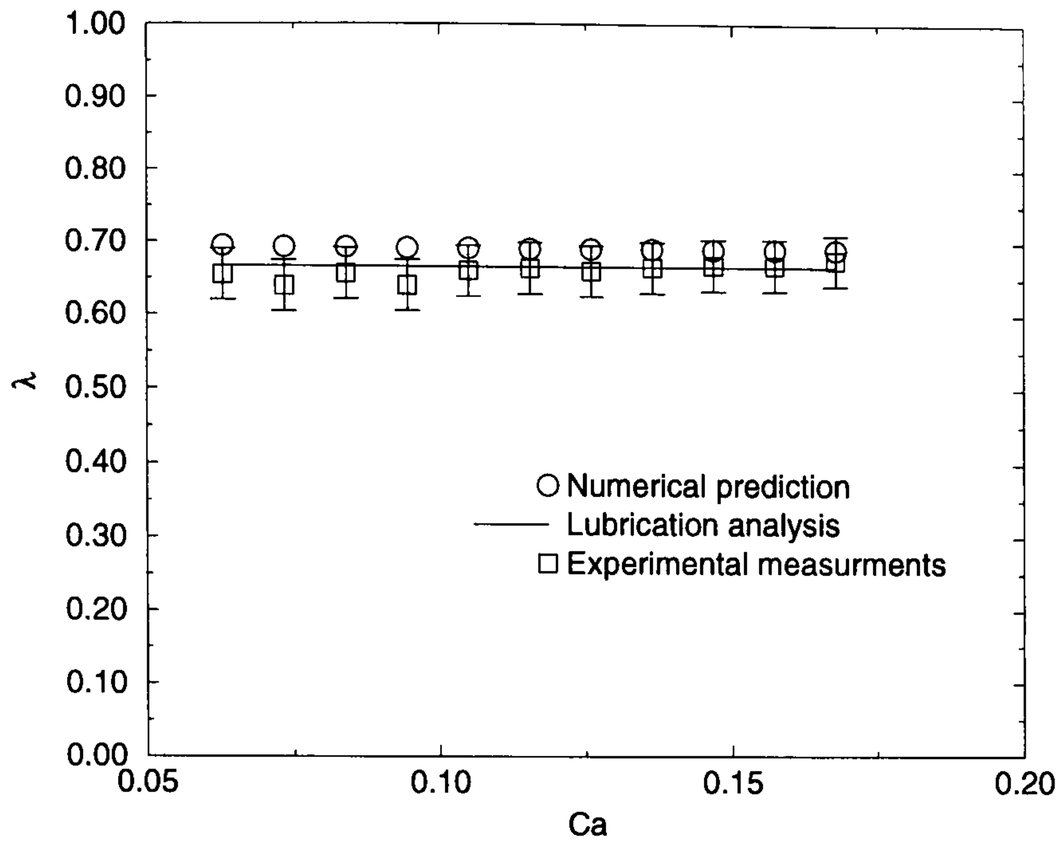

Figure 5.18: Comparison of experimental and numerical and analytical predictions for flux with a knife angle of 30°, $R/H_0 = 250$, $\theta_c = 35°$. The meniscus is pinned to the corner in all measurements.

5.7 Theoretical investigations

From the preceding section it is clear that the effect of the meniscus climbing the face of the plate has little effect on the flux at practical values of capillary number — however the climb length is strongly affected by capillary number. In practice it is desirable to reduce the climb length as this reduces the size of the closed eddy, the residence time distribution of the coating fluid and possibly the tendency of streaking or point defects on the final coated product.

5.7.1 The effect of capillary number on climb length

Figure 5.19 shows the effect of capillary number on climb length for plates with a corner angle of 90° and 70°. As the capillary number increases the climb length decreases monotonically, and the size of the associated vortex is correspondingly reduced. It is also of interest to consider the limit of the climb height. Figure 5.19

shows that as capillary number is reduced the computed climb height tends to a non–zero value. This limiting case can be understood by considering the shape a static meniscus would make when in contact with a plate, as shown in figure 5.20. Assuming that the meniscus can be represented by an arc of a circle, of radius R, then from a balance of forces

$$\Delta P = \frac{\sigma}{R} = \rho g H_{max}, \tag{5.47}$$

where H_{max} is the climb height above the surface of the fluid, and R is the radius of curvature of the meniscus. Relating H_{max} to R *via*

$$H_{max} = R(1 - \sin(90 + \theta_c - \beta)), \tag{5.48}$$

gives a limiting value for the climb height H_{max} at zero capillary number:

$$H_{max}^2 = \frac{\sigma(1 - \sin(90 + \theta_c - \beta))}{\rho g}, \tag{5.49}$$

with the climb height, H_{max}, related to the climb length, L_{max}, by

$$L_{max} = \frac{H_{max}}{\sin\beta} - (1 - \lambda)H_0, \tag{5.50}$$

where the term $(1 - \lambda)H_0$ is a correction to account for the difference in height of the equilibrium liquid surface and the corner of the plate. In fact this forms the basis of the Wilhelmy slide method used for the measurement of surface tension, Adamson (1982). Figure 5.19 does indeed show that as $Ca \to 0$ the climb length tends to the limiting case given by equation (5.49).

The maximum climb height as a function of the corner angle of the plate and the contact angle the fluid makes with the solid is shown in figure 5.21, clearly showing that a large contact angle and a small corner angle has the effect of reducing the climb height, and hence the strength of the eddy located by the contact line. The non–dimensional climb height decreases almost linearly from $1 \to 0$ as $(90 + \theta_c - \beta)$ increases from $0 \to 90°$.

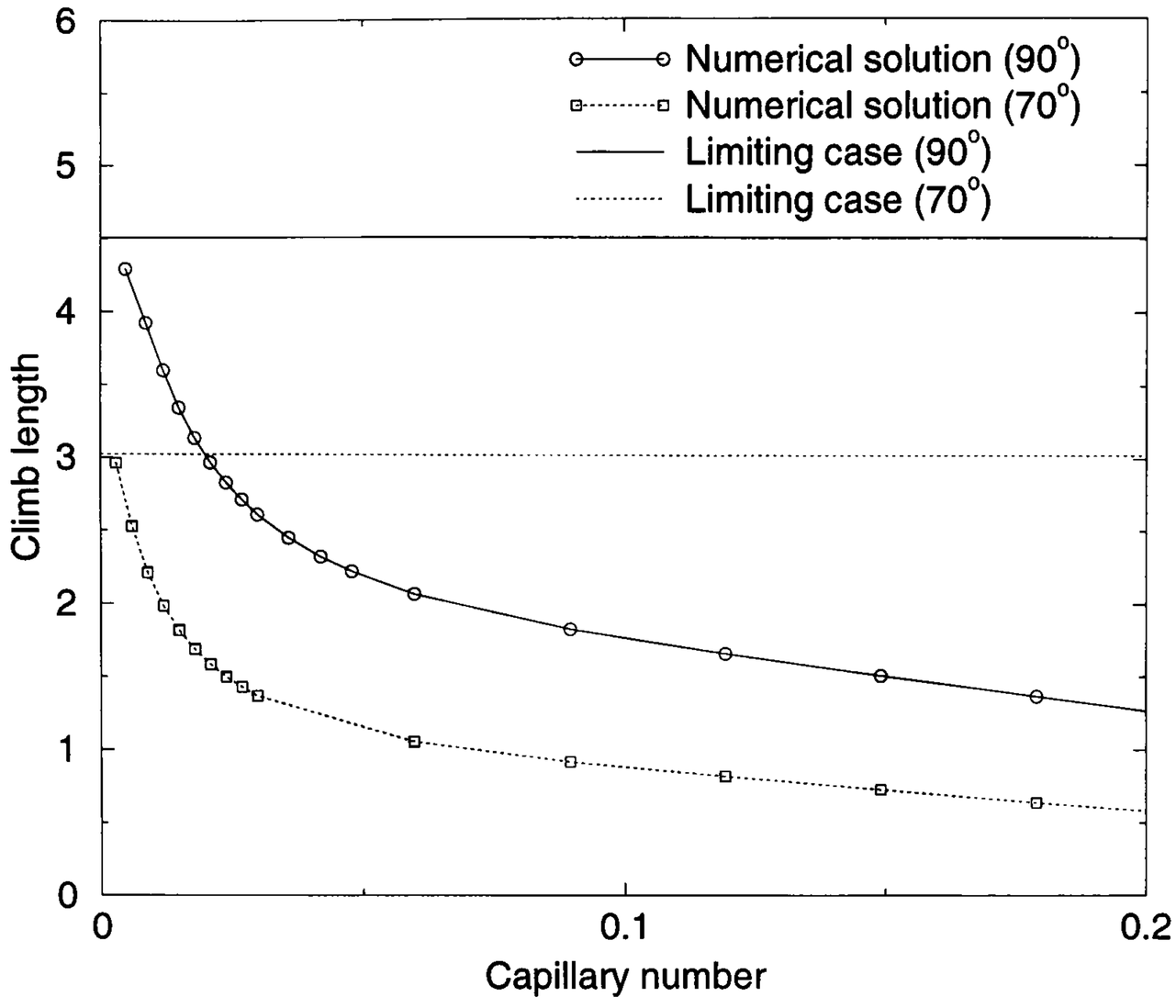

Figure 5.19: The effect of capillary number on the climb length. $R/H_0 = 250$, $\theta_c = 35°$, β as shown in figure.

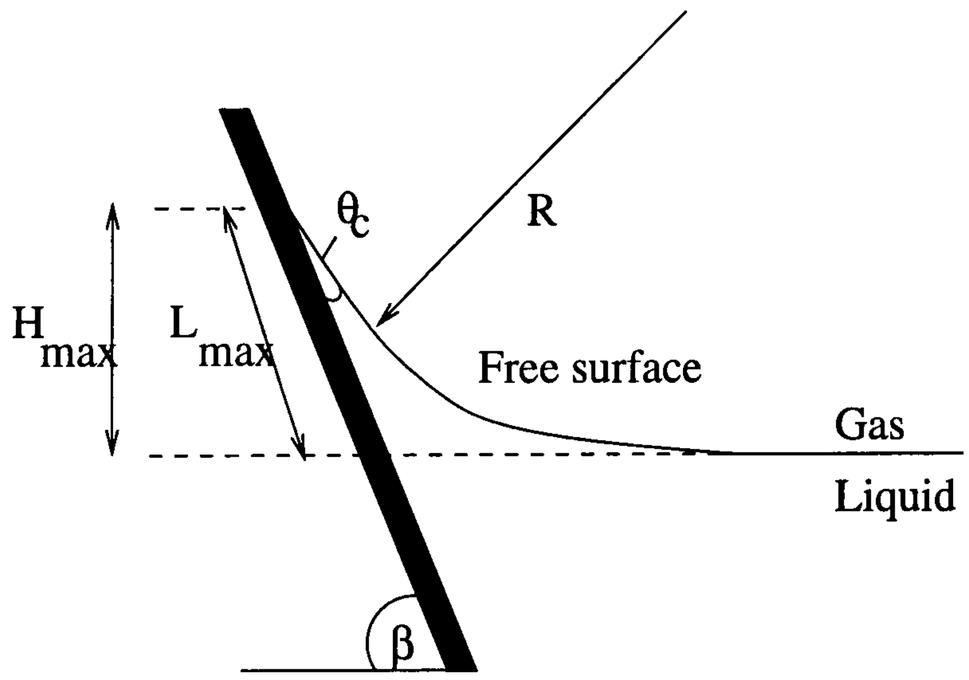

Figure 5.20: The limiting case of climb height up the face of the plate.

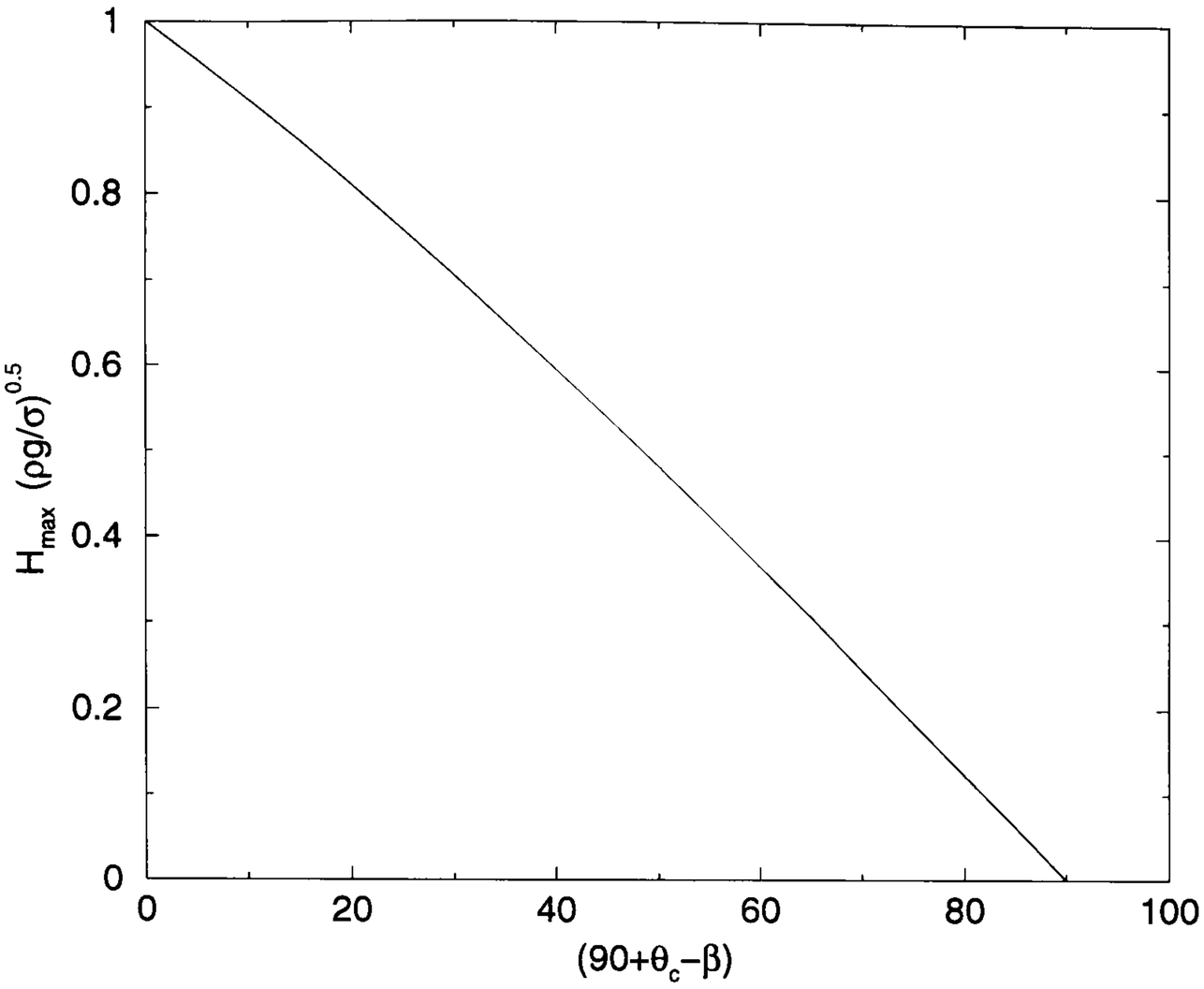

Figure 5.21: Graph showing the maximum climb height as a function of corner and contact angle.

5.7.2 The effect of corner angle on climb length

The corner angle of the plate plays an important role in determining the climb length of the meniscus, as clearly illustrated in the visualisations shown in figures 5.12 to 5.15. Figure 5.22 shows the effect of climb height as the corner angle, β, is varied for a constant capillary number of 3×10^{-3}, and figure 5.23 shows a range of streamline plots as the corner angle is reduced under the same set of conditions. The value of R/H_0 has been set at a large value to minimise the effect of roll curvature on the results to simplify the subsequent analysis.

Clearly as the corner angle is reduced the favourable condition of zero climb is approached. The limit of zero climb is best analysed using the Gibbs inequality (1906), which is a extension of the Young–Dupré equation. Oliver *et al.* (1977) confirmed the Gibbs inequality experimentally using a sapphire disk with a 90° angle, and to a lesser extent by using aluminium disks with a range of angles. Kistler

(1983) highlighted the effect of a sharp corner on the migration of the wetting line in a curtain coater, and expressed the Gibbs inequality as :

- contact line advance inhibited when

$$\theta \leq 180^\circ - \beta + \theta_A, \tag{5.51}$$

- contact line retreat inhibited when

$$\theta \geq \theta_R, \tag{5.52}$$

where θ_A and θ_R are the advancing and retreating contact angles respectively, and all other symbols take their usual meaning. Schweizer (1988) points out that in practice most coating fluids wet solids well, so θ_A and θ_R are relatively small although metals have a high surface energy and adsorb species quite readily, which can increase contact angle hysterisis significantly.

The value of the contact angle can be calculated for the case where the meniscus is pinned on the corner of the plate, as described in section 5.4.10. This solution, together with the values of the advancing and receding contact angle, can be used to determine whether the contact angle will climb the face of the plate, or whether it will retreat further into the gap. Once it has been established that the meniscus climbs the face, the static contact angle can be prescribed and the extent of the meniscus climb can be calculated (section 5.4.9). The effect of the contact receding into the gap is explored experimentally in section 5.7.4.

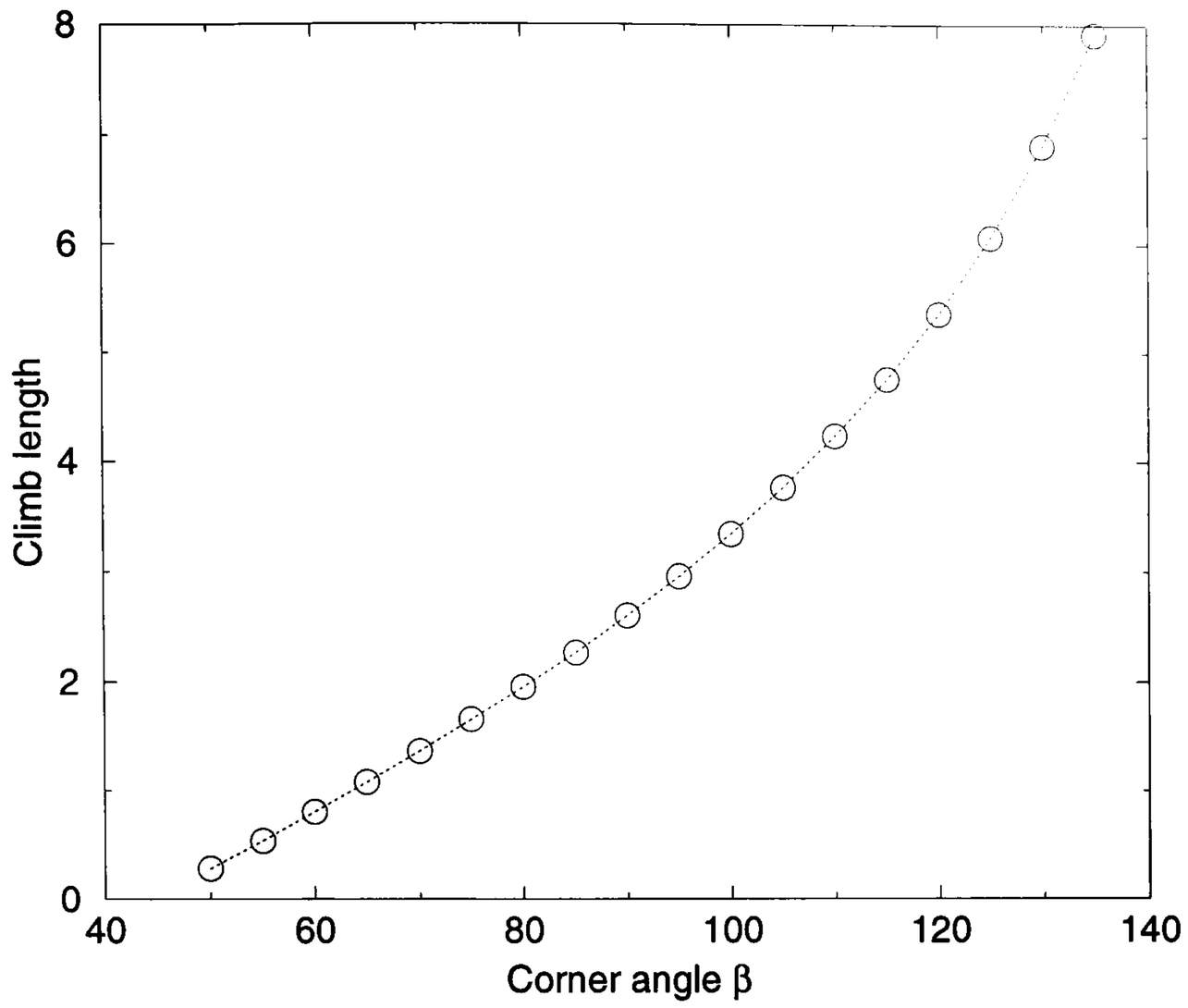

Figure 5.22: The effect of corner angle, β, on the climb length. $Ca = 3 \times 10^{-3}$, $R/H_0 = 10000$, $\theta_c = 35°$.

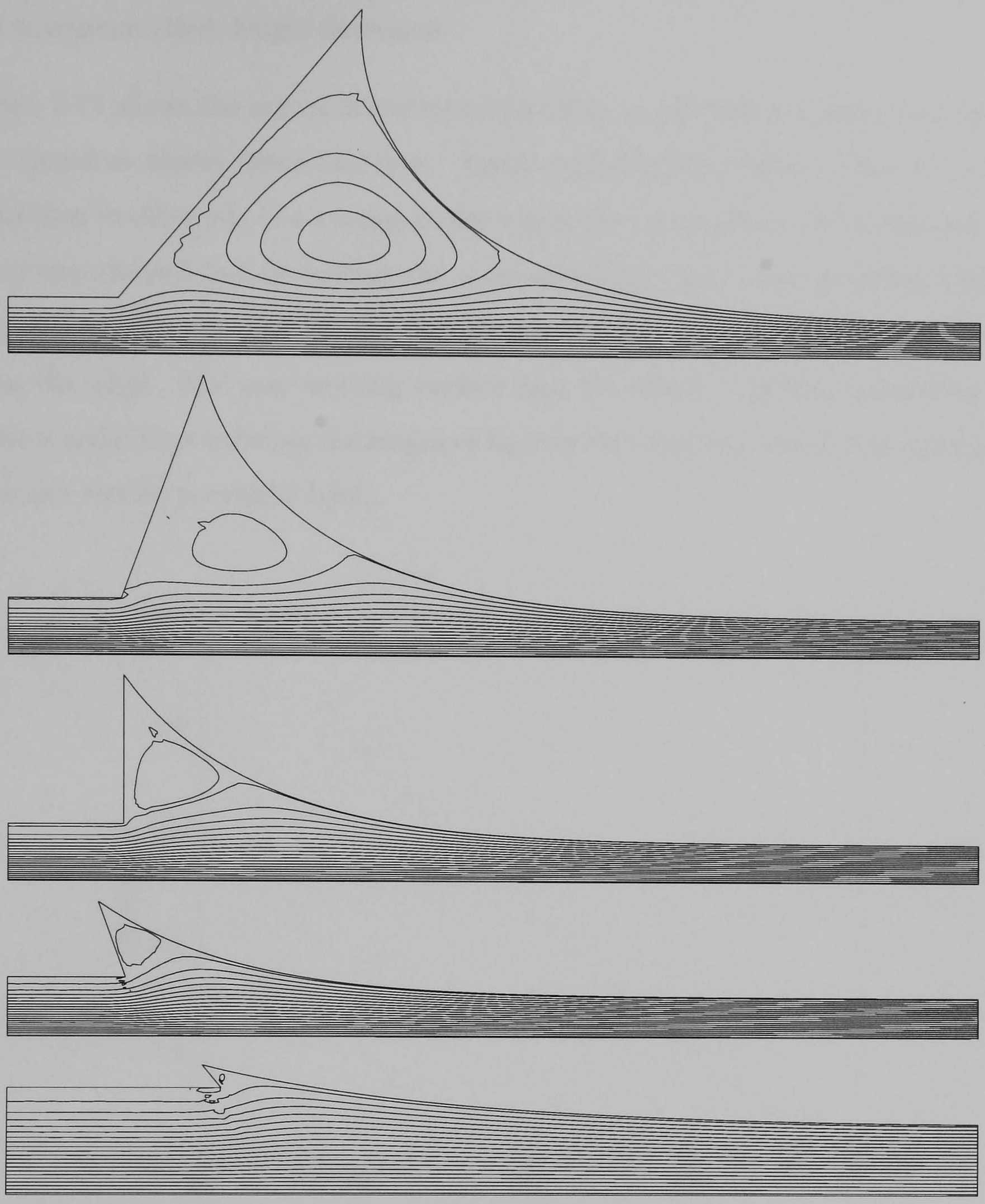

Figure 5.23: Streamline plots of the solution as the corner angle β is reduced from (top to bottom) $\beta = 130°, 110°, 90°, 70°$ and $50°$; with $Ca = 3 \times 10^{-3}$, $R/H_0 = 10000$, $\theta_c = 35°$.

5.7.3 The effect of contact angle on climb height

The static contact angle of the fluid/solid pair affects significantly the climb length of the meniscus — the effect of θ_c on the maximum climb height can be calculated from

equation (5.49) and is illustrated in figure 5.21 – as the contact angle is increased the maximum climb height decreases.

Figure 5.24 shows the extent of the meniscus climb; as the contact angle is increased the meniscus moves down the face. Kistler and Scriven (1994) observed similar behaviour in the study of a curtain coater where the underside of the lip was wetted. They also showed that by coating the underside with a non–wetting surface (Teflon tape, in this case) the contact line was almost completely prevented from advancing from the edge. The non–wetting surface had the effect of greatly increasing the contact angle thus reducing the length of lip that the bead wet, which is in agreement with the results presented here.

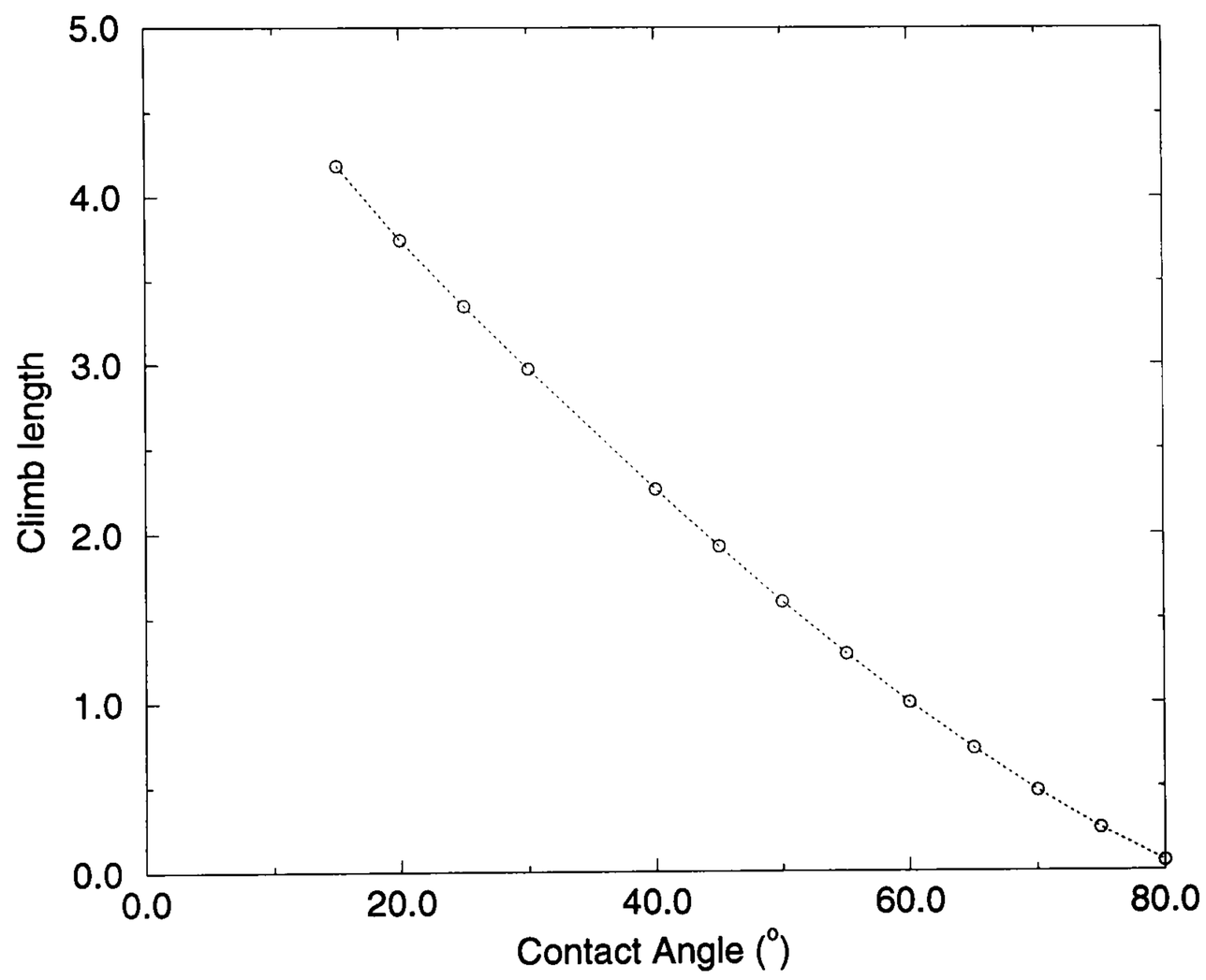

Figure 5.24: The effect of contact angle on the climb length. $Ca = 3 \times 10^{-3}$, $R/H_0 = 10000$, $\beta = 90°$.

5.7.4 The onset of the ribbing instability

In section 5.7.2 it was shown that two limits determine whether the contact line will pin to the corner of the plate, or if it will advance or recede away from this point.

It is now clear that when the contact line advances from the corner and up the face of the plate a recirculation exists in the flow in which bubbles or particulates can reside, giving rise to streaks or point defects on the final coated product.

Here the flow domain is varied so that the meniscus retreats away from the plate corner *into* the gap, so that the effect of a receding contact line may be investigated. This is achieved experimentally by moving the front face of the plate so it is positioned at positive X, instead of at $X = 0$ (as considered in the previous section), or by varying the gap.

Figure 5.25 shows the effect of advancing the front of the plate in the X–direction. With the face at $X = 0$ mm the meniscus is seen to climb the front of the plate. As the plate is advanced in an increasing X direction, the meniscus moves down the face of the plate until it pins on the corner when $X = 3$ mm. Advancing the plate past this point reveals that the meniscus remains pinned to the corner until $X = 5.5$ mm. Further increases in the X position of the plate give rise to the contact line un-pinning from the corner of the plate. For this to occur the contact angle has fallen below the limit given in equation (5.52). The contact line remains in the same location, even when the plate is advanced further, as it is no longer influenced by the geometry local to the corner. Similar behaviour was observed using the plate with a corner angle of 30°, however for $X = 0$ and all subsequent values, the meniscus does not climb the face of the plate, but instead remains pinned on the corner.

The effect of varying the gap also affects the position of the meniscus. With the plate positioned at $X = 0$ mm varying the gap affects the climb length up the face of the plate (for the corner angle of 90°), but no conditions are found where the meniscus pins at the corner, or retreats into the gap. To investigate the effect of changing the gap when the geometry allows the meniscus to un-pin from the corner, the front of the plate was first moved to $X = 3.5$ mm. At large gaps the meniscus is observed to climb the face as shown in figure 5.26. As the gap is reduced the meniscus moves down the face of the plate until pinned on the corner of the plate. A further reduction in the gap causes the meniscus to retreat towards the nip. This is due to the decrease in film thickness as the minimum gap is reduced, as illustrated schematically in figure 5.27. It is observed that with the contact line located in the

gap the ribbing instability could occur. Daniels (1998) analysed the stability of flow in a slot coater with the meniscus located in the gap between the roll and the underside of the slot.

An understanding of this effect may be gained by studying the stability hypothesis derived by Pitts and Greiller (1961) and Savage (1977b) which gives a sufficent condition for stability:

$$\frac{d}{dX}\left(P+\frac{\sigma}{R}\right)<0,$$
$$\text{or} \qquad \frac{dP}{dX}-\frac{\sigma}{R^2}\frac{dR}{dX}<0, \tag{5.53}$$

where R is the radius of curvature of the meniscus.

Consider now the case shown in figure 5.28. This is a similar geometry to that considered by Fall (1978,1982) who showed experimentally, and went on to analyse, the ribbing instability that can manifest itself in such an arrangement. The radius of curvature of the meniscus can be related to the height at film split; assuming an arc of a circle can be used to represent the meniscus then, using equation (5.53), the stability hypothesis can be written as

$$\frac{dP}{dX}-\frac{1}{1-\sin\left(90+\theta_c-\beta\right)}\frac{\sigma}{H^2}\frac{dH}{dX}<0, \tag{5.54}$$

for the onset of the ribbing instability. The gradient $\frac{dH}{dX}=\frac{\pi}{180}(180-\beta)$, and so $\frac{dH}{dX}$ increases as $\beta\rightarrow 90°$ (with $\beta<90°$).

As the corner angle, β, is reduced from a value initially greater than 90° (as in Fall's study) then

$$\frac{dH}{dX}\rightarrow\infty \text{ as } \beta\rightarrow 90°,$$

and the condition given by equation (5.54) will always be satisfied, so with a meniscus that climbs the face (and $\beta\leqslant 90°$) or when the meniscus is pinned on the corner of the plate the film will always be stable to the ribbing instability.

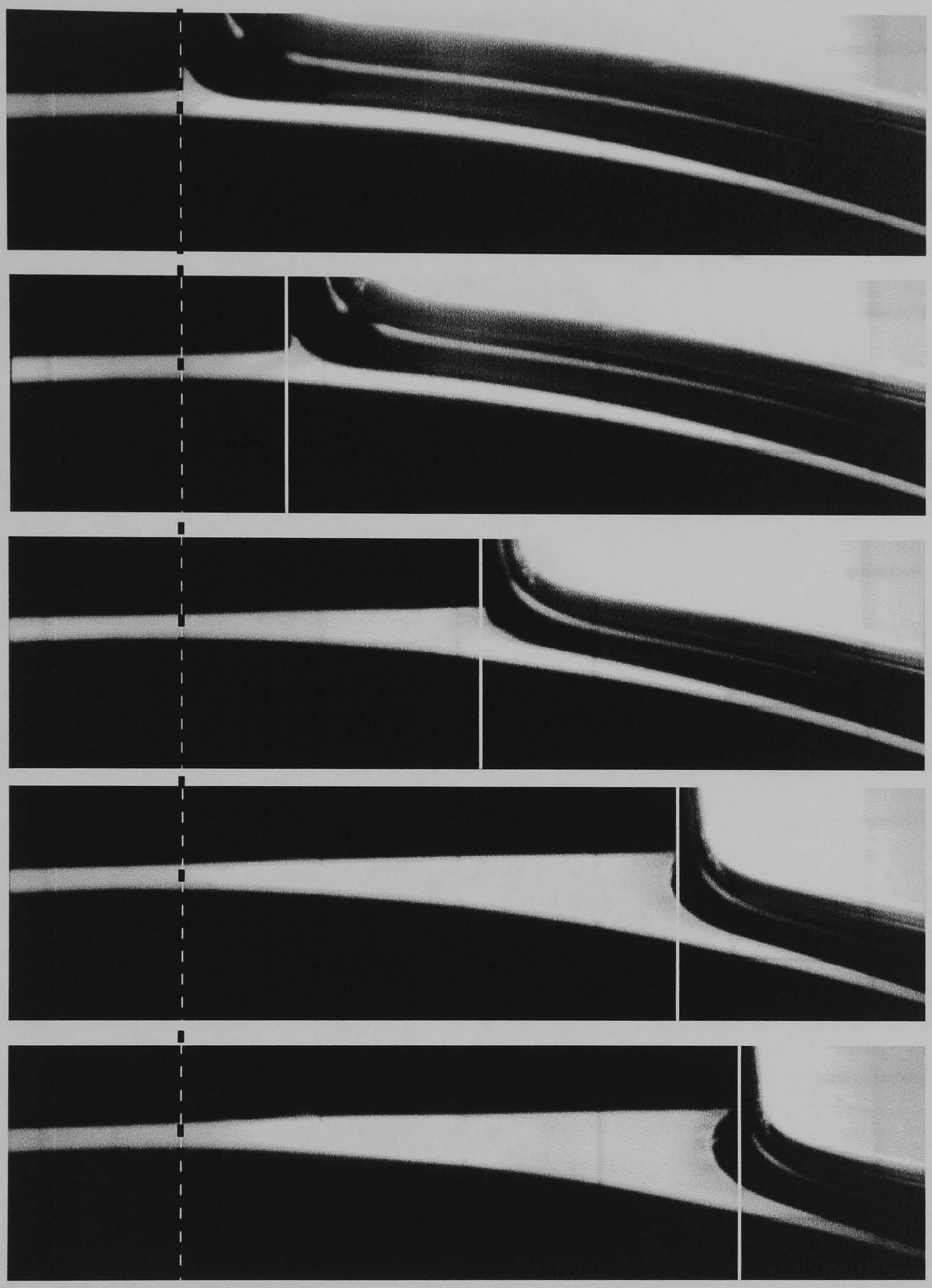

Figure 5.25: The effect of advancing the front of the plate on the position of the wetting line. Plate positioned (from top to bottom) at $X = 0, 1, 3, 5.5, 6$ mm, the dotted line indicates the position $X = 0$ mm , the solid line indicates the location of the front of the plate. Gap $H_0 = 200\mu$m, $Ca = 0.15$.

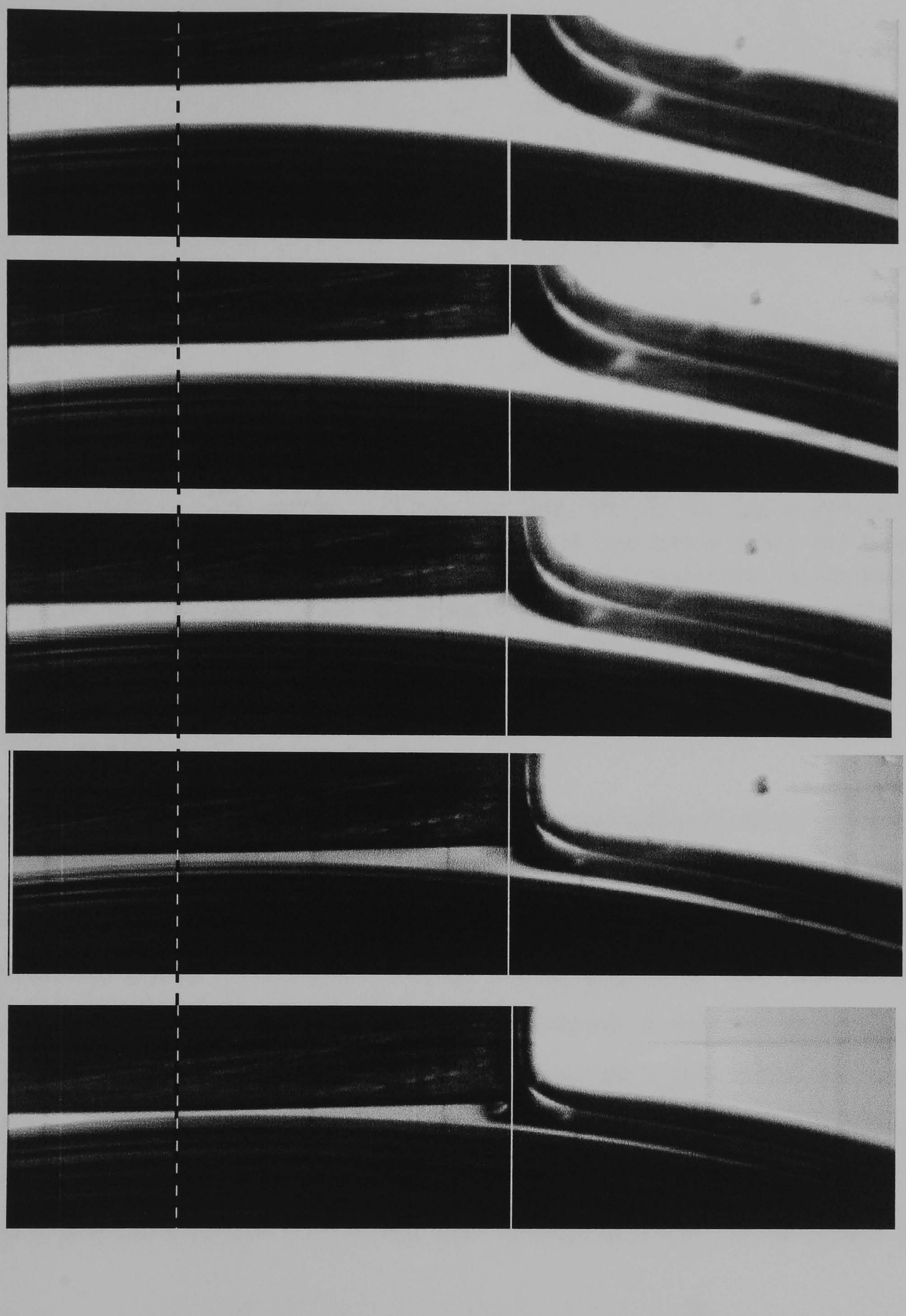

Figure 5.26: The effect of reducing the gap on the location of the wetting line. Front of plate positioned at $X = 3.5$ mm. Gap set at (from top to bottom) $H_0 = 0.4, 0.3, 0.2, 0.10.05$ mm, $Ca = 0.15$.

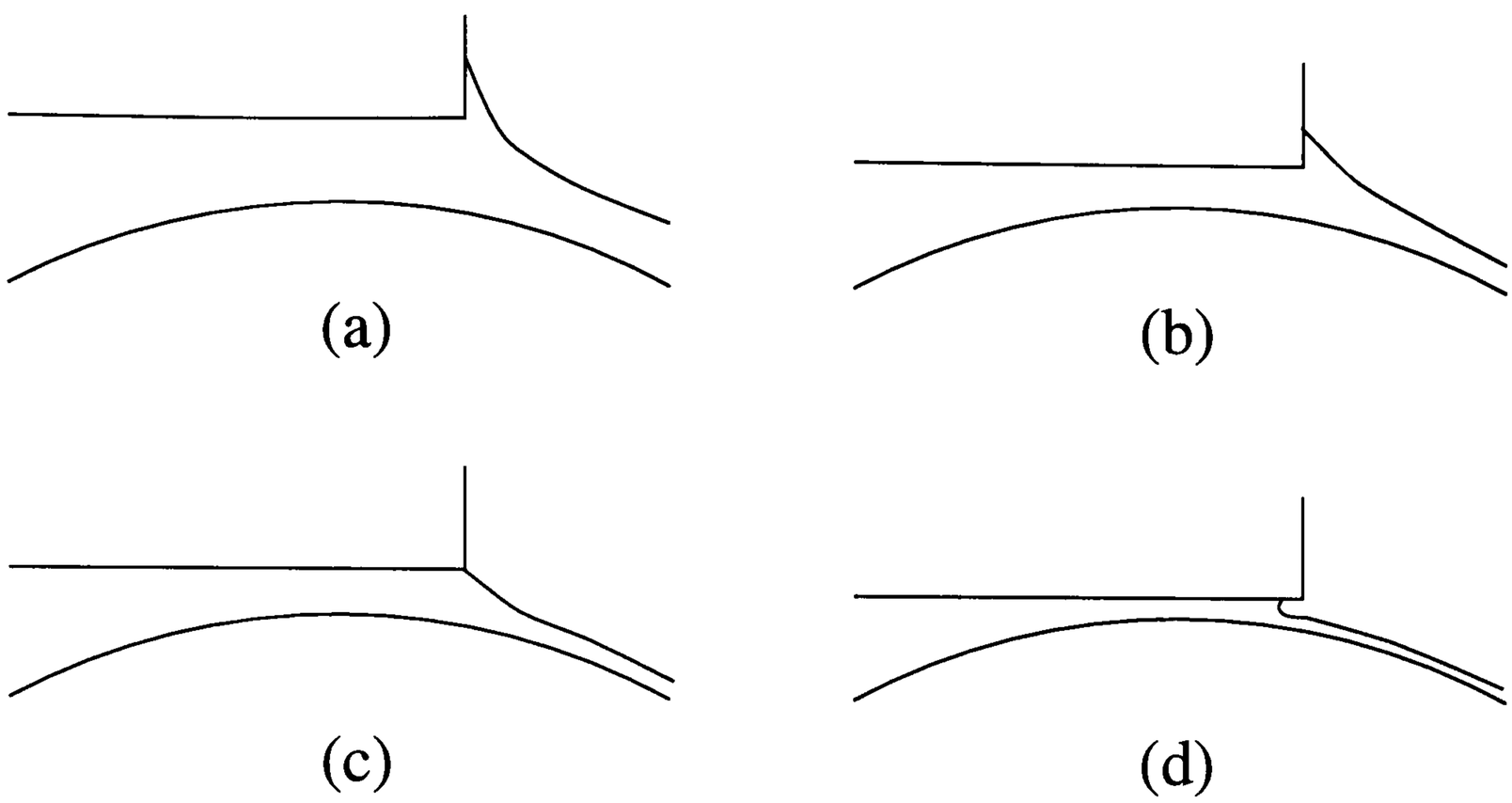

Figure 5.27: (a) The meniscus climbs the face. (b) As the gap is reduced the flux decreases and the contact line moves down the face until (c) it pins on the corner. Further reduction in the film thickness causes the contact angle to fall below the receding angle (equation (5.52)), and the contact angle moves away from the corner (d), such that it is positioned on the underside of the plate with a contact angle θ_c.

A similar mechanism could be responsible for the suppression of ribs in forward roll coating by placing a wire in the nip, first highlighted by Hasegawa and Sorimachi (1993) and investigated experimentally in some depth by Decré *et al.* (1996). Figure 5.29 shows a typical cross section through the coating bead, with each meniscus pinned to the wire. Each contact line is free to recede or advance its location on the wire. Decré *et al.* (1996) observe that, starting with a ribbed film, as the wire is advanced into the gap the formation of the two independent films pinned to the wire cause the film to stabilise. However, as the wire is moved further the two contact lines meet on the front of the wire to recreate a free ribbed surface with

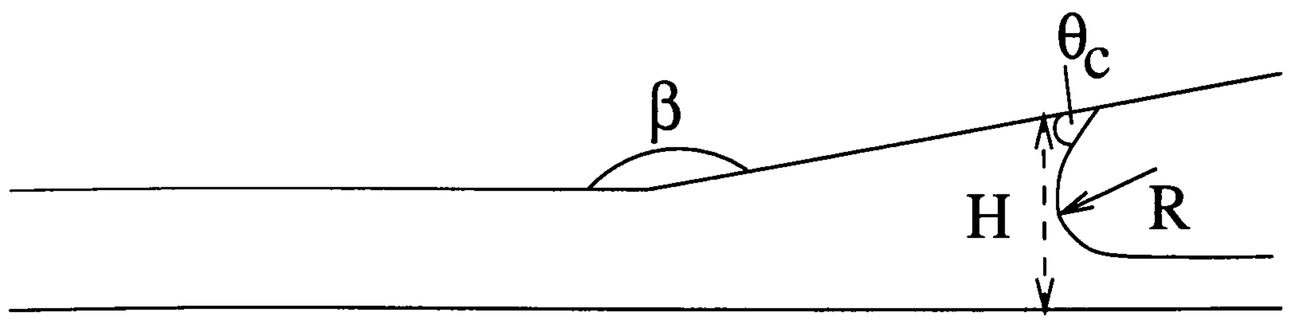

Figure 5.28: Cross section of the spreader investigated by Fall (1978, 1982).

the wire fully immersed. The stability of each meniscus and corresponding moving roll surface must be considered separately, as once the two have met the work of Decré *et al.* (1996) show the wire plays no further part in stabilising the film. Each meniscus makes a (static) contact angle of θ_C with the wire. As conditions vary and the contact line moves towards the front of the wire then, as in the meniscus climb problem, $\frac{dH}{dX}$ increases and at the leading edge of the wire

$$\frac{dH}{dX} \rightarrow \infty, \tag{5.55}$$

and, again, the condition for stability given by equation (5.54) will always be satisfied.

One interesting feature of this system is that just one of the films may become ribbed whilst the other remains stable. This could occur when the flow conditions give rise to a large pressure gradient at one meniscus and not the other, for example when the wire is positioned nearer one roll than the other, or when the rolls are running at different speeds.

The gradient of the height between the string and the roll, $\frac{dH}{dX}$, is finite (but positive) until the meniscus is positioned at the very front of the wire. Hence the condition given by equation 5.54 could be satisfied and just one film emerge ribbed. A wire with a large diameter would promote this situation as this reduces the stabilising effect due to the geometry — $\frac{dH}{dX}$. In fact, just such a result has been observed by Decré (1994).

5.8 Summary

A number of conclusions may be drawn from this work :

- The full numerical solution to the Navier Stokes equation provides a fair representation of the physical system, with the experimental and theoretical results for flux in close agreement and the climb length data in reasonable agreement.

- The Gibbs inequality in conjunction with a numerical solution for the menis-

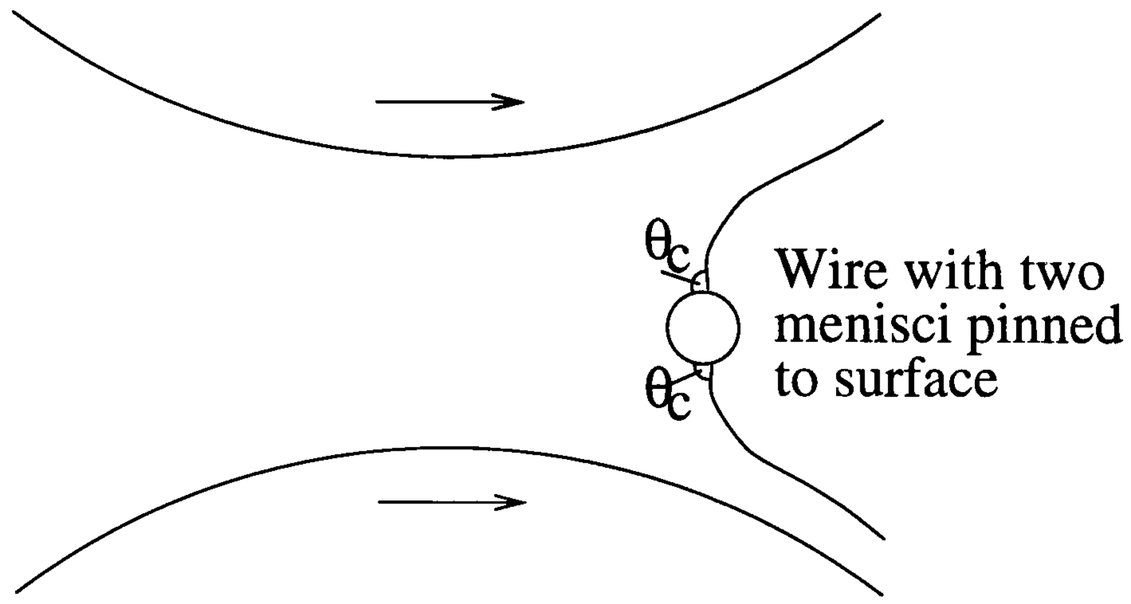

Figure 5.29: The suppression of ribs by the location of a wire in the nip of a forward roll coater.

cus pinned to the downstream corner may be used to determine whether the contact line will migrate up the face of the plate or recede into the gap.

- The climb of the meniscus up the face of the plate, and the associated eddy near the contact line could well be one source of streaks formed in knife coating, due to the entrapment of small particles in a closed eddy.

- A proven method of pinning the meniscus on the corner to prevent the climb action is to cut back the corner sharply, a second method would be to cover the face of the knife with a hydrophobic coating so that the contact angle is greatly increased.

- An upper limit to the climb height at zero capillary number is given by a balance of the surface tension and the hydrostatic head of the meniscus.

- The receding of the contact line into the gap provides the necessary conditions that can give rise to the ribbing instability. With the meniscus pinned on the downstream corner the ribbing instability is suppressed.

Chapter VI

Offset gravure and kiss coating

Contents

6.1 Introduction

This chapter is concerned with both the pre–metering of a film onto a smooth roll, and the subsequent transfer of the fluid film from the roll to the web using kiss coating.

Kiss coating is used in a number of coating operations to transfer fluid from a doctored roll to a moving web. The web is held against the roll with a tension T and a wrap angle β. Considered here, as is common in many industrial situations, is the case where the web and roll are running in opposite directions. Methods of pre–metering fluid onto the roll can include forward or reverse roll coating, but more typically offset gravure coating as this can be used to produce very thin films (10 μm and less) The arrangement of the twin roll and offset gravure systems in relation to the kiss coating bead are illustrated in figure 6.1.

Although offset gravure is a common technique for doctoring a film little is known about the process. Here forward offset gravure coating is considered, although it can also be used in reverse mode. Rees (1995) showed, qualitatively, that for a fixed speed of the metering roll, decreasing the speed of the gravure roll caused the film thickness, H_i, to increase to a maximum before it reduced. Rees also showed that as the force nipping the two rolls together was increased the metered film thickness decreased. This feature of being able to influence the film thickness over a wide range is one of the reasons why offset gravure is often used instead of direct gravure. Hanumanthu and Scriven (1996) showed experimentally that the film thickness characteristics of a forward offset gravure nip agreed qualitatively with those of smooth roll coating.

A kiss coater operating at $S < 1$ (where $S = U_1/U_2$ — see figure 6.2) is a self metering process in that, as the speed of the web is varied, the total flux of fluid deposited on the web varies. Rees (1995) used lubrication theory and incorporated a model for a fully flexible web to predict the thickness of fluid laid down onto the substrate. Storey (1996) extended this theory to include more realistic boundary conditions and web stiffness, although he showed this to be small in many practical situations. Further details of the lubication models derived by Rees and Storey

can be found in Gaskell *et al.* (1998b). Storey (1996) also presented a numerical solution to the problem using a Galerkin finite element formulation of the Navier-Stokes equations for the fluid flow in two dimensions incorporating a fully flexible web into the model.

Distinct from a self metering kiss coater operating at $S < 1$ is a kiss coater operating at $S > 1$ (figure 6.3). The latter is a pre-metered process as all fluid is transferred from the roll to the web due to the web touching the roll. Experimental evidence for this is given by Rees (1995) and also confirmed as part this study. For $S > 1$ experiments show that as speed ratio is increased (i.e. a thinner fluid film is layed on the web) a point is reached where disturbances in the puddle due to ribbing at the upstream meniscus (located at X_U, as shown in figure 6.3) causes loss of quality in the metered film, and hence a lower limit to the final film thickness, H_1, that may be deposited on the web.

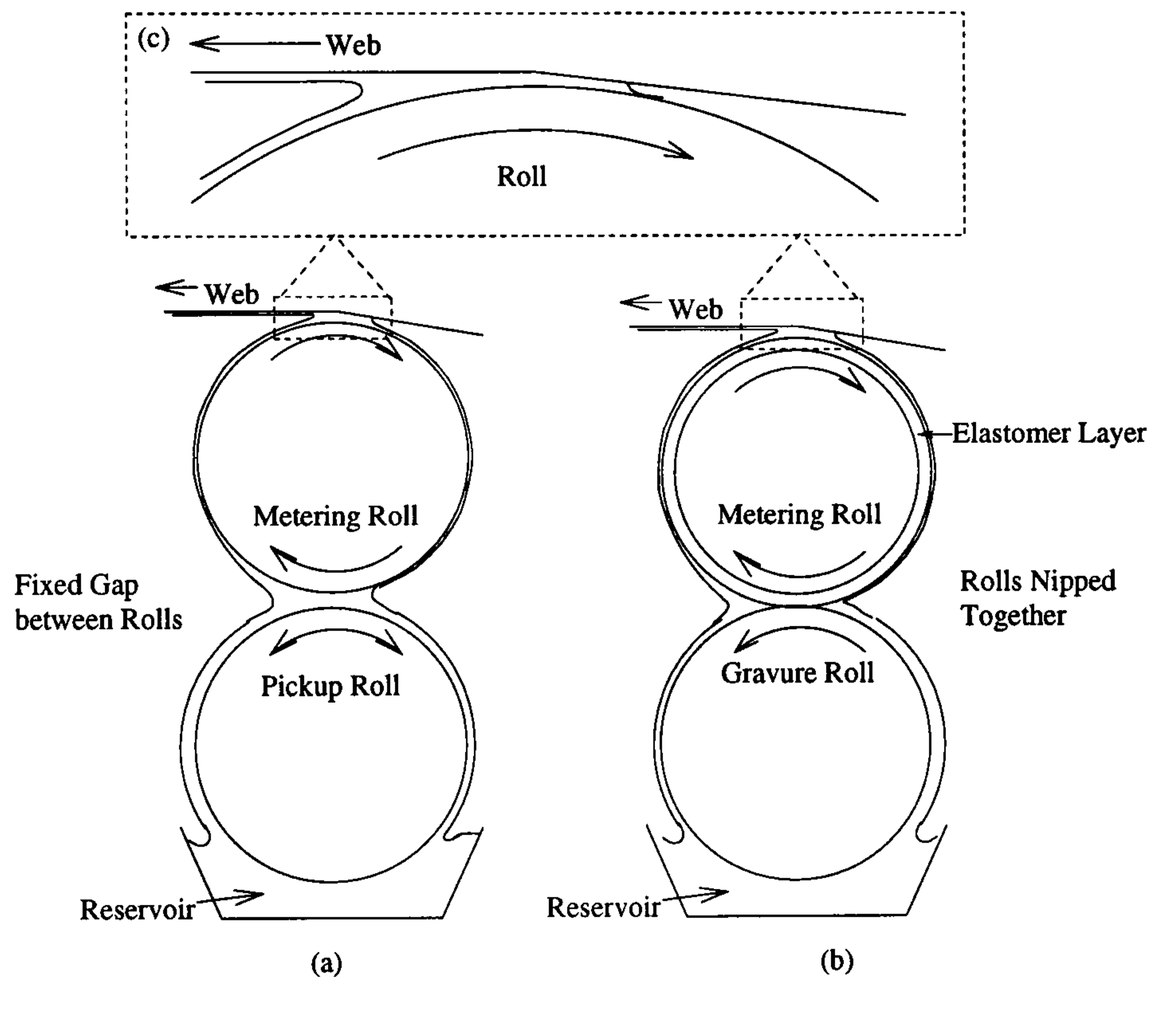

Figure 6.1: Methods of doctoring the incoming film using (a) forward or reverse coating, or (b) offset gravure coating. (c) is the kiss coating bead.

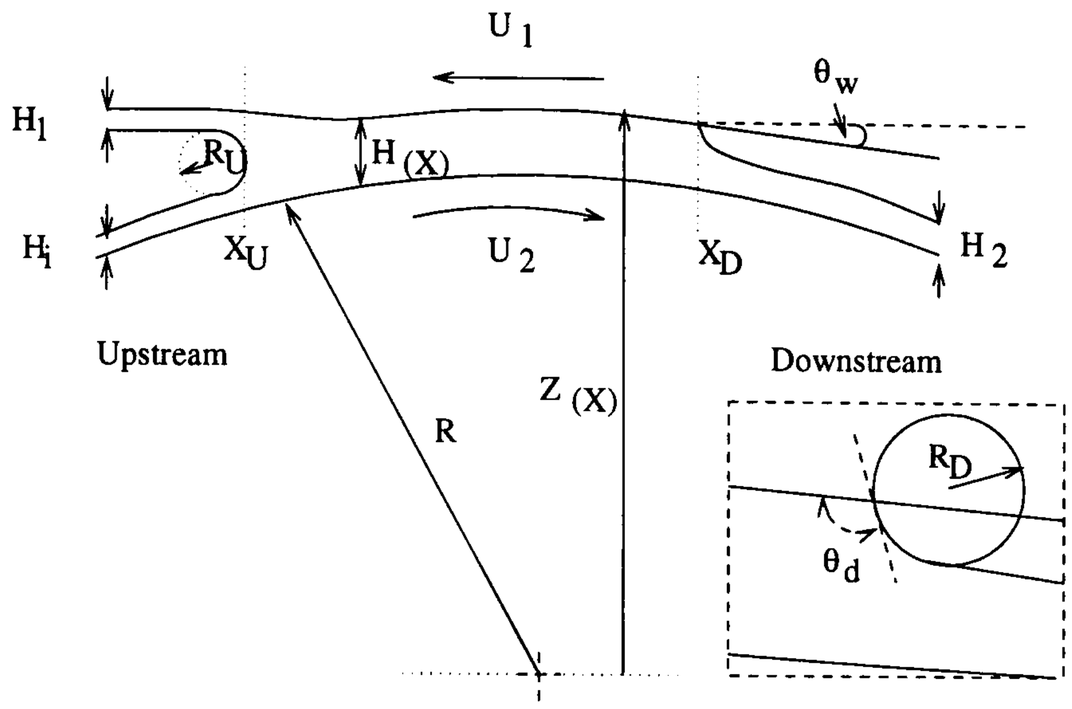

Figure 6.2: A kiss coater operating with $S < 1$, Rees (1995), Storey (1996).

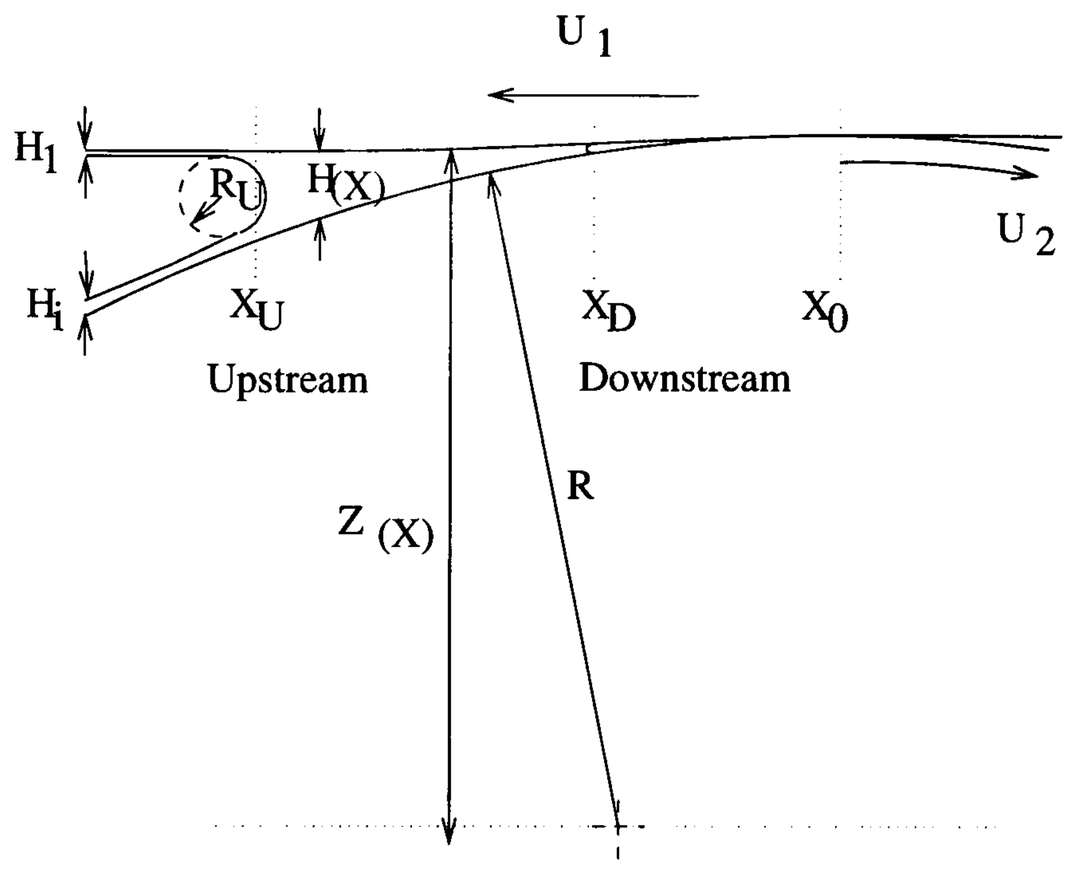

Figure 6.3: A kiss coater operating with $S > 1$ where the web makes contact with the roll.

6.2 Motivation

This chapter describes a study involving an offset gravure system consisting of (i) a nip region where both rolls have the same speed, U_2, in the forward mode of

operation and (ii) a kiss coating bead where fluid is transferred from the roll to the web running at speed U_1 such that $S > 1$ where $S = U_1/U_2$. The feature linking the two systems is that the offset gravure meters the inlet film, H_i, to the kiss coating bead.

The offset gravure action is considered experimentally, with the film thickness on the metering roll measured as a function of speed and nip pressure. In a kiss coater, operating at $S > 1$, determination of the final film thickness is trivial when the inlet film thickness and speed ratio are known since $H_i = SH_1$. However, the onset of ribbing is a key feature as it determines an upper bound to the speed ratio, and a lower bound for the final film thickness. A series of visualisations show the effect of speed ratio on the length and position of the fluid bead. Also presented is an experimental investigation into the onset of ribbing.

Two analytical models are derived for the steady flow in the kiss coating bead; the first assumes that the tension in the web is so high that the shape of the fluid domain can be described simply by a roll–flat plate geometry, whereas the second model allows for bending of the web due to the effect of fluid pressure. For both models a simple stability criterion is used to derive a necessary condition for stable flow.

6.3 Experimental investigation

6.3.1 Experimental method

Experiments were carried out on the pilot apparatus described in section 2.3. Briefly, a carriage that holds the deformable metering roll and the gravure roll in position is mounted below the web. The gravure roll sits in a reservoir of fluid such that as it rotates it entrains a thick film up to the nip region where the metering roll is pressed against the gravure roll. No doctor blade is used in this arrangement such that the inlet to the deformable/gravure roll pair remains fully flooded, with some fluid running back into the reservoir.

μ	1×10^{-3}	Pa s
σ	33.0×10^{-3}	N/m
ρ	992	kg m^{-3}

Table 6.1: Physical properties of the test fluid used in offset gravure and kiss coating experiments.

Five pneumatic cylinders sit beneath the carriage on which the gravure roll is mounted, allowing the 'nip force' between the two rolls to be controlled. In this study, the deformable/gravure pair were always driven at the same speed (U_2) as the motors were not powerful enough to drive the rolls at differential speeds, with speeds U_2 in the range of 4 to 70 m/min.

Four gravure rolls of diameter 0.05 m were used, one quadrangular roll with a cell count of 60 lpi, and three laser engraved ceramics with cell counts of 60, 100 and 200 lpi. Further details of these rolls can be found in section 2.3.2. The elastomer covered roll had a total diameter of 0.05 m, having a deformable layer of 10 mm thickness and nominal hardness of 70 shaw.

The web passes over the deformable roll in reverse mode at a speed U_1 in the range 5 to 75 m/min and the tension in the web (between 500 and 2000 N/m) controlled by the relative speeds of the unwind and rewind rolls. A thin Melinex web with a thickness of 23 μm was used throughout the experiments, to minimise any stiffness effects.

A fluid with the properties shown in table 6.1 was used in the experiments. The water/surfactant (Syperonic N) mixture was chosen as it is representative of typical coating fluids used in industrial offset gravure and kiss coating systems.

The first study concerned a deformable/gravure roll pair. The web was removed and a single scraper blade positioned against the top roll such that the metered film thickness H_i could be measured (see section 2.5). The three parameters varied were (i) the nip force, (ii) the gravure type and (iii) the speed of the two rolls (U_2).

Secondly, a study of the kiss coating bead was made. Here the speed U_2 of the gravure and deformable roll was pre–set and the speed ratio U_1/U_2 varied (by altering

the web speed) until the onset of ribbing occurred.

The bead was observed by using a CCD camera aligned directly above, looking down through the transparent substrate. Lighting the menisci, particularly at the downstream end, to give a good contrast with the surroundings proved difficult due to the small size of the menisci at the film split point. A 150 W halogen light source, fitted with fibre optic light guides, was used for this purpose.

For a given speed, U_2, the inlet film thickness H_i to the kiss coating bead is known for a particular gravure roll and nip pressure from the data acquired of the first study.

6.3.2 Offset gravure metering – results and discussion

The nip force

Figures 6.4 to 6.6 show the dependence of the film thickness H_i on the nip force for the three ceramic rolls and two roll speeds. As the nip force is increased the film thickness decreases for all the different gravure rolls, although the trend becomes less apparent for the 200 lpi laser engraved ceramic roll — as illustrated in figure 6.6 — due to the larger relative error when measuring such thin films. These results are in accord with the findings of Rees (1995) who also highlighted such variation of film thickness with nip force.

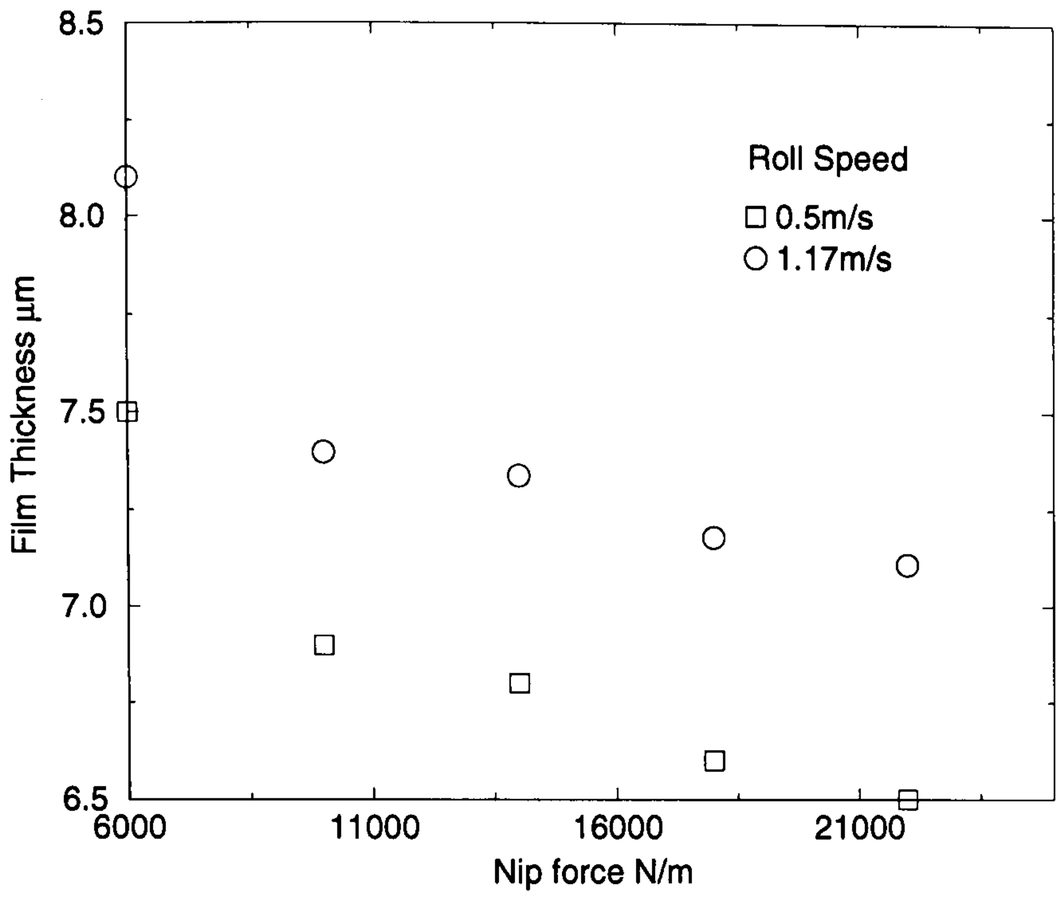

Figure 6.4: Dependence of the film thickness on the nip force for a 60 lpi laser engraved roll. Fluid properties as shown in table 6.1, roll radii 0.05 m.

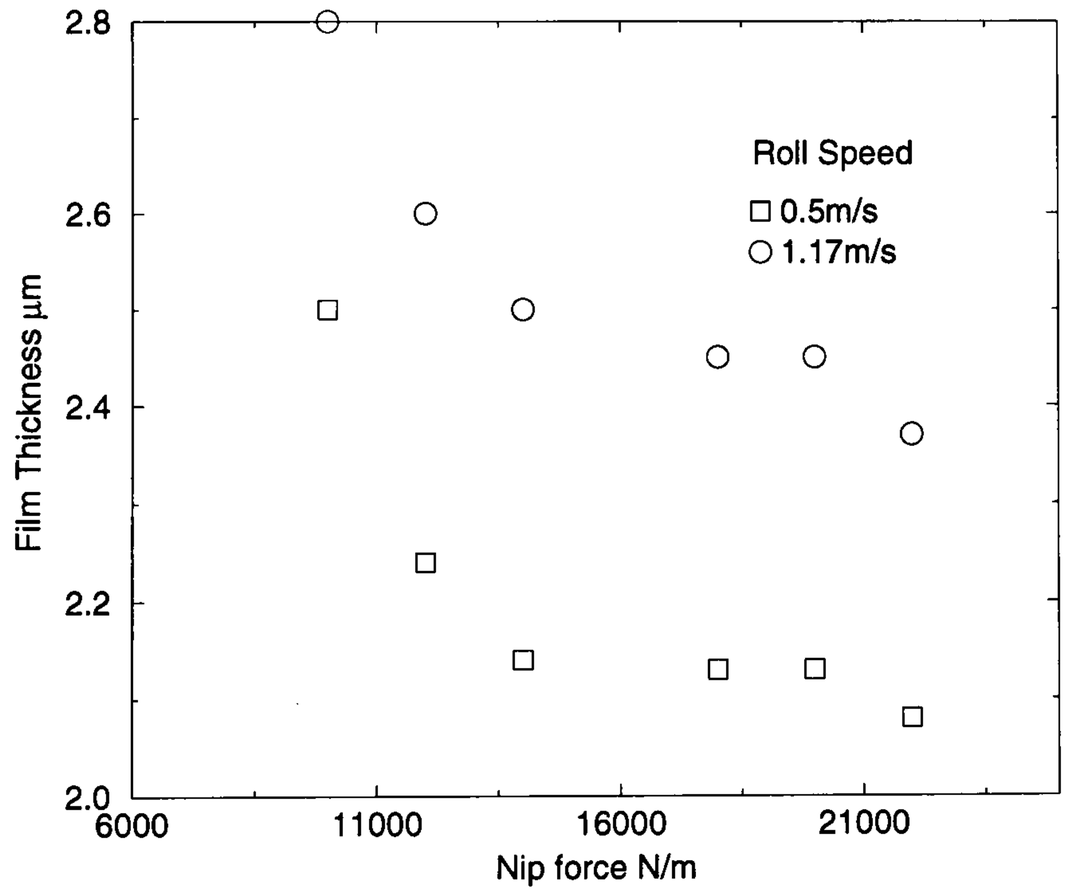

Figure 6.5: Dependence of the film thickness on the nip force for a 100 lpi laser engraved roll. Fluid properties as shown in table 6.1, roll radii 0.05 m.

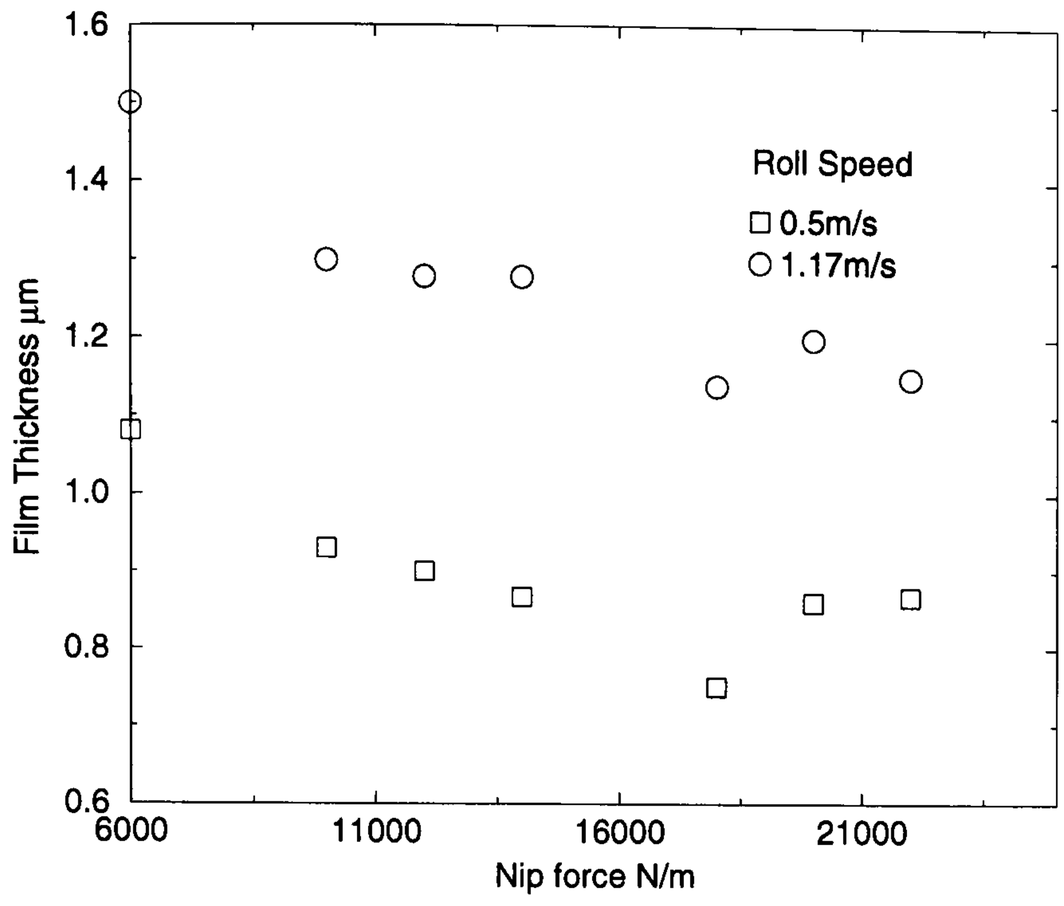

Figure 6.6: Dependence of the film thickness on the nip force for a 200 lpi laser engraved roll. Fluid properties as shown in table 6.1, roll radii 0.05 m.

Speed U_2 of the two rolls

Figure 6.7 shows the effect of the roll speed on the film thickness, H_i, leaving the offset gravure nip. This film ultimately forms the inlet film to the kiss coating bead. The speed ratio of the metering/gravure roll is fixed at one throughout this study. For all gravure patterns the film thickness increases with the roll speed; the greatest rate of increase is at low roll speeds. At typical speeds used in industrial situations the film thickness will be relatively insensitive to small changes in the roll speeds.

In figure 6.8 the film thickness data is re-plotted as fractional pickout defined as

$$\text{Fractional pickout} = \frac{\text{Flux leaving on metering roll}}{\text{Flux entering on gravure roll}} = S_{\text{offset}} \frac{H_i}{V_c} \qquad (6.1)$$

where $S_{\text{offset}} = 1$ here, H_i is the film thickness on the deformable roll and V_c is the the volume of cells per projected surface area of the roll. A more detailed discussion of this parameter can be found in section 7.1.1, and the data for V_c found in table 2.2. Clearly, as the roll speed is increased the fractional pickout also increases before

levelling off, as expected. The pickout for the 60 lpi ceramic roll is highest, followed by the 60 lpi quadrangular roll and then the smaller cells – the 200 lpi and 100 lpi laser engraved rolls. The 200 lpi laser engraved roll has a higher pickout than the 100 lpi laser engraved roll; this could be due to the higher aspect ratio (diameter of cell opening/depth of cell) (table 2.2). However, this is clearly not the only factor that defines the pickout characteristics since the 200 lpi laser engraved ceramic roll has a larger aspect ratio than even the 60 lpi laser engraved roll yet has a lower pickout. Other factors that could be important in determining the pickout are the physical size of the cell ,the area of cell opening per area of roll surface and the exact shape of the cell.

Clearly the dependence of the pickout on the geometry of the cells is a complex phenomena, something that is also observed in direct gravure coating systems as discussed in the next chapter.

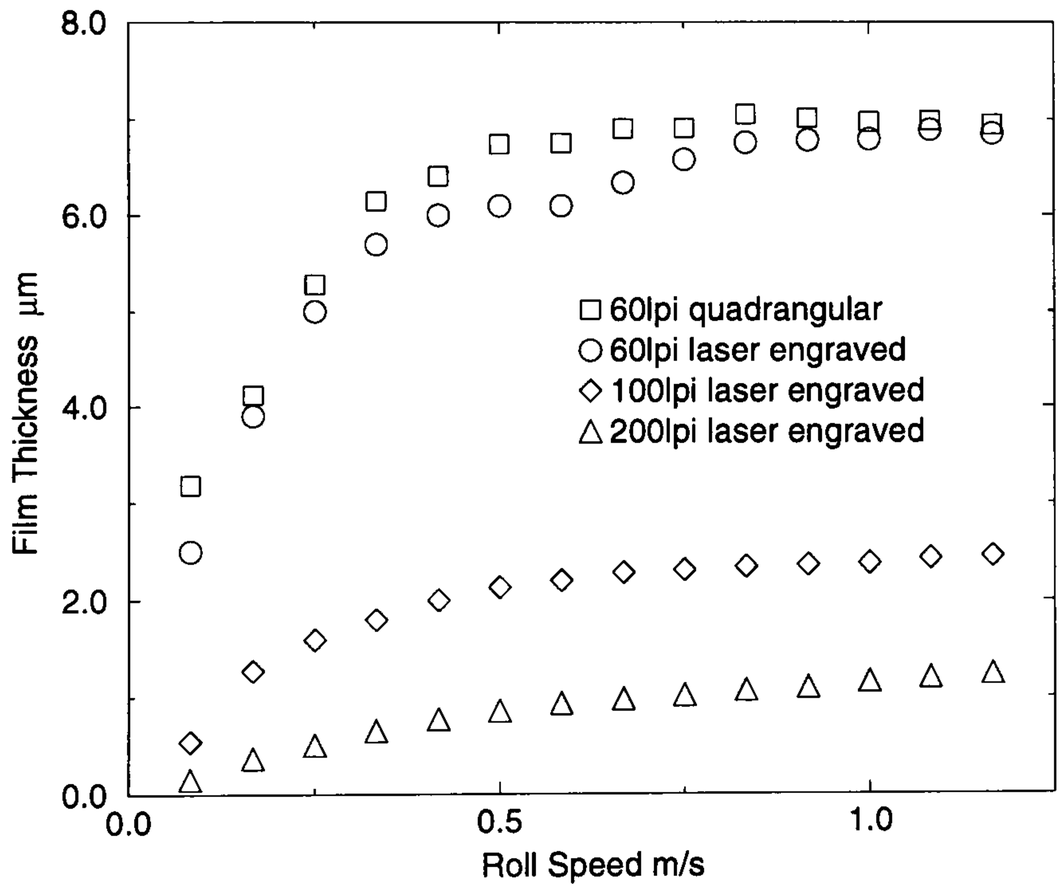

Figure 6.7: Film thickness H_i as function of roll speed for 4 different gravure patterns in offset gravure. Fluid properties as shown in table 6.1, nip force 21000 N/m.

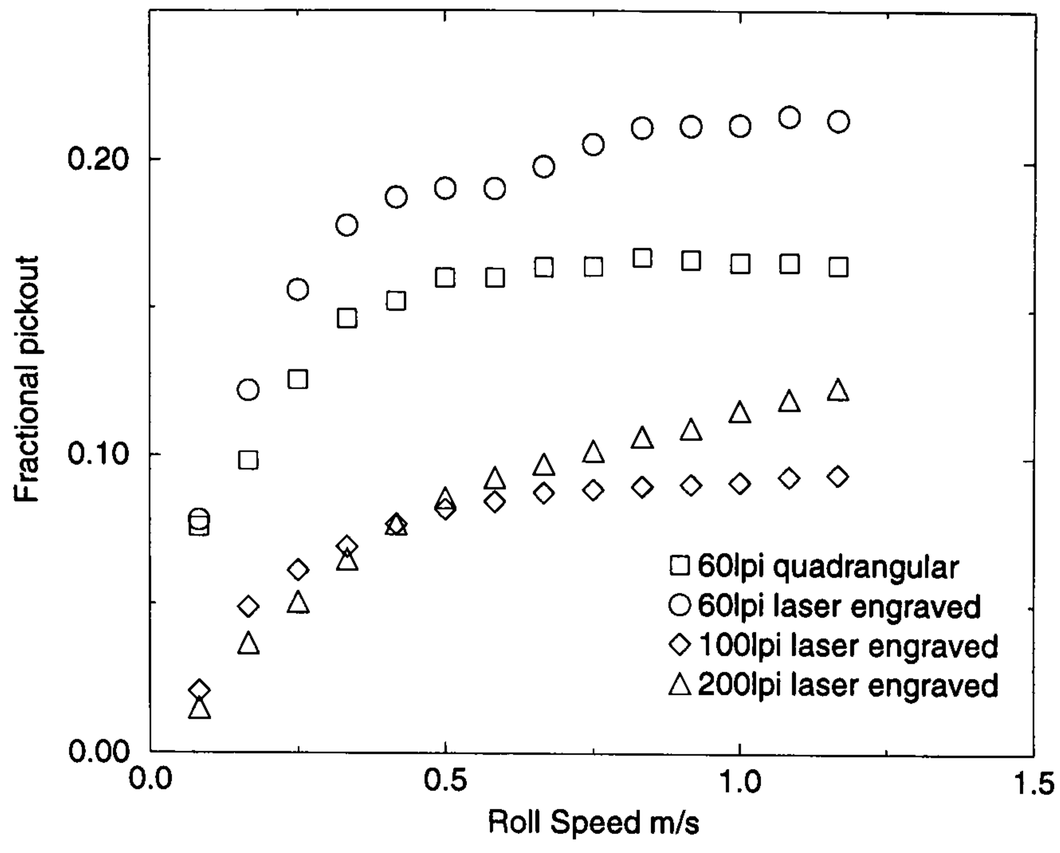

Figure 6.8: Fractional pickout from the gravure cell as a function of roll speed for 4 different gravure patterns in offset gravure. Conditions as per figure 6.7.

6.3.3 The kiss coat bead – results and discussion

Verifying the complete removal of the film

Prior to any investigation it was first necessary to verify the observation that at $S > 1$ all the fluid entering the kiss coating bead *via* the roll was removed by the action of the web. An absorbent tissue pad was pressed against the roll leaving the coating bead. At $S = 1$ a small residual film was detected on the roll, indicating that the fluid had not been removed completely from the roll surface. As the speed ratio was increased to $S = 1.1$ all the fluid was removed from the roll surface by the action of the web, as noted by Rees (1995).

Further evidence for the web and roll coming into contact was given by examining the roll surface after it had been in use for several tests. The width of the web was 0.1 m compared to a roll width of 0.2 m. Where the web had been run over the roll surface a distinct contrast in colour could be observed as shown in figure 6.9, and the roll surface had a slighly different texture, similar to that observed when a

rubber roll is ground using a fine grinding wheel.

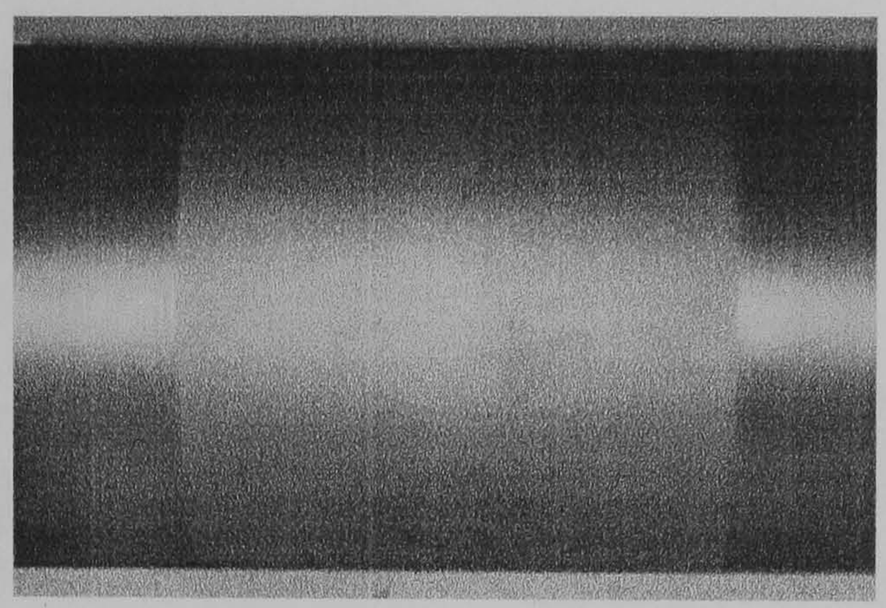

Figure 6.9: A photograph of the (dry) roll surface after using in the kiss coating ($S > 1$) tests. The matt region in the centre of the roll clearly shows where the web and roll have contacted.

Flow visualisations of the bead

Figure 6.10 shows a typical set of visualisations of the kiss coating bead taken by looking directly from above, through the transparent web. At $S = 1$ the downstream meniscus lies very slightly to the right of the top dead centre of the roll (X_0) (i.e. at positive X), and a thin film was detected on the roll downstream of the nip. As S was increased beyond one the downstream meniscus was observed to lie on the left of X_0.

As the speed ratio was increased the upstream meniscus, X_U, was observed to move closer towards the nip, whereas the downstream interface, X_D, was observed to move away from the nip resulting in a decrease in the overall length of the bead, as illustrated in figure 6.10. At high speed ratios (for the case shown at $S = 3.35$) the upstream interface was observed to become unstable which very rapidly caused the bead to break up into discrete sections. It proved very difficult to set the speed ratio so that the interface had a steady sinusoidal pattern along the axial direction, instead the upstream meniscus quickly became chaotic. The interface shapes were similar to those observed by, for example, Michalland *et al.* (1996) where a small quantity of fluid was placed in a narrow gap between two rotating cylinders. This chaotic motion of the meniscus was also exacerbated by the slight eccentricity of the roll ($\sim 50\ \mu$m).

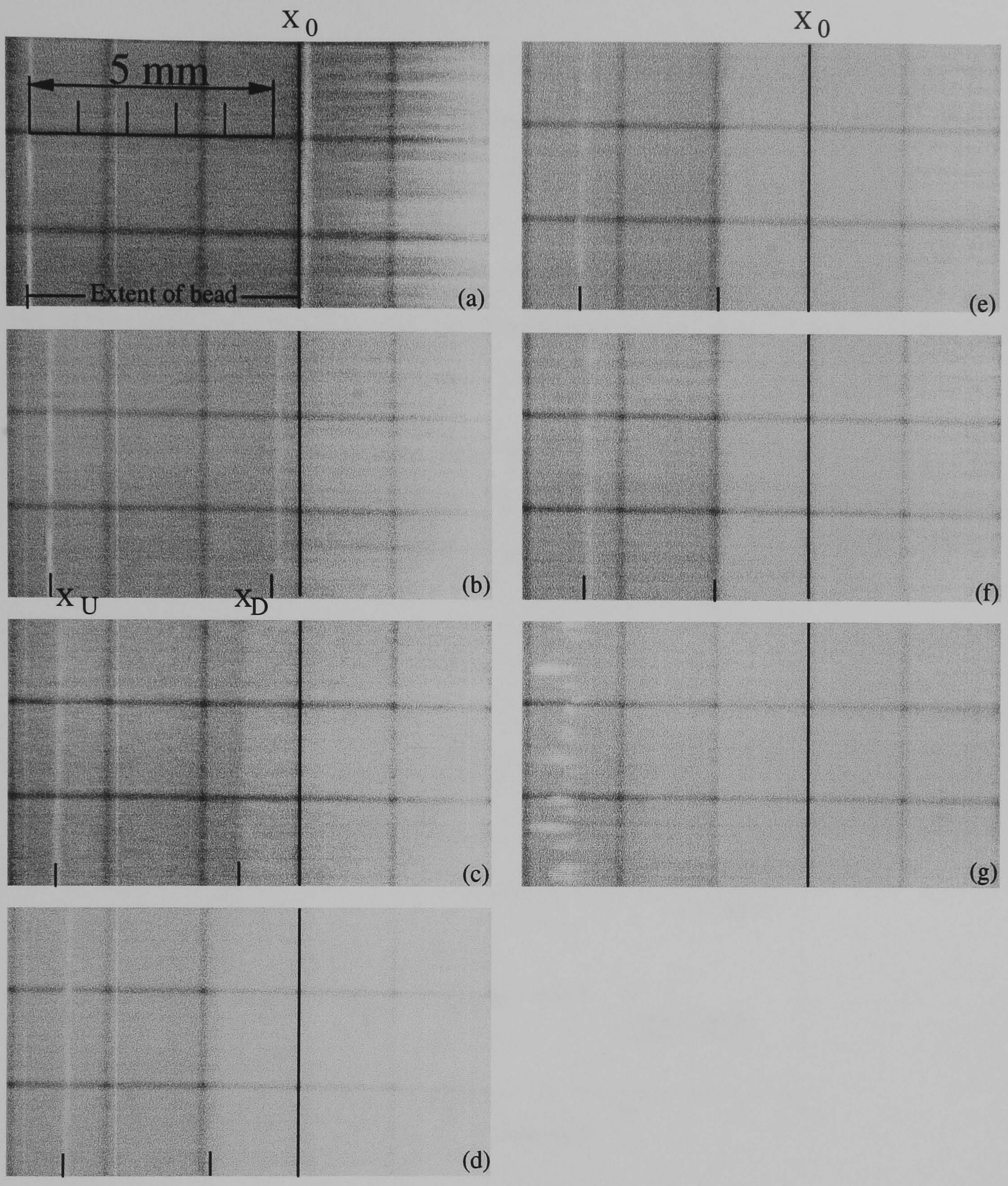

Figure 6.10: Visualisations of the kiss coating bead through the transparent web. Roll moving left to right, web moving right to left. (a) $S = 1.0$, (b) $S = 1.5$, (c) $S = 2.0$, (d) $S = 2.5$, (e) $S = 3.0$, (f) $S = 3.35$, (g) $S = 3.5$ (bead unstable). Roll speed 0.166 m/s, fluid properties as shown in table 6.1, inlet film thickness, H_i, 4.12 μm, roll radius 0.05 m, web tension 1000 N/m.

Meniscus positions in the kiss coating bead

Plotted in figure 6.11 are the upstream and downstream meniscus positions of the kiss coating bead as the speed ratio is varied. Two roll speeds U_2 were used, 0.166 m/s and 0.333 m/s. As highlighted in the previous section, as the speed ratio was increased the upstream meniscus moves in towards X_0. No variation of the upstream meniscus position with the speed of the roll was observed, even though at the higher roll speed of 0.333 m/s the film thickness (H_i) was 5.8 μm compared to a film thickness of 4.0 μm at the lower speed of 0.166 m/s.

The downstream meniscus moves away from X_0 as the speed ratio is increased. Again, from figure 6.11, no dependency of the meniscus position on the combination on the speed and inlet film thickness H_i was observed.

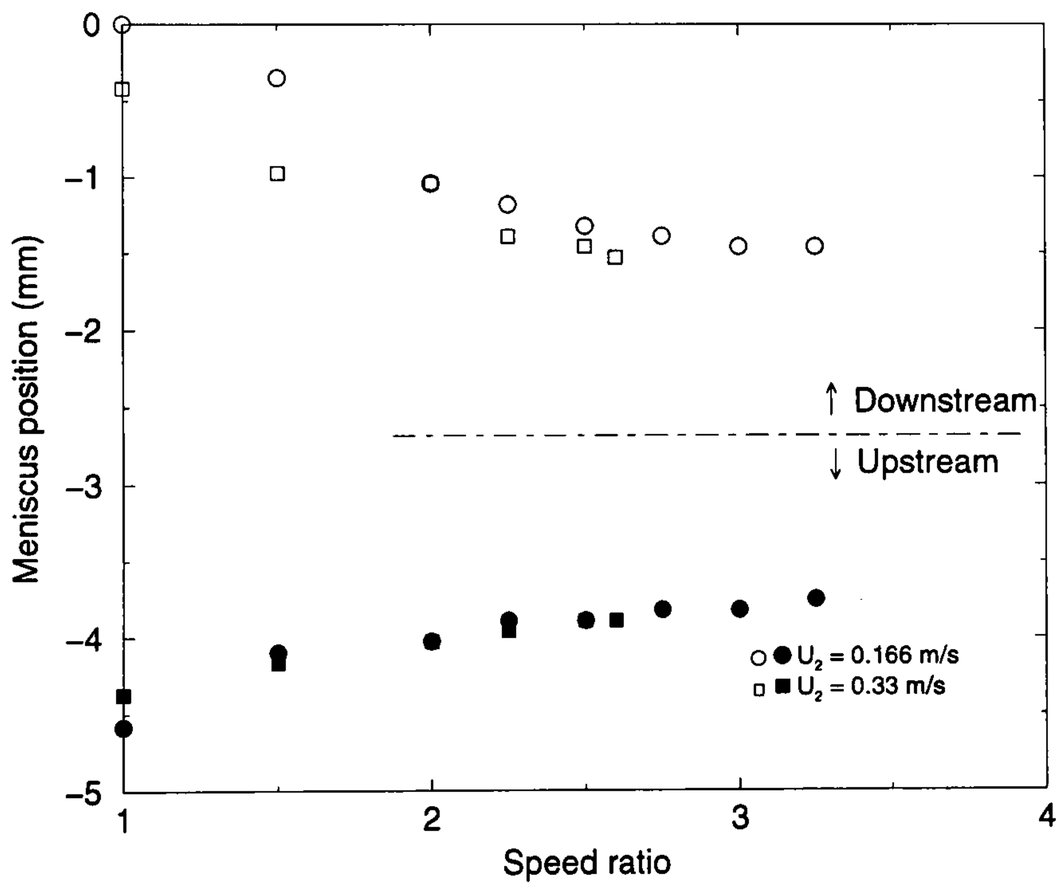

Figure 6.11: Experimentally determined positions of the menisci in a kiss coating bead. Fluid properties as shown in table 6.1, inlet film thickness: 4.0 μm at $U_2 = 0.166$ m/s, 5.8 μm at $U_2 = 0.33$ m/s, roll radius 0.05 m, web tension 1000 N/m. X_0 located at 0 mm.

Onset of ribbing in the kiss coating bead

Figure 6.12 shows the critical web speed (i.e. the web speed at which the upstream interface became unstable) as a function of the roll speed for the three laser engraved ceramic rolls used to meter the inlet film H_i by the offset coating method. The quadrangular roll was not used in these tests as it gave almost identical film thicknesses to the 60 lpi laser engraved ceramic roll. Clearly, in all cases as the roll speed was increased, the web speed at which the ribbing instability first arose also increased. As the roll speed was increased, the film thickness H_i would also increase as a consequence of using the offset gravure feed system, the data for which is shown figure 6.7. As a result of this the critical web speed shown in figure 6.12 is a function of both the roll speed and the inlet film thickness, however the data on these figures show no dependency of the critical web speed on the inlet film thickness, within the experimental error.

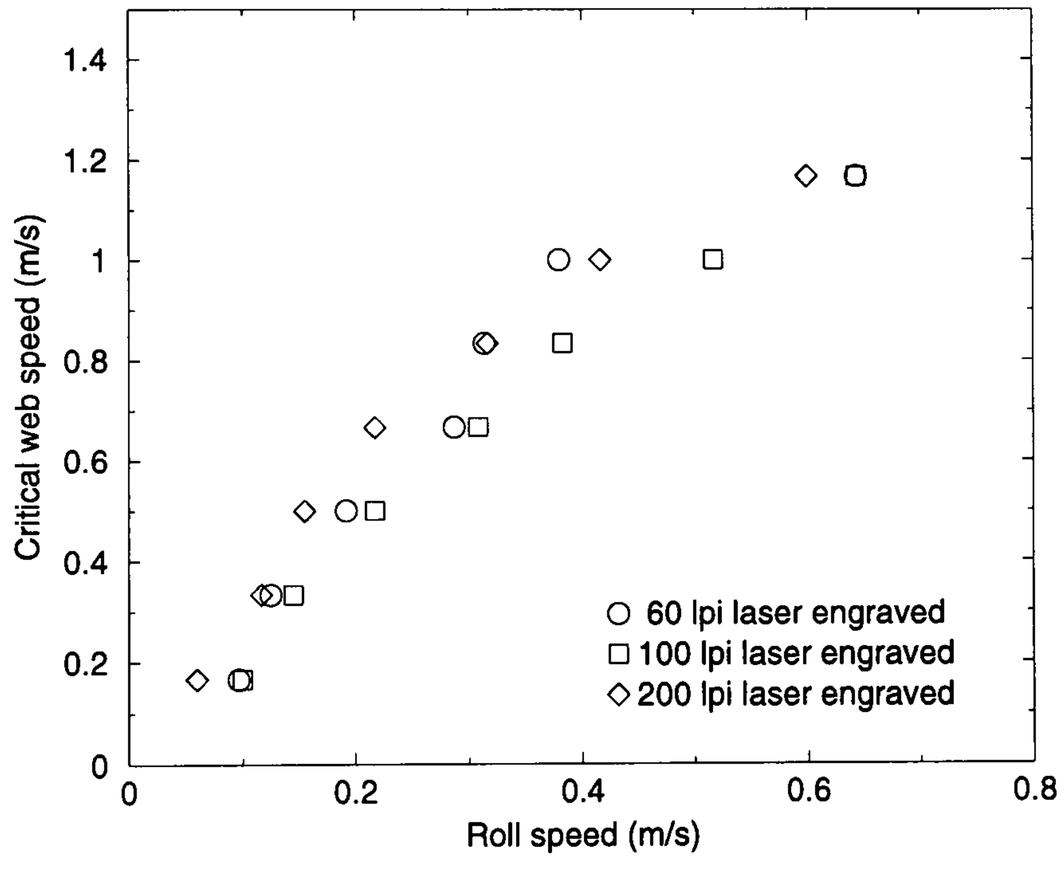

Figure 6.12: Experimentally determined critical web speed for the onset of ribbing in a kiss coater operating at $S > 1$. The symbols refer to the three different gravure geometries used to meter the inlet film H_i (see figure 6.7). Fluid properties shown in table 6.1, web tension 1000 N/m, roll radius 0.05 m.

6.4 Modelling the kiss coating bead – the stiff web model (SWM)

A simple model is now formulated to predict the onset of ribbing in a kiss coating bead at $S > 1$. Two steps are needed: (i) a base flow model that can be used to predict the location of the two menisci and the pressure profile within the bead; (ii) a criterion to determine the stability of the base flow solution – here a stability hypothesis is used to test whether the upstream meniscus is stable to small perturbations in its position.

6.4.1 Base flow model (SWM)

Lubrication theory is used to model the flow in the domain. Although not strictly valid in a converging domain where the flow is two–dimensional nevertheless it gives an accurate description provided the gap width and the slope are both small. Figure 6.3 gives details of the geometric parameters used in the problem.

Starting with Reynolds equation,

$$\frac{dP}{dX} = 6\mu\left(\frac{U}{H^2} - \frac{2Q}{H^3}\right) \quad \text{where } U = U_2 - U_1. \tag{6.2}$$

The flux is taken as zero at any station in X (valid when $S > 1$). Justification for this is taken from the experimental study, where it was shown that the speed ratio for complete removal of the film from the roll is just greater than one. Under these conditions the Reynolds equation reduces to

$$\frac{dP}{dX} = \frac{6\mu U}{H^2}. \tag{6.3}$$

In this model the web is assumed to be so highly tensioned that it remains flat as it passes over the bead allowing the shape of the domain close to the nip to be represented by a parabolic profile,

$$H(X) = \frac{X^2}{2R}, \tag{6.4}$$

where R is the radius of the roll. Equation (6.3) can be integrated to give

$$P = -\frac{8\mu U R^2}{X^3} + C_1. \tag{6.5}$$

One boundary condition is needed to solve equation (6.5):

1. A condition on pressure at the upstream meniscus is given by capillarity,

$$P(X_U) = -\frac{\sigma}{R_U} \tag{6.6}$$

where R_U is the radius of the upstream meniscus. To relate the radius of curvature of the meniscus to the outlet film thickness the analysis of Landau and Levich (1942) for withdrawal of a plate from a reservoir of liquid and later extended by Ruschak (1982) and Wilson (1982) for higher capillary numbers is used:

$$H_1 = aR_U Ca_1^b, \text{ where } H_i = SH_1. \tag{6.7}$$

The values of the constants a and b in equation (6.7) are

$$a = 1.34,\ b = 0.666 \quad Ca_1 < 0.01 \tag{6.8}$$
$$a = 0.54,\ b = 0.5 \quad 0.01 < Ca_1 < 0.1$$

Manipulation of equations (6.6) and (6.7) gives

$$P_{(X_U)} = -\frac{\sigma a Ca_1^b S}{H_i}, \tag{6.9}$$

which enables the constant C_1 to be found in equation (6.5) to give:

$$P = -8\mu U R^2 \left(\frac{1}{X^3} - \frac{1}{X_U^3}\right) - \frac{\sigma a Ca_1^b S}{H_i}. \tag{6.10}$$

The gap thickness at the upstream meniscus can be found by considering a simple model for the meniscus shape $H_U = 2R_U + H_1 + H_i$, as illustrated in figure 6.13, giving

$$H_U = \frac{H_i}{S}\left(\frac{2}{aCa_1^b} + S + 1\right). \tag{6.11}$$

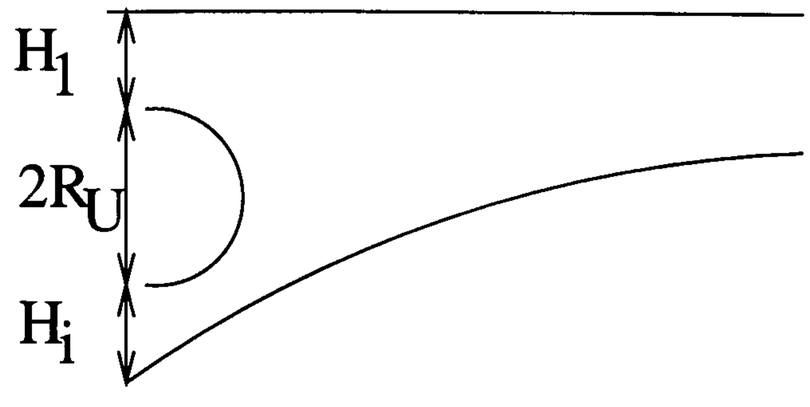

Figure 6.13: The model at the upstream meniscus used to relate the radius of curvature (R_U) and the film thicknesses (H_i and H_1) to the height at film split.

The upstream meniscus position, X_U, is therefore given by

$$X_U = -\sqrt{\frac{2RH_i}{S}\left(\frac{2}{aCa_1^b} + S + 1\right)}. \tag{6.12}$$

Equation (6.10) clearly shows that for, $S > 1$, $P \to -\infty$, as $X \to 0$. In practice when the fluid pressure falls below its vapour pressure (vaporous) cavitation would occur. This means that the fluid domain will terminate at X_D when $P = P_{vp}$ where P_{vp} is the vapour pressure of the fluid. For aqueous fluids, the vapour pressure is orders of magnitude lower than atmospheric pressure (for water $P_{vp} = -97760$ Pa) and P_{vp} may be taken as -10^5 Pa (gauge). The pressure in the cavity will differ from the fluid pressure due to curvature of the meniscus. However it is difficult to say what shape the meniscus will take, here any curvature will be neglected and the pressure in the region $X_D \to X_0^*$ will be taken as P_{vp}, the location X_0^* marking the point where the web and roll first touch.

Equation (6.10) can be manipulated to explicitly give X_D :

$$X_D = \left[\frac{1}{X_U^3} - \frac{1}{8\mu U R^2}\left(P_{vp} + \frac{\sigma a Ca_1^b S}{H_i}\right)\right]^{-\frac{1}{3}}. \tag{6.13}$$

Typically $P_{vp} \ll P_{X_U}$,and $\frac{1}{X_U^3} \ll \frac{1}{X_D^3}$ in which case equation (6.13) reduces to

$$X_D \approx \left(\frac{-8\mu U R^2}{P_{v.p}}\right)^{\frac{1}{3}} \tag{6.14}$$

6.4.2 Results of the base-flow (SWM)

Figure 6.14 shows the positions of the two menisci as speed ratio is varied. As speed ratio is increased the pressure gradient at the meniscus increases, causing the length of the fluid bead to decrease. This causes the upstream meniscus at X_U to move in towards the nip. The increase in pressure gradient also causes the meniscus at X_D to move away from the nip as the cavitation pressure is reached in a shorter distance.

Figure 6.15 shows a typical pressure profile through the bead of fluid. The fluid domain has been terminated when $P < P_{vp}$. The pressure is entirely sub-ambient, and the gradient is negative throughout. The pressure gradient is steepest as the position X_D is approached. As the speed ratio is increased, the length of the fluid bead decreases, and the pressure gradient becomes more negative.

One observation from the model is that when $S = 1$ the pressure gradient throughout the bead is zero (equation (6.3)) since $U = 0$. Under these conditions cavitation will not occur, and could be the reason why the speed ratio needs to be greater than one for complete removal of the fluid from the roll.

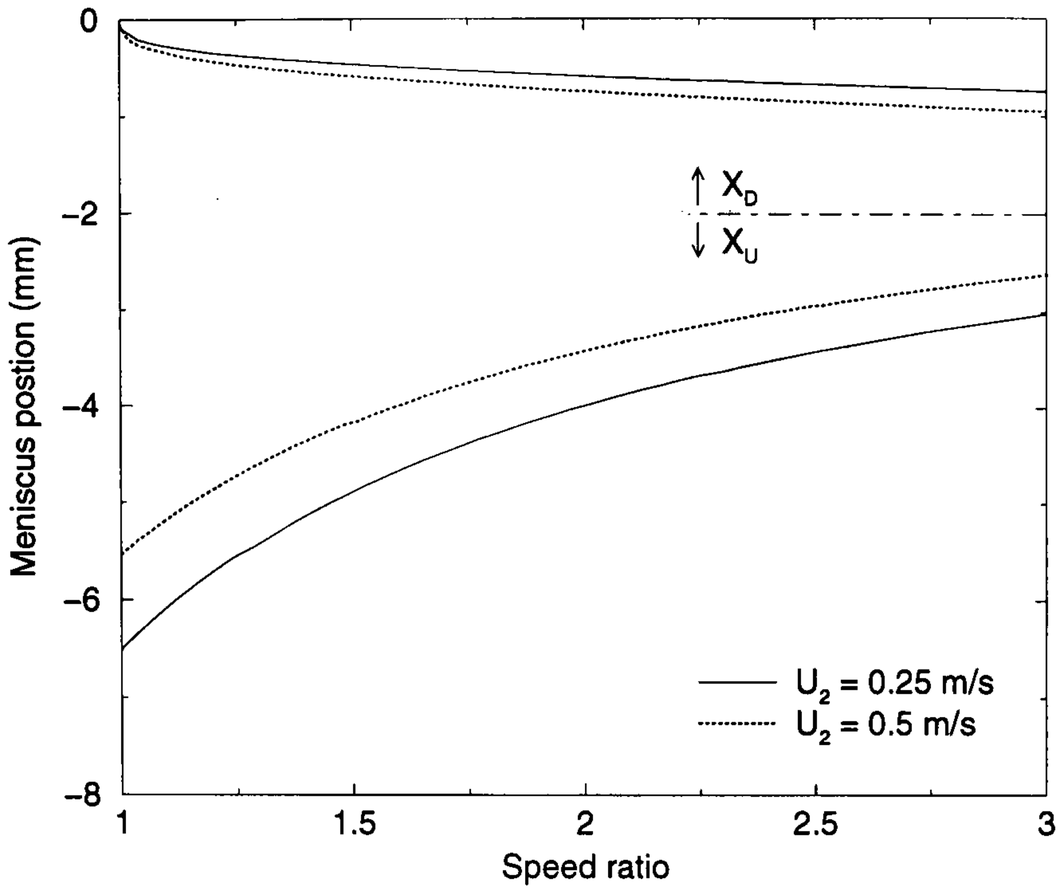

Figure 6.14: The locations of the two menisci as a function of speed ratio for the stiff web model. Conditions $\mu = 0.001$ Pa s, $\sigma = 0.03$ N/m, $H_i = 5 \times 10^{-6}$ m, $R = 0.1$ m, $P_{v.p.} = -10^5$ Pa. X_0 located at 0 mm.

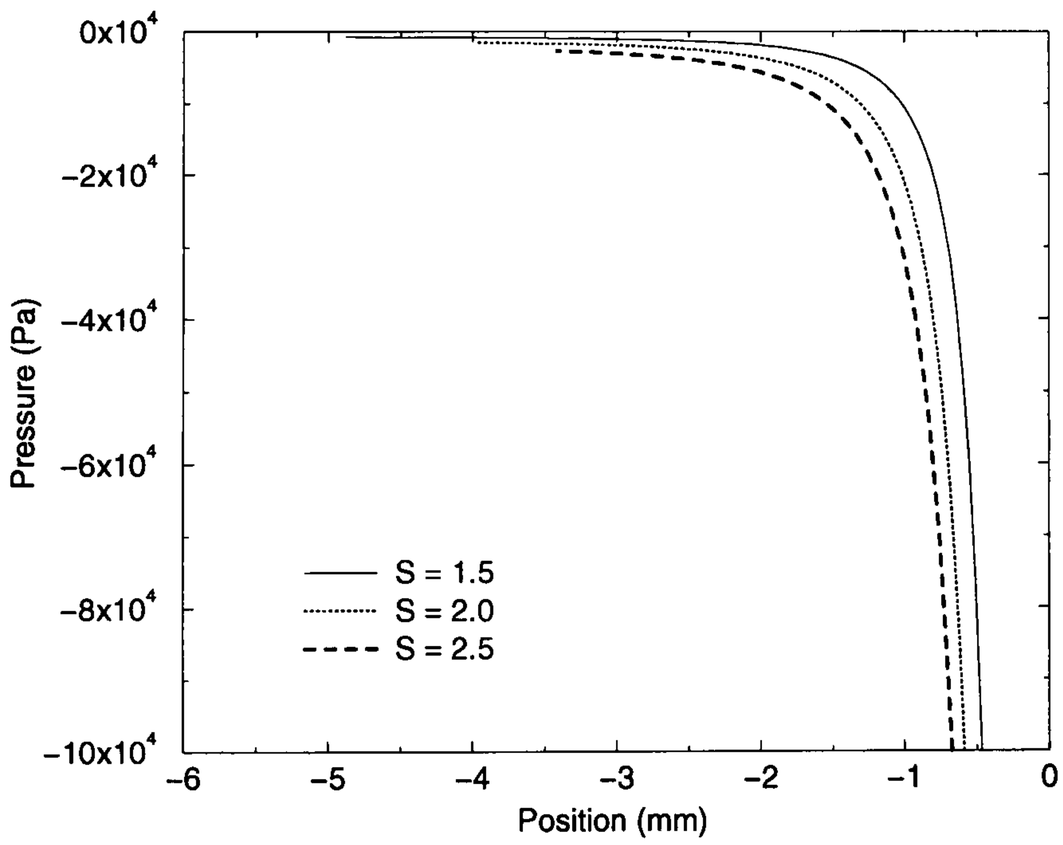

Figure 6.15: Typical pressure profiles through the fluid bead for the stiff web model. Conditions $U_2 = 0.25$ m/s and as per figure 6.14.

Comparison with experimental results (SWM)

Figure 6.16 shows the comparison between analytical prediction and experimental measurement for the menisci positions. The results from this simple model are in qualitative agreement with the experimental data — as the speed ratio is increased the downstream meniscus moves towards X_0 and the upstream meniscus moves away from X_0. However, both the position of the upstream and downstream menisci are under-predicted by the model. The analytical results also show more of a dependence on the film thickness than is observed experimentally.

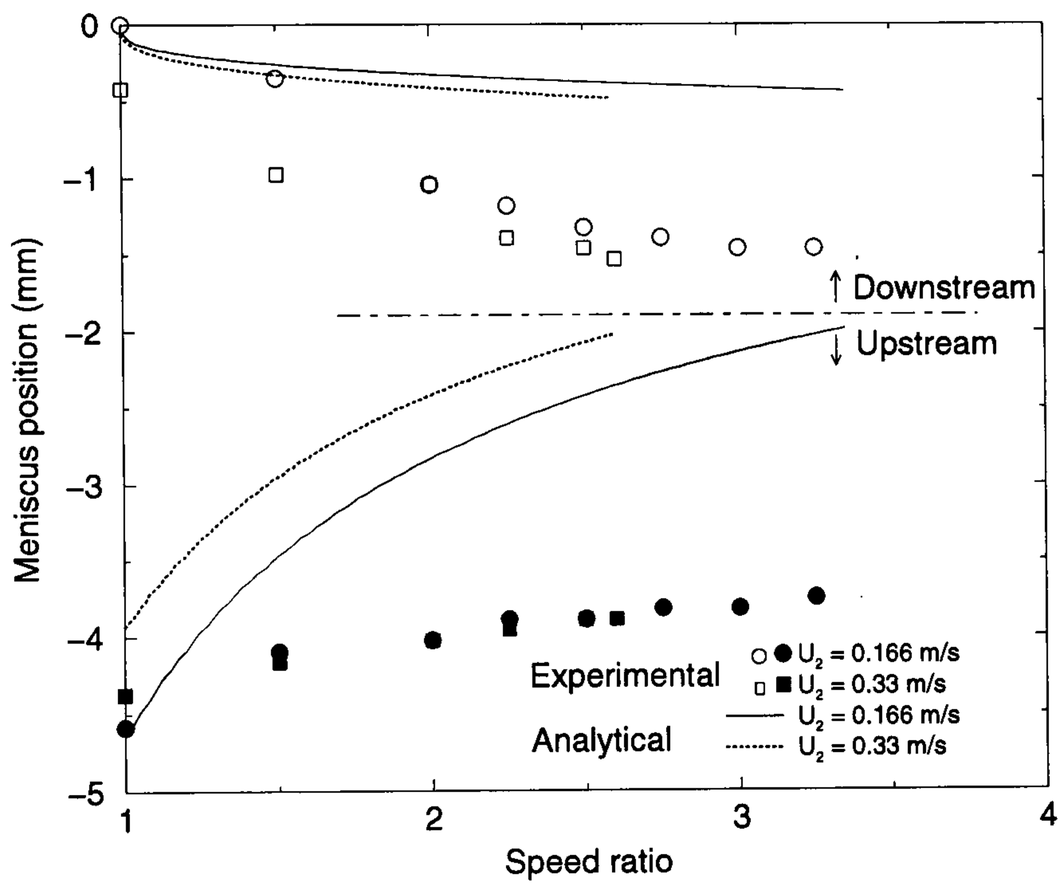

Figure 6.16: Comparison between the experimental meniscus positions and the predictions from the roll-flat plate model. All conditions as per figure 6.11. X_0 located at 0 mm.

6.4.3 Stability of the base flow (SWM)

A simple stability hypothesis has been used to determine the onset of ribbing for the kiss coater operating at speed ratios greater than one, based on the stiff web model, despite showing only a qualitative agreement with the experimentally determined meniscus locations. Similar to the method used in chapter 4 for determining the onset of the bead break instability, the response of the upstream meniscus to a

small perturbation in its position (ϵ) will be considered. This approximate way of determining the stability of an interface was derived by Pitts and Greiller (1961) and Savage (1977b).

At the meniscus the pressure is given by $P_U = -\frac{\sigma}{R_U}$. If the meniscus position is perturbed from X_U to $X_U - \epsilon$, as shown in figure 6.17, the net force acting on the interface in the negative x direction will be given by

$$F = P_{(X_U-\epsilon)} + \frac{\sigma}{R_{(X_U-\epsilon)}}, \tag{6.15}$$

where the pressure of the air has been taken at a reference value of zero.

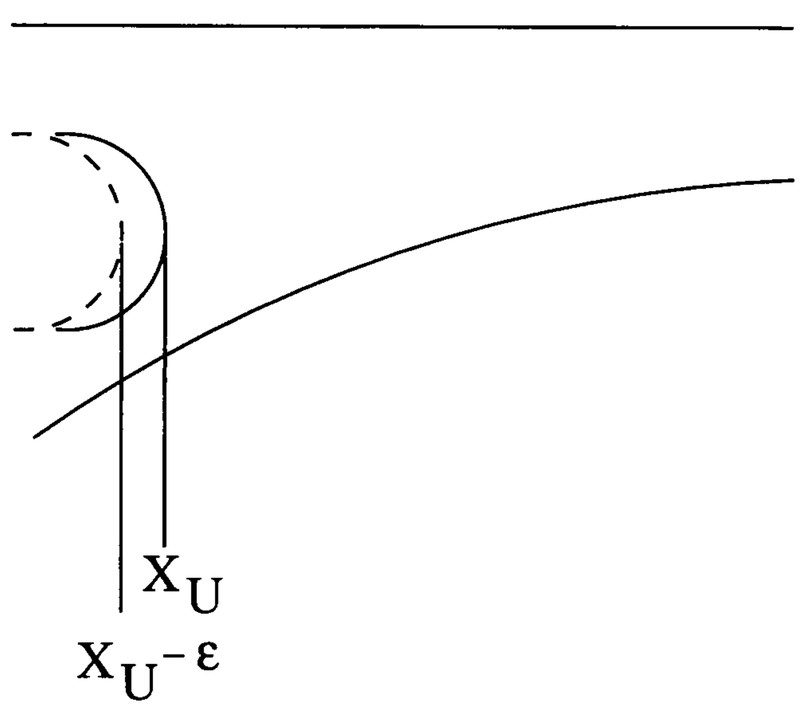

Figure 6.17: The perturbation of the meniscus position from X_U to $(X_U - \epsilon)$.

Linearising and taking terms of $O(\epsilon)$ via

$$P_{(X_U-\epsilon)} = P_{(X_U)} - \epsilon\frac{dP_{(X_U)}}{dX} + O(\epsilon^2) \tag{6.16}$$

$$\frac{\sigma}{R_{(X_U-\epsilon)}} = \frac{\sigma}{R_U} - \epsilon\sigma\frac{dR_U^{-1}}{dX} + O(\epsilon^2)$$

the net force, F, at the meniscus will be given by

$$F = -\epsilon\frac{d}{dX}\left(P + \frac{\sigma}{R_U}\right). \tag{6.17}$$

The sign of the net force on the interface, F, will determine whether the perturbation will diminish, remain neutrally stable (the onset of ribbing) or grow accordingly as:

$$\begin{aligned} F < 0 &\text{ the perturbation decays – interface returns to its equilibrium value} \\ F = 0 &\text{ the perturbation remains neutrally stable} \\ F > 0 &\text{ the perturbation grows – ribbing occurs.} \end{aligned} \tag{6.18}$$

For neutral stability a small disturbance to the interface will neither grow or diminish in size (the resulting force $F = 0$) and determines the critical point for the onset of ribbing. For this case equation (6.17) reduces to

$$F = -\frac{d}{dX}\left(P + \frac{\sigma}{R_U}\right)_{X_U} = 0. \tag{6.19}$$

The relationship between R_U and H_U is given by

$$R_U = \frac{H_U}{2 + (S+1)aCa_1^b}. \tag{6.20}$$

Starting with equation (6.19) and substituting the known expression relating R_U to H_U from equation (6.20) gives:

$$F = -\left(\frac{dP}{dX}\right)_{X_U} + \frac{\sigma(2 + (S+1)aCa_1^b)}{H_U^2}\left(\frac{dH}{dX}\right)_{X_U}. \tag{6.21}$$

which, for stability gives

$$\frac{\sigma(2 + (S+1)aCa_1^b)}{H_U^2}\left(\frac{dH}{dX}\right)_{X_U} > \left(\frac{dP}{dX}\right)_{X_U}. \tag{6.22}$$

Substituting equation (6.3) into 6.21 gives

$$\frac{6\mu U(2 + (S+1)a\mathrm{Ca}_1^b)}{\sigma} - \left(\frac{dH}{dX}\right)_{X_U} = 0 \tag{6.23}$$

at the point of neutral stability. Finally, differentiating equation (6.4) and substi-

tuting X_U from equation (6.12) gives

$$\frac{6\mu U(2+(S+1)a\mathrm{Ca}_1^b)}{\sigma}+\sqrt{\frac{2H_i}{SR}\left(\frac{2}{a\mathrm{Ca}_1^b}+S+1\right)}=0 \tag{6.24}$$

for neutral stability. Equation (6.24) can be solved (using, for example, a bisection method) by specifying all the parameters except U_1 which is varied, together with S, until equation (6.24) is satisfied.

6.4.4 Results of the stability model (SWM)

Figure 6.18 shows a family of neutral stability curves for the flat-plate roll geometry with varying inlet film thickness to roll radius ratio.

As the roll speed is increased, for a constant inlet film thickness, the critical speed ratio at which ribbing occurs decreases and tends to 1. Also shown is that as the inlet film thickness decreases, the critical speed ratio at which the onset of ribbing occurs also decreases, i.e. a thick inlet film has a stabilising effect. However, care must be taken when interpreting these results for an industrial situation since the outgoing film thickness H_1 and the web speed U_1 are now of most importance. The data shown in figure 6.18 have been replotted in figure 6.19 to show the web film thickness at criticality as a function of the web speed. An example from this figure shows that a desired outgoing film thickness of 2 μm can be achieved with: (i) a linespeed of 1.5 m and an inlet film thickness of 2.5 μm or (ii) a linespeed of 0.6 m and an inlet film thickness of 5 μm. Clearly when a high linespeed is important it is advantageous to operate with a thin inlet film.

Figure 6.20 shows a neutral stability curve for one inlet film thickness plotted against the roll capillary number. The larger the capillary number the closer the critical speed ratio is to 1. A more viscous fluid will destabilise the bead whilst a fluid with a higher surface tension will stabilise the bead. Equation (6.24) shows that at speed ratios of $S = 1$ i.e. $U = 0$ a stable bead always exists. This is because pressure gradient is zero and the gradient in gap height is always negative (due to the converging geometry).

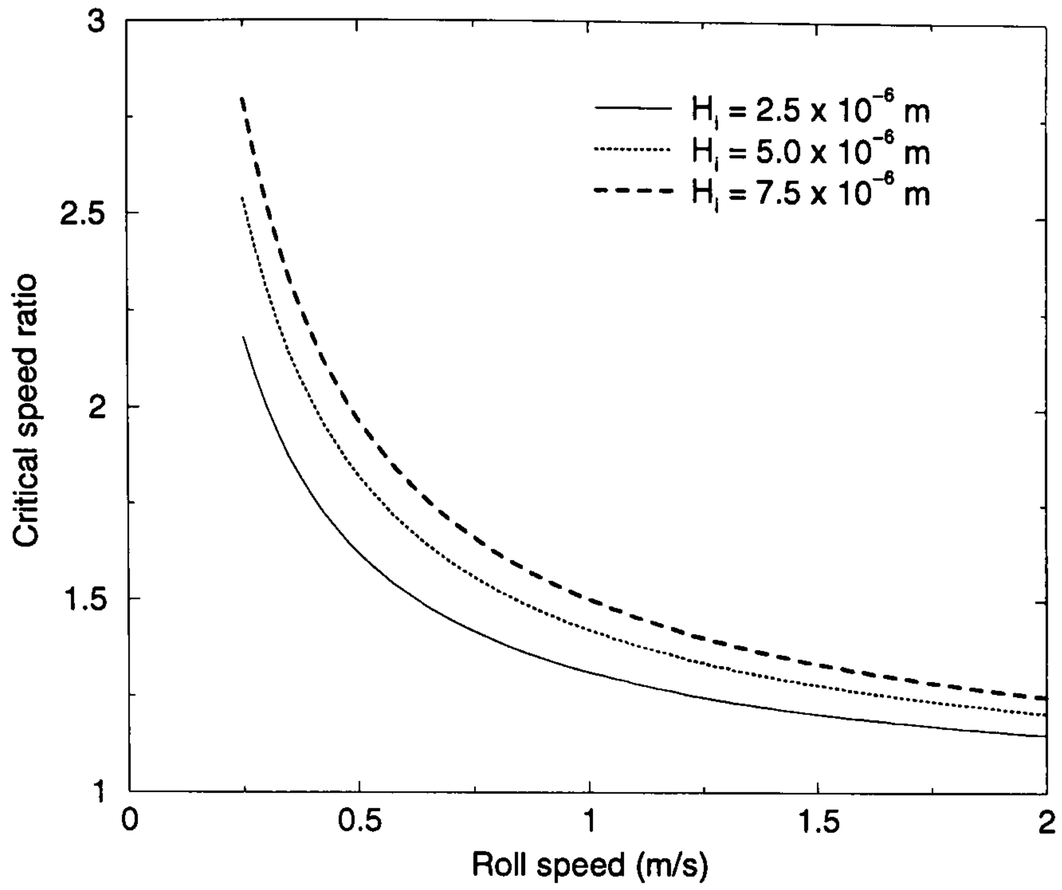

Figure 6.18: Effect of roll speed and inlet film thickness on the critical speed ratio for the onset of ribbing as predicted by the stiff web model. Conditions (other than inlet film thickness and roll speed U_2) as per figure 6.14.

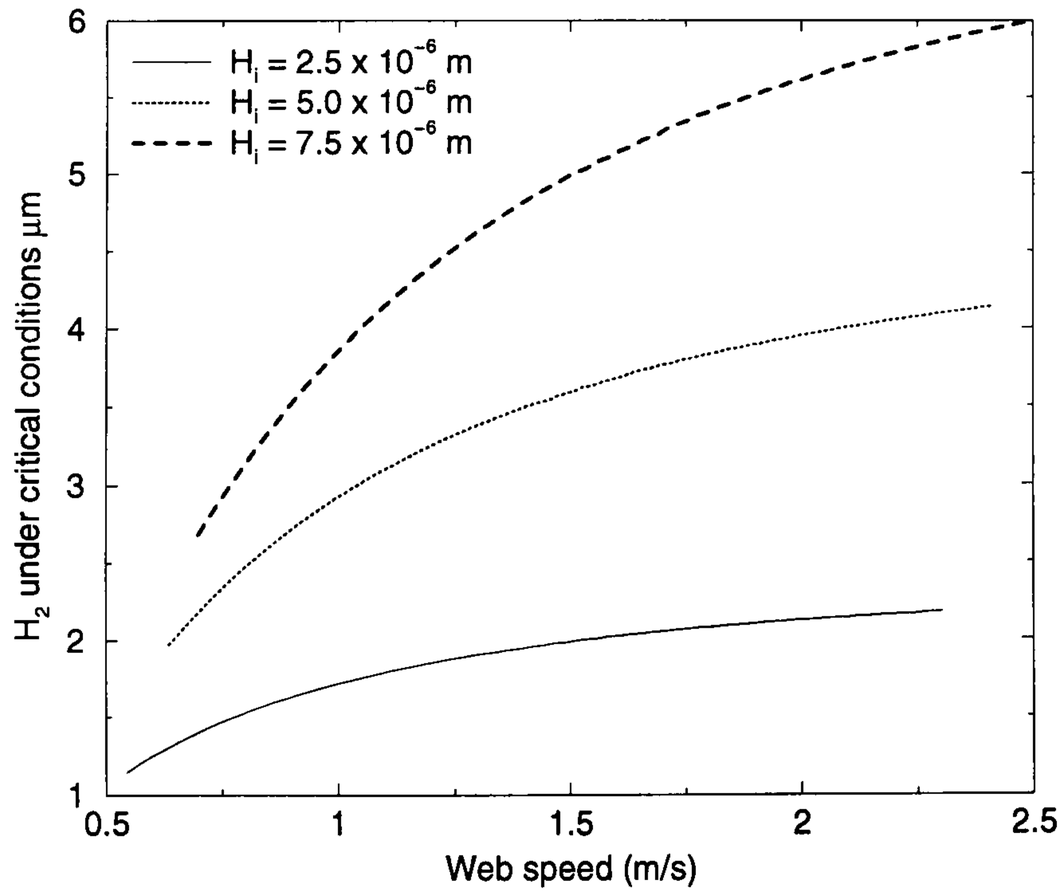

Figure 6.19: Effect of web speed on the web film thickness at the onset of ribbing as predicted by the stiff web model. Data replotted from figure 6.18.

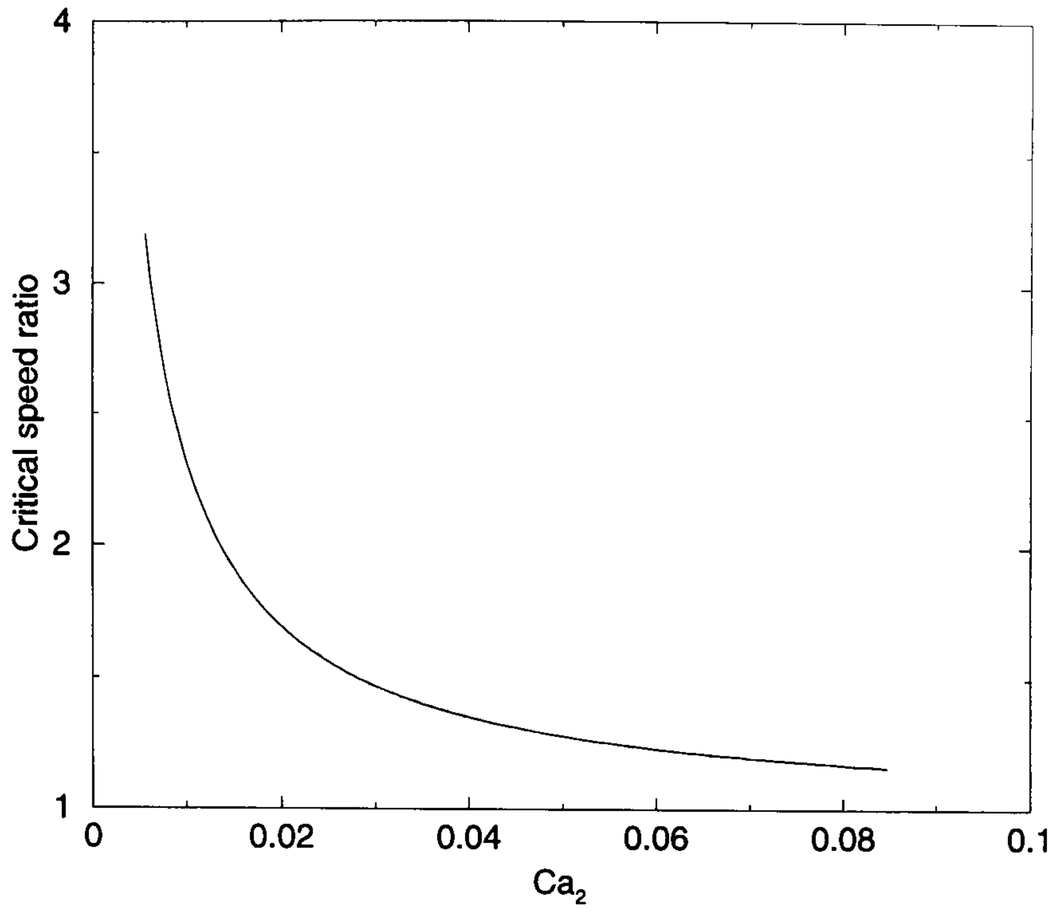

Figure 6.20: Effect of Ca_2 on the critical speed ratio for the onset of ribbing as predicted by the stiff web model. Conditions (other than Ca_2) as per figure 6.14.

Comparison with experimental results

Figure 6.21 shows the comparison between the experimental results for the onset of ribbing and the predictions of the simple stability hypothesis based on the roll–flat plate geometry. The analytic model requires the film thickness H_i to be specified as a input parameter – this is taken from figure 6.7 since the offset gravure method is used to meter the film H_i in these experiments. Once again the general trend of the analytical model is in agreement with the experimental results, with the critical web speed increasing with the roll speed. The analytic results suggest that there is some dependence of the critical web speed on the inlet film thickness H_i since the inlet film metered from the 60 lpi roll is greater than the films metered from the 100 lpi and 200 lpi rolls. However, the error associated with determining the onset of ribbing makes this difficult to test experimentally.

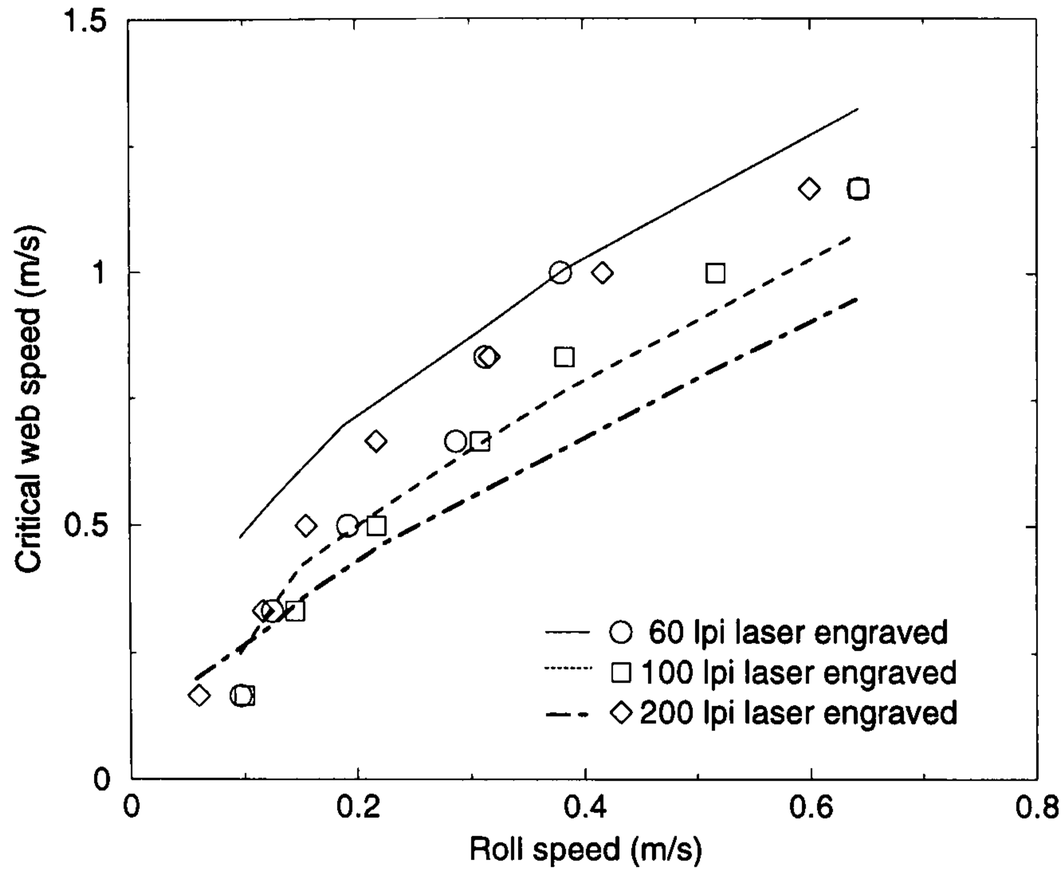

Figure 6.21: Comparison between the experimental (symbols) and analytic predictions (lines) from the roll flat plate model for the onset of ribbing. Conditions as per figure 6.12, inlet film thicknesses, H_i, for (SWM) model from figure 6.7.

6.5 Modelling the flow in the kiss coating bead – the flexible web model (FWM)

6.5.1 Base flow model (FWM)

Starting with the zero flux form of the Reynolds equation (6.3) and non-dimensionalising using the following quantities :

$$p = \frac{RP}{T},\ x = \frac{X}{\sqrt{RH_U}},\ z = \frac{Z}{H_U},\ h_{(x)} = \frac{H_{(X)}}{H_U},\ h_i = \frac{H_i}{H_U},\ h_1 = \frac{H_1}{H_U} \tag{6.25}$$

gives

$$\frac{dp}{dx} = \frac{\alpha}{h^2}, \tag{6.26}$$

where

$$\alpha = 6Ca_1 \left(\frac{\sigma}{T}\right)\left(\frac{1}{S} - 1\right)\left(\frac{R}{H_U}\right)^{\frac{3}{2}}, \tag{6.27}$$

and where H_U is unknown yet can be related to the inlet film thickness by equation (6.11).

Storey (1996), in a study of a kiss coater operating at $S < 1$, showed that a thin web can be treated as a membrane with a tension T. From a balance of the normal force along the web

$$P(X) = -\kappa T, \tag{6.28}$$

where κ is the local curvature of the web and air pressure is taken to be zero. This is equivelent to a surface tension of an interface, with the difference that the shear stress at the web is not zero but the speed is equal to U_1. In the coordinate system shown in figure 6.3

$$\kappa = \frac{\left(\frac{d^2Z}{dX^2}\right)}{\left(1+\left(\frac{dZ}{dX}\right)^2\right)^{3/2}}. \tag{6.29}$$

Since the model is formulated using lubrication theory then $\frac{dZ}{dX} \ll 1$ and therefore

$$\kappa = \frac{d^2Z}{dX^2}. \tag{6.30}$$

Equation (6.28) can now be written as

$$P(X) = -\frac{d^2Z}{dX^2}T \tag{6.31}$$

which can be non-dimensionalised *via* equation (6.25) to give

$$p(x) = -\frac{d^2z(x)}{dx^2}. \tag{6.32}$$

The shape of the roll close to X_0 can be represented by a parabolic approximation (refer to figure 6.3 for coordinate system):

$$Z = H + R - \frac{X^2}{2R} \tag{6.33}$$

and z(x) and its derivatives can be written as

$$z(x) = h(x) + \left(\frac{R}{H_U} - \frac{x^2}{2}\right), \tag{6.34}$$

μ	Pa s	1×10^{-3}	1×10^{-3}
σ	N/m	30×10^{-3}	72.9×10^{-3}
Web Tension T	N/m	10000	500
Web Speed U_1	m/s	0.3	1.5
Inlet Film T_i	m	10×10^{-6}	2×10^{-6}
α	-	4×10^{-5}	0.1

Table 6.2: Typical limiting value of α for an aqueous kiss coating system operating at $S > 1$ based on a roll radius of 0.1 m, and speed ratio 1.5.

$$\frac{dz}{dx} = \frac{dh}{dx} - x,$$
$$\frac{d^2z}{dx^2} = \frac{d^2h}{dx^2} - 1,$$
$$\frac{d^3z}{dx^3} = \frac{d^3h}{dx^3}.$$

From equations (6.32) and (6.35)

$$\frac{dp}{dx} = -\frac{d^3h}{dx^3}, \tag{6.35}$$

and equating with Reynolds equation (6.26) gives

$$\frac{d^3h}{dx^3} = -\frac{\alpha}{h^2} \text{ for } S > 1. \tag{6.36}$$

The constant α can vary over a wide range of values, based on a range of industrial parameters , as shown in table 6.2

6.5.2 Boundary conditions for the FWM model

The boundary conditions required to complete the roll–flexible web model are described below. The full domain consists of two regions – a liquid domain and a vaporous domain, as discussed in the stiff web model case.

(i) The liquid domain

Three conditions are applied at x_u. These are manipulated to give conditions on h, $\frac{dh}{dx}$ and $\frac{d^2h}{dx^2}$ there:

1. The first is from the non-dimensional scheme, equation (6.25),

$$h_{(x_u)} = 1. \tag{6.37}$$

2. Equations (6.6) and (6.7) give the pressure at the meniscus X_U which are non-dimensionalised to give

$$p_{x_u} = -\left(\frac{\sigma R}{T H_U}\right)\frac{1}{r_u} \tag{6.38}$$

and

$$h_1 = a r_u C a_1^b, \text{ where } h_1 = \frac{h_i}{S}. \tag{6.39}$$

Algebraic manipulation of equations (6.38) and (6.39) yields

$$p_{(x_u)} = -\left(\frac{\sigma R}{T H_U}\right)\frac{SaCa_1^b}{h_i}. \tag{6.40}$$

Substituting $h_i = \frac{H_i}{H_U}$ and using $p(x) = 1 - \frac{d^2h}{dx^2}$ (from equations (6.32) and (6.35)) leads to the second boundary condition

$$\left(\frac{d^2h}{dx^2}\right)_{x_u} = 1 + \frac{\sigma}{T}\frac{R}{H_i} SaCa_1^b. \tag{6.41}$$

3. Referring to figure 6.22 $|X_U| \ll |L|$, and the gradient of the web at X_U can be considered to be effectively zero:

$$\left(\frac{dz}{dx}\right)_{x_u} = 0. \tag{6.42}$$

Using equation (6.35) this can be written as

$$\left(\frac{dh}{dx}\right)_{x_u} = x_u. \tag{6.43}$$

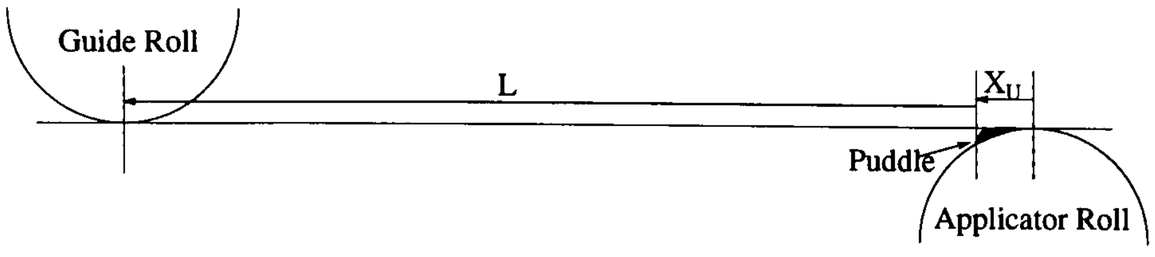

Figure 6.22: Typical arrangement of the kiss coater in relation to the offtake rolls.

(ii) The vaporous domain

Examination of equation (6.36) shows that as $h \to 0$ then $\frac{d^3h}{dx^3} \to -\infty$, i.e. $p \to -\infty$. As discussed in section 6.4.1, when the pressure in the fluid falls below the vapour pressure cavitation will occur. This location (x_d) will mark the end of the fluid domain and the start of a vaporous cavity beneath the web. In order to determine the shape of the web it is necessary to model the vaporous region and match the solutions at the fluid/vapour interface.

From Reynolds equation it is clear that as h decreases in the vaporous region the pressure gradient will tend to $-\infty$. However, this introduces a singularity in the solution, since at some point the height must go to zero to seal off the low pressure region. To alleviate this, and to simplify the solution method the pressure has been assumed to be constant throughout the vapour region, giving:

$$\frac{d^3h}{dx^3} = 0 \quad x_d < x < x_0^*. \tag{6.44}$$

By neglecting the curvature of the meniscus the pressure in the vapour region is set to the pressure in the fluid at x_d,

4. Hence the fourth condition, to locate x_d, is given by

$$p(x_d) = p_{v.p.} = 1 - \left(\frac{d^2h}{dx^2}\right)_{x_d}. \tag{6.45}$$

Finally two conditions are required to locate the end of the vaporous domain. The negative pressure in the bead means the web will be sucked down toward

the roll. Consequently, at some location x_0^*, the web will first touch the roll surface. The web will meet the roll at a tangent to the surface, giving the final two conditions at x_0^* required to solve the problem as:

5.

$$h(x_0^*) = 0, \tag{6.46}$$

6. and

$$\left(\frac{dh}{dx}\right)_{x_0^*} = 0. \tag{6.47}$$

In the region $x_0^* \to x_0$ the height, h, of the web above the roll will be zero. The conditions at x_0^* are equivalent to balancing the negative pressure within the bead and the load on the web,

$$\int_{X_U}^{X_0^*} P dX = T\left(\frac{dZ}{dX}\right)_{X_0^*}. \tag{6.48}$$

Summary of the boundary conditions for the FWM

A total of 6 conditions are required for a solution to the roll–flexible web model outlined above. Three are required to solve the 3rd order o.d.e., and a further three conditions to locate x_u, x_d and x_0^*. These, together with the appropriate equations, are shown in figure 6.23.

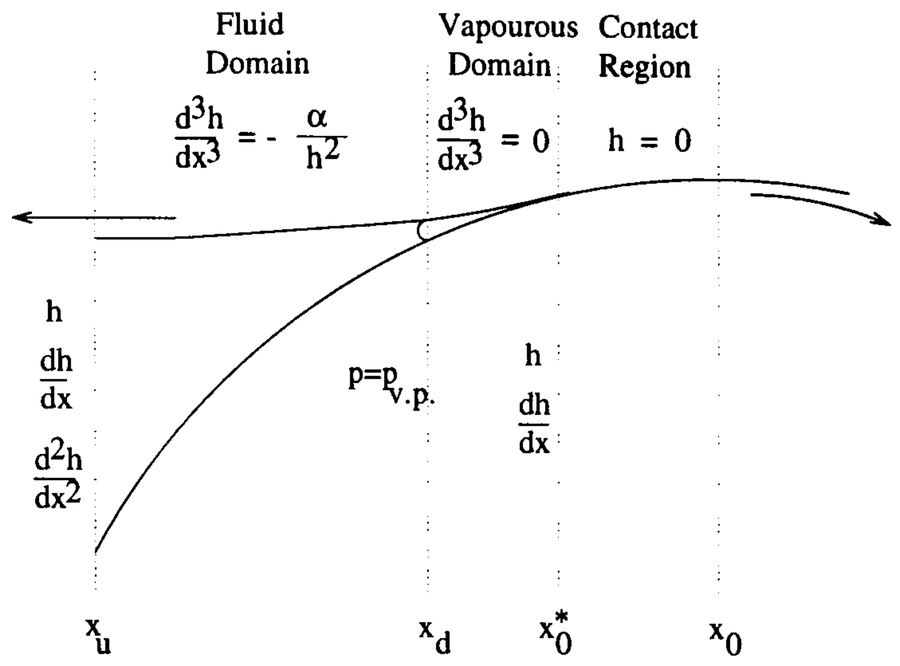

Figure 6.23: Boundary conditions and equations for the roll–flexible web kiss coating problem, $S > 1$.

6.5.3 Solution method for the FWM

The aim is now to solve the flexible web model outlined above for the flow/web shapes and the pressure profile through the bead. A numerical solution is sought to equations in the fluid domain and vapour domain shown in figure 6.23 subject to the boundary conditions discussed in section 6.5.2.

Figure 6.24 illustrates the scheme used to solve equations (6.36) and (6.44). A stiff initial value problem equation solver (NAg routine DO2 NBF) was used to integrate equation (6.36) subject to the conditions at x_0 given by equations (6.37), (6.41) and (6.43). This solver was used by Storey (1996) to solve the similar problem of kiss coating at $S < 1$.

To use an IVP solver, the location x_u and x_d need to be specified at the outset. An initial guess was made for the location x_d and the location x_u was varied by a bisection method until the condition $p(x_d) = p_{v.p.}$ given by equation (6.45) was met. Using the computed values of h, $\frac{dh}{dx}$ and $\frac{d^2h}{dx^2}$ at x_d, equation (6.44) describing the shape of the web in the vaporous region can be solved analytically to give the

constants c_1, c_2 and c_3 in the following equations:

$$\frac{d^2h}{dx^2} = c_1, \tag{6.49}$$

$$\frac{dh}{dx} = c_1 x + c_2, \tag{6.50}$$

$$h = \frac{c_1}{2}x^2 + c_2 x + c_3. \tag{6.51}$$

The final conditions that need to be met are at x_0^* where the web meets the roll at a tangent. From equation (6.47) $\frac{dh}{dx} = 0$ at x_0^* and matching the web shape for the vaporous region at x_d the location x_0^* is given (from equation (6.50)) by

$$x_0^* = -\frac{c_1}{c_2}. \tag{6.52}$$

All that remains is to determine whether the assumed position for the location x_d is correct. The calculated value of x_0^*, from equation (6.52) (where the gradient of the web matches that of the roll) is used to calculate the height at x_0^* from equation (6.51) which should be zero. Equation (6.46) gives the convergence criterion, tests showed a suitable value for $h_{(x_0^*)}$ to give a converged solution was $|h_{(x_0^*)}| < 1 \times 10^{-8}$.

If convergence was not achieved the location x_d was updated (again using a bisection method) and the calculation repeated from the start.

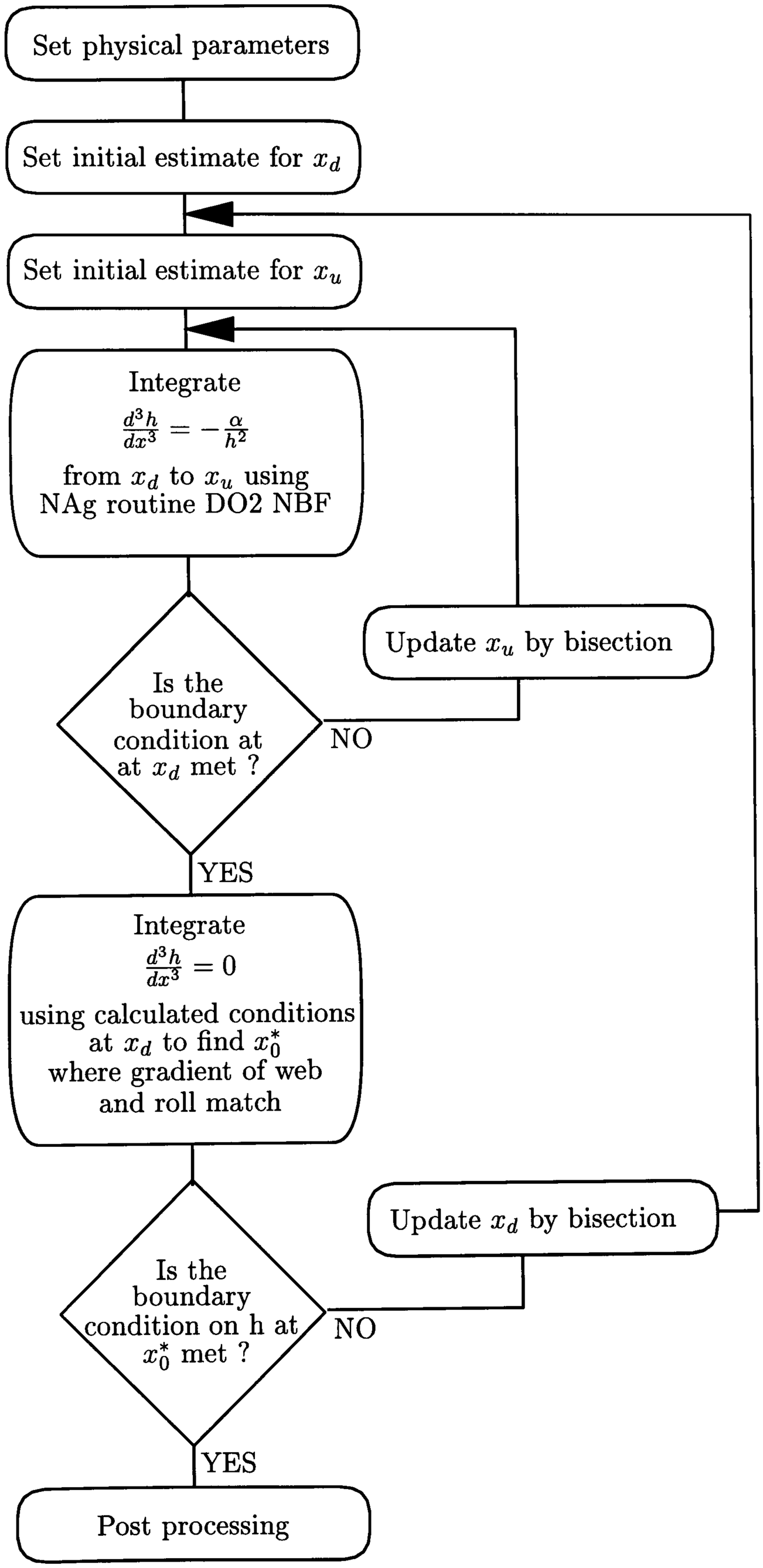

Figure 6.24: Solution scheme for the roll–flexible web kiss coating model.

6.5.4 Results for the base flow (FWM)

Figure 6.25 shows the predicted positions of the upstream meniscus at X_U and the internal locations at X_D and x_0^*. As the speed ratio is increased, as for the roll–plate model, the upstream meniscus moves towards X_0 and the downstream meniscus (X_D), that marks the end of the fluid domain, moves away from X_0. The contact point X_0^* lies very close to X_D, and as the speed ratio increases so does the width of the contact region. Clearly the length of the vaporous region is narrow, and the position X_d is dominated by X_0^*, making the choice of model for the vaporous domain relatively unimportant as long as it allows a large negative pressure (as it does here for the constant pressure model). Comparison with figure 6.14 shows that the menisci are predicted to lie further from X_0 than those calculated using the stiff web model.

The downstream meniscus positions for the two roll speeds lie close to each other, and show less of a variation in position with roll speed than is the case with the stiff web model shown in figure 6.14.

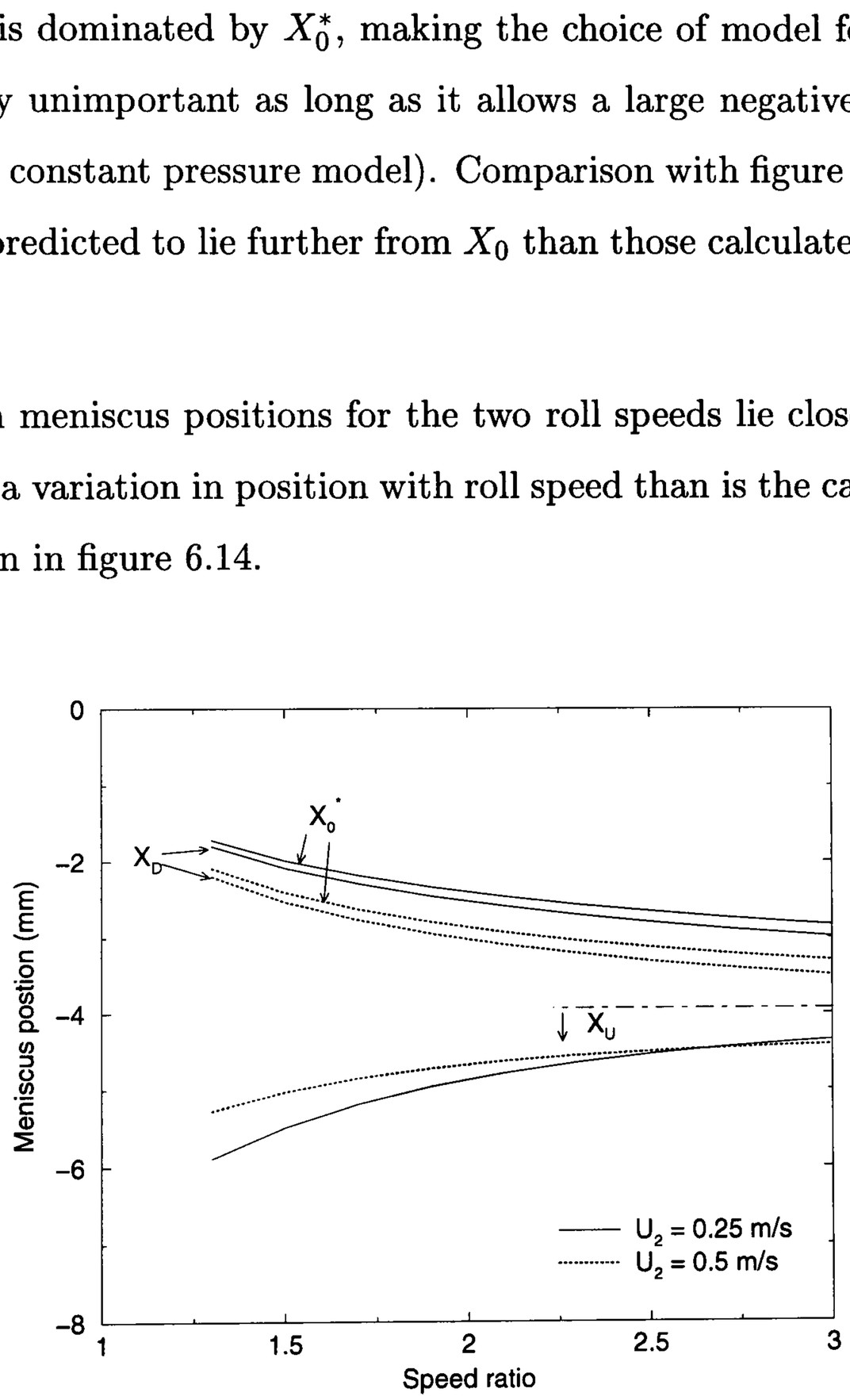

Figure 6.25: The locations of the two menisci and the contact point as a function of speed ratio for the roll–flexible web model. Conditions as per figure 6.14 and $T = 1000$ N/m. X_0 located at 0 mm.

Figure 6.26 shows three pressure profiles through the fluid bead as the speed ratio is increased. Once again, as for the stiff web model shown in figure 6.15, the pressure is entirely sub–ambient and the pressure gradient throughout the bead is negative. As the speed ratio is increased the length of the bead is reduced, and the pressure gradient steepens (i.e. becomes more negative). The fluid pressure throughout the bead is of the order of capillary pressure, but as h decreases the pressure rapidly falls to the vapour pressure at the downstream end.

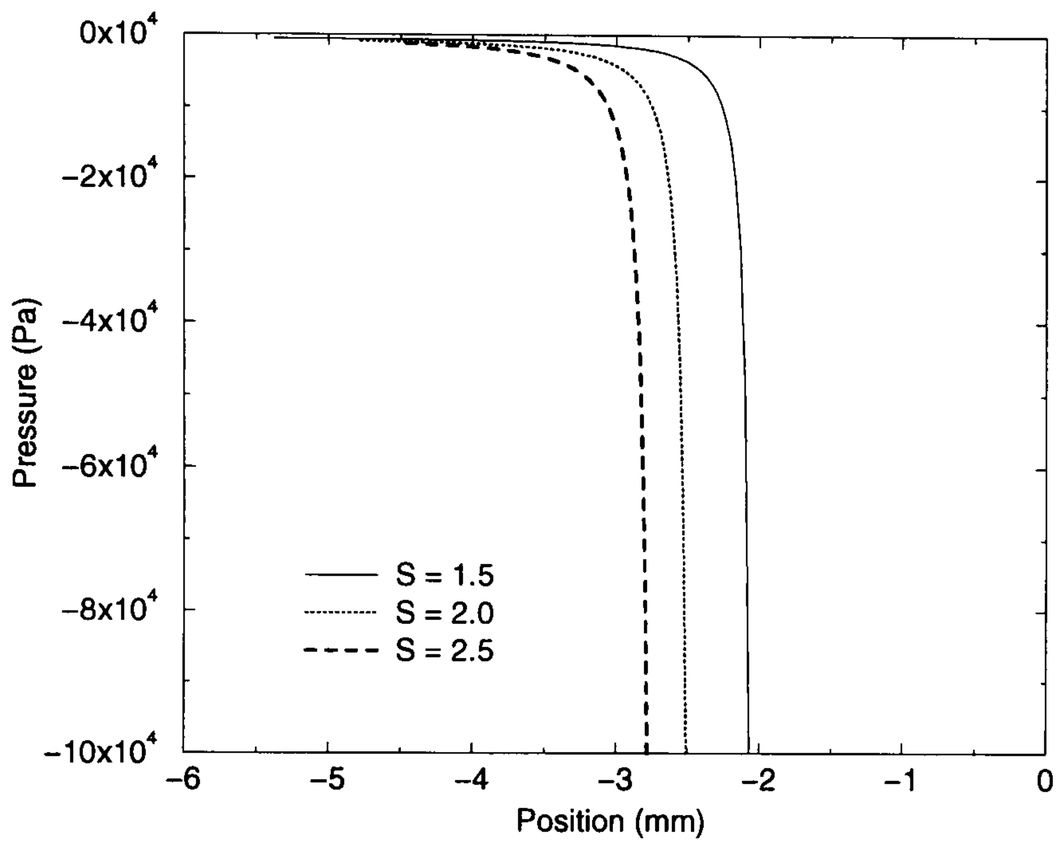

Figure 6.26: Typical pressure profiles through the fluid bead for the roll–flexible web model. Conditions $U_2 = 0.25$ m/s and as per figure 6.25.

Finally, figures 6.27 and 6.28 shows profiles of the web as the speed ratio is increased; the bead moves in the negative direction, as shown in figure 6.25. The web is most curved as the downstream meniscus position, X_D, is approached, which is where the pressure is most negative.

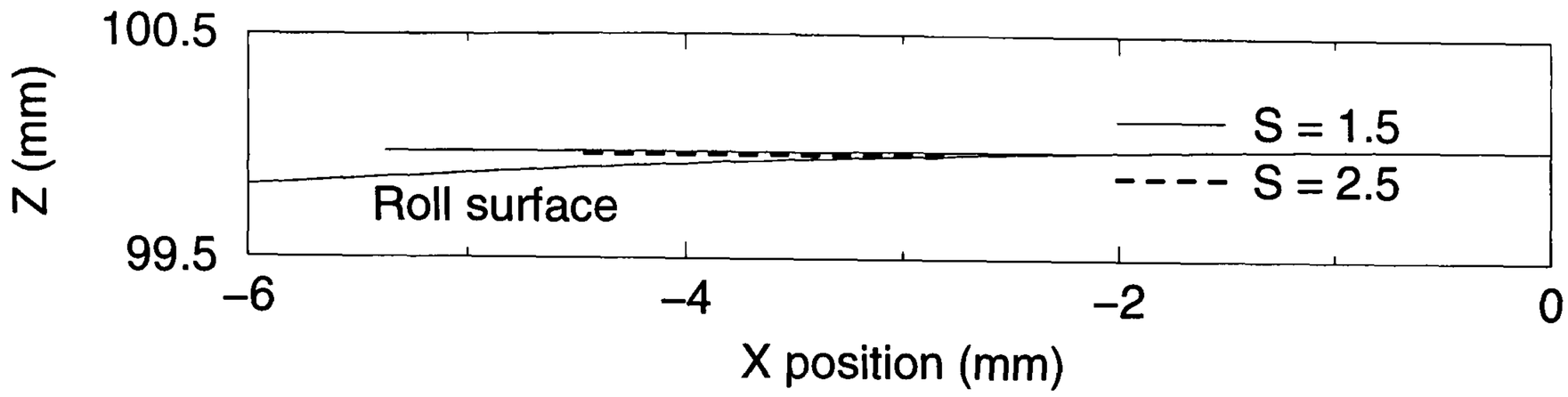

Figure 6.27: Typical web profiles for the roll–flexible web model. Conditions $U_2 = 0.25$ m/s and as per figure 6.25. Note the axes are on the same scale to illustrate the aspect ratio of the bead.

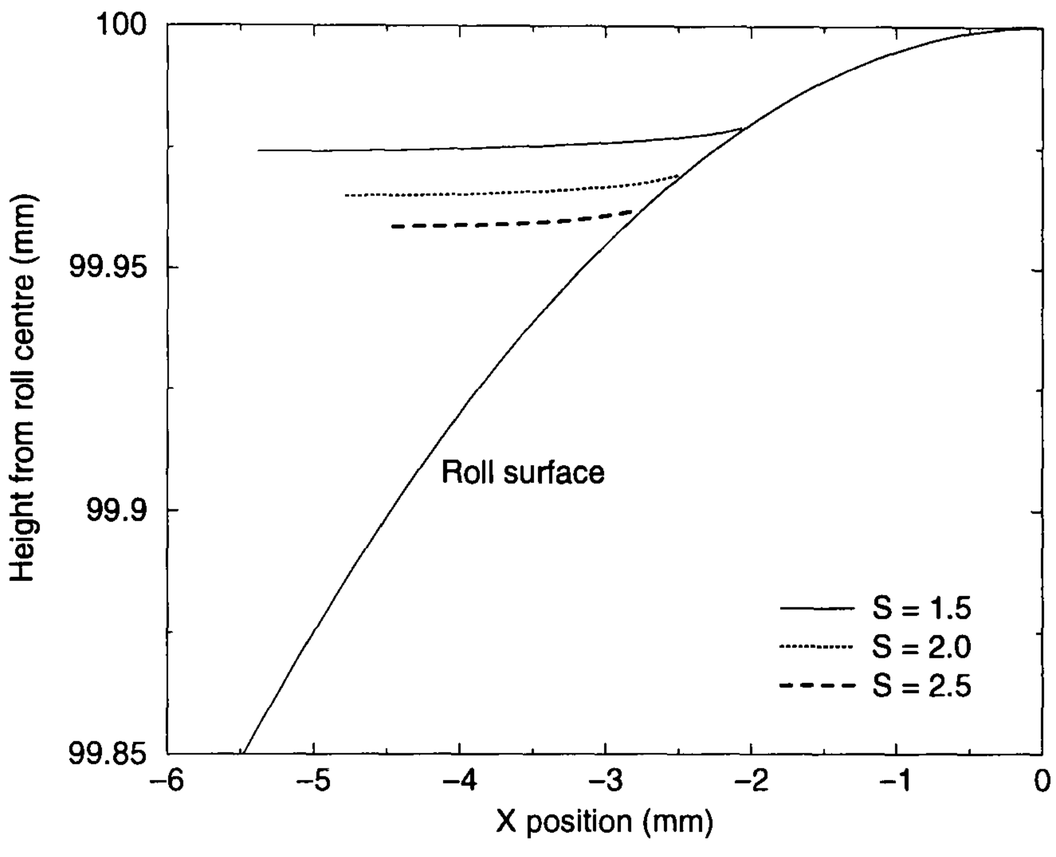

Figure 6.28: Typical web profiles for the roll–flexible web model. Conditions $U_2 = 0.25$ m/s and as per figure 6.25. Note the axes are not on the same scale.

Comparison with experimental results (FWM)

Figure 6.29 shows the comparison between the analytical predictions and the experimental measurements of the menisci positions. The results from this simple model are in good agreement with the experimental data — as the speed ratio is increased the upstream meniscus moves towards the top dead centre of the roll at X_0 and the

downstream meniscus moves away from X_0.

As expected, the agreement with experiments is much better than for the stiff web model, shown in figure 6.16, due to the inclusion of a flexible web.

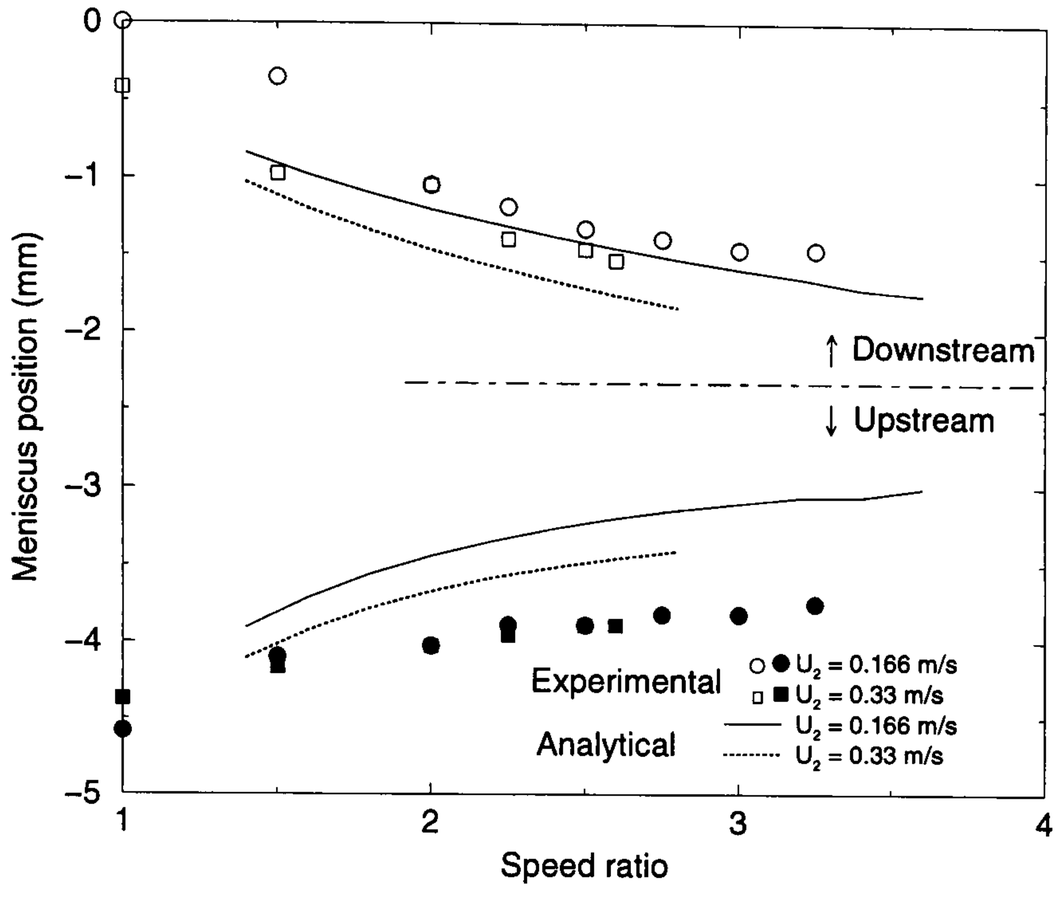

Figure 6.29: Comparison between the experimental meniscus positions and the predictions from the roll-flexible web model. All conditions as per figure 6.11. X_0 located at 0 mm.

6.5.5 Stability of the base flow (FWM)

An identical approach may be taken to analyse the stability of the meniscus for a flexible web–roll model as that used in the stiff web–roll model described in section 6.4.3; however the equations need to be cast in non–dimensional form. Equation (6.21) non–dimensionalised with respect to equation (6.25) leads to the following expression for the force at the downstream meniscus in the negative direction:

$$f = -\left(\frac{dp}{dx}\right)_{x_u} + \left(\frac{\sigma}{T}\right)\left(\frac{R}{H_U}\right)(2 + (S+1)aCa_1^b)\left(\frac{dh}{dx}\right)_{x_u}. \qquad (6.53)$$

where f is defined as $\left(f = \frac{1}{T}\left(\frac{R}{H_U}\right)^{1/2} F\right)$ and the sign of f will determine whether the perturbation will diminish, remain neutrally stable (the onset of ribbing) or

grow accordingly as:

$$\begin{aligned} f < 0 &\text{ the perturbation decays} \\ f = 0 &\text{ the perturbation remains neutrally stable} \\ f > 0 &\text{ the perturbation grows.} \end{aligned} \tag{6.54}$$

From equations (6.26) and (6.37) the pressure gradient term in equation (6.53) can be written as

$$\left(\frac{dp}{dx}\right)_{x_u} = \left(\frac{\alpha}{h^2}\right)_{x_u} = \alpha \quad \text{since} \quad h = 1 \quad \text{at } x_u, \tag{6.55}$$

and likewise from equation (6.43) the gradient in height can be rewritten, enabling the condition for neutral stability to be expressed as

$$\alpha = \frac{\sigma}{T}\frac{R}{H_U}(2 + (1+S)aCa_1^b)x_u. \tag{6.56}$$

Consequently, all that is required to determine if a base flow solution is stable are the physical parameters (the roll speed, speed ratio, inlet film thickness, roll radius, web tension and the fluid properties) and x_u from the base flow model for the roll–flexible web geometry described in section 6.5.1.

6.5.6 Results of the stability model (FWM)

Figure 6.30 shows the effect of the web tension on the stability of the bead. As the tension of the web is increased the critical speed ratio decreases. The reason for this is that as web tension increases the web flexes less, and as a result the meniscus at x_u moves towards its position predicted *via* the stiff web model. This results in a decrease in the stabilising force $\left(\frac{dh}{dx}\right)_{x_u}$ in equation (6.53).

As the web tension is increased, the critical speed ratio approaches the critical speed ratio predicted by the stiff web model asymptotically.

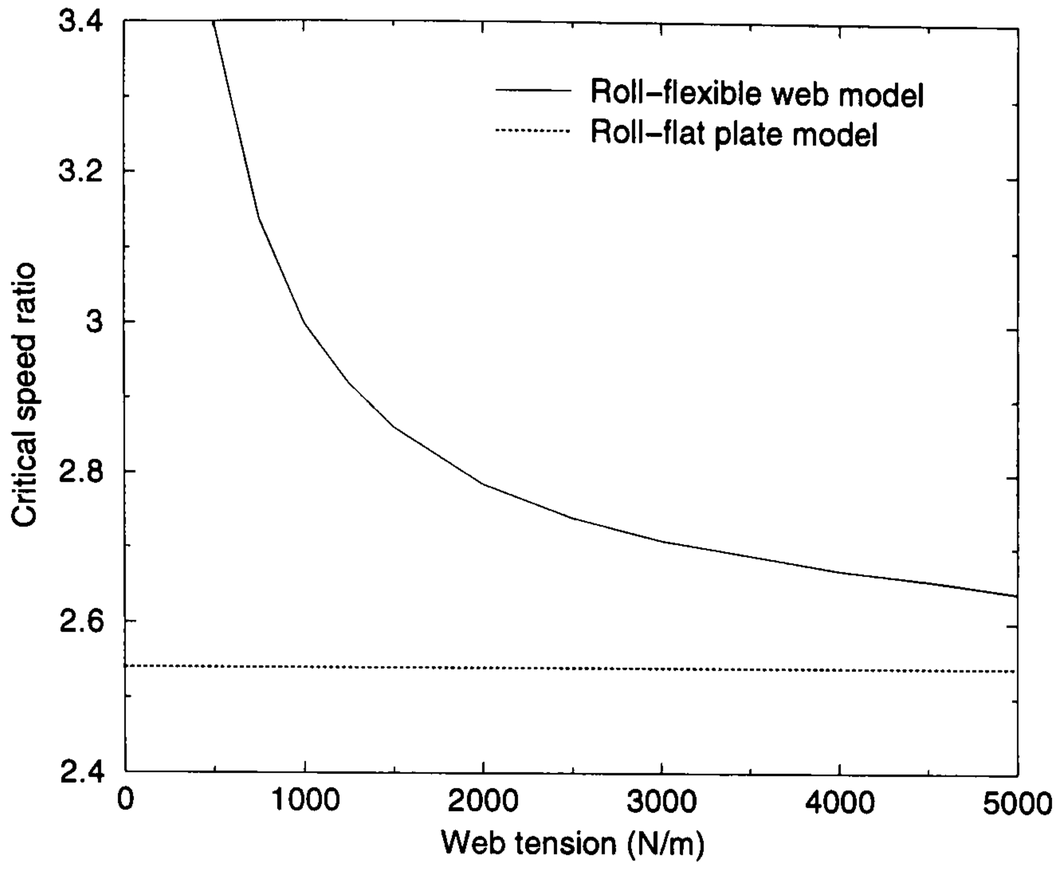

Figure 6.30: The effect of web tension on the critical speed ratio. Conditions $U_2 = 0.25$ m/s and as per figure 6.14.

Figure 6.31 shows the effect of roll speed on the critical speed ratio. As the roll speed is increased, the critical speed ratio decreases asymptotically. This was also observed for the stiff web model, as shown in figure 6.18. The critical speed ratio predicted from the roll–flexible web model is higher than that for the stiff web model, for the reasons stated above. Figure 6.31 also shows that a thicker inlet film has a stabilising effect; the most unstable bead, for a given roll speed, is the one with the thinnest inlet film. As for the roll–flat plate model, care must be taken when interpreting these results for typical industrial situations, see section 6.4.4.

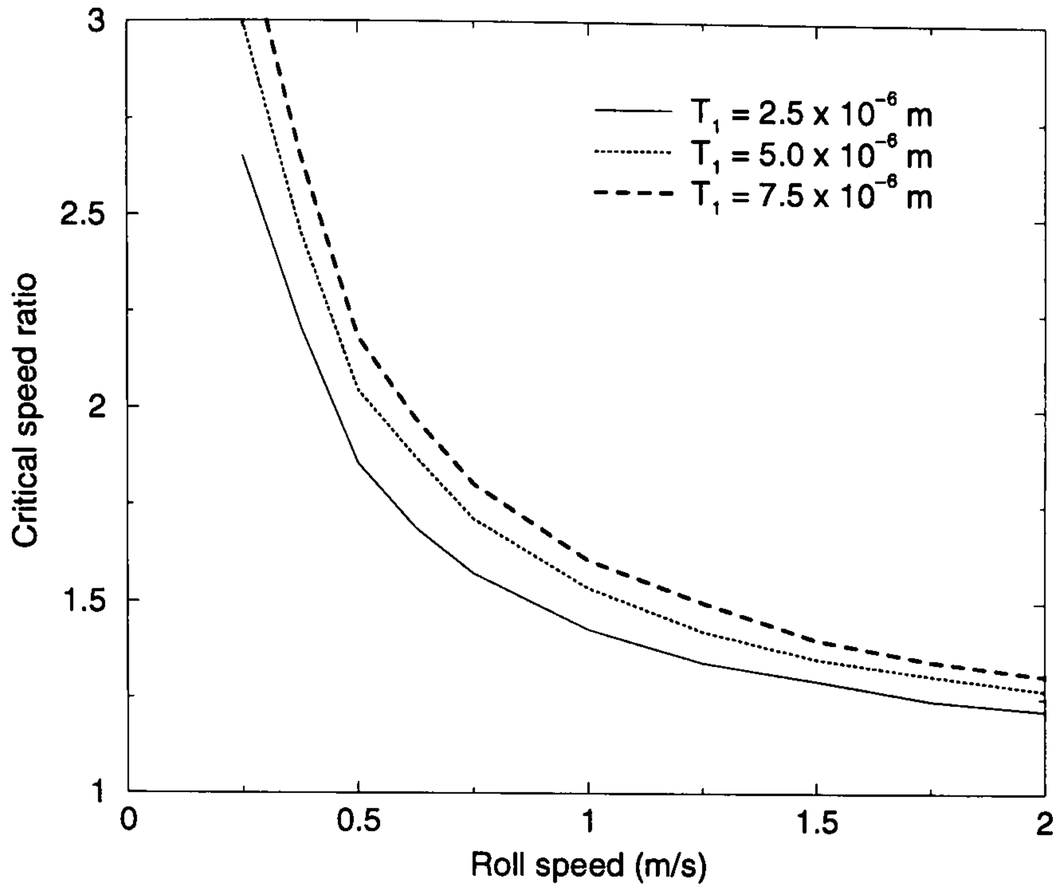

Figure 6.31: Effect of roll speed on the critical speed ratio for the onset of ribbing as predicted by the stiff web model. Conditions (other than inlet film thickness and roll speed U_2) as per figure 6.14.

Comparison with experimental results (SWM)

Figure 6.32 compares the experimental results for the onset of ribbing and the predictions of the simple stability hypothesis based on the roll–flexible web model. The model requires the film thickness H_i to be specified as an input parameter – this is taken from figure 6.7 since the offset gravure method is used to meter the inlet film in these experiments.

Once again, as for the stability of the stiff web model, the predictions are seen to be in good agreement with the experimental results, with the critical web speed increasing with the roll speed.

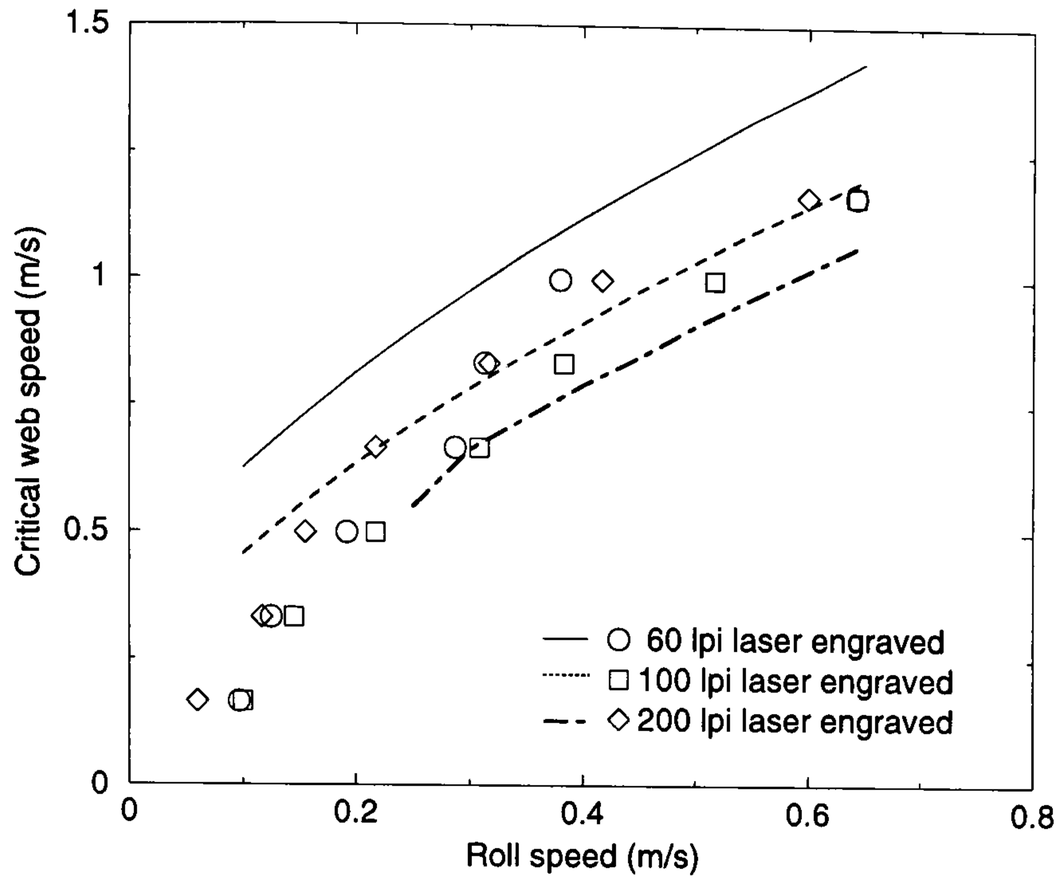

Figure 6.32: Comparison between the experimental (symbols) and analytic predictions (lines) from the roll flat plate model for the onset of ribbing. Conditions as per figure 6.12, inlet film thicknesses, H_i, for (FWM) model from figure 6.7.

6.6 Summary

A number of conclusions may be drawn from this work:

- The film thickness on the metering roll in an offset gravure coater can be influenced in two ways. Either increasing the nip force or decreasing the roll speeds causes a reduction in the metered film thickness.
- The choice of gravure pattern also influences the metered film thickness.
- At higher roll speeds, the metered film thickness tends to a limiting value, which depends on the choice of the gravure roll.
- For a kiss coater operating at $S > 1$, all the fluid is transferred from the metering roll to the web.
- A model based on lubrication theory incorporating a flexible web predicts well the positions of the upstream and downstream menisci.

- This model, used in conjunction with a stability hypothesis, gives predictions for the onset of the ribbing instability which are found to be in good agreement with the experimental data.

Chapter VII

Direct Gravure Coating

Contents

7.1 Introduction

This study is of a direct gravure coater where the roll is rotating in the opposite direction to that of the web, which passes over the roll with a tension T, and meets the roll at an angle β below the horizontal. The web is moving with speed U_1 and the roll with speed U_2 giving a speed ratio $S = \frac{U_1}{U_2}$. Fluid of viscosity μ, surface tension σ and density ρ is entrained from a bath, before being doctored by a blade held against the roll – the aim of which is to remove all fluid from above the 'lands' (the area between the gravure cells). The motion of the web passing over the roll causes a proportion of the fluid in the cells to be released as they pass the downstream meniscus; this is termed 'pickout'. The fluid is transferred to the web *via* a fluid bead that has a length in the axial direction of the roll, a width in the direction of the web motion and a height between the roll and web. Figure 7.1 illustrates the arrangement.

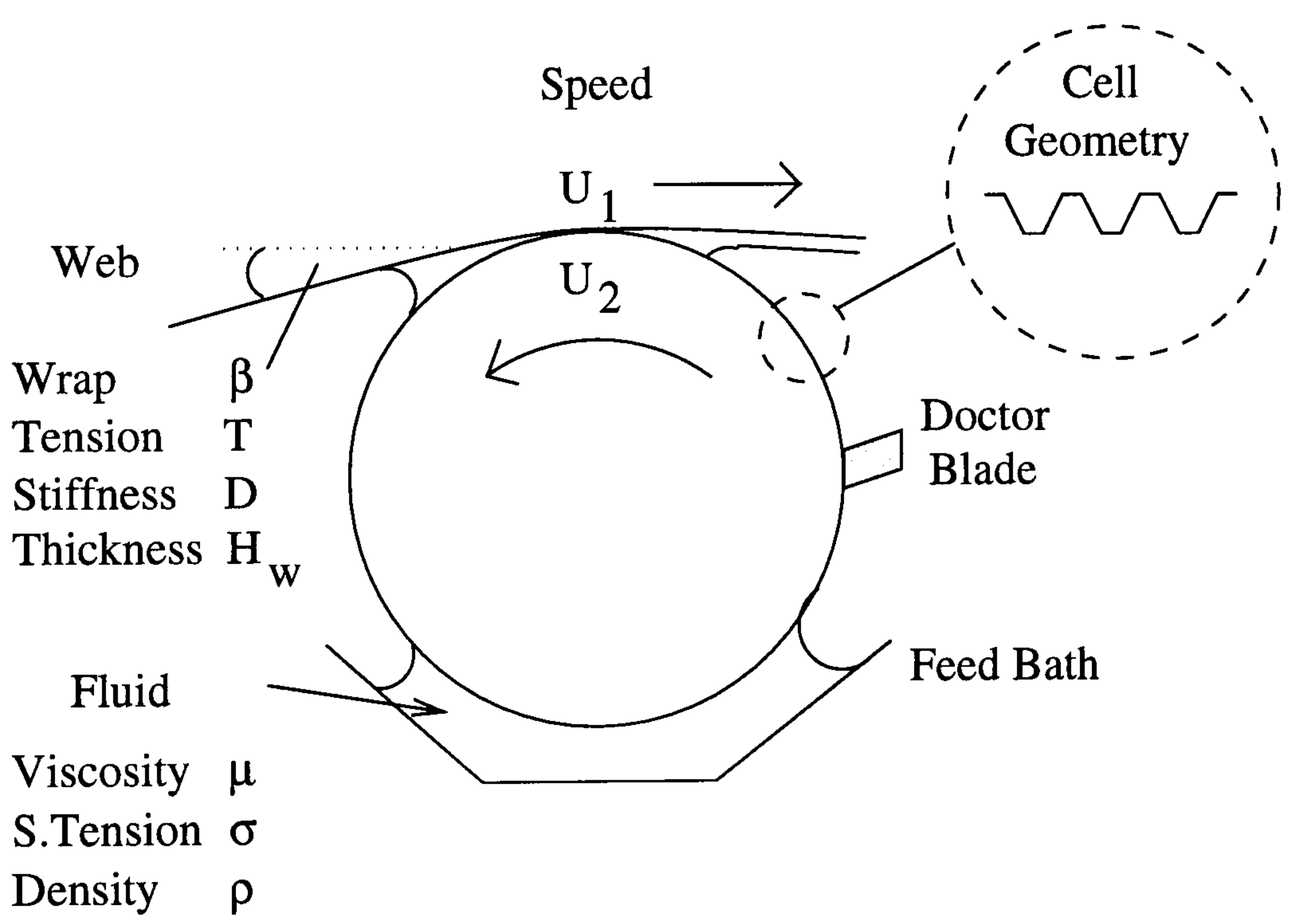

Figure 7.1: A schematic of a reverse direct gravure coater showing the variables in the system.

7.1.1 Definition of parameters

A range of non–dimensional parameters are used to describe the above gravure roll system. Although alluded to by others, this basis is shown here explicitly in the following section.

Parameters used in the present study

Consider a cell of volume V_1 with an opening of area A_1 that fits inside an area A_2 on the roll, as illustrated in figure 7.2.

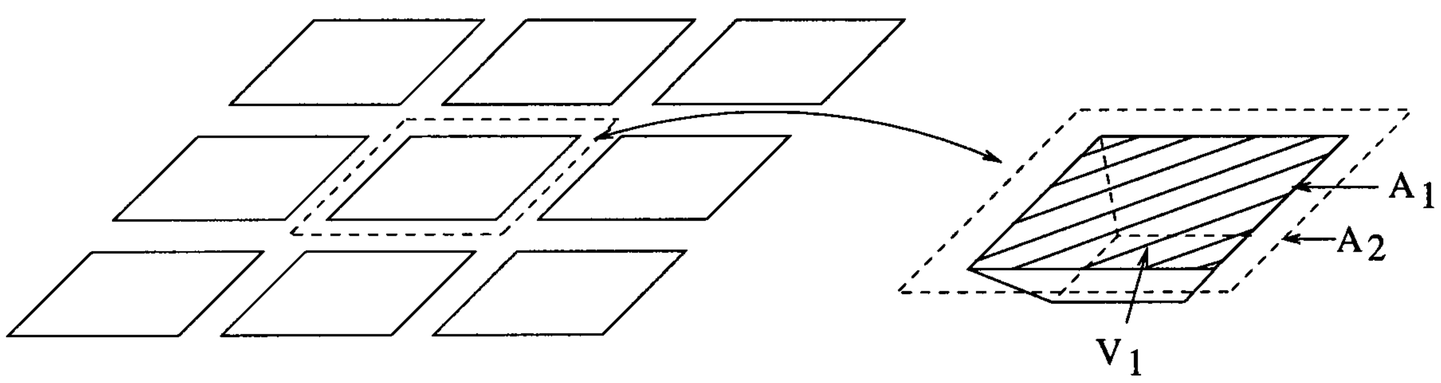

Figure 7.2: A typical array of cells and a unit cell.

- The cell volume, V_c, is defined as the volume of the cells per projected surface area of the roll and takes the dimensions of length. From figure 7.2 this is calculated as

$$V_c = \frac{V_1}{A_2}. \tag{7.1}$$

This value is equivalent to the film thickness the cell volume would give if it were spread onto a unit area of smooth roll and, as such, can be thought of as the inlet film thickness of the gravure roll.

- The fractional area of cell opening, A_c, is defined as the total area of cell opening per unit area of roll; in figure 7.2 this is shown as

$$A_c = \frac{A_1}{A_2}. \tag{7.2}$$

- The pickout is defined as the fraction of cell volume that is transferred to the

web in the coating operation, and can take a value of $0 \rightarrow 1$.

$$\text{Pickout} = \frac{\text{Flux on web}}{\text{Flux on roll}} = \frac{U_1}{U_2}\frac{H_1}{V_c} = S\frac{H_1}{V_c}, \tag{7.3}$$

where H_1 is the film thickness on the web.

Relation to the study to others

Pulkrabek and Munter (1983) describe the pickout in terms of equation (7.3) and their work is directly comparable with the studies described here.

Benkreira and Patel (1993) use a dimensional equation of the form

$$H_1 = const\frac{V_c}{A_c}, \tag{7.4}$$

to relate the film thickness on the web to the cell geometry, with the *const* being taken from experiments. Equation (7.4) can be rewritten as

$$H_1 = const\frac{V_1}{A_2}\frac{A_2}{A_1} = const\frac{V_1}{A_1}, \tag{7.5}$$

where $\frac{V_1}{A_1}$ is the actual average depth of the cell. In effect they are assuming that film thickness on the web is a constant fraction of the average depth of the cell (and is unaffected by speed ratio). Rewriting the above in terms of the pickout equation (7.3) gives

$$\text{Pickout}_{(BP)} = const\ \frac{S}{A_c}, \tag{7.6}$$

where $\text{Pickout}_{(BP)}$ denotes the pickout prediction due to Benkreira and Patel (1993). Although it is not made explicit in their paper it is clear that, by assuming a relationship of the form 7.4, it corresponds to a pickout that varies linearly with speed ratio.

Later Benkreira and Cohu (1998) describe results from a a study of forward gravure coating, that is where the web and roll surface move in the same direction, and

compare these with the same reverse data written as:

$$H_1 = const\ V_c, \tag{7.7}$$

where the experimentally determined value of *const* takes the same value of that in equation (7.4). In this case the pickout prediction of Benkreira and Cohu (1998) and earlier that due to Patel (1989) can be written as

$$\text{Pickout}_{(PBC)} = const\ S, \tag{7.8}$$

where once again pickout is proportional to S yet, rather surprisingly, the fraction A_c is absent. It is unclear which of the two equations, (7.4) or (7.8), is the intended one for use for design purposes.

7.1.2 Dominant factors in gravure coating

Figure 7.1 suggests that the gravure system under consideration can be broken down into a number of sub–systems, all of which can have an influence on the final coated film applied to the web. Each part of the system is reviewed below.

The feed mechanism

The feed mechanism is designed to supply an excess film to the doctor blade region where the blade removes the excess fluid from above the lands. Perhaps the simplest method, and that used here, is to place a reservoir of liquid below the roll and use viscous lifting to feed the doctor blade region, with excess liquid returned back to the bulk. This method does have some drawbacks. The gravure roll rotating in the liquid can cause air entrainment in the bath which could manifest itself on the coated web as bubbles, although no such defects were seen during the course of the experiments. An alternative method used by Patel and Benkreira (1991) is one where the fluid is pumped out of a small slot below the doctor blade.

A number of proprietary enclosed feed systems and fountain dies are available to

overcome the problems of air entrainment, foam generation, large volume liquid holdup and excessive solvent evaporation (Gravure Process and Technology, 1991).

The fluid properties

Little published work is available on the effect of fluid properties. Pulkrabek and Munter (1983) state that pickout from a trihelical gravure roll is inversely proportional to the fluid viscosity to a small degree, although it should be noted that their test fluids were non–Newtonian in nature, and the web and roll moved in the same direction. Benkreira and Patel (1993) suggest that, at high Reynolds number (greater than 75 where $Re = (\rho U_1/\mu) \times (V_c/A_c)$) the viscosity has no effect on the cell emptying characteristics, whilst at low web speeds they observe a slight decrease of film thickness with increasing viscosity.

Hanumanthu and Scriven (1996) showed that the capillary effects in reverse gravure coating with a backing roll (replacing the web) using a trihelical roll had no significant effect on flux.

The doctor blade

The doctor blade is of key importance in gravure coating. The blade should meter fluid off the lands whilst leaving the cells full. No theoretical work on the doctoring of gravure rolls is available in the literature, although the related problem of doctoring of fluid on a smooth roll with a trailing angle blade has been studied extensively (see for example, Saita and Scriven (1985), Pranckh and Scriven (1990)) and is illustrated in figure 7.3(a).

As discussed in section 1.5 for a trailing angle blade used to doctor a smooth roll, there is an interaction between the flexible blade and the hydrodynamic stresses generated in the fluid beneath the blade. No similar analysis is available for either a trailing angle blade on a gravure roll, or for a reverse angle blade on either a smooth roll or a gravure roll (figure 7.3(b)), although a reverse angle blade is commonly used where complete wiping of a roll surface is required (Pranckh and Coyle (1997)). The

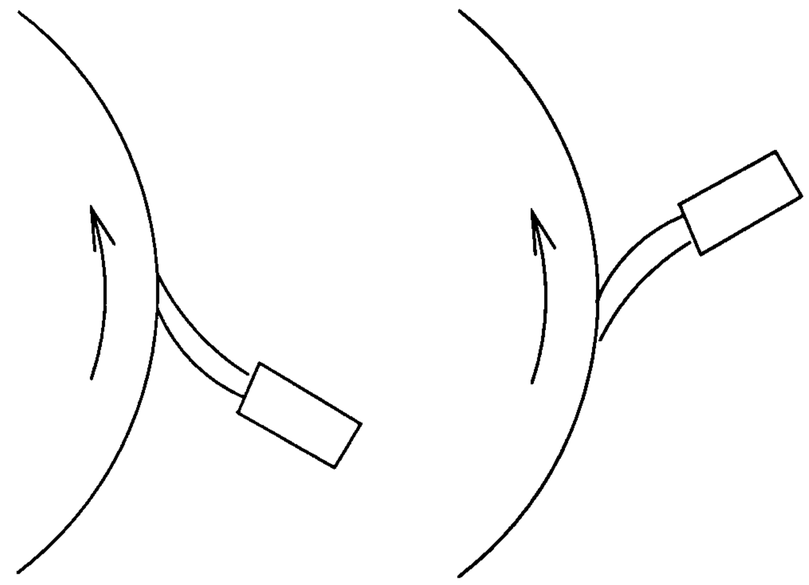

(a) (b)

Figure 7.3: (a) Trailing angle doctor blade and (b) reverse angle doctor blade.

printing industry have long used reverse angle blades to doctor a gravure roll (see, for example, Leach and Pierce (1993)).

Common materials for the blade include nylon, polyester or ultra–high molecular weight polyethylene of a thickness 0.15—0.25 mm. These have largely superseded spring steel blades to reduce roll wear (Leach and Pierce (1993)). The print industry typically use one of three methods to hold the blade against the roll: (i) pressure on the blade from a screw setting or using pneumatic cylinders; (ii) weights; (iii) pre-loaded springs. High speed presses often use a pre-doctor blade with 0.5 mm clearance to reduce the wear of the roll (Leach and Pierce (1993)).

Lindblad *et al.* (1988) carried out an experimental study of the doctoring of a tri–helical gravure roll with a trailing angle blade, and found that the blade can deform into the groove resulting in the cell being incompletely full. Munter (1998) has observed similar findings with a reverse angle blade.

Patel and Benkreira (1991) studied a similar system to the above but with a range of three gravure rolls. They varied the load on the doctor blade by changing the gap between the blade clamp and roll and found that as the gap was reduced the deformation of the blade caused the applied force to be spread over a wider area, resulting in a thicker film above the lands of the cells. They also showed that there was always a small residual film of fluid on the lands of the roll.

The web properties

The web passing over the roll has a thickness H_w and a bending stiffness D^*. Storey (1996) analysed the effect of including the bending stiffness terms in a lubrication type model for a kiss coater, and found that in practice D^* is so small as to make no difference to the shape of the web, the pressure field beneath it, or the film split. However no experimental evidence is available to substantiate this claim, either for a smooth or a gravure roll.

If the web is held against the roll with a tension, T, and meets the roll at a wrap angle β below the horizontal then the total load applied by the web is equal to $T \sin \beta$. Benkreira and Patel (1993) in a study of (reverse) direct gravure coating showed that varying the wrap angle over the range $0 - 12°$ had no discernible effect on final film thickness. They did not consider the effects of web tension, nor did they report the conditions at which this particular parameter was set.

The geometry of the gravure cell

The cell geometry has been identified as one of the most important parameters in controlling the average coat thickness. Pulkabrek and Munter (1983), in their study using a tri–helical gravure roll operating in the forward mode of operation, found that the quantity of fluid transferred to the web amounted to 59% of the volume of the cells. Benkreira and Patel (1993) in their study of reverse gravure coating concluded that the

$$\text{film thickness} = 0.3 \times \frac{\text{engraved volume per unit area of roll}}{\text{area cell opening per unit area of roll}},$$

independent of the engraving type. This result implies that the film thickness on the web is constant under all conditions. Later Benkreira and Cohu (1998) quote this result as

$$\text{film thickness} = 0.3 \times \text{engraved volume per unit area of roll},$$

see section 7.1.1 for further discussion on the significance of this.

Schwartz *et al.* (1998) modelled theoretically the liquid withdrawal from patterned (gravure) cavities by passing a substrate underneath a meniscus. However the boundary conditions they apply suggests that the model corresponds to laying down a layer over a patterned substrate.

The web and roll speed

In practice, the web and roll speeds of the reverse gravure system are selected such that $S \approxeq 1$ (Moussalli, 1998) where the speed ratio is defined as $S = \frac{U_1}{U_2}$. Again, the literature in this area is scarce. Benkreira and Patel (1993) suggest that their film thickness rule is valid for all speed–ratios.

7.1.3 Motivation for the study of reverse gravure coating

From the review above, it is clear that very little is known about reverse direct gravure coating, with little systematic experimental data reported in the open literature. Here an attempt is made to redress the balance and the effect of web properties, fluid properties and operating speeds on the final film thickness are systematically assessed. A second set of results report the film thickness and pickout data for a range of gravure rolls, to illustrate the important characteristics of the cell design. Finally the mechanism in the coating puddle that enables the fluid in the gravure cells to transfer to the web is investigated.

7.2 Experimental method

Experiments were carried out on the pilot coating rig described in section 2.3 and shown schematically in figure 7.1. Briefly, the carriage that holds the gravure roll is mounted below the web. Fluid is entrained from a coating pan beneath the roll, and doctored from the lands using a reverse angle doctor blade. The web meets the roll at a wrap angle β below the horizontal and is held with a tension T.

The flux on the web is measured by scraping the fluid using a wiper blade over a

known period of time (see section 2.5).

A monocular microscope was positioned directly above the web to visualise the fluid bead through the transparent web, and a CCD camera connected to a S-VHS video recorder was used to capture images of the bead (section 2.4).

7.2.1 Fluid properties

In total six aqueous test fluids were used in the study, the properties of which are shown in table 7.1. The viscosity was varied by mixing various concentrations of glycerine in water, figure 7.4, and surface tensions were varied by adding one of two surfactants – Syperonic-N (supplied by DuPont) to give a surface tension of 33×10^{-3} N/m or Lodyne-S103 (supplied by Ciba–Giegy) to give a surface tension of 22×10^{-3} N/m.

Fluid	Viscosity μ Pa s	Surface Tension σ N/m	Density ρ kg/m^3
A	1×10^{-3}	33×10^{-3}	992
B	2×10^{-3}	33×10^{-3}	1043
C	4×10^{-3}	33×10^{-3}	1088
D	1×10^{-3}	22×10^{-3}	992
E	2×10^{-3}	22×10^{-3}	1043
F	4×10^{-3}	22×10^{-3}	1088

Table 7.1: Physical properties of the fluids at $20°C$.

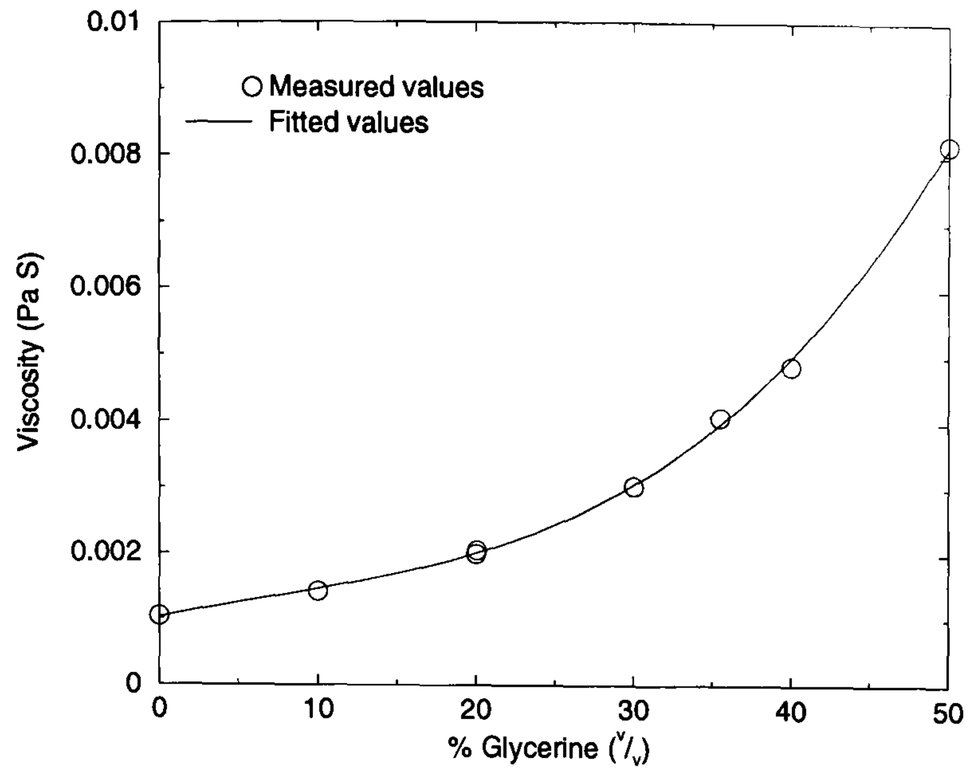

Figure 7.4: Blending chart for glycerine and water. Fitted function $y = 0.00102 + 5.05 \times 10^{-5}x - 1.33 \times 10^{-6}x^2 + 6.36 \times 10^{-8}x^3$.

7.2.2 The web

Three thicknesses of web were available for use in this study, as described in section 2.3.3.

7.2.3 The gravure pattern

Details of the gravure patterns for the four laser engraved rolls and two quadrangular rolls can be found in section 2.3.2.

7.2.4 Setting the doctor blade

The doctor blade plays a vital part in gravure coating. It is important to set the blade so the smallest possible liquid film is left on the lands. Here a reverse angle doctor blade (figure 7.3(b)) was used to remove the maximum quantity of fluid from the lands. A full study of the characteristics of reverse doctoring is beyond the scope of this thesis, however a range of data is collected here to validate the experimental method. The blade is positioned against the roll at an angle of 30°, as illustrated

in figure 7.5. It was found that angles greater than $40°$ caused the blade to vibrate against the roll — the most likely cause for this was 'dig-in' of the blade. Angles less than $15°$ were impractical with the current arrangement as the blade holder touched the roll surface. The doctor blade material was 175 μm thick melinex strip, held with 5 mm of blade exposed from the holder.

The force on the doctor blade was applied by a set of weights attached to the carriage of the blade. The weights used were in the range $1-10$ kg to give a force of between $75-750$ N/m. A 23 μm thick Melinex web was used in this study, with a wrap angle of $2.5°$ and web tension $T = 1000$ N/m. The roll was a 100 lpi laser engraved ceramic gravure roll.

Figure 7.6 shows the effect of increasing the applied force to the doctor blade on the flux on the web with all other parameters held constant. As the force on the doctor blade is increased the measured flux initially decreases. This is due to the reduction of film thickness above the lands causing a decrease in the transfer of fluid to the web. Increasing the force past the broken vertical line in figure 7.6 has no effect on the measured flux, so it is likely that only a minimum amount of fluid remains on the lands. With the loads used in this study the wear on the doctor blade became significant against the ceramic roll, and although it would be impractical in an industrial situation to meter the film in such a way, this does allow us to study direct gravure coating with a minimum residual film. No effect of blade length on pickout was noted (over the range 5 mm for a new blade and 3 mm for a worn blade), giving a repeatable method of doctoring the roll in direct gravure coating.

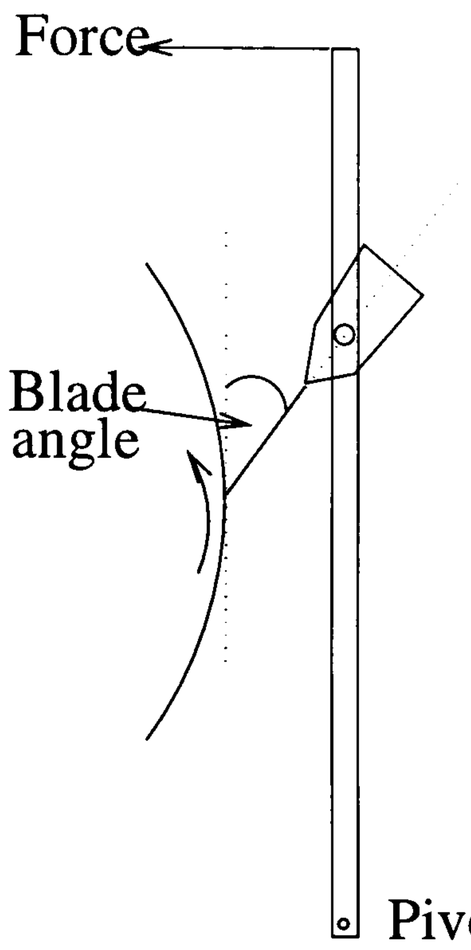

Figure 7.5: The arrangement of the doctor blade against the gravure roll.

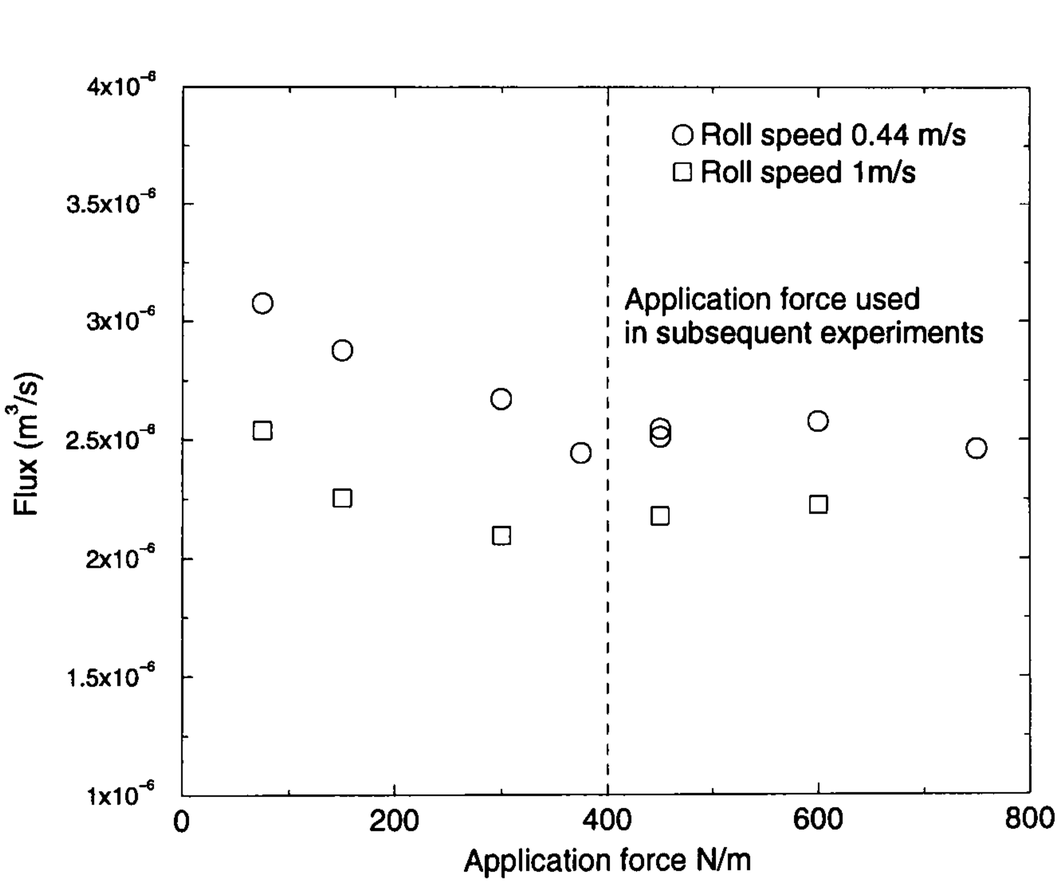

Figure 7.6: The effect of the force applied to the doctor blade on pickout. The broken vertical line shows the operating condition used for the rest of the experiments presented in this chapter. Conditions: web speed 0.66 m/s, 100 lpi laser engraved ceramic roll, test fluid A, 23 μm thick web, web tension 1000 N/m, wrap angle 2.5°.

7.3 Results and discussion

7.3.1 The effect of web load on pickout

The web load is controlled by two parameters, the wrap angle, β and the tension T. The effect of each of these parameters on pickout is considered independently.

Figure 7.7 shows the effect of wrap angle on the pickout of the gravure cell for the 100 lpi laser engraved ceramic roll, using test fluid A, a web of thickness 23 μm and a constant tension of 1000 N/m and 3 speed ratios with a constant roll speed of 0.66 m/s. It is clear from this figure that at low speed ratio $S = 0.66$ and 1.0, the wrap angle has no effect on the pickout from the gravure cell. At the higher speed ratio, $S = 1.5$, pickout decreased slightly as the wrap angle is increased, although this effect is small – less than 5% decrease over the range $\beta = 1°$ to $5°$. This result is in accord with Benkreira and Patel (1993) who similary detected no variation of film thickness with wrap angle over the range 0 to 12°.

Figure 7.8 similary shows that as web tension is increased, for a fixed wrap angle of 2.5°, no variation in pickout was measured for each of the 3 values of speed ratio. If the load, given by $T \sin \beta$, was a controlling parameter in determining the flux then at the higher speed ratio, $S = 1.5$, one may expect a decrease in flux as the tension is increased, corresponding to the decrease in flux with wrap angle (figure 7.7). This suggests that load is not the controlling parameter, rather the wrap angle of the web, and this only to a small degree.

Due to insensitivity of pickout with respect to wrap angle and web tension, these two parameters are held constant at $\beta = 2.5°$ and $T = 1000$ N/m (typical values that are used in production) for the remainder of the study.

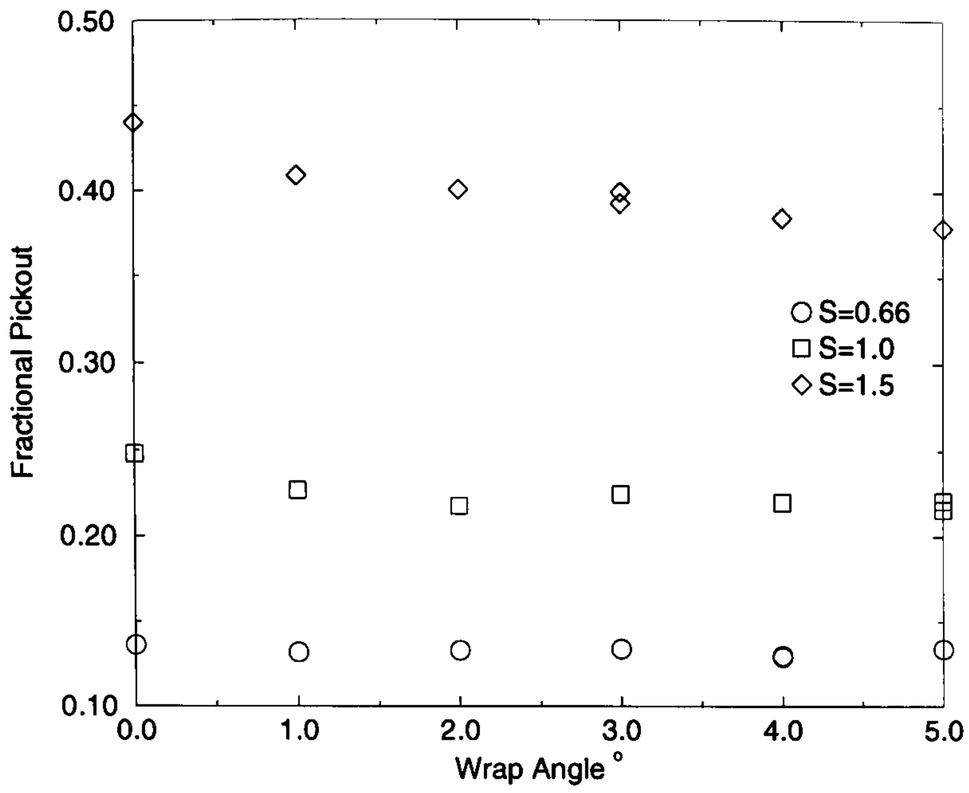

Figure 7.7: The effect of web wrap on pickout. Conditions roll speed 0.66 m/s, 100 lpi laser engraved ceramic roll, test fluid A, 23 μm thick web, web tension 1000 N/m.

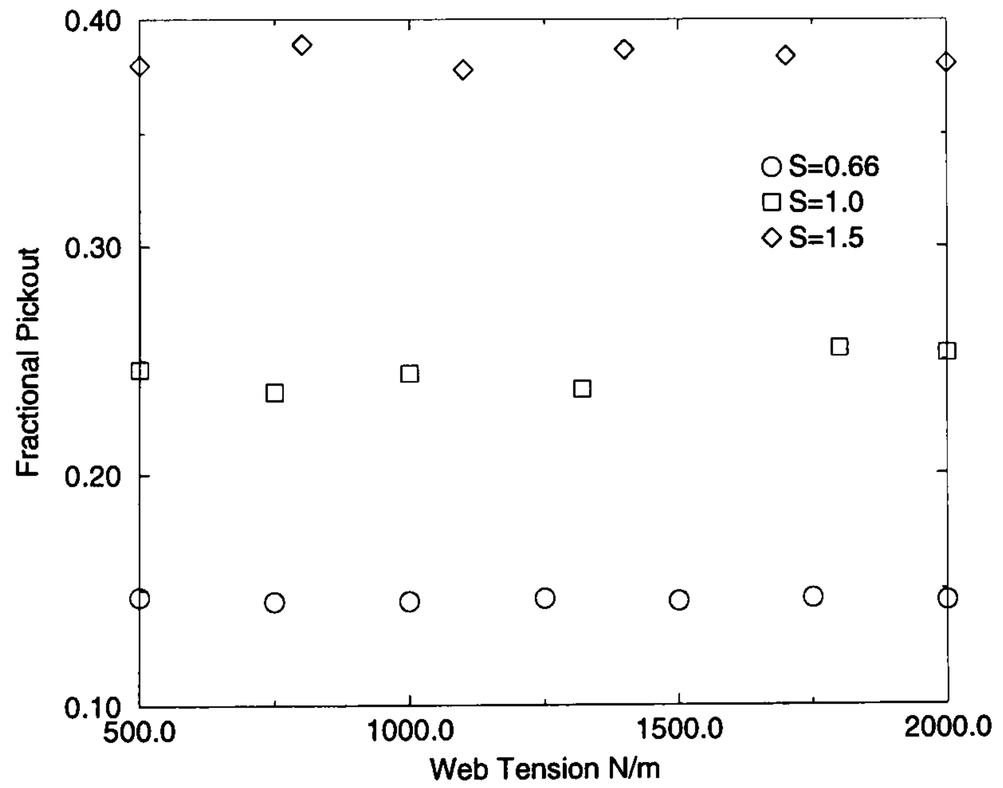

Figure 7.8: The effect of web tension on pickout.Conditions: roll speed 0.66 m/s, 100 lpi laser engraved ceramic roll, test fluid A, 23 μm thick web, wrap angle 2.5°.

7.3.2 The effect of web thickness on pickout

Data for 23 μm, 36 μm and 50 μm thick Melinex substrate are reported; thicker substrates (up to 175 μm) were not considered. The 50 μm substrate had a sputtered aluminium coating on one side although this was very thin (less than 1 μm thickness) and so unlikely to affect the bending stiffness of the web. The data were taken with a 100 lpi laser engraved ceramic roll, fluid A was used in these tests, the roll speed was kept constant at 0.66 m/s and the web speed varied.

Figure 7.9 shows the pickout as a function of speed ratio for the three web thicknesses. From this figure it is clear that, at least over the range investigated, there is no effect of substrate thickness on pickout. Consequently, results presented in subsequent sections are all collected using a 23 μm thick web.

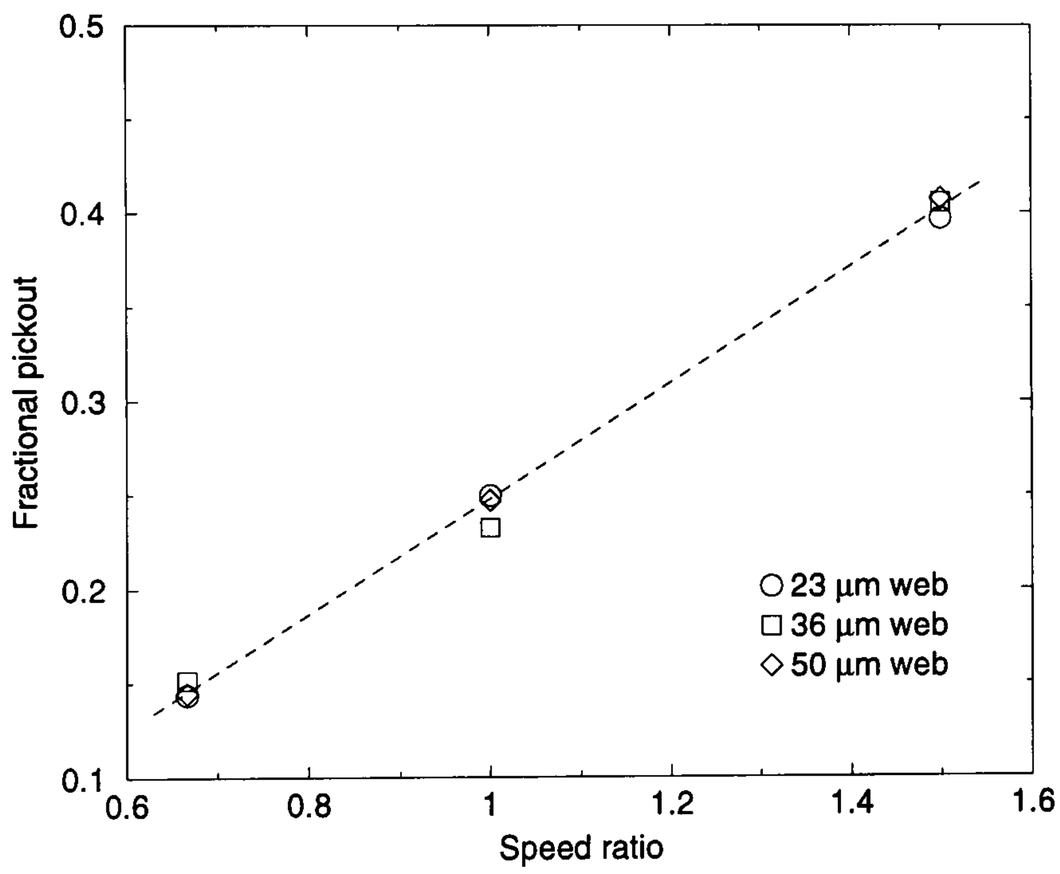

Figure 7.9: The effect of web thickness on pickout. Conditions: roll speed 0.66 m/s, 100 lpi laser engraved ceramic roll, test fluid A, web tension 1000 N/m, wrap angle 2.5°.

7.3.3 The effect of speed ratio on pickout

Coat weight was measured as a function of speed ratio for three different roll speeds. Figure 7.10 shows the measured film thickness on the substrate, and figure 7.11 the pickout from the cells, both as a function of speed ratio.

The plot of film thickness for a roll speed of 0.33 m/s — figure 7.10 — is chosen for discussion as it is covers the widest range of speed ratio. As the speed ratio is increased the film thickness on the web increases almost linearly until $S \approx 1.5$. Further increase in speed ratio does not result in any significant change to this limiting value of film thickness, until a speed ratio of $S \approx 3.5$ is reached, at which point the bead is observed to break up and streaking is seen on the web. This upper limit of speed ratio in gravure coating is discussed in section 7.3.7. Figure 7.10 also shows that as the roll speed is increased, then for a given speed ratio (i.e. the web speed has also been increased by the same fraction) the film thickness increases. At higher roll speeds, the same trend of film thickness increasing linearly with speed ratio is also observed. However, due to limitations of the upper speed of the coating apparatus, data to confirm the levelling off of the film thickness at higher speed ratios was unobtainable.

Figure 7.11 shows the same data with pickout plotted against speed ratio. It is immediately obvious that as speed ratio is increased the pickout of the cell increases. The relationship between pickout and speed ratio appears almost linear, particularly (in this case) for $S > 1$. For a given speed ratio, increasing the roll speed increases the pickout from the cell slightly.

Discussion

Interpretation of the above data gives rise to two key results:

1. Figure 7.11 shows pickout increasing with S, which is a quite unexpected result and one which has not appeared previously in the literature. It implies that, for a constant roll speed (and hence constant inlet flux) pickout increases with web speed.

Consider the data, figure 7.10, for a roll speed of 0.33 m/s - the curve can be approximated by two regions; where for (i) low speed ratio $S \leqslant 1.5$, $H \propto S$ and (ii) higher speed ratios $S \geqslant 1.5$, $H = const.$ Using equation (7.3) which relates pickout to film thickness it follows that in:

region (i)

$$\text{Pickout} \propto S^2, \quad S \leqslant 1.5 \text{ and}$$

region (ii)

$$\text{Pickout} \propto S, \quad S \geqslant 1.5.$$

Hence the conclusion from these experimental results is that for small speed ratios

$$\text{Pickout} \propto S^2 \quad (H \propto S)$$

while at higher speed ratios

$$\text{Pickout} \propto S \quad (H = const).$$

We can now return to the results of Benkreira and Patel (1993) and set them in this context. They concluded that, over their range of experiments, H remained effectively constant. This suggests that they were operating in the 'large S' regime where $H = const$ and pickout increases linearly with S (although, of course, the latter connection was not made).

2. The variation of film thickness with speed ratio has important practical implications. Available literature in the area would suggest that the only way to change film thickness is to change the gravure roll, whereas data presented here shows that speed ratio may be used to modify the final film thickness. Gravure coating is used to coat within quite a narrow band of film thicknesses — between 1 μm and 10 μm (Moussalli, 1998) and small changes in speed ratio can result in a large relative change in the final film thickness of $100 - 150\%$. This can be significant in many industrial operations, for example where increases in the film speed may be limited by drier capacity. Reducing the film

thickness by only a small amount could result in a corresponding increase in web speed, production and, ultimately, revenue.

A comparison between these experiments with the data of Benkreira and Patel (1993) is given in section 7.3.5.

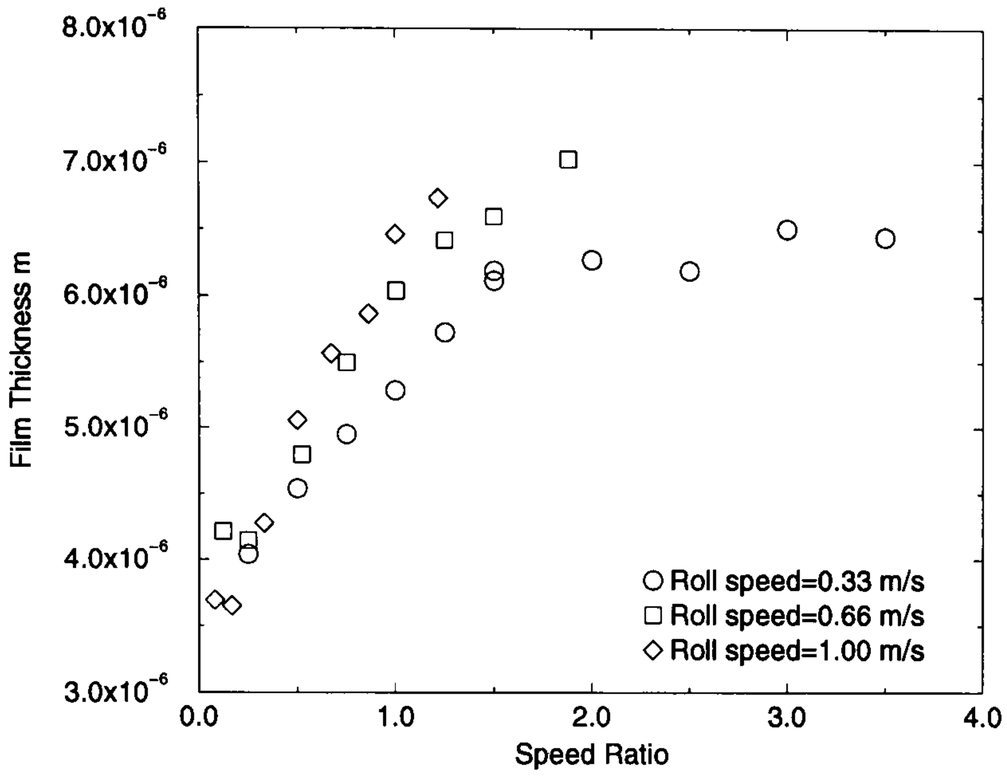

Figure 7.10: The effect of speed ratio on film thickness. Conditions: 100 lpi laser engraved ceramic roll, test fluid A, web thickness 23 μm, web tension 1000 N/m, wrap angle 2.5°.

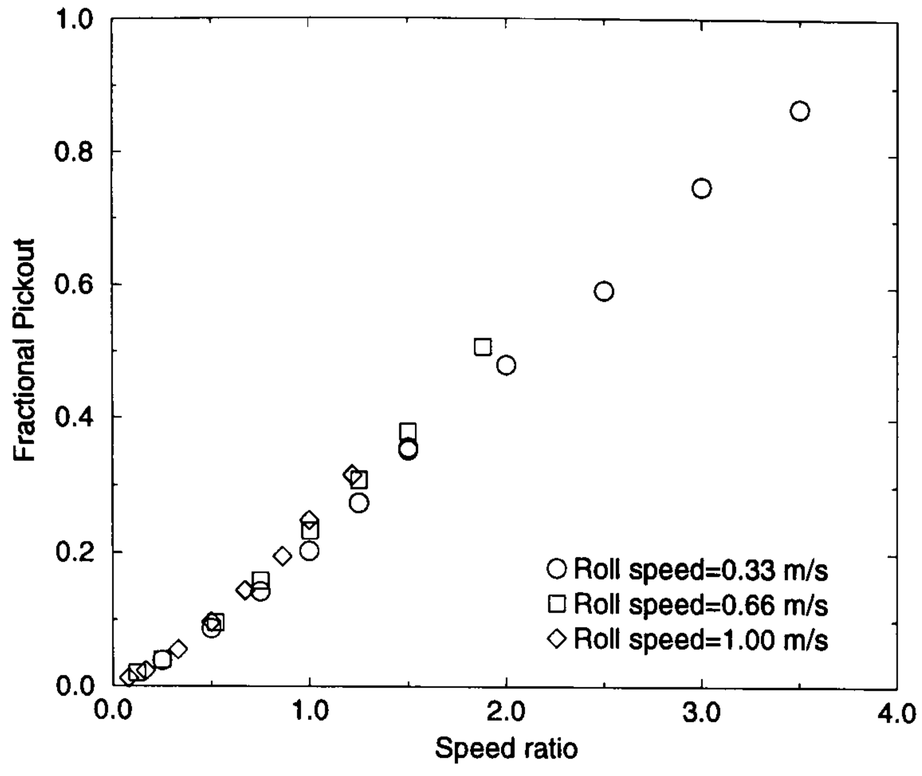

Figure 7.11: The effect of speed ratio on pickout. Conditions as per figure 7.10

7.3.4 The effect of fluid properties on pickout

The viscosity of fluids used in gravure coating typically lies in the range of 0.2 to 2 mPa s (Booth, 1970). The surface tension of aqueous fluids is generally between the range 18.7 mN/m and 72.9 mN/m although it was found that the maximum surface tension that allowed the Melinex web to be wetted was in the range 40 to 50 mN/m. The properties of the test fluids are shown in table 7.1 and the 100 lpi laser engraved ceramic roll was used. Figure 7.12 shows the effect of speed ratio on pickout for the six test fluids. For a given speed ratio an increase in viscosity resulted in an increase in the emptying behaviour from the cell, and hence a larger film thickness.

One possible explanation for this is that the increase in fluid viscosity causes a greater hydrodynamic stress beneath the blade (observed for a trailing angle blade running against a smooth roll (Pranckh and Scriven (1990)) resulting in a greater residual film on the lands of the gravure roll, although there are no studies to quantify this effect for the reverse angle case. However at low speed ratio, $S = 0.25$,

the pickout (figure 7.12) for the three fluids of differing viscosity (but the same surface tension) from the cell is identical. As the roll speed is kept constant during the test then any observed effects must be due to the gravure action in the top puddle. At higher speed ratios the effect of increasing the viscosity becomes more marked, with a higher viscosity fluid exhibiting larger pickout than a lower one.

Decreasing the surface tension of the liquid also results in a greater pickout from the cells. Again the effect becomes more marked as speed ratio is increased. For all cases increasing the speed ratio results in an increase in pickout from the cell.

The non–dimensional group that one associates with surface tension, speed and viscosity is capillary number. Indeed these findings show that this group is likely to be of importance here, with pickout increasing with viscosity and web speed, but decreasing with surface tension.

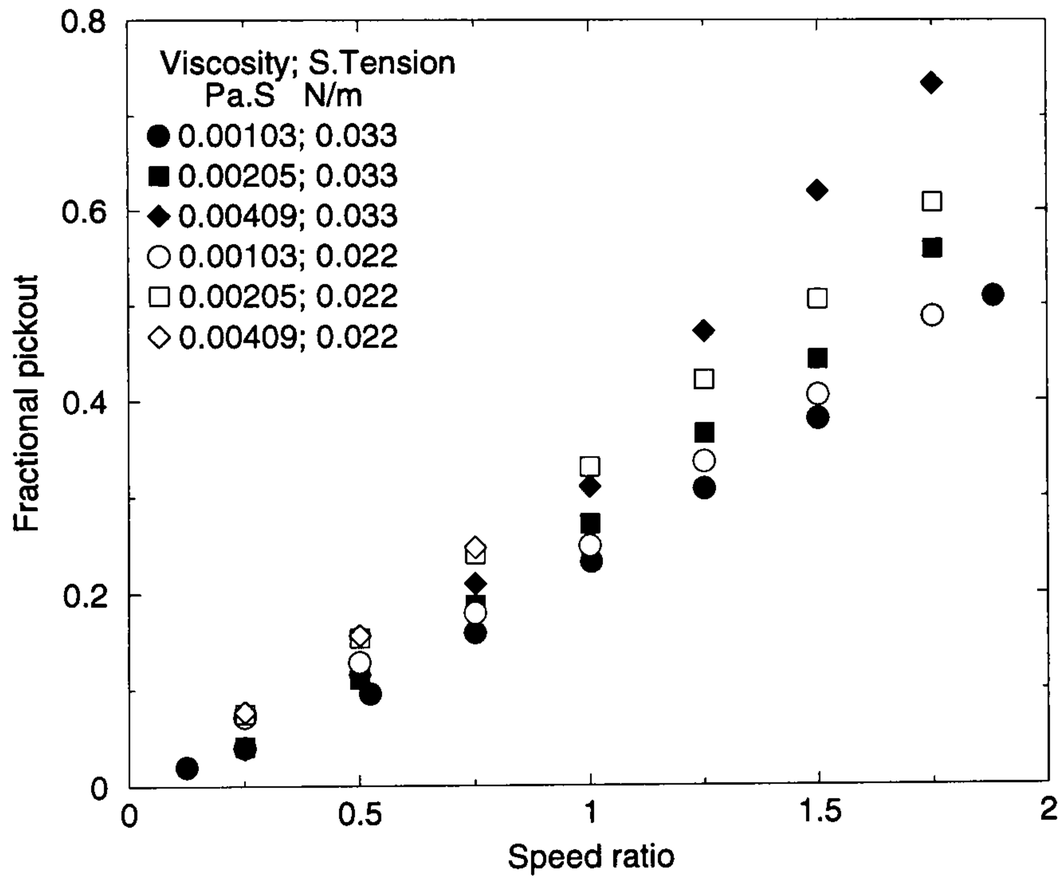

Figure 7.12: The effect of fluid properties on pickout. Conditions: roll speed 0.66 m/s, 100 lpi laser engraved ceramic roll, web thickness 23 μm, web tension 1000 N/m, wrap angle 2.5°.

7.3.5 The effect of cell geometry on pickout characteristics

Cell geometry plays an important part in determining the final film thickness in gravure coating. Here results found using six different gravure rolls described in section 2.3.2 and test fluid A (table 7.1) are reported.

Figure 7.13 shows the film thickness as a function of speed ratio for the six gravure cell patterns. In all cases film thickness increases with speed ratio, for a given roll speed; hence S may be used as a controlling parameter. Figure 7.14 shows film thickness as a function of cell volume at a speed ratio $S = 1$. Film thickness is clearly influenced by more than just cell volume, it also depends on the cell pattern and size. Figure 7.15 shows pickout data for the same six rolls. Considering a speed ratio $S = 1$ and just the laser engraved rolls, the 60 lpi roll has the highest pickout, followed by the 300 lpi, 100 lpi and 200 lpi rolls.

For the cells of the 60 lpi, 100 lpi and 200 lpi rolls, which all have similar aspect ratios (shown in figure 2.15), it is observed that the larger the cell the greater the pickout. However the cells of the 300 lpi roll exhibit greater pickout than those of both the 100 and 200 lpi rolls despite their smaller cell size (and even those of the 60 lpi roll at $S > 1.25$). This could be due to the larger aspect ratio of the cells on the 300 lpi roll, or smaller spacing between the cells (i.e. a small land area), or a combination of these two factors.

In contrast when one considers the quadrangular range of roll patterns then, despite the 200 lpi cell having a higher aspect ratio than the 60 lpi quadrangular cell, the pickout is only about half as efficient. This could be due to the smaller physical size of the cell or the higher land area (i.e. greater spacing between the cells).

Comparison of the pickout from the laser engraved rolls and the quadrangular rolls shows that for similar cell density patterns (60 lpi quadrangular and 60 lpi laser engraved, or 200 lpi quadrangular and 200 lpi laser engraved) the pickout is more efficient for laser engraved ceramics, despite their having a smaller volume per unit area and larger aspect ratio.

The effects of cell geometry and spacing are clearly very complex, with few general

rules, however from the above results the following conclusions can be drawn:

- Film thickness is a function of speed ratio for all cell patterns tested (with constant fluid properties).
- At a given speed ratio the film thickness is dependent on the geometry of the cell – not just the volume – with the cell aspect ratio, the cell spacing and the cell shape all affecting the pickout.
- Laser engraved ceramic patterns have better release characteristics than quadrangular rolls, for similar sized and spaced cells.

Possibly the most important observation in practice is that of control of the film thickness by altering the speed ratio. Here it was observed that the film thickness measured at $S = 0.5$ could be increased by between 25% and 110% depending on the cell pattern by increasing the speed ratio to $S = 1.75$. Secondly, when specifying a gravure roll from a vendor it is common practice just to specify the gravure cell count and the volume. However, this does not necessarily mean that two rolls specified in this way will come with cells of the same aspect ratio in which case the pickout characteristics of the rolls will be different. To be sure of an identical roll the cell volume, cell count and either the aspect ratio or the fractional opening of the cell would need to be specified.

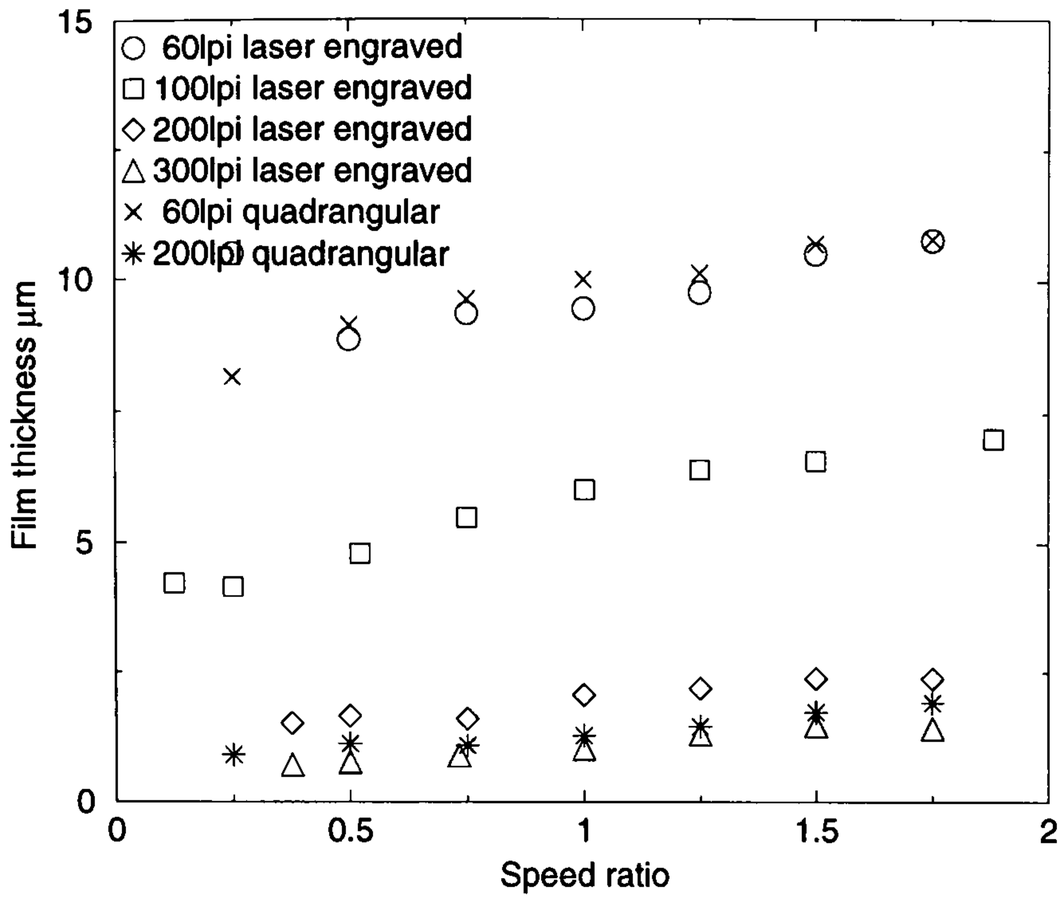

Figure 7.13: The effect of speed ratio on film thickness for a selection of gravure rolls. Conditions: roll speed 0.66 m/s, test fluid A, web thickness 23 μm, web tension 1000 N/m, wrap angle 2.5°.

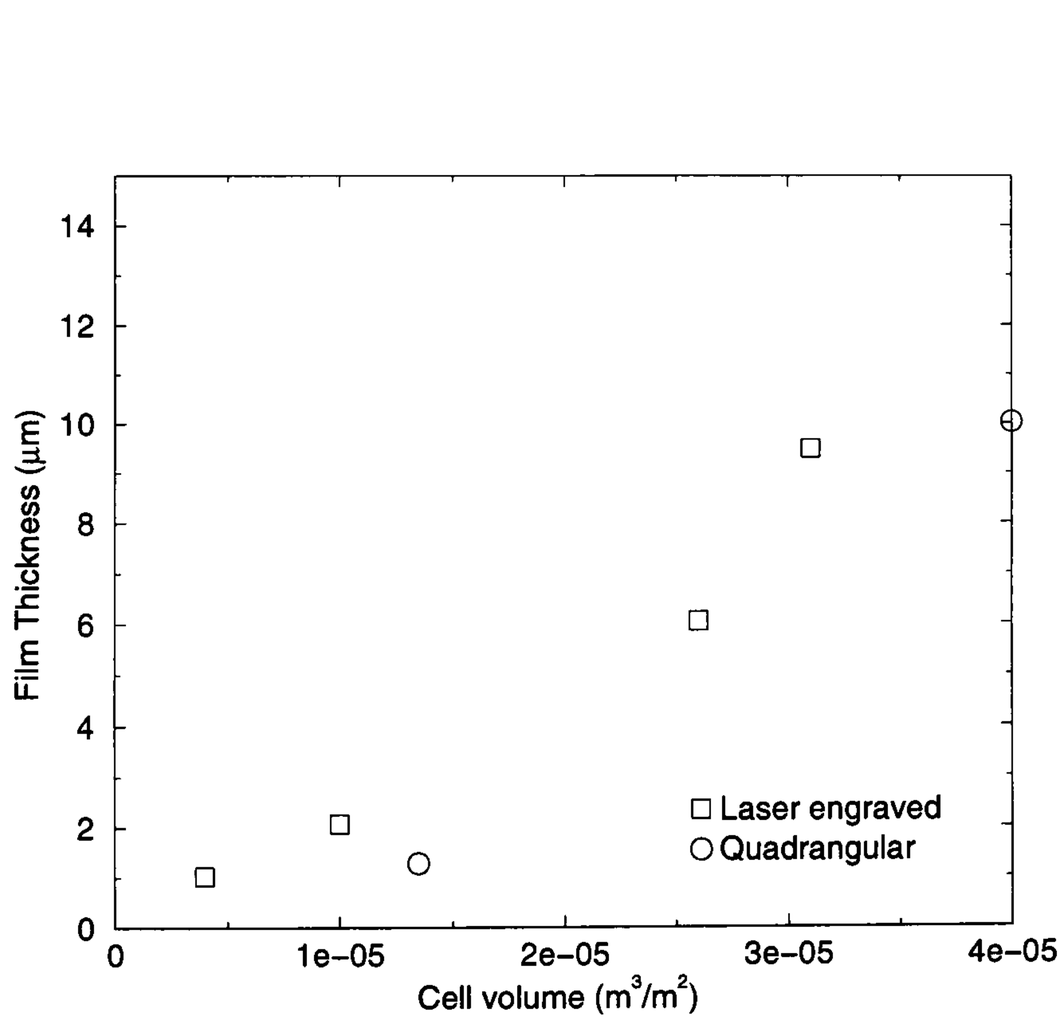

Figure 7.14: The effect of cell volume on film thickness at $S = 1$. Conditions as per figure 7.13.

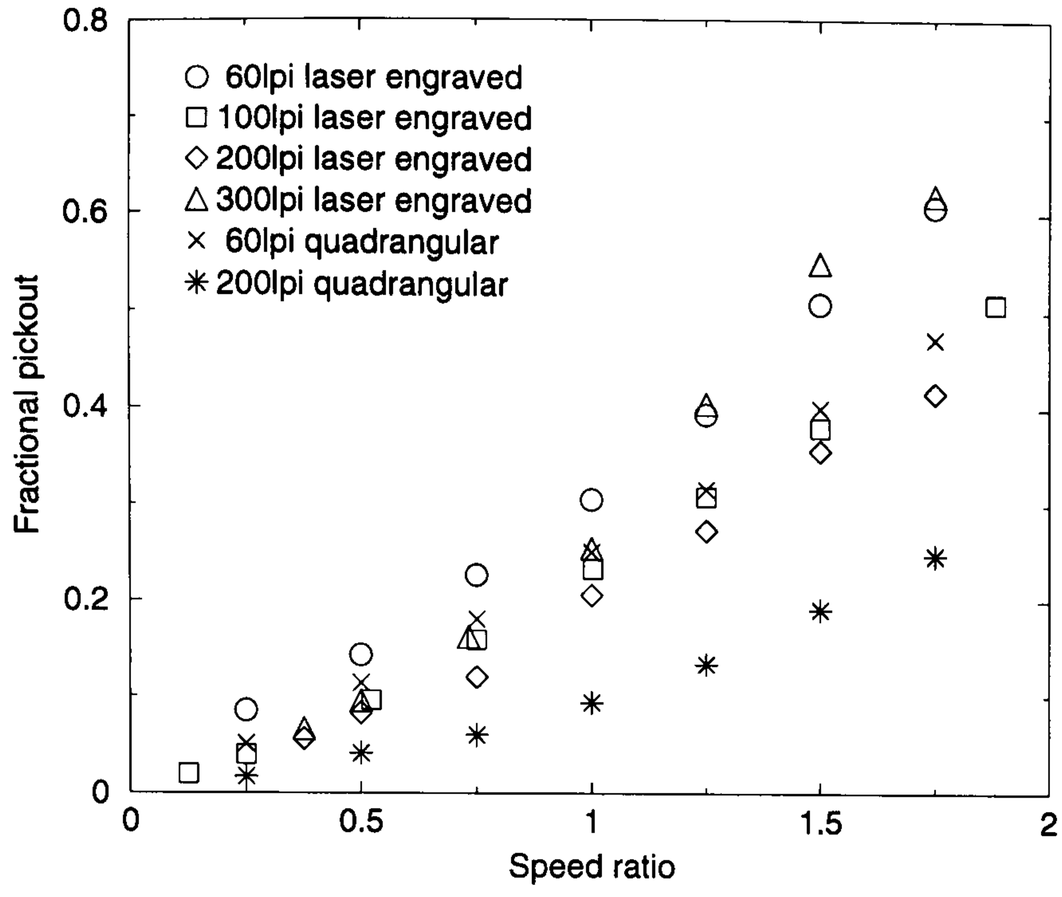

Figure 7.15: The effect of speed ratio on pickout for a selection of gravure rolls. Conditions as per figure 7.13.

Comparison with other workers

The results from this section are compared with the experimental results of Benkreira and Patel (1993) who relate the film thickness to the geometry of the cell *via* an empirical relationship, as discussed in section 7.1.1. The value of *const* in equation (7.4) is taken as 0.3 from their work.

As shown in figure 7.16 the design equation they propose consistently over-predicts the actual film thickness, in some cases by over 1500%. The comparison of pickout fractions is made in figure 7.17. Once again the pickout is over-predicted by a gross margin, and in many cases predicts a pickout of greater than one, clearly impossible unless the doctor roll was incompletely doctored. It is this authors opinion that the basis of modelling the gravure system used by Benkreira and Patel (1993) is fundamentally flawed as it will never be able to reproduce the behaviour of the gravure systems investigated in this thesis.

Pulkrabek and Munter (1983) record an average value of pickout of 0.59, which is within the range shown here, although this is from a *forward* direct gravure system.

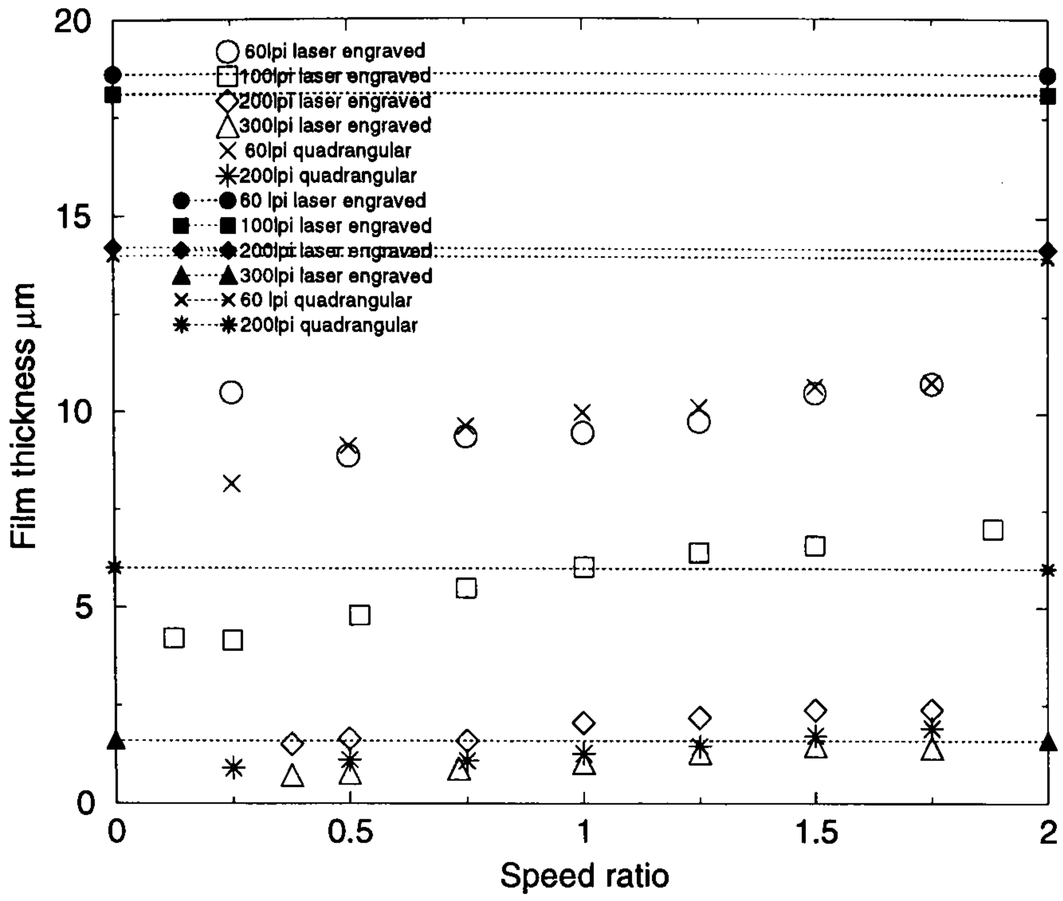

Figure 7.16: A comparison of film thickness H_1 from the experimental data of this study (unfilled symbols) and the predictive model of Benkreira and Patel (1993) (filled symbols and dotted lines). Conditions as per figure 7.13.

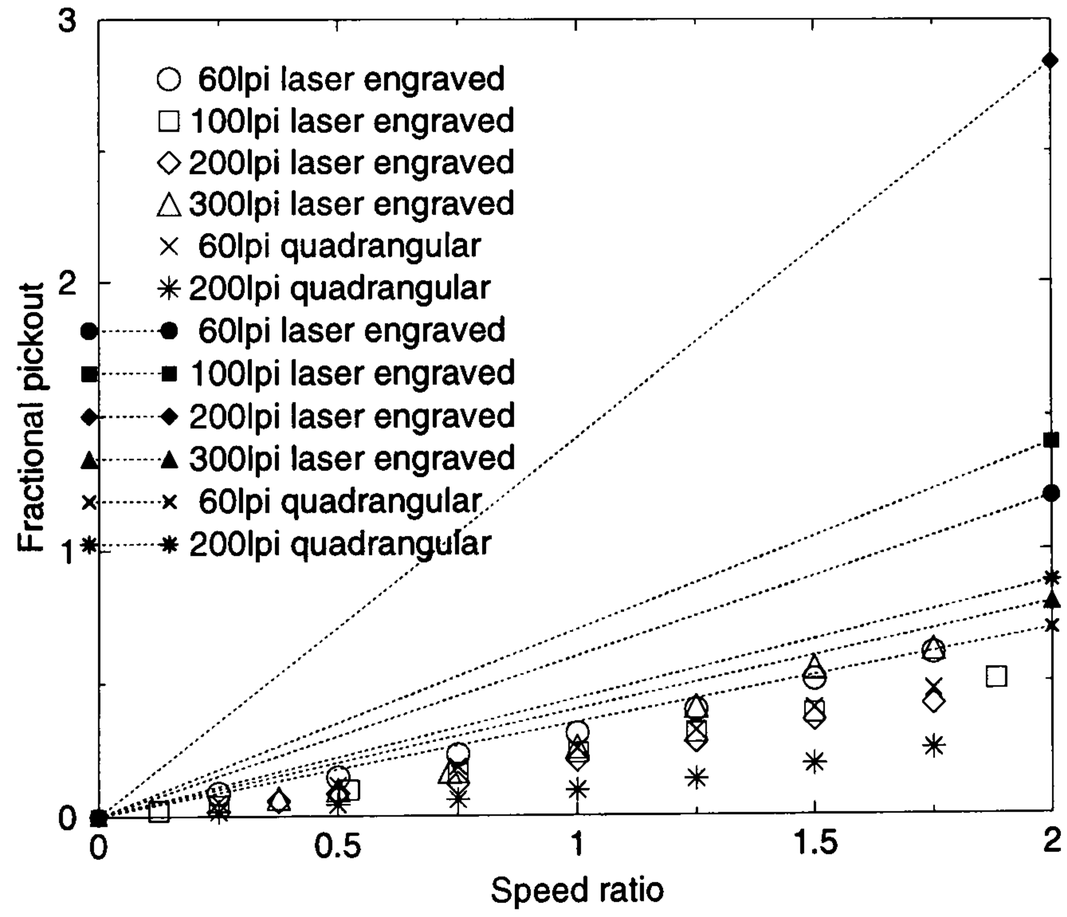

Figure 7.17: A comparison of pickout from the experimental data of this study(unfilled symbols) and the predictive model of Benkreira and Patel (1993) (filled symbols and dotted lines). Conditions as per figure 7.13.

7.3.6 Visualisations of the gravure bead

Presented in figures 7.18 and 7.19 are a series of visualisations of the gravure coating bead taken from above through the transparent web, as the speed ratio was increased. In all cases the web is moving from left to right, and the roll moving from right to left. The top dead centre of the roll is marked by the solid (right–hand) line, and the position at which the web would first meet the roll with no coating bead present (the 'dry roll contact point') is marked by the dotted (left–hand) line. The downstream interface can be seen on the left of the picutres and the upstream to the right of the top dead centre of the roll. The roll used for this study is the 100 lpi laser engraved ceramic and the coating liquid is fluid A. The roll speed was held at a constant value of 0.33 m/s in all of the pictures, except the first where the roll speed was 1 m/s to give a clear visualisation of the bead at a low speed ratio. The horizontal lines seen on the images of the bead extending from the left to the right are caused by the rotation of the roll.

Data showing the upstream and downstream meniscus positions taken from these figures are shown in figure 7.20. Again the location of the contact point between the web and roll are marked, and the top dead centre of the roll located at 0 mm.

Figure 7.21 shows magnified images of the upstream and downstream menisci.

The downstream interface

At low speed ratios (figure 7.18) a periodic wave is visible on the downstream interface, with a wavelength considerably bigger than that of the cell pattern. As the speed ratio in increased this instability disappears, although at $S = (0.25,\ 0.5)$ a wave of long wavelength and low amplitude can be observed in the experiments.

As speed ratio is increased further, the downstream interface moves towards the dry roll contact point, most clearly illustrated in figure 7.20. At $S = 3.5$ the downstream meniscus is observed to become temporally unstable, figure 7.19. At $S = 3.75$ fingers are seen to extend across the width of the bead, from the downstream to the upstream meniscus resulting in uncoated streaks on the web. The fingers are ir-

upstream meniscus resulting in uncoated streaks on the web. The fingers are irregularly spaced unlike in the ribbing instability. The approach of the downstream meniscus to the dry contact point is coincident with the onset of the fingering instability. A considerable number of air bubbles are trapped close to the downstream interface — seen as the lighter region of the bead in figure 7.18.

The magnified view of the downstream interface in figure 7.21 shows the interface to have a periodic shape, with a wavelength equal to that of the cells. Air bubbles are observed close to the interface, on the same scale as the cell size. The roll appears lighter after passing under the interface due to entrainment of fluid out of the cells into the puddle giving a more reflective roll surface.

The upstream interface

The upstream interface is located at positive X, i.e. to the right of top dead centre in figure 7.18 and 7.19. The position of this interface is relatively unaffected by the speed ratio, increases in web speed cause the upstream interface to move only very slightly in the (positive) X direction (clearly shown on figure 7.20). The upstream interface remains straight until disturbances on the downstream interface manifest themselves through the puddle.

Figure 7.21 shows that close to the upstream meniscus small air bubbles are trapped in a closed recirculation next to the interface. The upstream meniscus is essentially straight with small disturbances along the front of the same frequency as the cells that enter the bead.

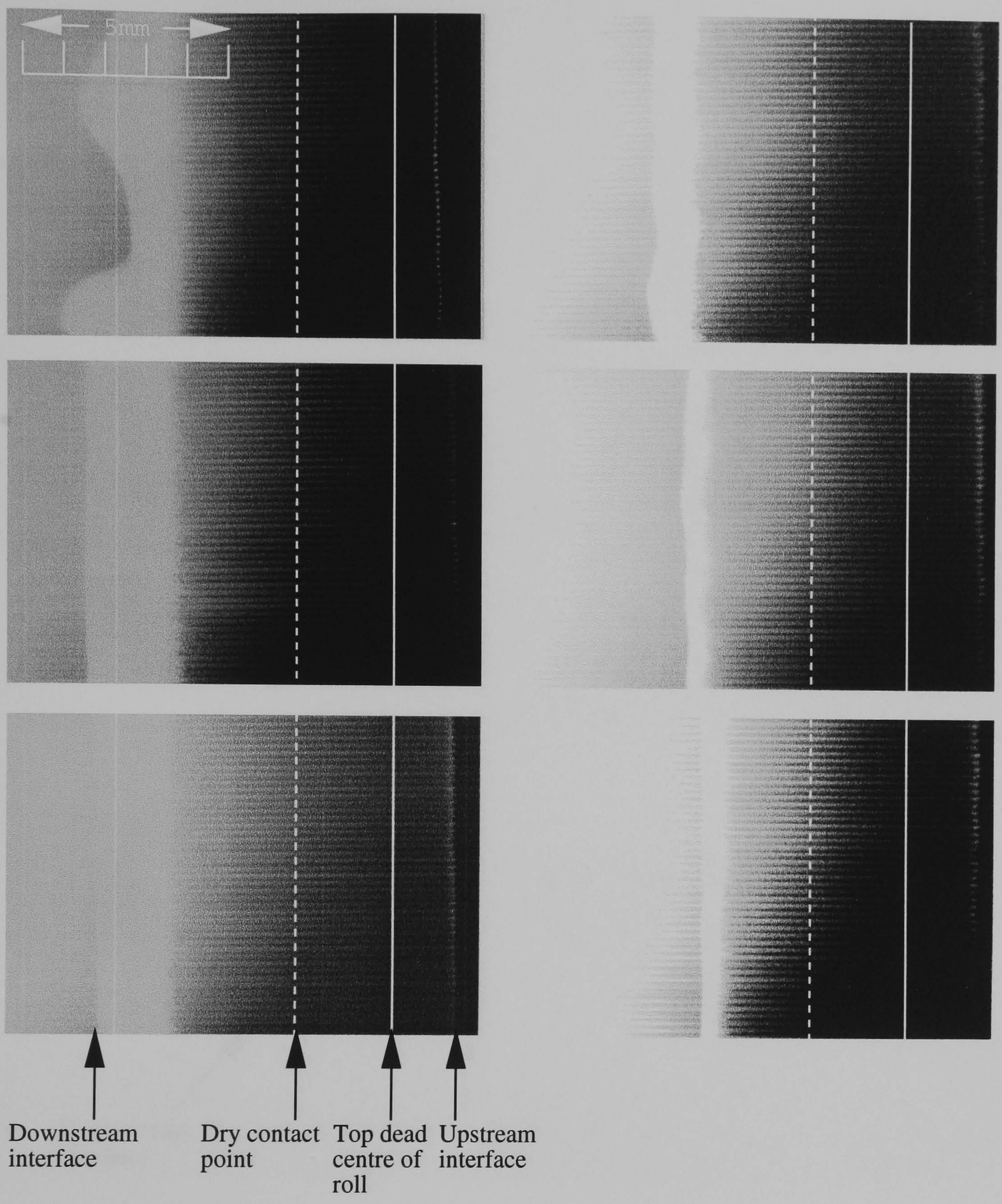

Figure 7.18: Images of the gravure bead at (from top left to bottom left, then top right to bottom right) $S = 0.1, 0.25, 0.5, 1.0, 1.5, 2.0$. Roll speed (top left) 1 m/s, remainder 0.33 m/s. Web moving left to right, roll moving right to left. Dotted line indicates where web and roll would meet with no fluid, solid line indicates top dead centre of roll. 100 lpi laser engraved ceramic, test fluid A, web thickness 23 μm, web tension 1000 N/m, wrap angle 2.5°.

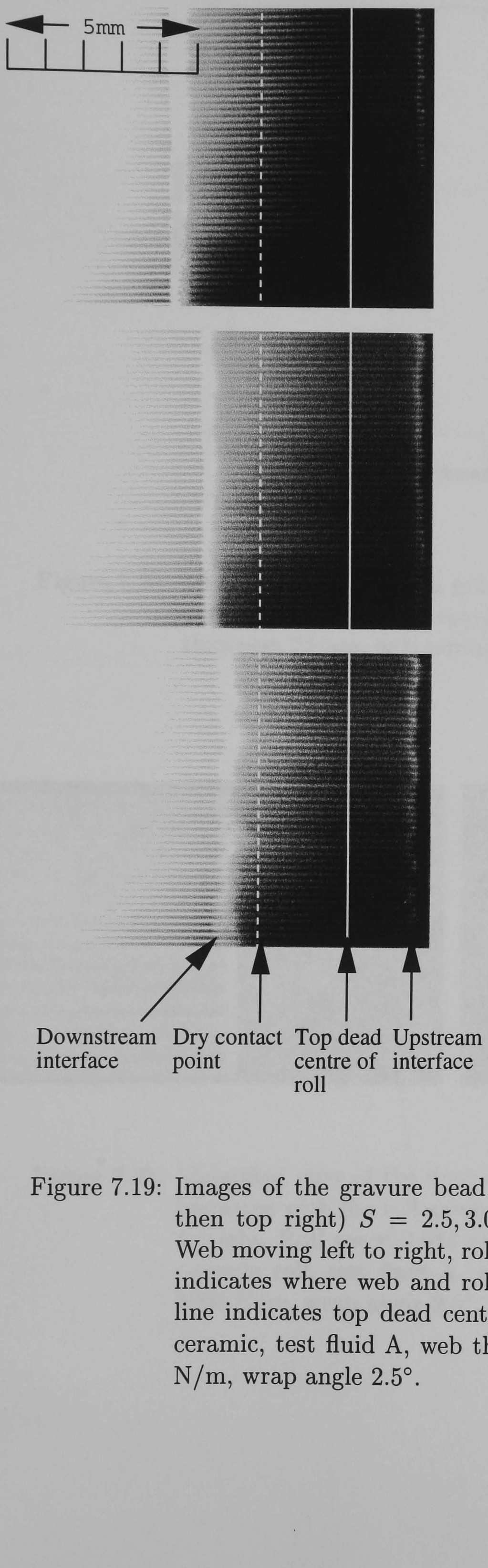

Figure 7.19: Images of the gravure bead at (from top left to bottom left, then top right) $S = 2.5, 3.0, 3.5, 3.75$. Roll speed 0.33 m/s. Web moving left to right, roll moving right to left. Dotted line indicates where web and roll would meet with no fluid, solid line indicates top dead centre of roll. 100 lpi laser engraved ceramic, test fluid A, web thickness 23 μm, web tension 1000 N/m, wrap angle 2.5°.

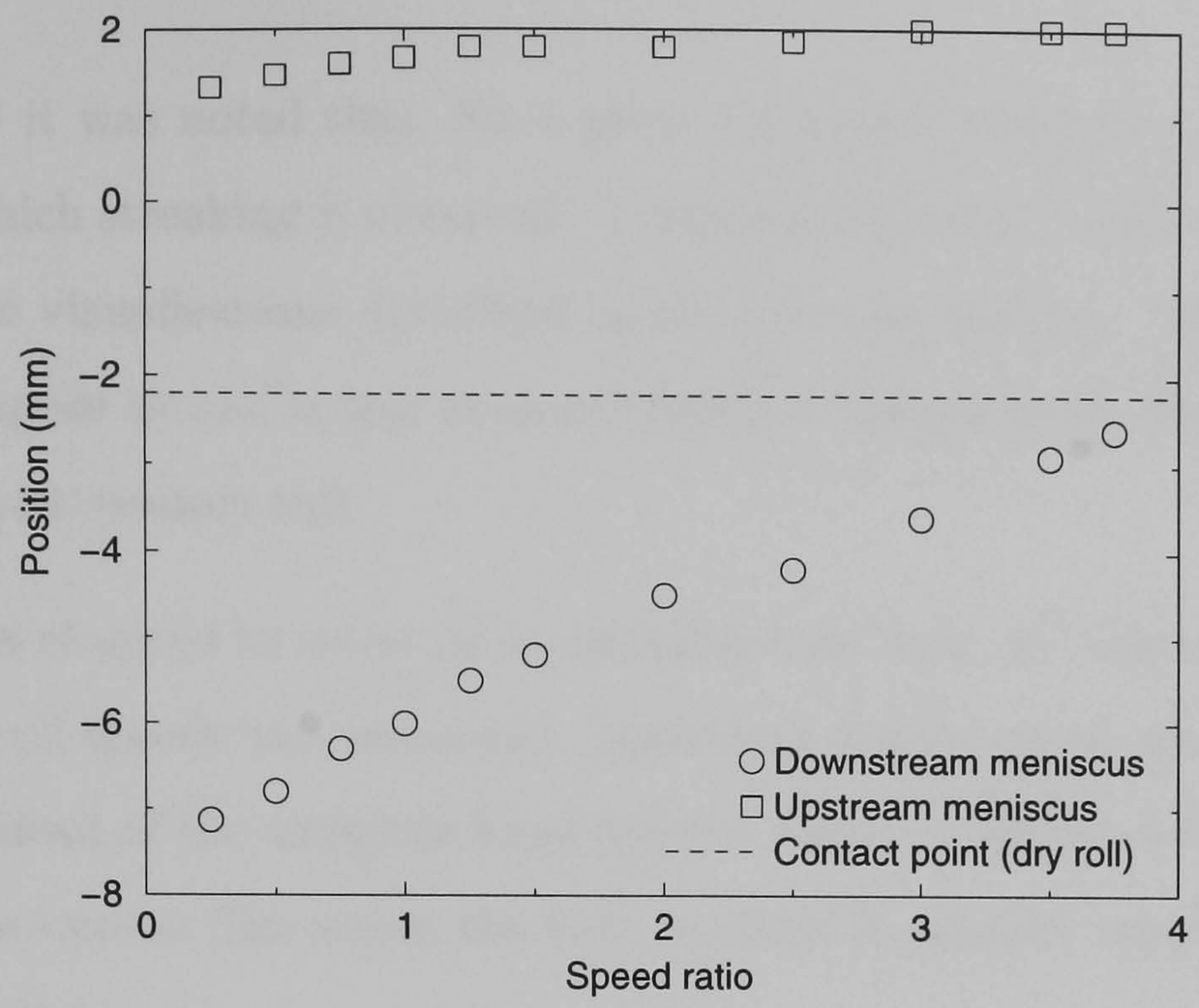

Figure 7.20: Meniscus positions of a gravure bead. Conditions: roll speed 0.33 m/s, 100 lpi laser engraved ceramic roll, test fluid A, web thickness 23 μm, web tension 1000 N/m, wrap angle 2.5°.

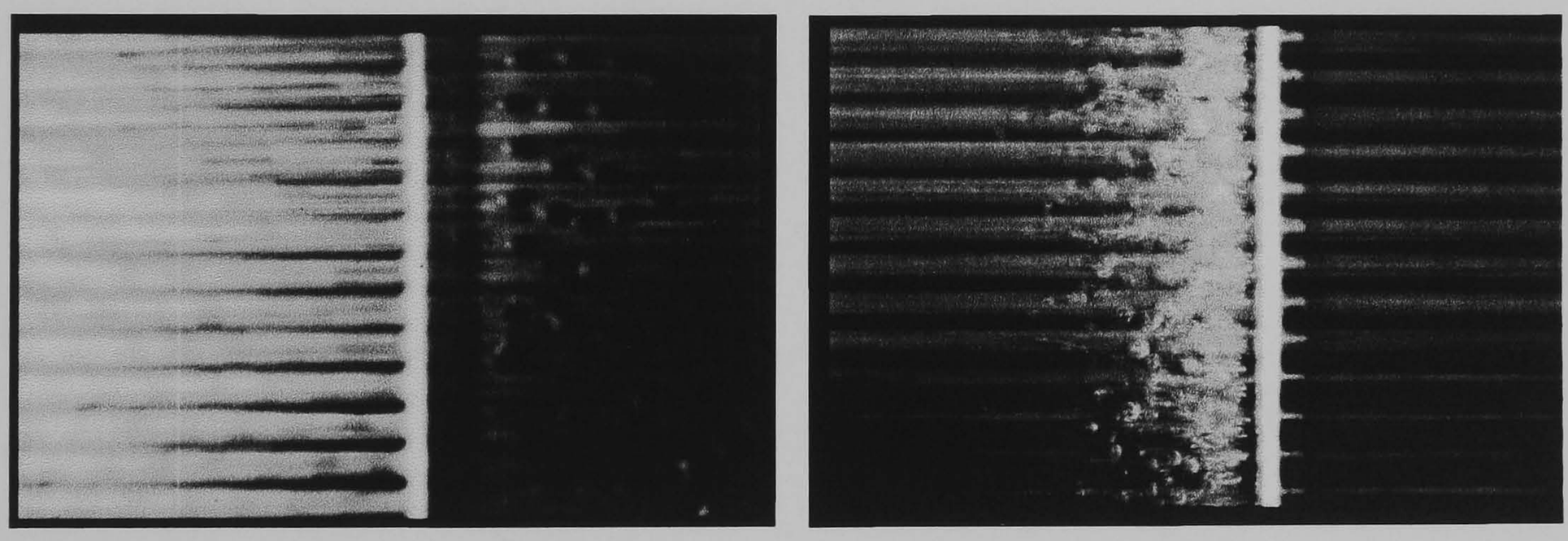

Figure 7.21: Magnified view of the downstream (left) and upstream (right) meniscus with the roll moving right to left and web moving left to right. Roll speed 0.083 m/s, $S = 1.0$, 100 lpi laser engraved ceramic roll, test fluid A, web thickness 23 μm, web tension 1000 N/m, wrap angle 2.5°.

7.3.7 The upper bound to gravure coating

In section 7.12 it was noted that, for a given roll speed, there is a maximum web speed above which streaking is observed. The break up of the coating bead was also observed in the visualisations described in the previous section. The effect of roll speed on this upper bound is now explored further, using coating fluid A and a 100 lpi laser engraved ceramic roll.

The web speeds required to cause (i) an unstable bead and (ii) streaking on the web for a range of roll speeds was measured. Both data points are shown in figure 7.22. Although the onset of the unstable bead did not result in visible streaking, it could well produce an uneven film across the web, so could in practice represent the upper bound of operation.

Figure 7.22 illustrates that as the roll speed increases the critical speed ratio for the onset of the instability decreases. The effects of wrap angle and tension on the instability were also assessed, in an effort to extend the window of operability. Changing the wrap angle between 0 and 5° or the tension between 500 N/m and 2000 N/m had no discernible effect on the critical speed ratio.

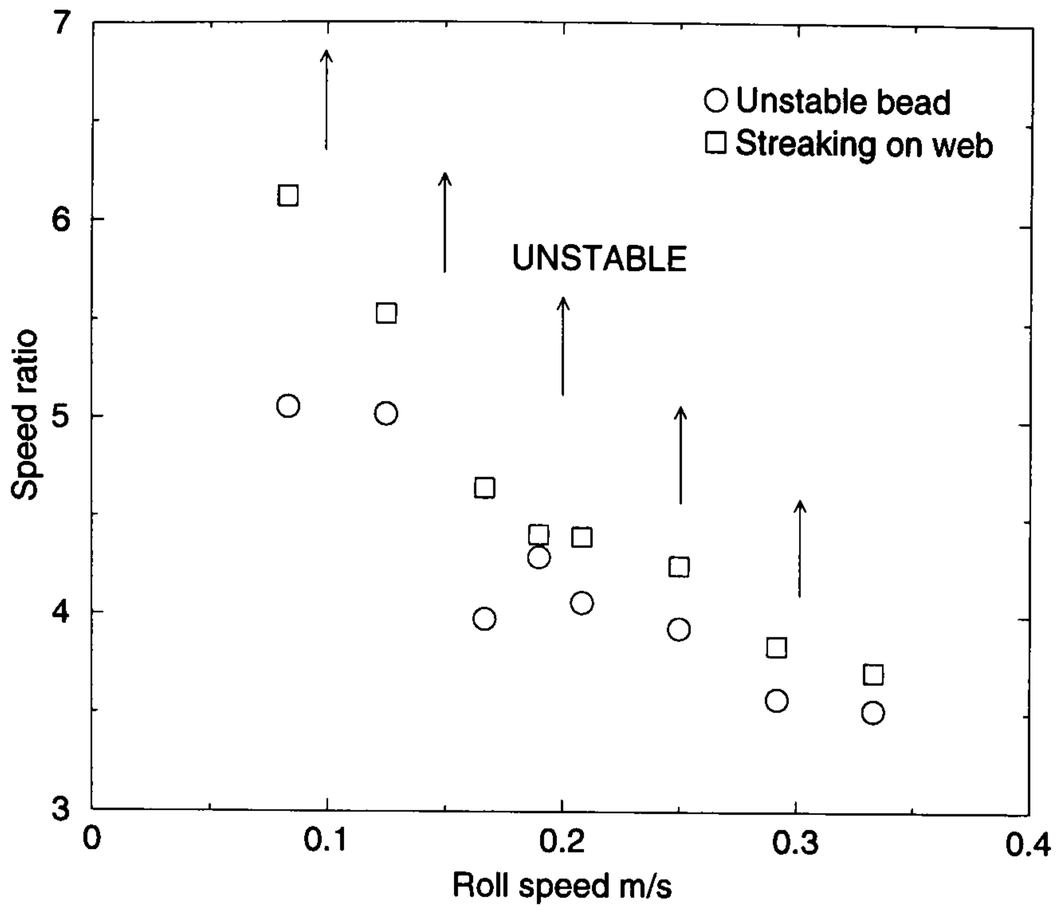

Figure 7.22: The effect of roll speed on critical speed ratio. Conditions: 100 lpi laser engraved ceramic roll, test fluid A, web thickness 23 μm, web tension 1000 N/m, wrap angle 2.5°.

7.4 The fluid dynamics of a gravure coating bead

"When you have eliminated all which is impossible, then whatever remains, however improbable, must be the truth." Sir Arthur Conan-Doyle (1859-1930).

Prior to considering the fluid dynamics of direct gravure coating, it is instructive to consider the dynamics that control the transfer of fluid in a kiss–coater. This is similar to a direct gravure coater, but the patterned gravure roll is replaced by a smooth one, and the inlet flux is a metered film that enters the bead on the roll surface. Such a kiss coater can be operated in two modes: when $S < 1$ the kiss–coater is self metering, whilst at $S > 1$ the web is observed to touch the roll with complete transfer of fluid (Booth, 1970).

For the case where $S < 1$, Rees (1995) developed a model for a web of predetermined shape passing over the roll and this was later extended by Storey (1996) to a flexible web with both a lubrication type model and a 2D finite element model for the fluid

domain. Storey highlighted important parameters that control the transfer of the fluid to the substrate, namely the web tension and the wrap angle, as well as fluid properties and the roll and web speed. A positive pressure profile in the fluid bead supports the web above the roll, see figure 7.23.

When $S > 1$ the web is observed to touch the roll and all the fluid is transferred to the web. In which case the pressure beneath the web is completely sub–ambient, and the fluid bead is observed to lie entirely on the inlet side of the roll (see chapter 6).

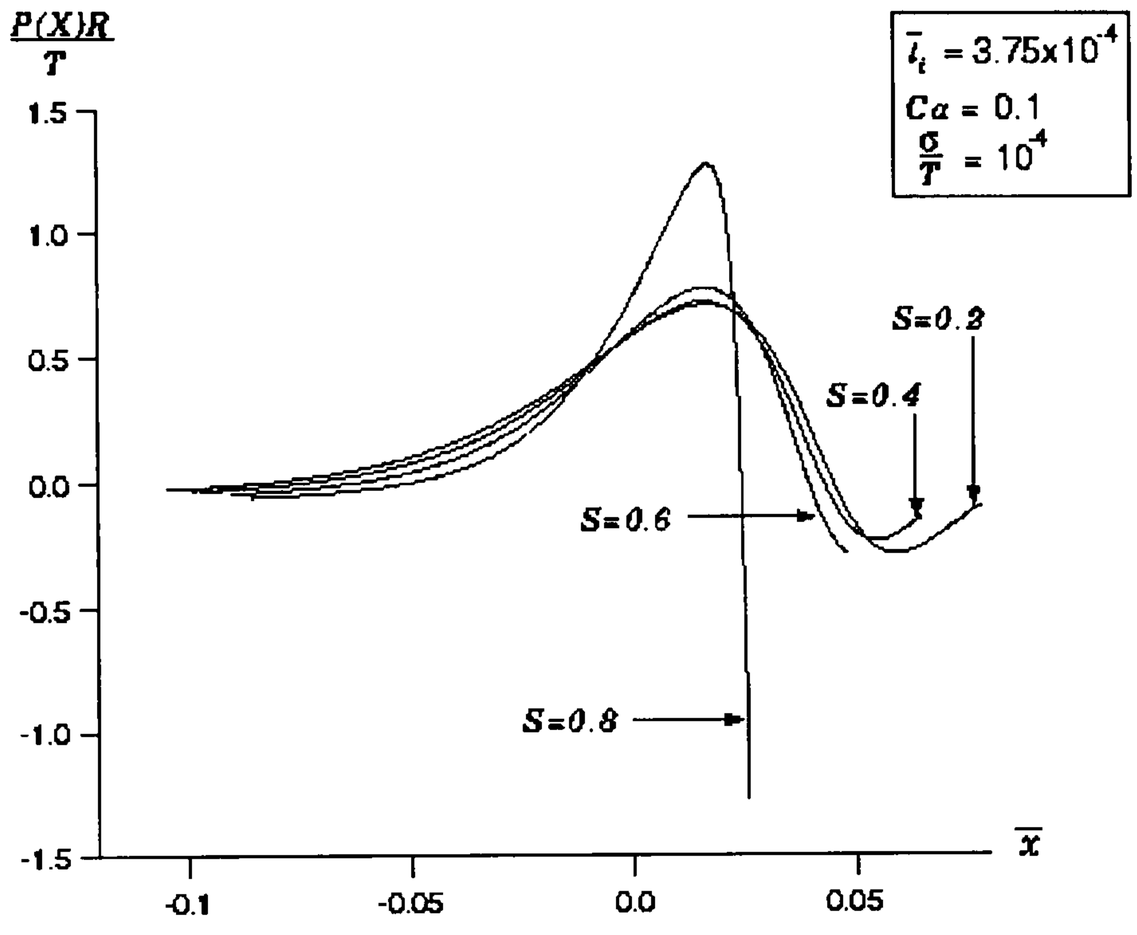

Figure 7.23: Typical pressure profile in a kiss coating bead at $S < 1$ taken from Storey (1996).

The experiments reported here show that gravure coating operates with a substantially different mechanism to that of a kiss coater with $S < 1$ or $S > 1$. Figures 7.7 and 7.8 reveal that neither the tension nor the wrap angle of the web have any significant effect on the proportion of fluid deposited on the web, over a range of speed ratios ($S < 1, S = 1$, and $S > 1$). Visualisations of the bead show that in all cases the fluid bead lies bounded by an upstream meniscus located at positive X and a downstream meniscus located at negative X, both outside of the region where the web would touch the roll with no fluid bead present (the 'dry contact region') –

this is shown schematically in figure 7.24. The evidence that the bead is bounded either side of the contact region indicates that the mechanism of transfer from the gravure cell to the web is not that of the kiss–coater operating at $S > 1$ since here the fluid has to transfer to the web before the contact region is approached. In view of this fact it becomes clear that the cells enter the bead full of fluid, pass under the upstream meniscus, throughout the contact region, and are evacuated at the downstream end of the domain.

Evidence that the cells are full in the contact region was obtained by impulsively stopping the coating apparatus (both web and roll) and examining the cells through the web. No air bubbles were visible, which would necessarily be the case if the pickout had occurred at the upstream meniscus.

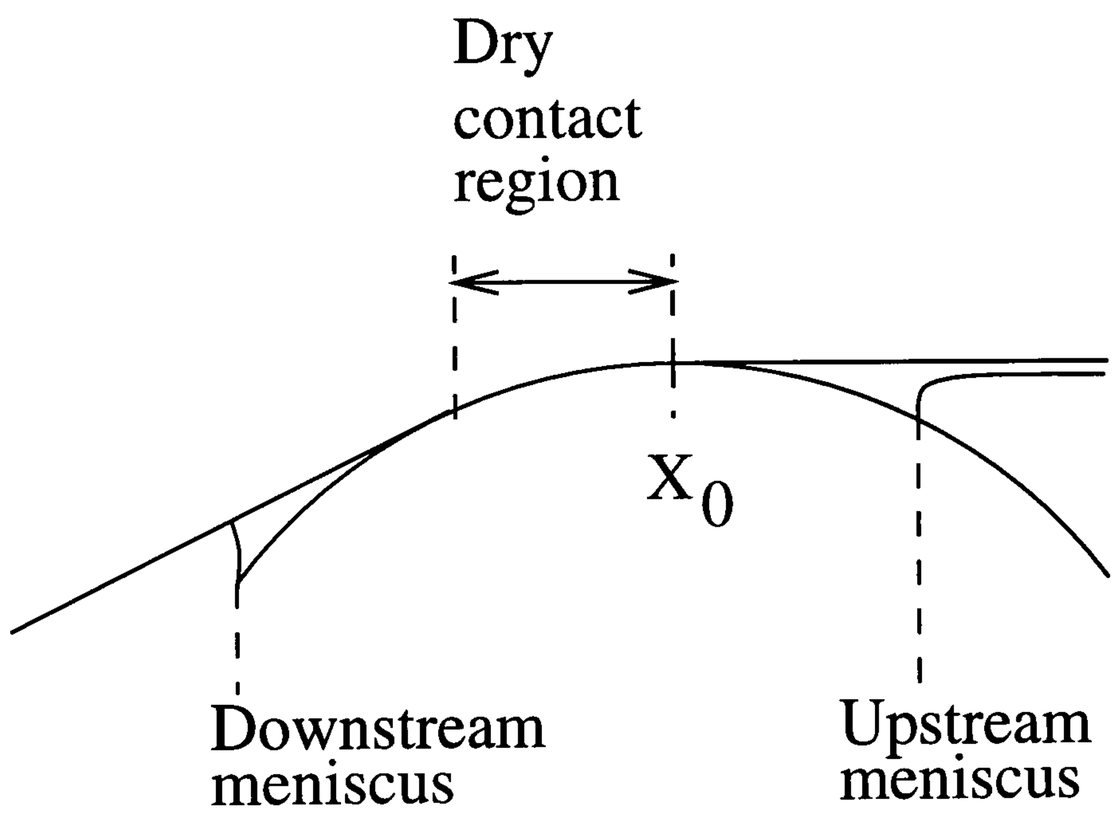

Figure 7.24: A schematic of the bead showing the location of the upstream and downstream menisci, and the path would follow with no bead present.

A second possible mechanism for the transfer of fluid from the downstream to the upstream region is one similar to that dominant in a kiss–coater operating at $S < 1$. One characteristic of this transfer mechanism is the large positive pressure developed in the fluid which supports the applied load and lifts the web off the roll surface and provides a gap for the transfer. In fact it was just such reasoning that prompted

the development of the laser–ranging system described in section 2.6 to measure the web profile as it passed over the fluid bead.

Preliminary results of such a study proved inconclusive. The first set were taken using a 23 μm thick clear web, and the second for a 50 μm thick web with a very thin aluminium coating on one side to provide a good reflective surface. Both sets of data gave the appearance of a great deal of 'noise' in the contact region, for both the dry and the wet roll. The data did not suggest a positive gap between the web and roll when the fluid bead was present. This suggests that the load applied by the web (a function of wrap angle and web tension) could be supported directly by the roll with no lubricating film present. This is in accord with the findings illustrated in figures 7.7 and 7.8 which show that the applied load makes little difference to the cell pickout.

Further evidence that the web and roll are in contact between the two menisci was obtained when running with the aluminium coated web. Here scratching is seen on the soft aluminium surface, as shown in figure 7.25. Scratching was also observed on the 23 μm thick Melinex film although it were very faint and difficult to see. Pulkrabek and Munter (1983), in their investigation into trihelical rolls quote that the roll and web contact, although no mechanism for transfer of the fluid out of a line (as opposed to a discrete cell) is proposed. Indeed it may be the case when using trihelical rolls that all the fluid dynamics occurs in a 'line' (or groove), since one groove provides a continual channel from the downstream to the upstream meniscus. The fluid dynamics of a trihelical roll may be similar to a reverse roll coater operating in a starved regime, since the lands of the trihelical grooves effectively establish a gap between the web and roll, and the scraped inlet film is metered to the height of the channel. This is illustrated in figure 7.26. Figure 7.27 shows a schematic of the flow field in reverse meniscus roll coating, which is one possible way the film could be metered onto the web from a trihelical groove.

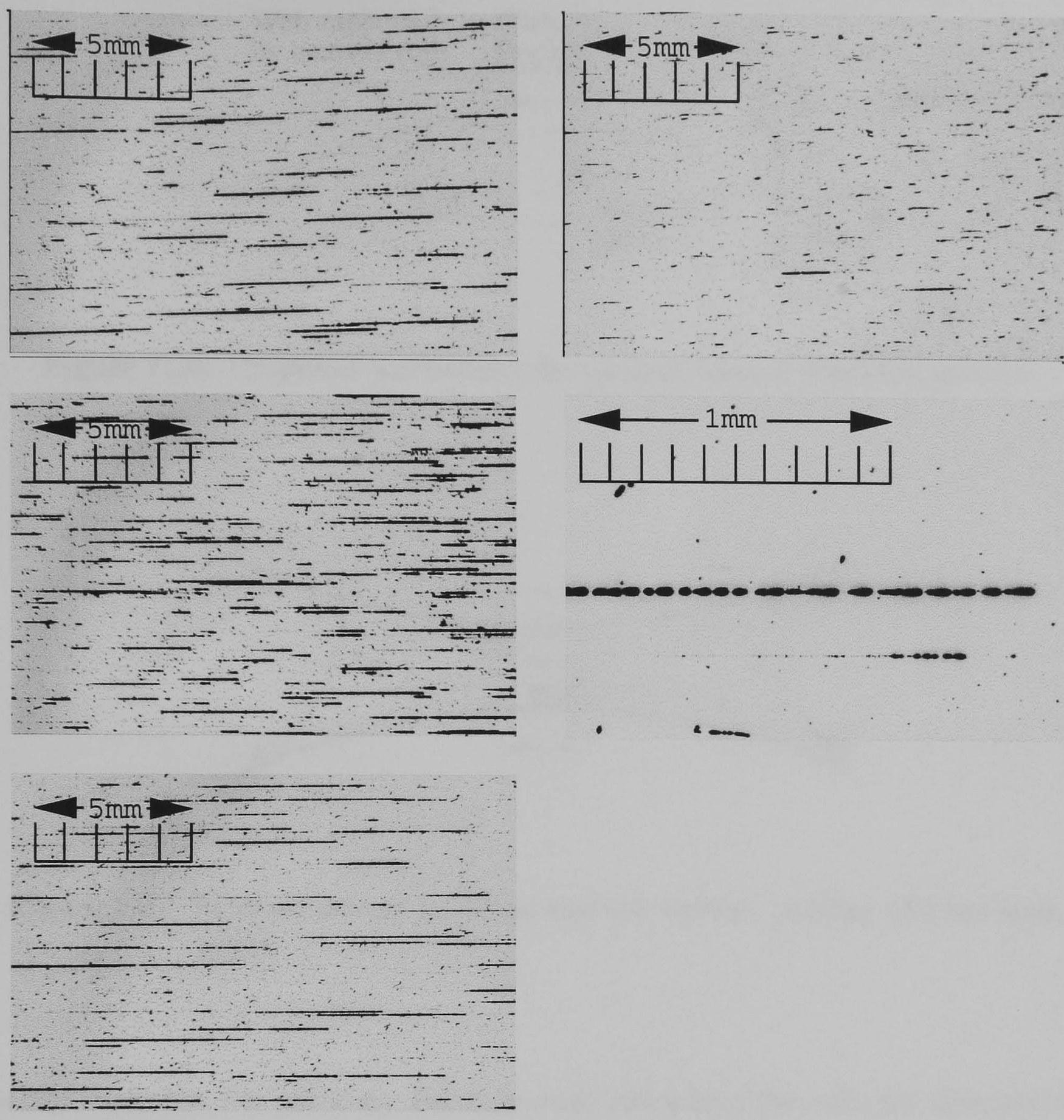

Figure 7.25: Scratches on the aluminium coated web in direct gravure coating. Roll speed 0.33 m/s, 100 lpi laser engraved ceramic roll, test fluid A, web thickness 50 μm, web tension $T = 1000$ N/m, wrap angle $\beta = 2.5°$. From top left to bottom left $S = 0.5, 1, 2$. Right hand column – wrap angle $= 0°$, $S = 1$, detail of a typical scratch.

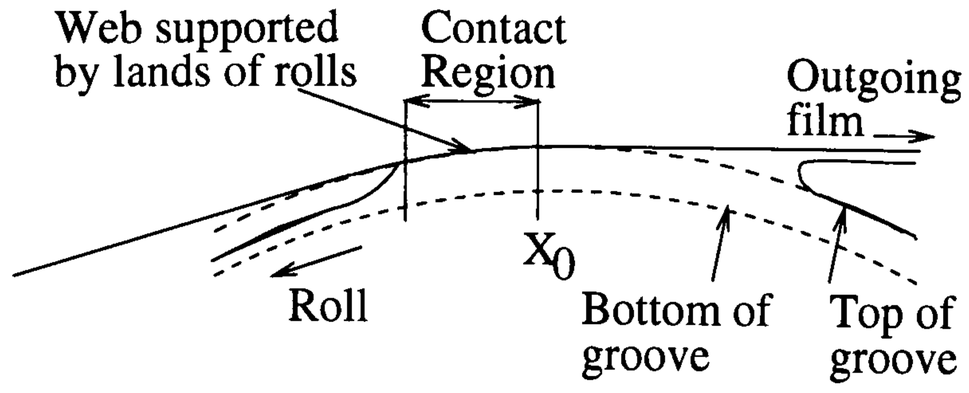

Figure 7.26: Proposed mechanism for pickout from a trihelical groove.

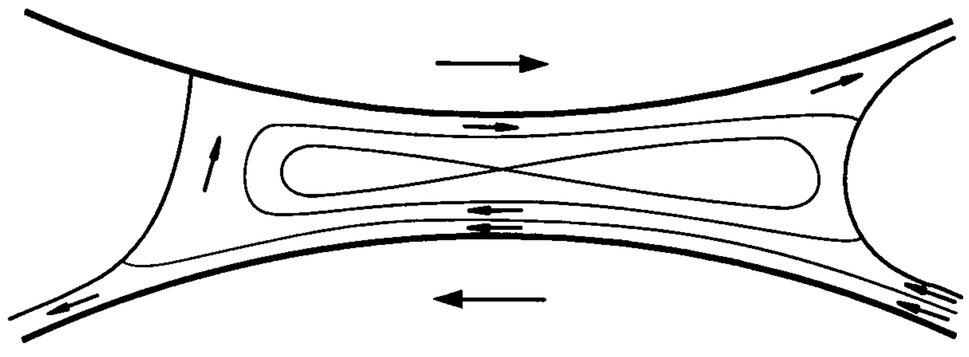

Figure 7.27: Flow structure in ultra–starved reverse coating (Richardson, 1996).

However, here lies the paradox. For a gravure roll where the cells are discrete, fluid is emptied from the cell at the downstream meniscus and leaves on the web at the upstream meniscus, but the web and roll appear to be in contact such that the load is supported by the roll.

At this point, it is worth reassessing the assumption of two–dimensional flow in the bead. The tension in the web is solely in the direction of web motion. Across the web no tension is applied and hence it is free to flex. From a careful visual inspection of the contact region it was observed that the pattern of lands and cells on the roll produced a series of small corrugations on the web in the axial direction. The positions of the corrugations were seen to fluctuate with the motion of the web over the roll. At any once instant in time, a series of these corrugations would allow fluid to pass from the upstream to downstream region (as in a trihelical groove) **and** allow the load applied by the web to be supported by the roll, as shown in figure

7.28. Further evidence for this conjecture is sought in the next section.

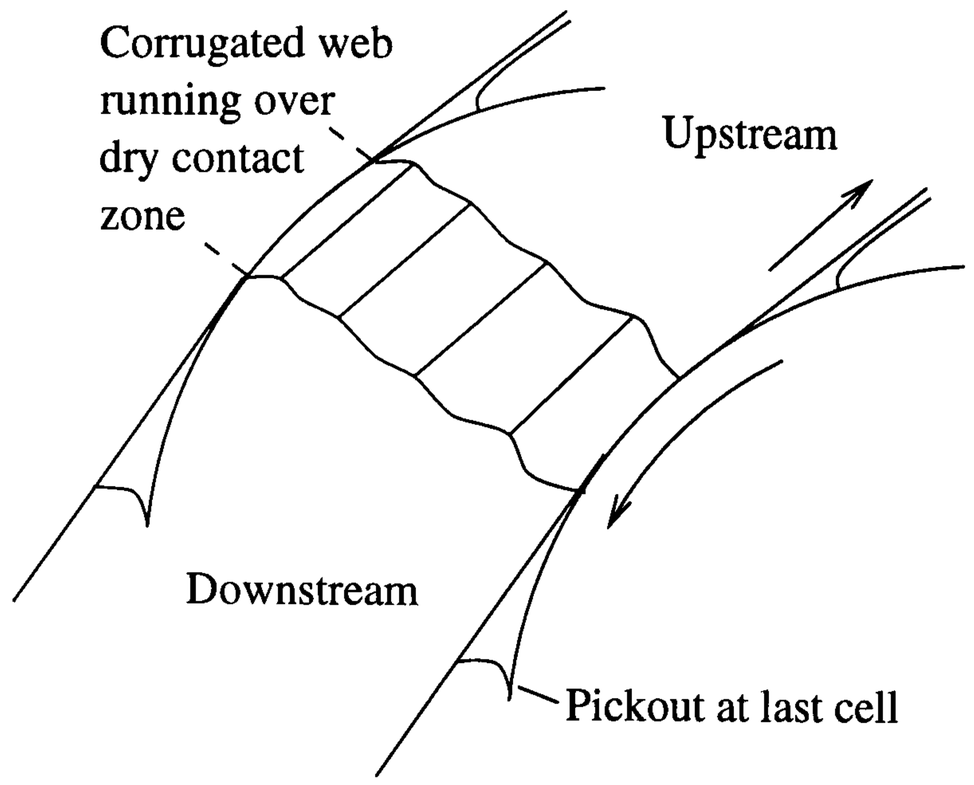

Figure 7.28: Possible method of transfer from the downstream to the upstream zone.

7.4.1 Investigating the top puddle

Experimental technique.

Here a technique similar to that used by Coyle *et al.* (1990a) for the study of a ribbed film, and by Shapiro (1954) to visualise transient wave patterns on water is described to show the corrugations of the web as is passes over the contact region. The experimental setup is illustrated in figure 7.29. A 150 W light source fitted with fibre optic light guides was positioned a large distance away from the coating apparatus to give an essentially parallel beam of light incident to the web at 45°. The reflected light from the web was projected onto a sheet of white card, where it formed an image.

The principle of operation of this arrangement is shown in figure 7.30 with the shape of the web causing a corresponding change in the light intensity of the reflected image. By positioning the sheet of paper at right–angles to the roll part of the formed image was out of focus, however this allows a photographic record to be

taken with a camera positioned in front of the coating apparatus using a high shutter speed (1000 s^{-1}) and an appropriate high speed film (1600 ASA).

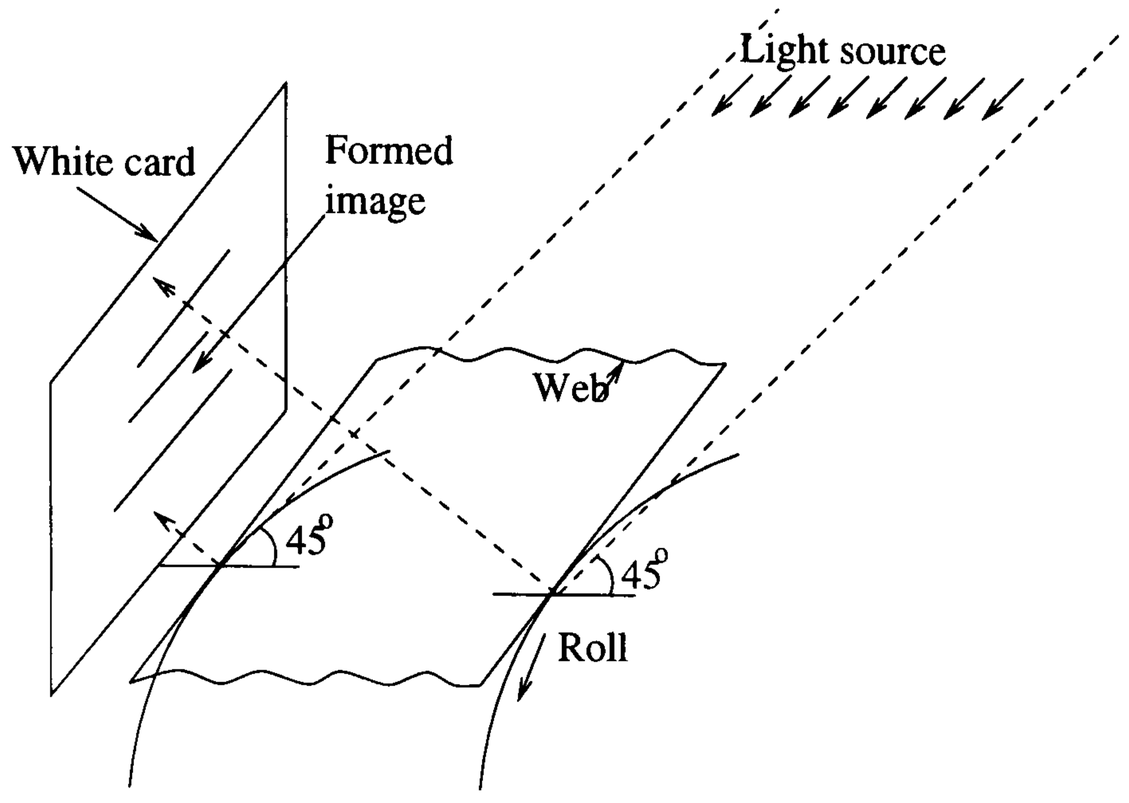

Figure 7.29: Arrangement of the apparatus to show web corrugations.

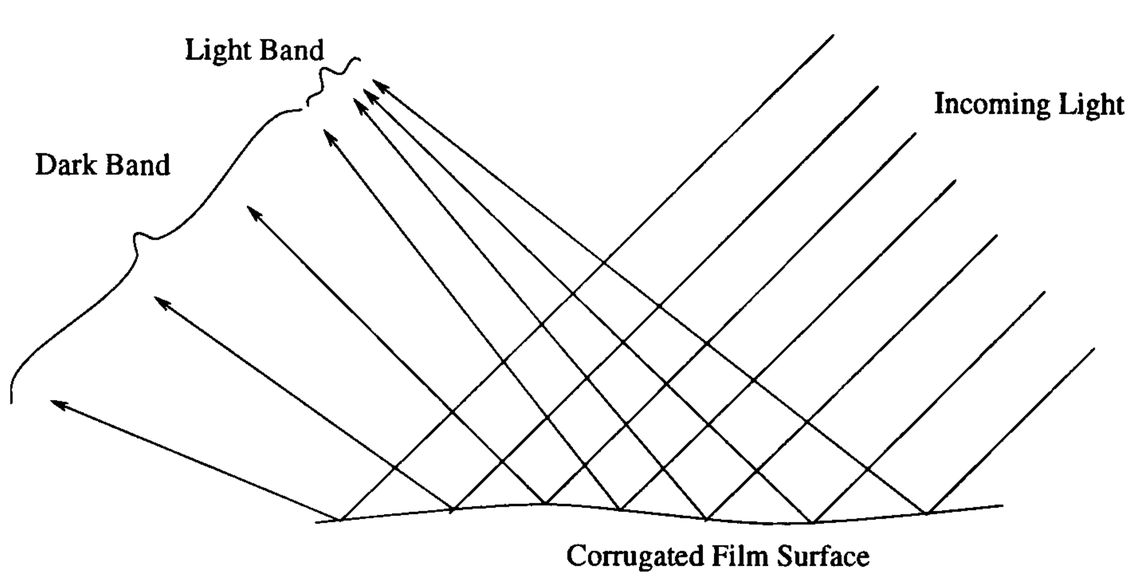

Figure 7.30: Principle of the operation of the apparatus used to show corrugations of the web.

Figure 7.31 shows a photograph of a typical image projected onto the card for the case of a 100 lpi laser engraved ceramic gravure roll at speed ratio 0.66, and figure 7.32 shows the same but with a smooth roll. In figure 7.31 the bands of white and dark on either side of the centre contact region (seen as a dark region) represent the corrugations of the web with a given corrugation matching across the contact zone from the upstream to the downstream region, whilst for the case of the smooth roll (figure 7.32) the web is observed to remain smooth across the fluid bead beneath it.

Further tests with the gravure coater taken at speed ratios 1.0 and 1.5 also show

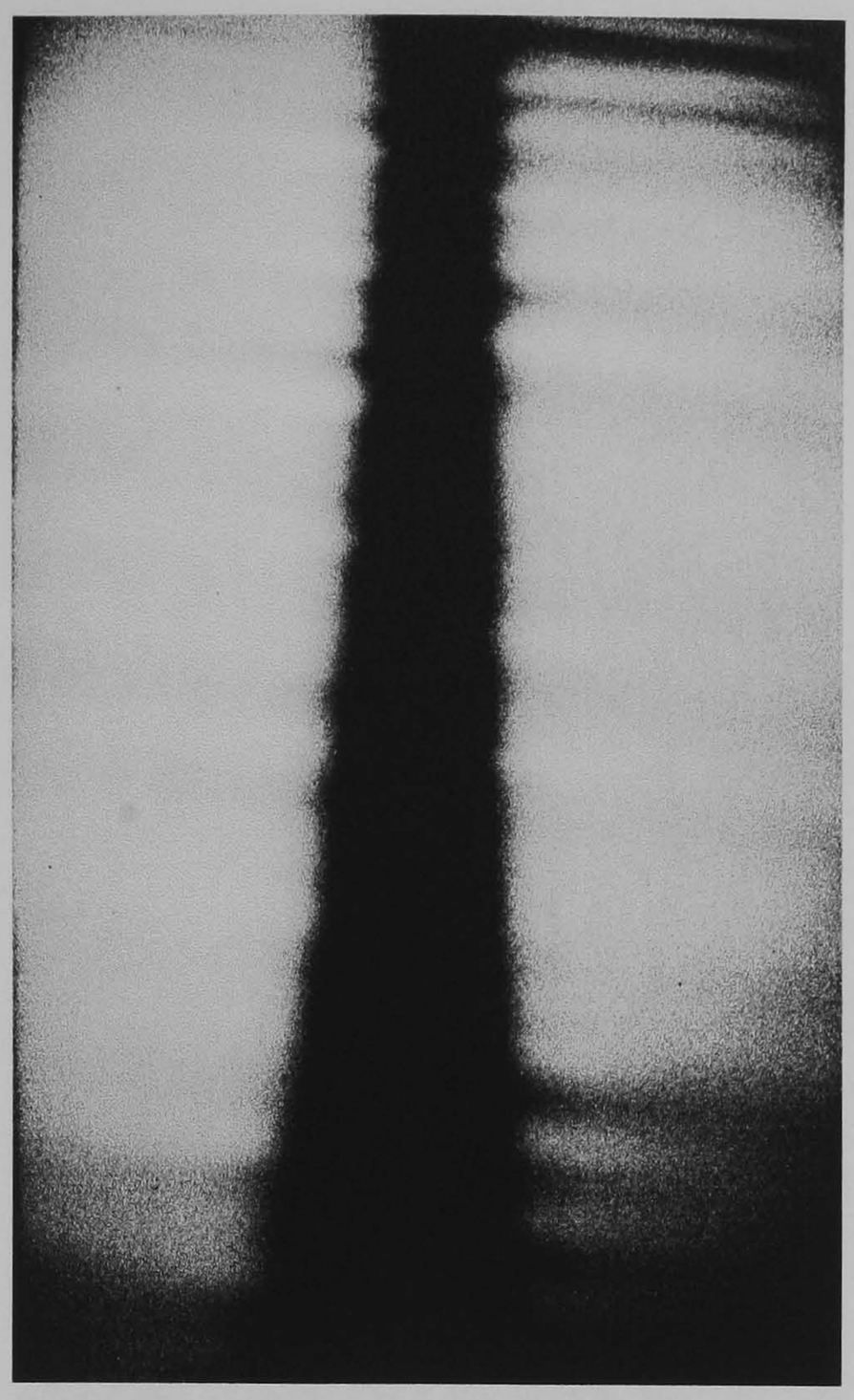

Figure 7.31: Shadowgraph of the web passing over a gravure roll at wrap 2.5°. Conditions: roll speed 0.083 m/s, speed ratio 0.66, test fluid A, web thickness 23 μm, web tension 1000 N/m.

the same characteristic pattern of light and dark bands that correspond to the web being corrugated. Even with an initial positive gap and the web depressed onto the roll (see section 7.4.2 for discussion of this behaviour) to form a stable bead (with the wrap angle, β, very close to 0°) the shadowgraph (figure 7.33) shows the web is still corrugated either side of a very narrow contact zone. In all cases the corrugations of the web either side of the contact zone match from the upstream to the downstream.

From these figures one can conclude that one mechanism for transfer of fluid from the downstream to the upstream region across the contact zone is through web corrugations formed in the axial direction of the roll. It appears this mechanism operates at all values of speed ratio, unlike the kiss–coater where a distinction needs to be made between the cases of $S < 1$ and $S > 1$.

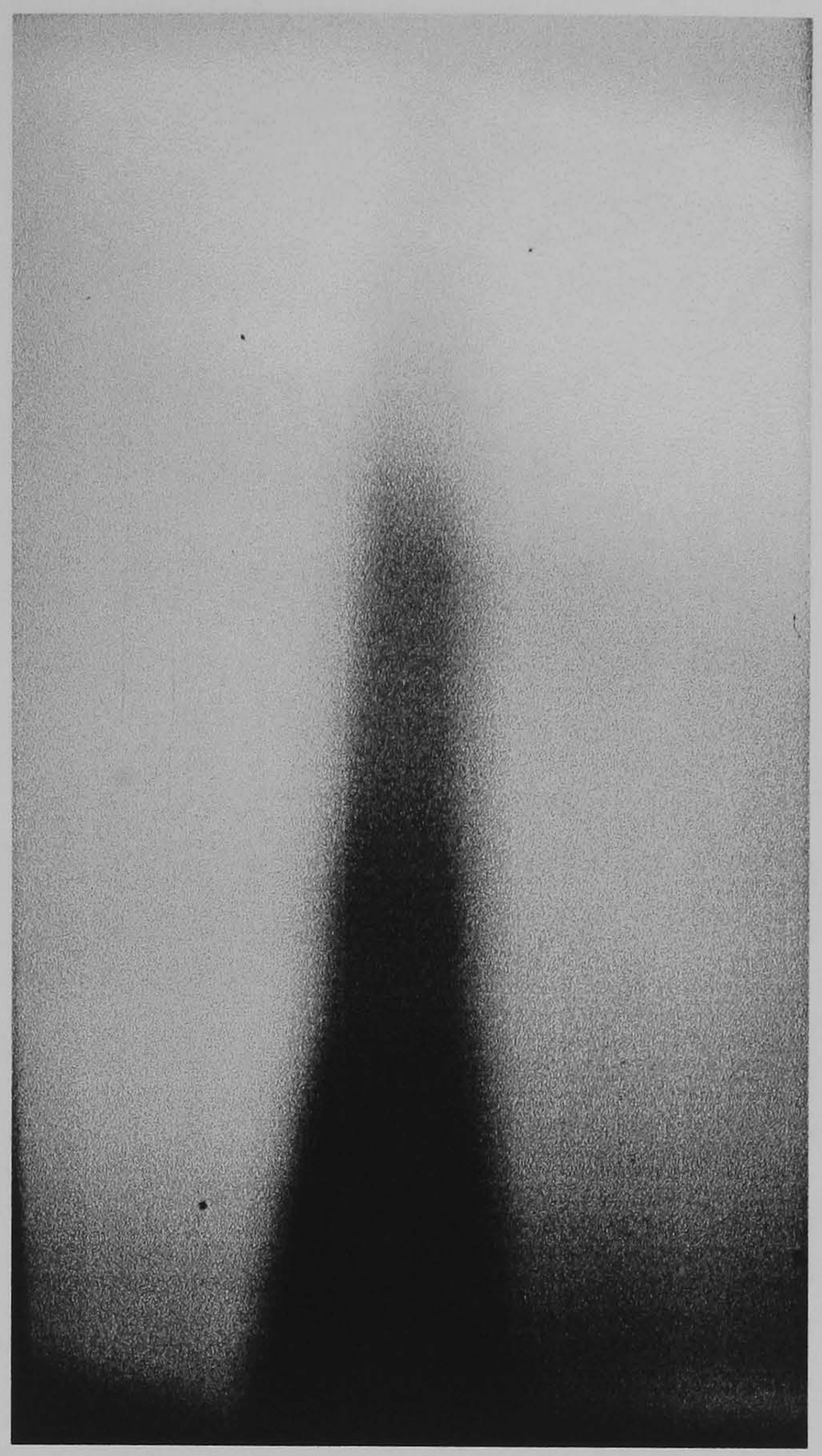

Figure 7.32: Shadowgraph of the web passing over a smooth roll at wrap 5°. Conditions: roll speed 0.083 m/s, speed ratio 0.66, test fluid A, web thickness 23 μm, web tension 1000 N/m.

7.4.2 The pressure distribution within the bead

This section outlines two possible pressure profiles that could exist within the bead. However, before this, observations of a gravure bead started initially with a small gap between the web and the roll are discussed.

It was observed that if the gap between the web and roll was below a certain tolerance (with no fluid transfer from the roll to the web) a stable bead could be formed by momentarily depressing the web onto the roll surface. The small bead would grow in length until it extended from one edge of the web to the other. Using the shadowgraph technique described in section 7.4.1 it was shown that corrugations formed along the length of the bead and that some scratching was observed on the

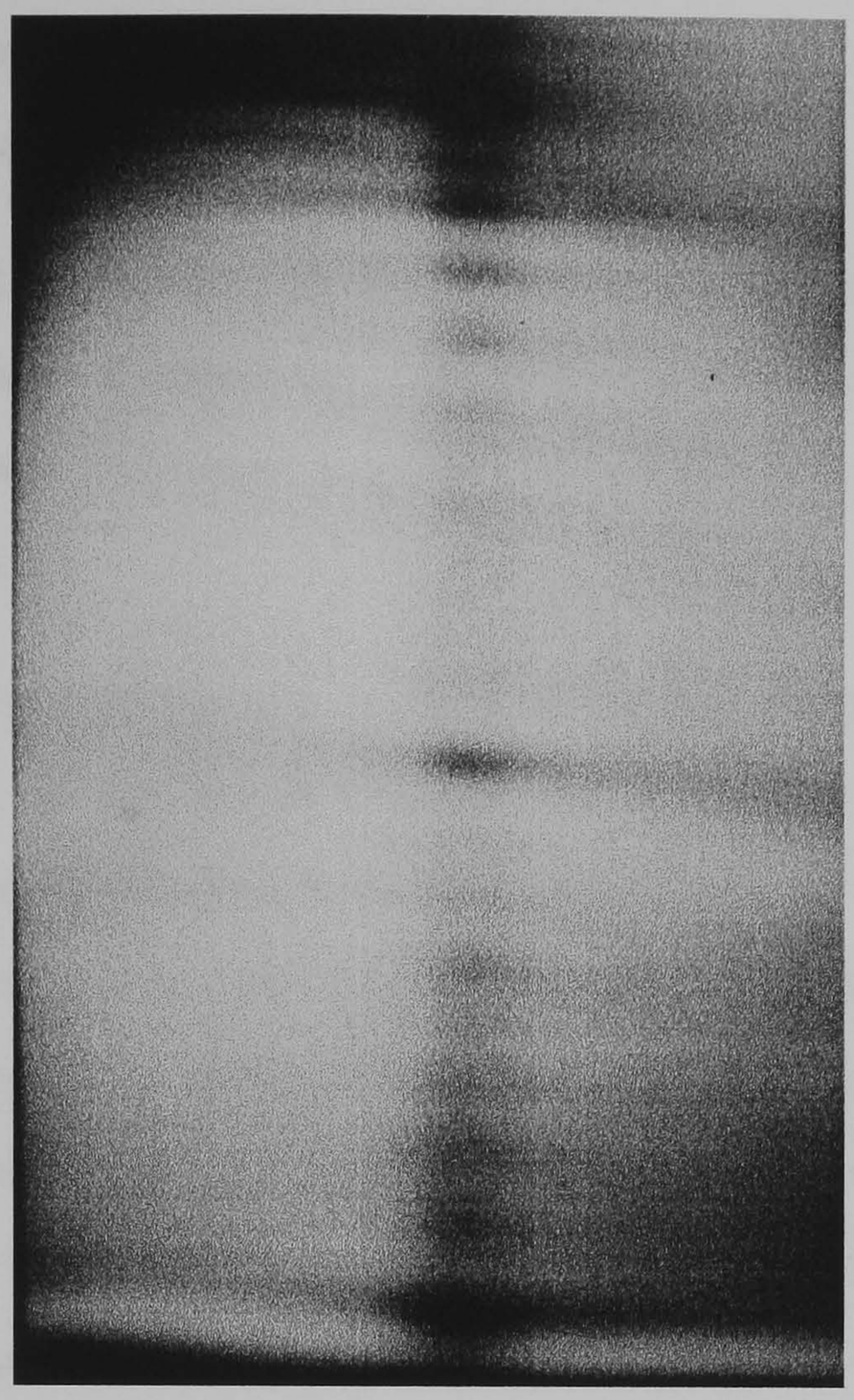

Figure 7.33: Shadowgraph of the web passing over a gravure roll at wrap 0°. Conditions: roll speed 0.083 m/s, speed ratio 0.66, test fluid A, web thickness 23 μm, web tension 1000 N/m.

web – although not to the same extent as that seen with a positive wrap angle. A natural conclusion of this is that there must be an overall negative pressure within the bead in order to balance the upward load (in this special case) due to the tension in the web. This was observed over the full range of speed ratios.

An estimate of the pressure at either interface can be derived by evaluating the capillary pressure due to curvature of the menisci. The radius of curvature can be estimated from the height at the wetting line, here this is taken from the measured position of the interface (figure 7.20) and by assuming that the path of the web is the same with or without a fluid bead present (although this may not necessarily be the case). The radius of curvature of the upstream meniscus is taken as $O(H_U)$, where H_U is the height between the web and roll at the upstream meniscus, and that of the downstream is taken as $O(H_D/2)$, where H_D is the height between the

web and roll at the downstream meniscus, although the trends discussed below are relatively insensitive to the choice of expression.

At low speed ratios, the pressure at the upstream interface is lower than that at the downstream interface. Conversely, at high speed ratio the pressure at the downstream interface is lower (i.e. more negative) than that at the upstream since the meniscus lies closer to X_0.

The shape of the pressure profile also needs to be elucidated for a full understanding of the fluid dynamics on the length scale of the fluid bead. The pressure profile associated with the time dependent formation and collapse of the corrugations in the dry contact region is unknown and clearly very complex. Further work is required in this area to develop these ideas and greater understanding of the mechanisms responsible for the gravure action. One additional observation is made related to the length of the fluid bead outside the dry contact region. Shown in figure 7.34 are the upstream and downstream meniscus locations as the wrap angle is increased, for a fixed web and roll speed. As the wrap angle increases the upstream meniscus position remains constant whilst the downstream meniscus moves in an increasingly negative direction. The corrected distance from the downstream meniscus to the dry contact region has also been plotted as a function of wrap angle, shown in 7.34. Remarkably, the corrected width of the fluid domain (i.e. neglecting the dry contact region) remains constant as the wrap angle is increased i.e. the length of the fluid bead outside the dry contact region is unaffected by the wrap angle of the web.

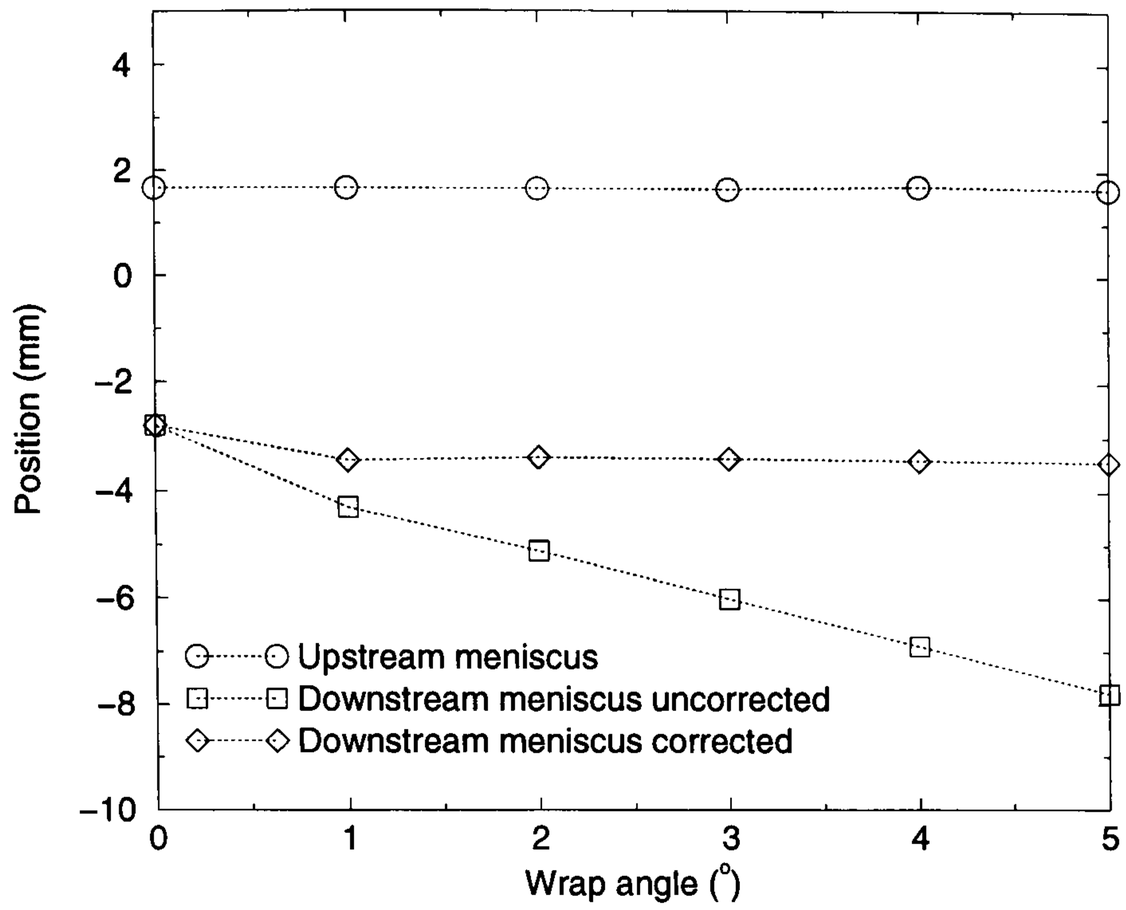

Figure 7.34: The location of the upstream and downstream menisci as the wrap angle is varied. Also shown is the position of the downstream bead outside the contact region. Conditions: roll speed 0.66 m/s, speed ratio 1.0, 100 lpi laser engraved ceramic roll, test fluid A, web thickness 23 μm, web tension 1000 N/m.

7.5 Summary

A number of conclusions may be drawn from this work:

- The tension, wrap angle and web thickness have no effect on the thickness of the final coated film.
- For a fixed roll speed, increasing the web speed (and speed ratio) at first causes the film thickness to increase. At higher speed ratios the film thickness becomes insensitive to the web speed.
- The surface tension and viscosity of the coating solution are important in determining the film thickness. A more viscous fluid or one with a lower surface tension gives a greater film thickness.
- The gravure cell shape and size are both important in determining the film

thickness.

- At high speed ratios, the coating bead becomes unstable which results in streaking on the web. As the roll speed is increased the critical speed ratio for the onset of the instability decreases. Neither the wrap angle nor the web tension affect the point of onset of the instability.

- The mechanism of transfer from the downstream to the upstream is clearly complex. Over the dry contact region the web is corrugated and touches the roll at discrete points.

Chapter VIII

Conclusions and further work

Contents

8.1 General discussion

The main findings of the research presented in this thesis are now summarised, and suggestions are made for ways the work might be extended.

Chapter 1 presented a review of the relevant literature and highlighted some of the the common features of coating flows.

Chapter 2 described the range of experimental techniques and the relevant apparatus used in this thesis for studying the coating flows under investigation. Associated flow visualisation and flux measuring techniques were discussed in the context of other work in the field while the precision equipment and careful systematic methods needed to explore the fluid dynamics of such small scale flows were highlighted.

In chapter 3, a reverse roll coater operating with the reservoir positioned directly above a horizontally aligned roll pair was investigated. Measurements of the outgoing film thickness and the position of the wetting line were made for a range of speed ratios and depths of fluid in the reservoir. Two interesting trends were noted: Initially, as the speed ratio was increased, the web film thickness first fell, until $S \approx 1$, after which further increases in speed ratio caused the film thickness to rise; at low speed ratios, a lower hydrostatic head caused a thinner film to be deposited on the web, but at high speed ratios this trend was reversed.

The position of the wetting line was used to explain these trends. With the wetting line located downstream of the nip, reducing the hydrostatic head or increasing the speed ratio caused the wetting line to move towards the point of minimum separation between the roll surfaces, X_0. This resulted in the gap between the two roll surfaces at the film split point, H_D, decreasing. H_D is intimately linked with the outgoing film thickness, as shown using the work of Landau and Levich (1942); a smaller H_D results in a thinner film. Similarly, with the wetting line located upstream of the nip, reducing the hydrostatic head or increasing the speed ratio caused the wetting line to move in the negative X direction, i.e. away from X_0, resulting in a larger value for H_D and consequently a thicker film.

Finally, a sequence of visualisations of the flow in both the reservoir and the nip

region of the reverse coater were presented. The flow structures were compared against a finite element solution of the Navier–Stokes equations and found to be in excellent agreement.

Following the earlier work of Malone (1992) the bead–break instability arising in forward meniscus roll coating was investigated in chapter 4. A lubrication model based on the work of Gaskell *et al.* (1995) was formulated for the stable bead and a perturbation hypothesis used to determine the necessary conditions for the upstream meniscus to remain stable.

The stable bead model was found to predict either two, one or zero positions for the upstream meniscus depending on the speed ratio (with all other parameters held constant). By using the perturbation hypothesis it was shown that: (i) where two upstream meniscus positions are predicted just one of these is stable to perturbations (and hence observable in practice); (ii) when only one upstream meniscus position is predicted this corresponds to the onset of the bead–break instability; (iii) when no upstream meniscus position is predicted a stable bead cannot exist.

A detailed experimental investigation is made, and the positions of the upstream and downstream menisci for the stable bead were shown to be in good agreement with those calculated using the analytical model, for a wide range of inlet fluxes, minimum gap settings and speed ratios. A series of striking pictures of the bead were presented showing graphically its evolution as speed ratio was increased.

The onset of the bead break instability was also investigated experimentally. The lower roll speed was fixed and the speed ratio increased until the upstream meniscus became unstable; marked by the point where the upstream meniscus accelerated rapidly towards the downstream one such that the two collide and the coating bead collapses. This results in loss of transfer of fluid from the lower to the upper roll. The agreement between the predictions of the perturbation model and the experimental data is excellent, particularly when one considers the dynamic contact angle was fixed at one value throughout the analysis.

Finally a design criterion based on the bead–break instability was outlined. This specifies a maximum speed for the web and a minimum speed for the lower roll (roll

2) to minimise air entrainment into the feed reservoir.

Chapter 5 demonstrates the use of the finite element method to solve the Navier–Stokes equations in two–dimensions for free surface coating flow problems. The capillary climb effect of a meniscus up the face of a knife coater was investigated both computationally and experimentally. This particular arrangement was chosen as it is representative of a number of coating systems — a flexible blade coater, a roll flat–plate, the face of many slot coaters and the doctor blades used in direct gravure coating.

Results from the computational model are compared with experiments when the meniscus climbs the knife face. The predictions show good agreement with experimental data, in terms of the flow topology within the coating bead, the climb length up the face of the blade and film thickness measurements. A simple lubrication model used to predict the flux was also found to be in close agreement with experimental results. Both the computational and experimental results reveal the existence of a small eddy within the climb region.

Results show that as the corner angle of the blade was reduced the climb length decreased. This could have practical significance since reducing the size of the recirculation minimises the potential problem of air bubbles or particulates becoming trapped in the eddy — one possible cause of streaks on the final coated film.

Finally, an experimental investigation into the onset of ribbing was described. Starting with a set of conditions under which the meniscus was observed to climb the face of the blade, the effect of either (i) reducing the gap or (ii) advancing the corner of the plate in the X direction was explored. In both cases the climb length was observed to decrease before the meniscus pinned on the corner of the plate. Ribbing was not observed until the meniscus detached from the corner and retreated into the gap. The stability hypothesis of Pitts and Greiller (1961) and Savage (1977b) was used to analyse the apparent stabilising effect of the corner. It was shown that this was due to the large height gradient between the roll and plate at this point. This idea was extended to offer an explanation of the phenomena highlighted by Hasegawa and Sorimachi (1993) and Decré *et al.* (1996), who showed that a

taut wire positioned at the downstream meniscus can be used to stabilise a ribbed free–surface.

Chapter 6 gave details of a combined investigation into offset gravure (at a speed ratio of 1) and kiss coating (at a speed ratio greater than one). An investigation the offset gravure coating nip (where a deformable roll was pressed against a gravure roll) showed that as the nip pressure increased the film thickness of the deformable roll decreased. Also shown was that as the roll speeds increased, so did the film thickness on the deformable roll. This film thickness appeared to asymptote to a limiting value at higher roll speeds, the value of which was observed to depend on the gravure pattern.

For the kiss coating bead, with the web running faster than the roll, all the fluid on the incoming roll was observed to transfer to the web, and the two came into contact due to the generation of a sub–ambient pressure field within the bead. Based on these findings two analytical models using lubrication theory were derived; the first assumed that the tension in the web was so high that the fluid pressure did not affect the shape of the domain, whereas the second allowed for flexing of the web in response to the pressure in the fluid bead. The stiff web model was found to predict trends in agreement with experimental measurements of the meniscus positions but did not quantitatively match the corresponding experimental data. However, the flexible web model showed much better agreement with the same experimental data due to the inclusion of more realistic boundary conditions.

A perturbation hypothesis was used in conjunction with the two models, and the predictions compared with experimental data of critical web speed for the onset of ribbing, taken over a wide range of roll speeds and inlet film thicknesses. Both of the stability models showed good agreement with the experimental data.

Chapter 7 described a detailed, systematic, experimental study of reverse mode, direct gravure coating. Previous work in this area was reviewed in some depth so as to highlight the current shortcomings of our understanding about this particular coating process. A large parametric study into the effect of (i) web tension, wrap angle and thickness, (ii) web and roll speeds, (iii) fluid properties and (iv) cell

geometry, on the final wet coated web was made.

Neither the tension, wrap angle or web thickness were observed to have any effect on the wet film thickness on the web.

For a fixed gravure roll speed, the speed of the web had a remarkable effect. As the web speed was increased so too did the film thickness, up to a limiting value. At low speed ratios, S, the pickout from the gravure cell was found to be proportional to S^2, whilst at the higher speed ratios the pickout was proportional to S. This variation of film thickness could be used to influence the final coated film thickness in a typical industrial situation. It was also noted that for a fixed speed ratio a higher roll speed produces a thicker film on the web.

The effect of fluid properties, although considered by other workers as unimportant, were also shown to have an effect on the final film thickness. Decreasing the surface tension or increasing the viscosity both resulted in increased pickout from the gravure cells, and hence a thicker film. This, together with the data showing the effect of the web speed, revealed that the capillary number is, as in many coating processes, important in determining the film thickness.

The size of the gravure cell has been highlighted by other workers as an important parameter in determining the thickness of the coated film. However it was shown here, by studying the pickout characteristics of 6 different gravure rolls, that the effect of the cell shape, density and volume can *all* all affect the thickness of the final coated film. The empirical model of Benkreira and Patel (1993) was compared to the data presented here, and found to consistently overpredict the film thickness by up to an order of magnitude.

A series of visualisations of a typical gravure coating bead were taken by viewing it through the transparent web. As the speed ratio was increased the downstream meniscus was observed to move towards the position where the web and roll would first touch (due to the wrap angle) – the dry contact region – if no fluid were present. When the downstream meniscus came close to this point it became unstable, causing break up of the bead and streak formation on the web. As the roll speed was increased, the critical speed ratio for the onset of the fingering instability decreased.

Finally, some of the complex mechanisms underlying the gravure coating process were highlighted:

- The mechanism that transfers fluid from the downstream to the upstream meniscus operated at all speed–ratios, unlike the kiss–coater described in chapter 6.
- The web and roll came into contact at discrete positions along the length of the bead (i.e. in the axial direction of the roll) which caused scratching.
- A net negative pressure within the bead was also inferred, since the web could be momentarily depressed onto the gravure roll causing a stable bead to form.
- The web appeared to corrugate over the dry contact region, as illustrated using a shadowgraph technique.
- The length of the fluid bead outside the dry contact region was observed to remain constant as the wrap angle was increased.

Clearly the fluid dynamics of a gravure coating bead are extremely complicated, and require further investigation.

8.2 Suggestions for future work

In chapter 3, reverse coating with a hydrostatic head was described. A natural extension to this work would be to investigate the onset of the ribbing and cascade instabilities, and whether the onset of these can be influenced by the depth of fluid in the reservoir.

Chapter 4 introduced the bead–break instability in the context of forward roll coating. This work could be extended to reverse meniscus coating. A preliminary investigation has already been completed, which showed that either of the two menisci can lose stability. This would need to feature in any future model formulated to predict the onset of bead–break. The experimental investigation could also be extended to include the case where both the incoming roll surfaces have a film on them, as

studied by Wilson (1997). The bead–break instability could also be explored in the flow between two eccentric cylinders, as studied by Rabaud *et al.* (1990), Rabaud and Hakim (1991), Michelland (1992), Michelland *et al.* (1996) and Reinelt (1995).

Chapter 5 clearly showed the effect of a meniscus climbing the face of a knife coater resulting in a recirculation at the downstream tip. This work could be extended to different geometries, for example a flexible blade coater which can be used to coat at up to 5 m/s with viscosities up to 1 Pa s (Aidun and Triantafillipoulous (1997)). The conjecture about how a wire placed at a ribbed meniscus has a stabilising effect should also be studied further.

Chapter 6 gave details of a brief investigation into offset gravure coating operating at $S = 1$. The case when $S \neq 1$ should also be investigated, since this is commonly used in industrial situations. Also shown was an investigation into kiss coating at $S > 1$. The model was based on the Landau and Levich (1942) relationship, so is strictly valid for low capillary numbers only. By solving a model based on the Navier–Stokes equations and incorporating a flexible web this could be extended to higher capillary number regimes with the fluid domain better represented. A more sensitive experimental technique should also be developed to mark the onset of the ribbing instability observed here.

Chapter 7 showed details of a large parametric study into direct gravure coating. Despite this, there are still a many unanswered questions about the process. A range of well–defined, model gravure cells should be constructed, for example where the aspect ratio and shape of the cell is kept constant and just the volume of the cells varied, so that a systematic study into the effect of cell geometry on the film thickness can be carried out. The pressure profile in the bead also needs to be elucidated for a fuller understanding of the process, an arduous task when one considers the very small length scales associated with this three-dimensional time dependent flow.

References

AIDUN C.K. AND TRIANTAFILLOPOULOS N.G. 1997 Self–metered coating processes: High speed blade coating in *Liquid film coating* (*ed.* S.Kistler, P.M.Schweizer) Chapman and Hall.

ADACHI, T.J. *et al.* 1988 Coating studies between rotating roller and deformable flat–plate in *AIChE Spring National Meeting, New Orleans.*

ADRIAN, R.J. 1991 Particle-imaging techniques for experimental fluid-mechanics *Ann. Rev. Fluid Mech.* **23**, 261–304

ATKINS P.W. 1998 *Physical chemistry* Oxford University Press.

BABUSKA, I. AND AZIZ, A.K. 1972 Lectures on the mathematical foundations of the finite element method. *Mathematical foundations of the finite element method with applications to partial differential equations,* (*ed.* A.K. Aziz). Academic Press, New York, *pp.* 1–135.

BARLOW, E.J. 1967a Derivation of governing equations for self-acting foil bearings. *Trans. ASME, J. Lubr. Technol.* **89**(3), 334-340.

BARLOW, E.J. 1967b Self-acting foil bearings of infinite width. *Trans. ASME, J. Lubr. Technol.* **89**(3), 341-345.

BENJAMIN, D.F. 1994 Roll coating flows and multiple roll systems. PhD thesis. University of Minnesota.

BENJAMIN, D.F., ANDERSON, T.J. AND SCRIVEN, L.E. 1995 Multiple roll systems: steady-state operation. *AIChE J.* **41**(5), 1045–1060.

BENJAMIN, D.F. AND SCRIVEN, L.E. 1992 Coaters analyzed by form and function. *Ind. Coating Res.* **2**, 1–31.

BENKREIRA, H. AND COHU, O. 1998 Direct forward gravure coating on unsupported web. *Chem. Eng. Sci.* **53**(6),1223–1231.

BENKREIRA, H., EDWARDS, M.F. AND WILKINSON, W.L. 1981 Roll coating of purely viscous liquids. *Chem. Eng. Sci.* **36**, 429–434.

BENKREIRA, H., EDWARDS, M.F. AND WILKINSON, W.L. 1982 Mathematical modelling of the reverse and metering roll coating flow of Newtonian fluids. *Chem. Eng. Sci.* **37**(2), 277–282.

BENKREIRA, H. AND PATEL, R. 1993 Direct gravure roll coating. *Chem. Eng. Sci.* **48**(12), 2329–2335.

BIXLER, N.E. 1982 Stability of a coating flow. PhD thesis. University of Minnesota, Minneapolis.

BLAKE, T.D. AND RUSCHAK, K.J. 1979 A maximum speed of wetting. *Nature* **282**, 489–491.

BOLTON, B. AND MIDDLEMAN, S. 1980 Air entrainment in a roll coating system. *Chem. Engng. Sci.* **31**, 901–911.

BOOTH, G.L. 1970 *Coating equipment and processes.* Lockwood Publishing Company, New York.

BOURGIN, P. AND TAHIRI, N. 1995 Generalised Jeffery-Hamel flow: application to high velocity coating in *Mechanics of thin film coatings* (*ed.* Gaskell, Savage and Summers) World Scientific.

BRANSTON, R.E., CLARK, P.C., ERRICO, M., SCRIVEN, L.E., SHEEHAN, J.G., SUSZYNSKI, W.J., TAKAMURA,K. AND VODNICK, J.L. 1993 Weeping in blade coating .1. High-speed video and still macrophotography *Tappi J.* **77**(1), 131–138.

BRETHERTON, F.P. 1961 The motion of long bubbles in tubes. *J. Fluid Mech.* **10**, 166–188.

BROUGHTON, G., EGAN, L.W. AND STURKEN, C. 1950 The reverse roll principle of coating. *Tappi J.* **33**(7), 314–317.

BURLEY, R. AND KENNEDY, B.S. 1976 An experimental study of air entrainment at a solid/liquid/gas interface. *Chem. Eng. Sci.* **31**, 901–911.

BURLEY, R. AND JOLLY, R.P.S. 1984 Entrainment of air into liquids by a high speed continuous solid surface. *Chem. Eng. Sci.* **39** 1357–1372.

CARTER, G.C. 1985 The modelling and analysis of coating processes. PhD thesis. University of Leeds.

CARTER, G.C. AND SAVAGE, M.D. 1987 Ribbing in a variable speed two-roll coater. *Math. Engin. Ind.* **1**(1), 83–95.

CARVALHO, M.S. 1995 PhD Thesis. University of Minnesota, Minneapolis.

CARVALHO M.S. AND SCRIVEN L.E. 1995 Deformable roll coating: modelling of steady flow in gaps and nips in *Mechanics of thin film coatings* (*ed.* Gaskell, Savage and Summers) World Scientific.

CASTILLO M.E.G. AND PATERA A.T., 1997 Three–dimensional ribbing instability in symmetric forward–roll film–coating processes.*J. Fluid Mech.* **335**, 323–359

CHENG, D.C-H. AND SAVAGE, M.D. 1978 Onset of ribbing in direct rolling of Newtonian fluids. *T.L.P. Report No. 40, Warren Spring Laboratories.*

CLARKE, A. 1995 The application of particle tracking velocimetry and flow visualization to curtain coating. *Chem. Eng. Sci.* **50**(15), 2397–2407.

COHU, O. AND MAGNIN, A. 1995 Experimental investigations on roll coating with deformable rolls in *Mechanics of thin film coatings* (*ed.* Gaskell, Savage and Summers) World Scientific.

CONAN-DOYLE, A. in *Return of Sherlock Holmes*, Penguin 1982

COYLE, D.J. 1984 The fluid mechanics of roll coating: steady flows, stability, and rheology. PhD thesis. University of Minnesota, Minneapolis.

COYLE, D.J. 1997 Self–metered coating processes – Knife and roll coating in *Liquid film coating* (*ed.* S.Kistler, P.M.Schweizer) Chapman and Hall.

COYLE, D.J. 1988a Experimental studies of flows between deformable rollers in *A.I.Ch.E. Spring National Meeting, New Orleans.*

COYLE, D.J. 1988b Forward roll coating with deformable rolls: A simple one-dimensional elastohydrodynamic model. *Chem. Eng. Sci.* **43**(10), 2673–2684.

COYLE, D.J., MACOSKO, C.W. AND SCRIVEN, L.E. 1986 Film-splitting flows in forward roll coating. *J. Fluid Mech.* **171**, 183–207.

COYLE, D.J., MACOSKO, C.W. AND SCRIVEN, L.E. 1990*a* A simple model of reverse roll coating. *Ind. Eng. Chem. Res.* **29**(7), 1416–1419.

COYLE, D.J., MACOSKO, C.W. AND SCRIVEN, L.E. 1990*b* The fluid-dynamics of reverse roll coating. *AIChE J.* **36**(2), 161–174.

COYNE, J.C. AND ELROD, H.G. 1969 An exact asymptotic solution for a separating film. *Trans. A.S.M.E., J. Lub. Tech.* October, 651–652.

COYNE, J.C. AND ELROD, H.G. 1970 Conditions for the rupture of a lubricating film. Part 1: Theoretical model. *Trans. A.S.M.E., J. Lub. Tech.* **92**(3), 451–456.

COYNE, J.C. AND ELROD, H.G. 1971 Conditions for the rupture of a lubricating film. Part 2: New boundary conditions for Reynolds equation. *Trans. A.S.M.E., J. Lub. Tech.* **93**, 156–167.

DANIELS N., 1999 Instabilities in roll and slot coating flows. PhD Thesis. University of Leeds.

DECRÉ, M. 1994 Etude experimentale des comportements de l'interface dans l'enduisage par rouleaux. PhD Thesis. U.Paris VI.

DECRÉ, M. 1997 Thin liquid films and coating processes: Diagnostics for coating processes. *von Karman Institute for Fluid Dynamics, Lecture Series 1997–06.*

DECRÉ, M., GAILLY, E. AND BUCHLIN, J.M. 1995 Meniscus shape experiments in forward roll coating. *Phys. Fluids* **7**(3), 458–467.

DECRE, M., GAILLY, E. AND BUCHLIN, J.M. 1996 Meniscus control by string in roll coating experiment. *AIChE J.* **42**(6), 1583–1589.

DERYAGIN, B.M. AND LEVI, S.M. 1964 *Film coating theory.* Focal Press, London and New York.

DOWSON, D. AND TAYLOR, C.M. 1979 Cavitation in bearings. *Ann. Rev. Fluid Mech.* **11**, 35–66.

DUSSAN V., E.B. 1979 On the spreading of liquids on solid surfaces: static and dynamic contact lines. *Ann. Rev. Fluid Mech.* **11**, 371–400.

DURST, F. AND WAGNER, H. 1997 in *Liquid film coating* (*ed.* S.Kistler, P.M.Schweizer) Chapman and Hall.

ENGSTRÖM, G. AND RIGDAHL, M. 1989 Stalagmite formation during blade coating – effects of process conditions. *Coating conference proceedings – Atlanta*, 59–63 TAPPI press

ESHEL, A. AND ELROD, H.G., JR. 1965 The theory of the infinitely wide, perfectly flexible, self-acting foil bearing. *Trans. A.S.M.E., J. Basic Eng.* **87**, 831–836.

ESHEL,A. AND ELROD,H.G., JR. 1967 Stiffness effects on the infinitely wide foil bearing. *Trans. A.S.M.E., J. Lub. Technol.* **89**(1), 92–97.

FALL, C. 1978 Surface ribbing of a thin viscous fluid film emerging from a spreader or roller. *Trans. A.S.M.E. J. Lub. Technol.* **100**, 462–466.

FALL, C. 1982 A theoretical model of striated film-rupture. *Trans. A.S.M.E. J. Lub. Technol.* **104**, 164–167.

FALL, C. 1985 A theoretical model of striated film-rupture applied to the cylinder plane. *Trans. A.S.M.E. J. Tribol.* **107**, 419–422.

FRENKEL, J. 1946 Kinetic theory of liquids. Oxford University Press, Oxford.

FUKAZAWA, K., BENJAMIN, D.F. AND SCRIVEN, L.E. 1992 Reverse roll coater model. *AIChE* 5^{th} *Int. Coat. Proc. Sci. Tech. Symp.*

GASKELL, P.H. 1990 Private communication.

GASKELL, P.H., INNES, G.E. AND SAVAGE, M.D. 1998a An experimental investigation of meniscus roll coating. *J.Fluid Mech.* **355**, 17–44.

GASKELL, P.H., KAPUR, N. AND SAVAGE, M.D. 1999a Bead–break in forward meniscus coating – *in preparation.*

GASKELL, P.H., KAPUR, N., SAVAGE, M.D. AND THOMPSON, H.M. 1999b Reservoir fed reverse roll coating – *in preparation.*

GASKELL, P.H., REES, S.R., SAVAGE, M.D. AND STOREY, S.P. 1998b A mathematical model of roll-to-web kiss coating. *Trans. I. Chem. E.* **76**(A), 29–37.

GASKELL, P.H., SAVAGE, M.D., SUMMERS, J.L. AND THOMPSON, H.M. 1995 Modelling and analysis of meniscus roll coating. *J. Fluid Mech.* **298**, 113–137.

GASKELL, P.H., SAVAGE, M.D. AND THOMPSON, H.M. 1998c Stagnation-saddle points and flow patterns in Stokes flow between contra-rotating cylinders, *J.Fluid Mech.* **370**, 221–247.

GATCOMBE, E.K. 1945 Lubrication characteristics of involute spur gears — a theoretical investigation. *Trans. A.S.M.E.* **67**, 177–188.

GIBBS, J.W. 1906 Scientific Papers.**1** 326 Dover Reprint, Dover, New York, (1961)

GLAISTER, P. 1995 A numerical scheme for steady-supercritical flows with boundary fitted coordinates. *Int. J. Num. Methods for Heat and Fluid Flow* **5**(5), 923–931.

GRALD, E.W., CHAKRABARTI, M. AND SUBBIAH, S. 1994 The spectral element method and its application to modelling coating flows. *AIChE 7th Int.Coat.Proc.Sci.Tech.Symp.*

GRAVURE PROCESS AND TECHNOLOGY 1991 Gravure process and Technology *pub. Gravure Association of America Rochester, NY.*

GREENER, J. AND MIDDLEMAN, S. 1981 Reverse roll coating of viscous and viscoelastic liquids. *Ind. Eng. Chem. Fundam.* **20**, 63–66.

HANUMANTHU, R. AND SCRIVEN, L.E. 1996 Coating with patterned rolls and rods. *TAPPI J.* **79**(5), 126–137.

HASEGAWA, T. AND SORIMACHI, K. 1993 Wavelength and depth of ribbing in roll coating and its elimination. *AIChE J.* **39** (6), 935–945.

HARDING, R.T. 1993 Private communication.

HEINRICH, J.C. AND CONNOLLY, D. 1992 Three Dimensional Finite Element Analysis of Self-Acting Foil Bearings. *Comp. Meth. Appl. Mech. Eng.***100**, 31–43.

HIGGINS, B.G. AND SCRIVEN, L.E. 1980 Capillary pressure and viscous pressure drop. set bounds on coating bead operability, *Chem.Eng.Sci.* **35**, 673–682.

HO, W.S. AND HOLLAND, F.A. 1978 Between-rolls metering coating technique: a theoretical and experimental study. *Tappi J.* **61**(2), 53–56.

HOOD, P. 1976 Frontal solution program for unsymmetric matrices. *Int. J. Num. Meth. Eng.* **10**, 379–399.

HOPKINS, M.R. 1957 Viscous flow between rotating cylinders and a sheet moving between them. *Brit. J. Appl. Phys.* **8**, 442–444.

INNES, G.E. 1993 An experimental and theoretical study of viscous lifting in tribology. PhD thesis. University of Leeds.

INNES, G.E. 1995 Private communication.

INNES, G.E., GASKELL, P.H. AND SAVAGE, M.D. 1998 Cusps as a source of air entrainment in roll coating systems. *Ind. Coating Res.* **4**, 19–40.

IRONS, B.M. 1970 A frontal solution program for finite element analysis. *Int. J. Num. Meth. Eng.* **2**, 5–32.

ISAKSSON, P., RIGDAHL, M., AND BOUSFIELD, D.W. 1997 Development of subambient pressures and cavitation in the blade coating process. *Ind. Eng. Chem. Res.* **36**(7), 2834–2840.

KAHLINA, S.J. AND EDLUND D.E. 1978 Factors influencing the coat weight in blade coating with beveled blades: theory and practice. *TAPPI Coating Conference Proceedings – Atlanta*, 13–29 TAPPI press.

KELMANSON, M.A. 1983 Boundary integral equation solution of viscous flows with free surfaces. *J. Eng. Math.* **17**, 329–343.

KHESHGI H.S. 1997 Physics and material interactions of coating processes: The fate of thin liquid films after coating in *Liquid film coating* (*ed.* S.Kistler, P.M.Schweizer) Chapman and Hall.

KISTLER, S.F. 1983 The fluid mechanics of curtain coating and related viscous free surface flows with contact lines. PhD thesis. University of Minnesota, Minneapolis.

KISTLER, S.F. AND SCRIVEN, L.E. 1983 Coating flows. In *Computational analysis of polymer processing* (*eds.* J.R.A. Pearson AND S.M. Richardson), London and New York: Applied Science, 243–299.

KISTLER, S.F. AND SCRIVEN, L.E. 1984 Coating flow theory by finite-element and asymptotic analysis of the Navier-Stokes system. *Int. J. Num. Meth. Fluids* **4**(3), 207–229.

KISTLER, S.F. AND SCRIVEN, L.E. 1994 The teapot effect — sheet-forming flows with deflection, wetting and hysteresis. *J. Fluid Mech.* **263**, 19–62.

LANDAU, L. AND LEVICH, B. 1942 Dragging of a liquid by a moving plate. *Acta Physicochimica U.R.S.S.* **XVII**(1–2), 42–54.

LARKIN, M.J. 1984 Gravure coaters in *Web processing and converting technology and equipment*(*ed.* D. Satas) Van Nostrand Reinhold Company.

LEACH, R.H. AND PIERCE, R.J. 1993 The printing ink manual. BluePrint

LIAO, S.J. AND CHWANG, A.T. 1996 General boundary-element method for non-linear problems. *Int. J. Num. Meth. Fluids* **23**(5), 467–483.

LICHT, L. 1968 An experimental study of elastohydrodynamic lubrication of foil bearings. Part 1 - displacement in the central zone. *Trans. A.S.M.E. J., Lubr. Tech.* **90**(1), 199–220.

LINDBLAD, N.R., TIFT, R. AND WATSON P.K. 1988 The metering of ink in the grooves of a gravure roll. *J. Imaging Technol.* **14**, 140–143

LODGE, R 1994 Private communication.

MALONE, B. 1992 An experimental investigation of roll coating phenomena. PhD thesis. University of Leeds.

MERZKIRCH, W. 1974 Flow visualisation. Academic Press Inc. London UK

MICHALLAND, S. 1992 PhD thesis. U. Paris VI

MICHALLAND, S., RABAUD, M. AND COUDER, Y. 1996 Instabilities of the upstream meniscus in directional viscous fingering. *J. Fluid Mech.* **312**, 125–148.

MOHANTY, K.K. 1981 Fluids in porous media: two phase distribution and flow. PhD thesis. University of Minnesota, Minneapolis.

MOUSSALLI, P. 1998 Private communication.

MUNTER, J.D. 1998 Private communication.

O'CONNELL, A. 1989 Observations of Air Entrainment and the Limits of Coatability. PhD Thesis. Herriot-Watt University.

OLIVER, J.F., HUH, C. AND MASON, S.G. 1977 Resistance to spreading of liquids by sharp edges *J. Colloid Interf. Sci.***59**(3)

PADDAY, J.F. 1971 Cohesive properties of thin films of liquids adhering to a solid surface in *Special discussion Faraday Soc. on 'Thin liquid films and boundary layers'* 64–74 Academic Press, London.

PATEL, R. 1989 Fluid mechanics of direct gravure roll coating. PhD Thesis. University of Bradford.

PATEL, R. AND BENKREIRA H. 1991 Gravure roll coating of newtonian liquids. *Chem. Eng. Sci.* **46**(3), 751–756.

PEARSON, J.R.A 1985 *Mechanics of Polymer Processing*, Elsevier Applied Science.

PEARSON, J.R.A. 1960 The instability of uniform viscous flow under rollers and spreaders. *J. Fluid Mech.* **7**, 481–500.

PITTS, E. AND GREILLER, J. 1961 The flow of thin liquid films between rollers. *J. Fluid Mech.* **11**, 33–50.

POWELL, C.A. 1999 A theoretical investigation of gravure coating. PhD thesis. University of Leeds.

PRANCKH, F.R. AND COYLE D.J. 1997 Self metered coating processes – Elastrodynamic coating systems in *Liquid film coating* (*ed.* S.Kistler, P.M.Schweizer) Chapman and Hall.

PRANCKH, F.R. AND SCRIVEN, L.E. 1990 Elastrohydrodynamics of blade coating. *A.I.Ch.E.J* **36**(4), 587–597 TAPPI press.

PRANDTL, L. 1904 Motion of fluids with very little viscosity. *Tech. Memor. Nat. Adv. Comm.* **452**

PULKRABREK, W.V. AND MUNTER, J.D. 1983 Knurl roll design for stable rotogravure coating. *Chem. Eng. Sci.* **38**(8), 1309–1314.

RABAUD, M. AND HAKIM V. 1991 In *instabilities and non equilibrium structures III* (*ed.* Tirapegui and Zeller) Kluwer Academic, Dordrecht

RABAUD, M., MICHALLAND, S. AND COUDER Y. 1990 Dynamical regimes of directional viscous fingering - spatiotemporal chaos and wave-propagation *Phys Rev. Lett.* **64**(2), 184–187.

RAMP, J.W. 1983 The angle of tip tube blade coating. *Coating conference proceedings – Atlanta*, 83–95 TAPPI press.

REES, S. 1995 An experimental and theoretical investigation of gravure roll coating. PhD thesis. University of Leeds.

REINELT, D.A. 1995 The primary and inverse instabilities of directional viscous fingering. *J. Fluid Mech.* **285**, 303–327.

REYNOLDS, O. 1886 On the theory of lubrication and its application to Mr. Beauchap Towers experiments, including an experimental determination of the viscosity of olive oil. *Phil. Trans. Roy. Soc.* A**177**, 157–234.

RICHARDSON, C.A. 1996 A theoretical investigation of reverse roll coating. PhD thesis. University of Leeds.

ROPER, J., III AND ATTAL, J.F. 1993 Evaluations of high–speed runnability using pilot coater data, rheological measurements, and computer modelling. *Coating conference proceedings – Atlanta*, 107–114 TAPPI press.

RUSCHAK, K.J. 1976 Limiting flow in a pre-metered coating device. *Chem. Eng. Sci.* **31**, 1057–1060.

RUSCHAK, K.J. 1980 A method for incorporating free boundaries with surface tension in finite element fluid-flow simulators. *Int. J. Num. Meth. Eng.* **15**, 639–648.

RUSCHAK, K.J. 1982 Boundary conditions at a liquid/air interface in lubrication flows. *J. Fluid Mech.* **119**, 107–120.

RUSCHAK, K.J. 1985 Coating flows. *Ann. Rev. Fluid Mech.* **17**, 65–89.

SAITA, D.A. AND SCRIVEN L.E. 1985 Elastohydrodynamics and flexible blade coating. *Coating conference proceedings – Atlanta*, 13–21 TAPPI press.

SAITO, H. AND SCRIVEN, L.E. 1981 Study of coating flow by the finite element method. *J.Comput.Phys.* **42**, 53–76.

SARTOR, L., 1990 Slot coating: fluid mechanics and die design. PhD thesis. University of Minnesota, Minneapolis.

SAVAGE, M.D. 1977a Cavitation in lubrication. Part 1. On boundary conditions and cavity-fluid interfaces. *J. Fluid Mech.* **80**(4), 743–755.

SAVAGE, M.D. 1977b Cavitation in lubrication. Part 2. Analysis of Wavy Interfaces. *J. Fluid Mech.* **80**(4), 757–767.

SAVAGE, M.D. 1982 Mathematical models for coating processes. *J. Fluid Mech.* **117**, 443–455.

SAVAGE, M.D. 1984 Mathematical model for the onset of ribbing. *AIChE Journal* **30**(6), 999–1001.

SAVAGE, M.D. 1992 Film split ratios in forward roll coating. *A.I.Ch.E. National Meeting, New Orleans.*

SCHWARTZ, L.W., MOUSSALLI, P., CAMPBELL, P. AND ELEY, R.R. 1998 Numerical modelling of liquid withdrawal from gravure cavities in coating operations. *Trans. I. Chem. E.* **76**(A), 22–28.

SCHWEIZER, P.M. 1988 Visualisation of coating flows *J.Fluid Mech.* **193**, 285–302

SCHWEIZER, P.M. 1997 Methods of investigating coating processes: Experimental methods *Liquid film coating* (*ed.* S.Kistler, P.M.Schweizer) Chapman and Hall.

SHAPIRO, A.H. 1954 Free surface water table. *Physical Measurements in Gas Dynamics and Combustion High Speed Aerodynamics and Jet Propulsion* **9**, 309–321 pub. Princeton University Press, Princeton, New Jersey.

SHIKHMURZAEV, Y.D. 1993 The moving contact line on a smooth solid surface. *Int. J. Multiphase Flow* **19**(4), 589–610.

SHIKHMURZAEV, Y.D. 1994 Mathematical modelling of wetting hydrodynamics. *Fluid Dyn. Res.* **13**(1), 45–64.

SHIKHMURZAEV, Y.D. 1996 Dynamic contact angles and flow in the vicinity of moving a contact line. *AIChE J.* **42**(3), 601–612.

SILLIMAN, W.J. AND SCRIVEN, L.E. 1980 Separation flow near a static contact line: Slip at a wall and shape of a free surface. *J.Comput.Phys.* **34**, 287–313.

STAHL, J.W., WHITE, K.J. AND DECKERT, K.L. 1974 Dynamic response of self-acting foil bearings. *I.B.M. J. of R. and D.* **18**, 513–520.

STIEBER, W. 1933 *Das Schwimmlager, V.D.I. (Berlin).*

STOREY, S.P. 1996 A theoretical investigation of the flow between a web and roll, with application to gravure coating. PhD thesis. University of Leeds.

SULLIVAN, T., MIDDLEMAN, S. AND KEUNINGS, R. 1987 Use of a finite-element method to interpret rheological effects in blade coating. *AIChE J.* **33**(12), 2047–2056

SWIFT, H.W. 1931 The stability analysis of lubricating films in journal bearings. *Proc. Inst. Civ. Engrs.* **223**, 267.

TAYLOR,G.I. 1963 Cavitation of a Viscous Fluid in Narrow Passages. *J. Fluid Mech.* **16**, 595-619.

THIERY, L., PRENEL, J.P. AND PORCAR R. 1996 Theoretical and experimental intensity analysis of laser light sheets for flow visualization *Optics Communications* **123**(4–6), 801–809.

THOMPSON, H.M. 1992 A theoretical investigation of roll coating phenomena. PhD Thesis. University of Leeds.

THARMALINGHAM, S. AND WILKINSON W.L. 1978 The coating of Newtonian liquids onto a roll rotating at low speeds. *Polymer Engineering and Science* **18**(15)

TRIANTAFILLOPOULOS N.G. AND ALTUG N. 1991 A comparitative study of forces in blade coating. *AIChE Forest Products Symposium Proceedings - Atlanta*, 141–158 TAPPI press.

TRICOT, Y-M 1997 Surfactants: static and dynamic surface tension in *Liquid film coating* (*ed.* S.Kistler, P.M.Schweizer) Chapman and Hall.

VODNICK, J.L. *et al.*, 1993 Weeping in blade coating. Part II: SEM and X-ray microanalysis of microtome–sectioned weeps. *Coating conference proceedings – Atlanta*, 87–96 TAPPI press.

VOGEL, S.M. AND GROOM, J.L. 1974 White light interferometry of elastohydrodynamic lubrication of foil bearings. *I.B.M. J. of R. and D.* **18**, 521–528.

WALKER, D.J. 1995 A computational and theoretical investigation of slide and forward roll coating phenomena. PhD thesis. University of Leeds.

WANG, F.J. AND DOMOTO, G.A. 1994 Free-surface Taylor vortices. *J. Fluid Mech.* **261**, 169–198.

WICKS, P.J., DECRÉ, M., PLANQUART, Ph. AND BUCHLIN, J.M. 1995 Flow topology associated with disjoint eddies in an asymmetric film-splitting problem. *Phys. Rev.* E **52**(2), R1281–R1284.

WILKINSON W.L. 1975 Entrainment of air by a solid surface entering a liquid/air interface. *Chem. Eng. Sci.* **30**, 1227–1230.

WILSON, M. 1997 Free surface flows between co–rotating and contra–rotating cylinders. PhD Thesis. University of Leeds.

WILSON, S.D.R. 1982 The drag-out problem in film coating theory. *J. Eng. Math.* **16**, 209–221.

YOUNG, T. 1805 An essay on the cohesion of fluids. *Phil. Trans. R. Soc. Lond.* **95**, 65–87.

YOUNG, A.E. 1997 A theoretical and experimental investigation of deformable roll coating. PhD Thesis. University of Leeds.

ZIENKIEWICZ, O.C. 1977 *The finite element method* (3*rd* edition). McGraw-Hill.

ZINK, S.C. 1979 Coating processes in *Encyclopedia of chem. tech. (3rd ed.)* John Wiley.